DISSERTATION

SIMULATION OF SUCCESSIVE EVENTS FOR MULTI-HAZARD COMMUNITY RESILIENCE ANALYSIS

Submitted by

Mojtaba Harati

Department of Civil and Environmental Engineering

In partial fulfillment of the requirements

For the Degree of Doctor of Philosophy

Colorado State University

Fort Collins, Colorado

Fall 2024

Doctoral Committee:

Advisor: John W. van de Lindt

Martin Shields
Paul Heyliger
Gaofeng Jia

ABSTRACT

SIMULATION OF SUCCESSIVE EVENTS FOR MULTI-HAZARD COMMUNITY RESILIENCE ANALYSIS

This dissertation, entitled "*Simulation of Successive Events for Multi-hazard Community Resilience Analysis*," aims to present an integrated framework for enhancing community resilience against natural hazards, with a specific focus on earthquakes and their associated impacts, such as aftershocks and tsunamis. These natural hazards pose significant threats to both coastal and non-coastal communities, leading to loss of life, injuries, and substantial socio-economic damage.

A key approach to mitigating these risks is through community resilience analysis, which involves modeling the vulnerability of community infrastructure to combined source earthquake and its subsequent risks—aftershocks or tsunamis in coastal zones. In contrast to using separate fragility curves, this study develops combined earthquake-tsunami and mainshock-aftershock fragility models for a basic portfolio of reinforced concrete (RC) and woodframe structures. Governing parameters for 2D and 3D fragility functions tailored to these prototype buildings are presented, providing accessible tools for informed decision-making and mitigation strategies in community-level studies.

The primary objectives are to model infrastructure vulnerability to successive seismic events and provide insights for resilience-informed decision-making. By identifying key vulnerabilities and assessing risk-based damage, dislocation, and functional recovery, the research significantly contributes to multi-hazard engineering. The proposed methodology and fragility models aim to enhance resilience-informed decision-making, allowing for strategies to improve community resilience.

DEDICATION

To my beloved parents and sister!

ACKNOWLEDGEMENTS

I am profoundly grateful to my advisor, Professor John van de Lindt, for his invaluable guidance, support, insights, and constant encouragement throughout my Ph.D. studies. His mentorship not only steered me through the complexities of my research but also encouraged me to explore a wide array of intriguing topics within my field. Under his thoughtful and enthusiastic direction, I have grown immensely both professionally and personally. I also extend my gratitude to the other esteemed members of my doctoral committee, Dr. Martin Shields, Dr. Paul Heyliger, and Dr. Gaofeng Jia, for their additional guidance, valuable ideas, and constructive critiques, which have been crucial in shaping my research journey.

This research was generously supported by the Center for Risk-Based Community Resilience Planning, a NIST-funded Center of Excellence. The Center is funded through a cooperative agreement between the U.S. National Institute of Standards and Technology and Colorado State University (NIST Financial Assistance Award Numbers: 70NANB15H044 and 70NANB20H008). The views expressed are those of the presenter and may not represent the official position of the National Institute of Standards and Technology or the U.S. Department of Commerce. During my graduate studies, I was honored to receive several prestigious awards and scholarships, including the Anthony P. Chrest Memorial Graduate Scholarship from Colorado State University, recognition as a PhD Fellow at the 2023 UNL Durham School of Architectural Engineering and Construction PhD Symposium, the CEE Department Scholarship from Colorado State University in 2022 & 2023, and a scholarship from the Harold H. Short Chair endowment in 2021. Additionally, I acknowledge the Department of Civil and Environmental Engineering at

Colorado State University for offering me a teaching opportunity in the summer of 2024, which significantly enhanced my educational experience.

I am deeply appreciative of the support, encouragement, and friendship of my fellow graduate students at Colorado State University, who have been my companions and confidantes throughout this academic journey. Finally, my heartfelt thanks go to my parents and family for their unconditional love, sacrifices, guidance, and encouragement. Their unwavering support has been my foundation, and without them, I would not have reached this significant milestone in my life. Their belief in my abilities has always pushed me to excel and persevere, even under challenging circumstances.

TABLE OF CONTENTS

LIST OF TABLES

LIST OF FIGURES

CHAPTER 1: INTRODUCTION

1.1 Background and Motivations

Although tsunamis are less frequent than other coastal-related natural hazards such as hurricanes and floods, they can lead to catastrophic economic losses and fatalities in coastal communities. The structural and non-structural damage to the built environments is often significant and associated with long-term consequences cascading into adverse social and economic systems. This is mainly due to the fact that tsunami damage is inherently from successive hazards composed of earthquake and tsunami. In this regard, tsunami usually hits a building that already got damaged by the source earthquake. In the 2011 Tohoku-oki earthquake and tsunami, it was reported that approximately 19000 people lost their lives and 6000 people were injured, and another 342000 were dislocated from their homes (Fraser et al., 2013; Kajitani et al., 2013). It is also estimated by Kajitani et al., (2013) that the earthquake and tsunami caused 211 billion US dollars in direct damage, where significant national-scale economic impacts were observed that were well beyond the directly impacted region, substantially disrupting numerous business sectors. In this regard, Figure 1-1 shows the direct losses (in billions of US dollars) for different events and countries in the past.

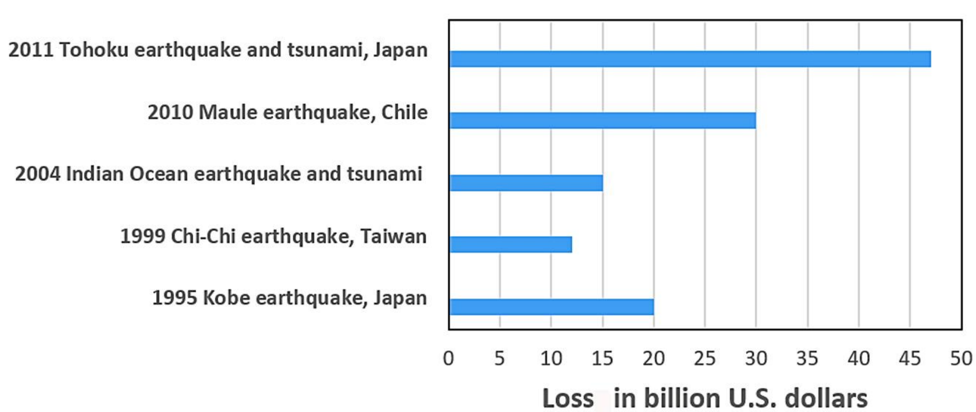

Figure 1-1. Direct economic loss due to successive events (here, earthquake and tsunami) after 1995

Another example of having structural and non-structural damage from successive events is when a community is exposed to relatively strong earthquakes with its following aftershocks. In this regard, structural systems can get softened when subjected to mainshocks. So, the aftershocks can impart more damage on them since they already got damaged by the source earthquake.

The impacts of natural hazards on the built environment can be mitigated by using community resilience as an analytical tool to manage, absorb, and adjust to the abrupt changes within the community and to return to the former (or improved) community functional condition in a reasonable timeframe following a natural hazard such as a tsunami and the source earthquake (Koliou et al., 2020). After an event, the recovery process of a community depends not only on the degree of infrastructure damage (Wang and van de Lindt, 2021) but also on a number of other non-physical conditions. In other words, the initial damage to the infrastructure significantly impacts the functionality and recovery path of complex socioeconomic institutions within a community (Wang et al., 2021; Wang and van de Lindt, 2022; Watson et al., 2020; Zhang and Peacock, 2009). Regardless, community resilience frameworks require an appropriate estimate of the initial damage to a community's infrastructure following a natural hazard.

As mentioned earlier, resilience is defined as the ability to plan for, absorb, and rapidly recovery from adverse events (PPD, 2014). Planning to ensure this rapid recovery ideally requires the ability to model communities to select polices that impact resilience. Community resilience modeling is often based on quantifying metrics that can help with decision-making and mitigation planning. These metrics provide quantitative measures to assess post-event impacts of natural hazards on physical and socio-economic systems within a community. Resilience and performance-based design (PBD) frameworks on different single- and multi-hazard events have been proposed in the literature, initially inspired by the successful implementation of PBD in earthquake engineering and seismic provisions (Günay and Mosalam, 2013), enabling a community-scale study. In recent years, PBD frameworks have been extended from seismic areas to different natural hazards, including the PBD methodologies on coastal (González-Dueñas and Padgett, 2021) and hurricane-related (Barbato et al., 2013) research, wind engineering (Spence and Arunachalam, 2022), and tsunami engineering (Attary et al., 2017a, 2021), among others. Uncertainty propagation from several elementary parts lies at the intersection of these PBD frameworks, where the risk of probability of failure is disaggregated into several components using the total probability theorem (Barbato et al., 2013). Although there are minor variations in these elementary parts across different PBD frameworks concerning various natural hazards, the failure risk of a system or a community block can be generally disaggregated into some primary categories incorporating hazard analysis, characterization of structural systems, structural analysis, damage analysis, and risk analysis. The steps of structural characterization and structural analysis for PBD methods are often merged to form functions known as fragility curves/functions. In order to develop a community-scale model, fragility functions must be developed for different types of buildings and assigned to each building to predict damage.

Earthquake fragility curves are prevalent in the literature (Akhoondi and Behnamfar, 2021; Bandyopadhyay et al., 1990; Chen et al., 2022; Kazantzi et al., 2008; Li et al., 2014; C. Xu et al., 2018). Additionally, there is a growing body of research on the tsunami fragility curves for building structures, which include both empirical and physics-based fragility functions. The majority numbers of tsunami fragility curves developed in the past (e.g., Chua et al., 2021; Paez-Ramirez et al., 2020; Suppasri et al., 2011) are created through empirical and statistical methods based on the inundation depth of the tsunami as the reference intensity measure (IM). Inundation depth is often selected as the IM for empirical-based tsunami fragility curves because the damage levels witnessed in the aftermath of a tsunami can be better correlated with the tsunami inundation depth observed and recorded from the external walls of building structures (Petrone et al., 2017); and presumably the exact velocity in not known in most cases. Nonetheless, numerical evidence suggests that incorporating flow velocity can enhance fragility models, especially in predicting severe structural damage states. It proves particularly significant for coastal sites where inundation depth may not be exceedingly high (Borrero et al., 2015; Charvet et al., 2015; De Risi et al., 2017).

Several past studies focused on the generation of physics-based tsunami fragility curves for building structures. These studies used the Nonlinear Static Procedure (NSP) as the primary structural analysis approach to derive fragility curves with the total tsunami force distributed along the height of a probabilistic-based structural model (Alam et al., 2018a; Attary et al., 2017b; Belliazzi et al., 2021; Del Zoppo et al., 2021, 2022; Ferrotto and Cavaleri, 2021; Karafagka et al., 2018; Ma et al., 2021; Medina et al., 2019; Petrone et al., 2017). However, a common aspect of these studies, especially those focusing on far-field tsunami events, is that they often derive physics-based tsunami fragility curves based solely on the estimated tsunami force. They tend to overlook the potential damaging effects of the source earthquake that triggers the tsunami. This approach is generally applicable in locations affected by far-field tsunamis, as these areas are typically distant from the earthquake epicenter and, consequently, are not directly impacted by the seismic waves of the initiating earthquakes. As a result, most resilience-based frameworks for earthquake and tsunami hazards employ two separated fragility curves with one for earthquake events and the other for far-field tsunami hazards, and then use a statistics-based superposition approach to combine the effects of the two correlated hazards on the built environments (e.g., Burns et al., 2021; Capozzo et al., 2019; Goda, 2020; Goda et al., 2021; Ishibashi et al., 2021).

However, there are some studies that tried to develop fragility functions incorporating the effects of both the source earthquake and near-field tsunami hazards simultaneously.

Park et al. (2012) generated collapse-level tsunami fragility curves using an equivalent single degree of freedom (SDOF) system and a two-phase successive analysis to incorporate both earthquake and tsunami hazards. The deterministic SDOF model was first subjected to several ground motions (GMs) scaled to two different intensity levels, i.e., the design basis earthquake (DBE) and maximum considered earthquake (MCE) levels, through nonlinear time history analysis (NTHA). Subsequently, tsunami forces are applied to the damaged model using an NSP analysis to determine the final coupled demands of the source earthquake and tsunami. They reported that the inclusion of earthquake effects considerably increased the collapse failure probability. Rossetto et al. (2019) later confirmed that a successive analysis procedure, including the NTHA and NSP phases, is an appropriate analytical approach for response prediction of a structure subjected to earthquakes and earthquake-trigged tsunami events. To encompass the effects of both hazards for the fragility curve development, Petrone et al. (2020) used a two-phase sequential NTHA procedure, one NTHA for earthquake and the other for tsunami loading. In contrast to the simple SDOF model used by Park et al. (2012) for successive simulation, Petrone et al. (2020) utilized a more complex nonlinear multi-story building model with deterministic parameters but without including uncertainty propagation for the studied structural model. They then used correlated time histories for earthquake and tsunami that are simulated for the same seismic source; the 2011 M9 Tohoku earthquake-tsunami event. Although the variability between earthquake and tsunami time histories was not fully considered, and a deterministic structural model was utilized for the simulation, they still reported that the permanent displacement response of the structure as well as the tsunami fragility curves were meaningfully impacted by the prior earthquake damage.

This dissertation first develops a methodology for generating earthquake-tsunami fragility surfaces and then extends it to develop fragility curves for mainshock and mainshock-aftershock sequences. This is applied to a building portfolio composed of RC and woodframe structures of various typologies and sizes, ranging from single-story to twenty-story levels, utilizing a multi-distributed methodology proposed in Chapter 2. The selected RC frame archetypes include both ductile and non-ductile systems, representing a fair cross-section of RC frames found in US coastal and non-coastal communities. Additionally, typical woodframe structures up to 2-story levels have been included as part of the proposed building archetypes in this dissertation.

Community-scale studies are then conducted using these fragility models to evaluate the cumulative damage to buildings within the established archetypes in both real and simulated testbed communities. This approach allows for the direct integration of cascading effects resulting from two events, whether it involves tsunamis or aftershocks as the subsequent event, into spatial damage assessments, loss estimations, population displacement, and functional recovery analyses at the community level. This comprehensive analysis aids in the realistic assessment of a community's performance, resilience, and recovery, whether it be prior to or following a multi-hazard scenario comprising an initial earthquake and its subsequent consequences.

1.2 Community Modeling Procedure within IN-CORE Platform

The **I**nterdependent **N**etworked **Co**mmunity **R**esilience Modeling **E**nvironment (IN-CORE) is a computational platform designed for resilience analysis. It facilitates the modeling of natural hazard impacts on communities and assesses their resilience. This environment seamlessly integrates risk analysis with the decision-making process, enabling a quantitative comparison of different resilience strategies (van de Lindt et al., 2018). Figure 2-2 provides an overview of IN-CORE's key components, including pyincore, IN-CORE web services and tools, and IN-CORE lab. Pyincore, a Python package, empowers users to apply hazards to infrastructure and evaluate the resulting physical damage's socio-economic impact. IN-CORE web services comprise a suite of tools for accessing hazard and fragility data that can be utilized within Pyincore. IN-CORE web tools consist of various viewers enabling users to visualize hazards, fragility curves, and recovery trajectories, with the option to download these resources for use in Pyincore or other analysis platforms. Consequently, the community-level decision models presented in this dissertation will be implemented using IN-CORE. This includes integrating models into IN-CORE web services, such as hazard, exposure, and vulnerability models, and showcasing their application through detailed examples.

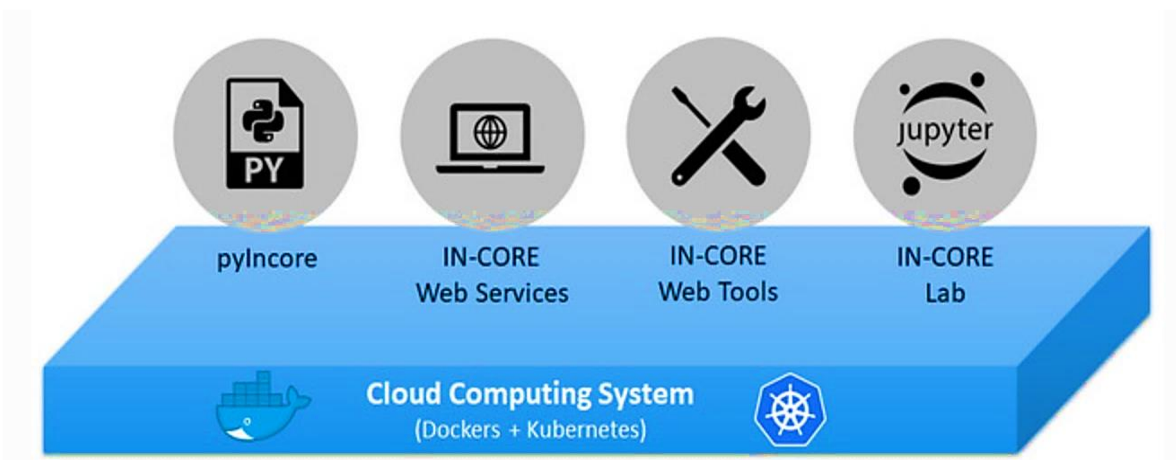

Figure 1-2. Computational chained components of IN-CORE (2024)

1.3 Successive Events Risk Analysis and Quantification

Earthquakes generate multiple hazards affecting both coastal and non-coastal communities. These hazards encompass mainshocks, aftershocks, tsunamis, and flood-following tsunami events, with varying intensities across time and space. To comprehensively assess the spatiotemporal risk variations associated with earthquake-induced hazards, a multi-hazard earthquake-triggering risk model at the community level is proposed. This model aims to capture the diverse mechanisms through which seismic-related hazards impact-built environments and their subsequent socio-economic consequences. Communities are categorized into coastal and non-coastal based on their vulnerability to earthquake-induced hazards. A risk analysis framework will be established to quantify earthquake-induced losses for each community type, utilizing high-resolution and physics-based models encompassing hazard, exposure, and vulnerability components.

1.3.1 Integrated Modeling of Successive Hazards/Events

In this dissertation, the outcomes of the Probabilistic Seismic and Tsunami Hazard Analysis (PSTHA) are employed, as described in Park et al. (2017) for the city of Seaside, Oregon. The PSTHA approach employed a logical tree framework that considered the scenario of a full rupture of the Cascadia Subduction Zone (CSZ). This analysis encompassed three primary models: the earthquake source model, earthquake simulation model, and tsunami model.

The earthquake fault source models and their respective characteristics were derived utilizing a tapered Gutenberg-Richer distribution method (Rong et al. 2014). Seismic intensity measures were obtained through the earthquake simulation model, employing ground motion prediction equations (Abrahamson et al. 2016). Subsequently, given the earthquake source modeling, the analysis computed tsunami hazards by solving the nonlinear shallow water equations, as described in Lynett et al. (2002) and Titov et al. (2011).

At a specific location on the considered testbed community, the annual exceedance probabilities for both earthquake and tsunami hazards were calculated, encompassing parameters such as peak ground acceleration (PGA), elastic spectral acceleration (SA), maximum flow depth (H_{max}), and tsunami momentum flux (MF). This comprehensive analysis yielded seismic and tsunami hazard maps associated with seven recurrence intervals: 100, 250, 500, 1000, 2500, 5000, and 10,000 years. In this regard, the MF has been selected for the intensity measure (IM) of tsunami hazard while the SA and H_{max} are going to be employed as the IMs of earthquake and flood-following tsunami hazards accordingly. For more information regarding the hazard modeling in this dissertation, readers are referred to Chapter 5 and 7 of this study.

1.3.2 Exposure Modeling of Building Structures

In the context of seismic events originating in oceanic regions, coastal communities are faced with a multifaceted array of hazards. These events, often characterized as earthquakes, have the potential not only to generate seismic waves but also to pose a significant threat in the form of tsunamis. This complex multi-hazard senario presents distinct challenges, particularly for coastal areas, including the looming risk of post-earthquake tsunamis. It is essential to acknowledge that the impact of these hazards is not uniform and varies significantly based on a community's proximity to the coastline and its susceptibility to tsunami events. This dissertation explores the diverse hazard zones that emerge from this context, delving into distinct regions of exposure and vulnerability that play a pivotal role in shaping the resilience strategies and disaster preparedness efforts of coastal and non-coastal communities.

1. **Coastal Hazard Zone (Zone A)**: This zone encompasses the immediate coastal region, extending up to about one kilometer from the shoreline. It is characterized by the highest intensity of hazards, including earthquake-induced ground shaking, tsunami inundation, and flood-following tsunamis. Buildings in this zone should be teoraticaly designed to withstand both seismic and tsunami impacts, with elevated structures and reinforced foundations to mitigate the effects of flood-follwong tsunamis.
2. **Transitional Hazard Zone (Zone B)**: Located at a distance of one to three kilometers from the coastline, this zone occupies a critical position in the hazard landscape. While the

hazards it faces exhibit a diminishing intensity compared to the immediate coastal zone, they remain substantial and warrant careful consideration. The primary threats within this zone encompass tsunami inundation, the potential for flood-following tsunamis, and the impact of seismic waves generated by earthquakes originating in oceanic regions. Structures within this zone are seismically designed with elevated foundations, a resilient architectural response aimed at mitigating the perils associated with coastal flooding and tsunami-related events. As we traverse this transitional zone, we encounter a nuanced interplay of hazards that necessitates a bespoke approach to resilience and risk reduction.

3. **Inland Hazard Zone (Zone C)**: Extending from three kilometers to thirty kilometers from the shoreline, this zone primarily faces earthquake-induced ground shaking, with reduced tsunami and flood hazards. Buildings in this zone are designed to withstand seismic events, and their construction accounts for lower tsunami risks.

4. **Seismic-only Zone (Zone D)**: Positioned beyond thirty kilometers from the coastline or in immediate coastal proximity without exposure to tsunami-triggering earthquakes, Zone D exists in a relatively low-risk environment when it comes to tsunami events. Instead, its predominant exposure revolves around seismic hazards, including mainshocks and the potential risk of aftershocks.

Assessing building vulnerabilities within a community exposed to a range of hazards requires the utilization of a diverse portfolio of building archetypes, meticulously selected to accurately represent the community's susceptibility. Each hazard demands its distinct set of building archetypes, tailored to mirror the hazard's unique characteristics and its specific implications for various building types.

1.3.3 Vulnerability Modeling (Fragility Functions)

The impact of earthquake-induced hazards on buildings varies across different zones, and the effects can be compounded in certain areas. In zones A, B, and C, the combined impact of earthquake and tsunami hazards on building structural systems necessitates the use of a multi-variate vulnerability function employing a 3D fragility surface. Conversely, the impact of floods following a tsunami in these zones is considered independent and can be computed separately using a single-variable vulnerability function.

In zone D, the impact of static flooding from tsunami hazards on buildings in inland communities is minimal, and structures are primarily exposed to earthquake shaking. Therefore, fragility functions obtained from a successive analysis procedure using mainshock and aftershock (MA) sequences are required for this zone.

Building damage caused by earthquakes and associated hazards can be categorized into two primary components: structural damage and content damage. Structural damage can be further divided into damage arising from earthquake-induced loads and damage resulting from tsunami-induced loads. This dissertation employs earthquake-tsunami fragility functions, as established by Harati and van de Lindt (2024) for zones A-C (detailed in Chapters 2, 3, and 4), alongside MA earthquake fragility curves (detailed in Chapter 7) developed by the same authors for Zone D. These functions will enable a comprehensive characterization of structural damage to the building envelope, a pivotal aspect of this dissertation. Additionally, we will utilize the static (no velocity component included in the damage estiamtion) flood fragility functions devised by Nofal and van de Lindt (2020a) (detailed in Chapter 5) to account for content damage in zones A to C. This holistic approach ensures that all potential damage scenarios are thoroughly addressed, providing a robust framework for understanding and mitigating the impacts of successive hazards on community resilience.

1.3.4 Risk and Loss Estimation Analysis

Building damages and economic losses within the considered building inventory are assessed through the utilization of the community resilience model in IN-CORE and its accompanying Python package, Pyincore (van de Lindt et al., 2023). IN-CORE serves as an invaluable open-source community resilience modeling environment, enabling not only the modeling of immediate impacts stemming from natural hazards on the built environment but also the exploration of subsequent effects, encompassing societal and economic losses, as well as post-disaster recovery dynamics. In the context of this dissertation, the modules for building damage and economic loss in Pyincore are strategically employed.

The core process involves placing hazard layers on top of the building inventory, which enables the retrieval of hazard intensity data at each specific building location. It's worth noting that IN-CORE provides the flexibility to either create hazards or use externally obtained hazard layers. In this study, we've opted for the latter approach, utilizing hazard layers obtained from a probabilistic seismic-tsunami hazard analysis discussed earlier in this dissertation. These hazard layers are crucial as they offer hazard intensity data at various spatial points across seven distinct recurrence intervals, facilitating comprehensive comparisons across different event magnitudes. Building damage assessment relies on these extracted hazard intensity measures at each building location, which are then compared against corresponding fragility functions.

1.4 Overview of Dissertation

This dissertation presents a series of interconnected studies focusing on the development and application of advanced methodologies for assessing and enhancing community resilience against multi-hazard events, particularly earthquakes and tsunamis. Given the increasing frequency and intensity of natural hazards, understanding the compounded impacts of successive events is crucial for effective resilience planning. By leveraging computational techniques, structural modeling, and machine learning, the research aims to provide high-resolution, probabilistic assessments that inform resilience planning and mitigation strategies. Each chapter systematically explores various facets of multi-hazard resilience, including the effects of initial and successive hazards, the role of long-duration earthquakes, integrated risk assessments, and innovative fragility modeling approaches.

Chapter 2 presents the development of near-continuous earthquake-tsunami fragility surfaces through a two-phase successive analysis. Initially, the structural response to earthquake ground motions is simulated using the Multiple Strip Analysis (MSA) method, followed by the evaluation of tsunami impacts via a force-based pushover analysis. The framework integrates advanced computational techniques, leveraging multi-distributed parallel processing to manage the substantial computational demands of millions of nonlinear analyses. A four-story RC building serves as an illustrative example, and the methodology aims to enhance tools like IN-CORE for comprehensive multi-hazard assessments. The study employs a detailed structural model in OpenSeesPy, incorporating randomness in various parameters to reflect inherent uncertainties. Results show that the generated fragility surfaces can be applied in community resilience planning, demonstrating the effectiveness of the proposed parallel framework in achieving high-resolution, probabilistic multi-hazard assessments.

Chapter 3 presents the development of earthquake-tsunami fragility surfaces for a portfolio of RC buildings and woodframe structures. The study employs community resilience frameworks as an emergency management tool, focusing on strategies such as resource allocation, infrastructure recovery, and social support systems to mitigate the impacts of natural hazards like earthquakes and tsunamis. It aims to facilitate adaptive responses that enable communities to recover critical functions and return to stable operations within an acceptable timeframe. The chapter emphasizes the importance of initial infrastructure damage on community recovery and the need for accurate fragility functions to estimate this damage. By applying the methodology from Chapter 2, the research develops fragility surfaces for various building typologies, focusing on both ductile and non-ductile RC frames, as well as woodframe structures. The study employs a detailed structural modeling process using OpenSeesPy, integrating randomness in various parameters to reflect inherent uncertainties and utilizing a multiprocessing distributed framework for efficient computational analysis. Results show that the generated fragility surfaces can be applied in community resilience planning, providing valuable insights into the effects of successive earthquake and tsunami events on different building structures.

Chapter 4 presents an investigation into the effects of long-duration earthquakes on the fragility surfaces of buildings subjected to successive earthquake and tsunami hazards. Unlike previous studies that primarily focused on far-field tsunamis, recent research has explored near-field tsunami fragility functions, emphasizing the importance of considering both earthquake and tsunami loadings. However, the impact of long-duration earthquakes has not been adequately addressed in these analyses. This chapter employs the methodology proposed by Harati and van de Lindt (2024) to quantify the influence of long-duration earthquakes on the topological behavior of earthquake-tsunami fragility surfaces for a portfolio of RC frames and woodframe buildings. By applying both long-duration and regular-duration earthquake motions, the study evaluates the compounded damage on RC frames, highlighting the necessity of incorporating long-duration seismic events in multi-hazard resilience assessments for coastal communities.

Chapter 5 presents a multi-hazard community resilience analysis, focusing on the combined effects of earthquake and tsunami hazards using integrated earthquake-tsunami fragility surfaces. Traditional methods, which use separate fragility curves for each hazard, fail to capture the compounded vulnerabilities from successive earthquake and tsunami events. This chapter addresses this gap by employing a probabilistic methodology, integrating Nonlinear Time History Analysis (NTHA) and Nonlinear Static Pushover (NSP) to generate fragility surfaces for RC and woodframe structures, tailored for regular- and long-duration earthquakes. The analysis applies these surfaces to a "Pseudo Seaside" testbed, a modified community model of the existing Seaside, Oregon, testbed model to assess structural and content damage and direct economic losses under varied seismic and tsunami scenarios. The results demonstrate that traditional FEMA combination rules may underestimate cumulative damage at higher seismic intensities, while the proposed integrated approach offers a more accurate risk assessment, highlighting the critical need for refined methodologies in multi-hazard resilience planning for coastal communities.

Chapter 6 introduces a physics-informed machine learning (ML) approach to generate multi-hazard fragility surfaces for earthquake and tsunami scenarios, addressing the limitations of conventional sequential analysis methods. By leveraging tree-based ML algorithms like Extreme Gradient Boosting (XGBoost) and Random Forest (RF), the study aims to synthesize 3D fragility surfaces from 2D fragility curves of individual hazards, significantly reducing computational demands and enhancing flexibility for tasks such as seismic retrofitting. The methodology, validated through extensive data preprocessing, hyperparameter tuning, and robust evaluation metrics, demonstrates the RF algorithm's superior performance. Applications of the model show its capability to generate accurate synthesized fragility surfaces and facilitate fragility-oriented structural retrofitting, illustrating substantial reductions in damage levels in community resilience scenarios. This innovative approach offers a practical, efficient solution for integrating multi-hazard risk assessments into resilience planning frameworks.

Chapter 7 presents a comprehensive methodology for developing and applying mainshock-aftershock fragility functions in community resilience modeling. The chapter emphasizes the importance of understanding the compounded effects of sequential seismic events, as illustrated by recent earthquakes in Turkey and Syria, and integrates nonlinear structural response simulations with Incremental Dynamic Analysis (IDA) and Multiple Strip Analysis (MSA). Utilizing a parallel processing scheme and Monte Carlo simulations, the study constructs fragility functions for various building typologies, including ductile and non-ductile reinforced concrete (RC) frames and woodframe structures. The developed fragility functions are applied to the Pseudo Seaside testbed, demonstrating significant increases in damage probabilities and economic losses when aftershock effects are included. The methodology underscores the necessity of incorporating aftershock impacts into seismic vulnerability assessments to improve accuracy in predicting structural damage and economic losses, thereby enhancing community resilience planning and mitigation strategies.

Chapter 8 presents a comprehensive analysis of functional and residential recovery in communities exposed to successive events and hazards. The post-event recovery phase holds immense significance in community resilience modeling. While completely preventing hazards is not possible, measures can be taken to mitigate their impact and prevent catastrophic disasters. Earthquake-induced hazards, whether direct or indirect, have wide-ranging effects on a community's economy and social institutions, giving rise to diverse recovery challenges. Quantifying the losses incurred by these hazards across different community sectors is crucial, as it delineates the extent of the recovery journey. Estimating damage at both the building and community levels plays a pivotal role. These assessments not only aid in evaluating immediate functionality post-event but also lay the foundation for initiating probabilistic recovery analysis. This approach enables engineers and scientists to comprehensively model the recovery process, equipping communities with valuable insights into resilience enhancement strategies. By integrating advanced computational techniques and probabilistic methodologies, Chapter 8 aims to provide a detailed framework for assessing and modeling the recovery trajectory of communities impacted by successive earthquake and tsunami events.

The comprehensive studies presented in this dissertation offer significant advancements in the field of multi-hazard community resilience analysis. By developing sophisticated methodologies for assessing the compounded impacts of successive natural hazards, integrating long-duration seismic events, and utilizing machine learning for fragility modeling, the research provides valuable tools and insights for enhancing resilience planning. These innovative approaches not only improve the accuracy of risk assessments but also inform the development of effective mitigation strategies. Additionally, by presenting a detailed framework for assessing and modeling the recovery trajectory of communities impacted by successive hazards or events, the research equips engineers and scientists with essential insights into resilience enhancement strategies. Ultimately, this work contributes to the resilience and safety of communities facing the growing threats of natural hazards. Finally, the overall summary of the conclusions, the anticipated contributions to the profession, and recommendations for future research studies are provided in Chapter 9 of this dissertation.

CHAPTER 2: METHODOLOGY TO GENERATE EARTHQUAKE-TSUNAMI FRAGILITY SURFACES[1]

2.1 Introduction

Recent advancements in multi-hazard fragility surfaces have focused on earthquake and near-field tsunami scenarios. Multi-hazard fragility surfaces for earthquake and near-field tsunami were recently developed for bridges (Xu et al., 2021) and a steel building (Attary et al., 2021) through probabilistic-based structural modeling approaches, where a successive analysis composed of NTHA and a subsequently NSP analysis was used for the response prediction of the earthquake and tsunami events, respectively. However, the fragility surfaces developed by Attary et al. (2021) are not continuous functions with respect to the selected earthquake IM though they used a more sophisticated structural model capable of performing collapse-level simulation, compared to the model employed in the study by Xu et al. (2021). In this way, the fragility surfaces developed by Attary et al. (2021) present challenges when attempting to condense them into a single continuous function, thereby making their implementation in risk and reliability platforms, such as IN-CORE (van de Lindt et al., 2023), more difficult. Additionally, this characteristic limit their effectiveness in scenarios focused solely on earthquake or tsunami hazards, particularly in far-field earthquakes or tsunamis crucial for coastal community resilience analysis. Moreover, it is also important to note that uncertainty propagation model of Attary et al. (2021) considered 10 ground motion records for the NTHA part and considered the yield strength (f_y) of steel as the sole uncertainty parameter in the numerical structural model.

[1] This chapter is based on the paper: Harati, M., and van de Lindt, J.W. (2024). "Methodology to generate earthquake-tsunami fragility surfaces for community resilience modeling." Engineering Structures, DOI: 10.1016/j.engstruct.2024.117700

To account for uncertainties associated with a two-phase successive analysis at different levels, including the uncertainties related to input earthquake GMs required for the NTHA procedure, the uncertainties pertinent to the detailed structural modeling, and essential variables for creating different tsunami loading profiles for the tsunami NSP analysis, millions of nonlinear successive analyses must be completed to incorporate the cascading and hence fully couple the effects of the earthquake and tsunami loading.

Consequently, advanced computational methods are essential to solve this problem. Multi-distributed parallel processing methods and architectures for clusters and supercomputers have been proposed in the past for various problems, including research related to flood simulations (Ginting and Mundani, 2019), earthquake simulations (Wijerathne et al., 2013), structural optimization (París et al., 2013; Umesha et al., 2007), large-scale structural analysis and design (Hardyniec and Charney, 2015; Toma et al., 2016; Vicente da Silva et al., 2015; Yu et al., 2020), structural reliability (Fiorillo and Ghosn, 2018), and collapse simulation (Hardyniec and Charney, 2015), to name a few past efforts intended to manage the expected massive computational demands. This study presents an architecture for a multi-distributed framework to cope with the difficulties associated with the computational demands required to produce near-continuous functions for 3D Earthquake-tsunami fragility surfaces. Furthermore, this multi-distributed and parallel processing framework enables the use of refined structural models in the two-phase analysis of NTHA and NSP procedure enabling of a large number of structural and hazard uncertainties.

In this chapter, the ability to generate near-continuous combined earthquake-tsunami surfaces is presented through a parallelization algorithm that includes tsunami profile updating and relevant sources of uncertainty in both the structure and hazards. Although surfaces have been generated in the past, the level of detail and ability to incorporate these near-continuous functions with tsunami profile updating with the intent of moving to community-level analysis provides an avenue to future studies on risk- and resilience-informed decision-making. A four-story reinforced concrete (RC) building is used as an illustrative example in this study, but the methodology is intended to be general and can be applied to develop a fragility suite. The aim, therefore, is to provide a more integrated and flexible multi-hazard fragility services for models such as IN-CORE, thereby enhancing its utility for more comprehensive and accurate multi-hazard assessments.

2.2 Sequential Analysis Procedure

In order to develop earthquake-tsunami fragility surface, the simulation of both the earthquake and tsunami response for the structure is needed and should be performed sequentially and accounting the cumulative effects of the cascading seismic and tsunami loading. As shown in Figure 2-1, in the first phase, the structural response exposed to earthquake ground motion is obtained using the Multiple Strip Analysis (MSA), as suggested by Baker (2015). For the incremental-based simulation in the MSA procedure, the spectral acceleration (Sa) at the first mode period of the system is selected as the earthquake IM, and then each ground motion (GM) is scaled using a point scaling method to increase the level of Sa.

Following each analysis of a different seismic intensity, peak inter-story drift ratio (SDR) is calculated and represents the engineering demand parameter (EDP). Accordingly, slight (DS1), moderate (DS2), and complete (DS3) damage states related to the selected EDP are defined according to the recommendations proposed by HAZUS (2020), as shown in Table 2-1. These damage state thresholds act as failure criteria in the successive simulation, acknowledging the inherent uncertainties in their derivation. The integration of HAZUS guideline into the proposed framework in this chapter of dissertation not only offers a standard for performance criteria but also aids in probabilistically addressing the uncertainties associated with defining damage states within the Monte Carlo simulation context.

Table 2-1. Damage limits considered for both earthquake and tsunami hazards

Hazard	EDPs	DS1	DS2	DS3
Earthquake	SDR (%)	0.9 %	2.3 %	6%
Tsunami	*SDR (%) + Column Shear Failure*	*0.9 %*	*2.3 %*	*6% or Column Shear Failure*

Since the waves of near-field tsunami arrive at the location of the structure later than the earthquake waves, the analysis with degraded strength and stiffness at the end of each MSA procedure is used in the tsunami simulation as the next phase of the analysis. The structural response under equivalent tsunami loads is then predicted using a force-based NSP or Pushover procedure starting after a free vibration analysis between successive analyses. In this study, the seismically damaged structural system from the previous stage is subjected to an equivalent tsunami force along the height of the building using the Variable Depth Pushover (VDPO) (Tagle et al., 2021). This study, similar to others (Alam et al., 2018a; Attary et al., 2017b, 2021), only considers the hydrodynamic force of the tsunami wave as the equivalent lateral load. To include the effect of openings on the structural response estimation, the hydrodynamic component of tsunami force is slightly modified and can be expressed as:

$$F_h = \frac{1}{2} \ \rho_s \ \ C_d \ \ B \ \ C_o \ (hu^2) \tag{2-1}$$

where ρ_s is the fluid density of water including sediments; the parameter B is the breadth of a wall or breadth of a building in general, which is perpendicular to the direction of tsunami flow; C_d is the drag coefficient recommended to be within the range of 1.25-2 (ASCE 7, 2002); h is the total height of the water measured from the foundation level of the building, and u is the flow velocity of the tsunami. The term hu^2 is the momentum flux; and C_o is the de-amplifying factor (or closure ratio) to include the effects of building openings in the tsunami analysis.

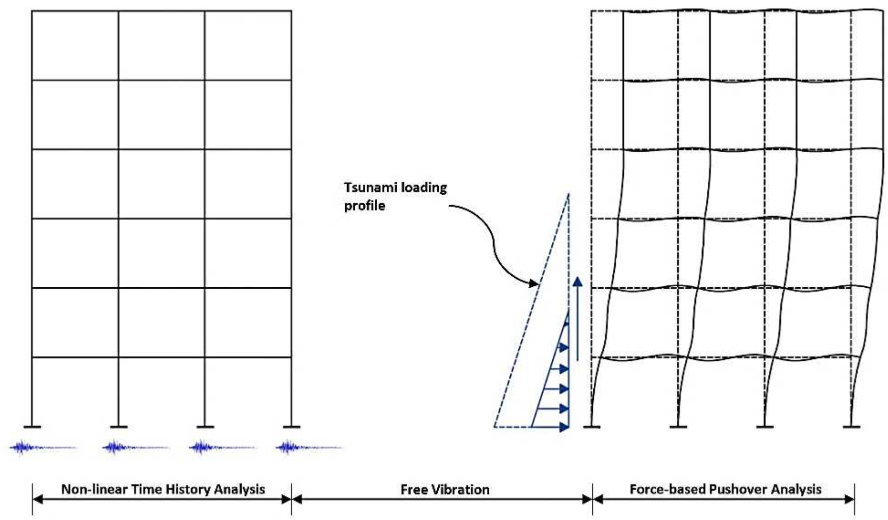

Figure 2-1. Successive analysis with two phases to model the cascading effects of earthquake and tsunami loadings

It should be noted that new openings may also be created due to the failure/breakage of windows, doors, and non-structural panels when a tsunami wave hits a building. Various values of the C_o factor is recommended, but it is usually selected to be less than unity. It was reported by Attary et al. (2017b) that the C_o should be greater than 0.7 because of the presence of interior walls in addition to exterior walls that can be damaged during tsunami loading. However, Alam et al. (2018) recommended a different range for the values of C_o based on their observations and the validation procedure they followed. In this study, it was decided to randomly vary C_o between 0.35 to 1, as Alam et al. (2018) suggested. This specific range was chosen as the structural system modeled by Alam et al. (2018) is a Moment Resisting Frame (MRF) system, which bears a close resemblance to the RC building explored in this research. The relevance and implications of this similarity for the RC building under investigation will be elaborated and discussed later in this chapter of dissertation.

Per American Society of Civil Engineers (ASCE) Standard 7, Chapter 6, load calculations for buildings should assume a minimum closure ratio of 70% (or C_o= 0.7) of the inundated projected area along the building's perimeter. This standard is altered for Open Structures, defined as structures where the portion within the inundation depth has no more than 20% closure ratio. For such Open Structures, the influence of debris accumulation – both against and within the structure – must be factored in, necessitating a minimum closure ratio of 50% of the inundated projected area along the perimeter of the open structure. This distinction in load calculation criteria underscores the variation in structural designs and the consequential impact of debris in scenarios involving flooding or inundation. The recommendations by Alam et al. (2018) for a minimum closure ratio are more conservative than the ASCE Standard 7-22, encompassing a spectrum from nearly open to completely solid structural walls.

As can be seen from Eq (2-1), there is a linear relationship between the momentum flux (MF) and the total tsunami force (F), and previous investigations demonstrated that the structural damage response is well correlated to MF (e.g., Attary et al. 2017b) and total tsunami force (Petrone et al., 2017). As a result, the momentum flux (hu^2) is selected as the IM for tsunami in this study.

For the second phase of successive analysis, the shear capacity of the columns at the seaward side of the structure is considered as the EDPs in addition to the peak SDR selected for this purpose before. So as recommended by previous studies (e.g., Petrone et al., 2017), the failure criteria for this analysis phase are a combination of damage states related to story drift (for all damage states) and defining a different metric to check the shear capacity of the columns (for complete damage state only) through a post-processing procedure recommended by Biskinis et al. (2004). For the shear failure model of the columns at the DS3, the equation (8) of the study conducted by Biskinis et al. (2004) has been selected as the shear capacity model.

2.3 Methodology

In order to generate earthquake-tsunami fragility surfaces, probabilistic models for both the structural systems and the earthquake and tsunami loading are needed to quantify the underlying uncertainty in the models and process. Numerous successive analyses were performed in order to generate enough data to include considered uncertainty sources in the modeling procedure; However, this results in high computational demands for this robust multi-hazard fragility simulation. In addition, detailed structural models are applied in this study for building fragility assessment, enabling the prediction of the complete collapse for either of the considered hazards. As a result, performing millions of successive simulations with high-resolution structural models can be highly inefficient if the analysis is a typical sequential analysis. To overcome these demands, this study proposes and applied a multiprocessing distributed framework to improve the analytical time efficiency of a high-resolution and physics-based method for generating 3D fragility earthquake and tsunami surfaces. In this section, the multi-distributed algorithm controlling the parallel processing mechanism of the framework is explained. Then a sequential algorithm used within each core/CPU of the distributed framework is further explored and explained.

2.3.1 Distributed Framework

Clusters and supercomputers are composed of a large multiple numbers of machines, each of which has ten to hundreds of CPUs or GPUs, resulting in thousands of nodes that can work together on a shared memory space. This chapter of dissertation takes advantage of a cluster with 1160 CPUs that consists of 29 different computers, each with 40 CPUs. As shown in Figure 2-2 and Figure 2-3, a multi-distributed framework is developed using parallel programming with a Message Passing Interface (MPI). In this MPI framework, the send and receive protocol has been utilized to simultaneously send all jobs (N jobs) from the manager node to all available worker nodes. These worker nodes can be located all in a single cluster or supercomputer. Still, nodes from external clusters can also be added and utilized as the currently available worker nodes in this framework. The required computation on every worker node and its CPUs is carried out independently. Then the computational outcomes are sent again to the manager node enabling it to collect results from all worker nodes and save them in a single file.

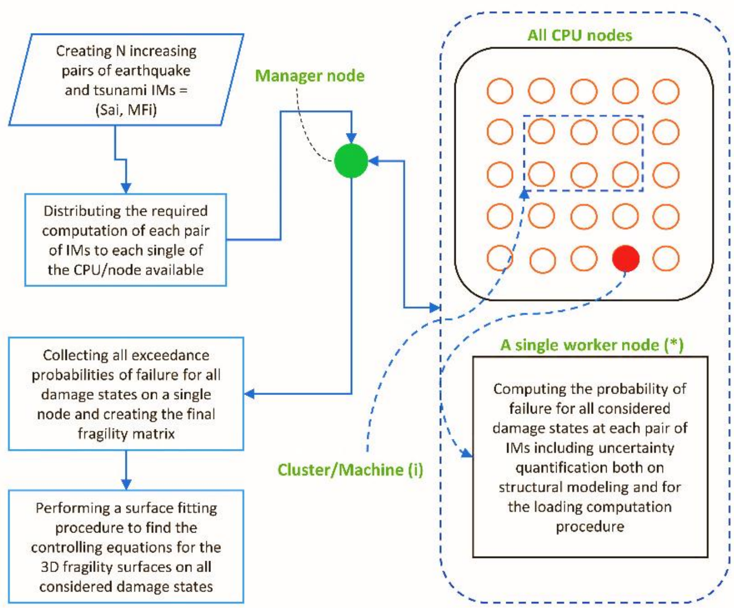

Figure 2-2. Multi-distributed parallel processing framework for the generation of earthquake-tsunami fragility surfaces

In this computational framework, the first two columns are the IM's; specifically the first for earthquake IM (Sa(T1)) and the second for the tsunami IM (MF). In this matrix, N pairs of values of IM's are created, which form the rows of this input file having an increasing trend in both IM directions. But before creating this input matrix, the discretization on each axis should be properly defined. For example, to have 900 points of joint IM's, 30 points on each IM axis are required. In this way, for each value of earthquake IM, there are 30 increasing values of tsunami IM.

Each row of the input matrix has two IM values, the Sa and a value for MF. Using the MPI programming as shown in Figure 2-2, N sequential algorithms are duplicated with N joint input values (Sa_i, MF_i) and then sent to the manager node that can distribute them among N worker cores/CPUs. Then N cores can be used simultaneously for computing the exceedance probabilities of failure for all desired damage states. The failure probabilities of damage states for each row of the input matrix are computed within a single core on the cluster. The computation required to assess the probability of failure within each core is accomplished through a probabilistic successive analysis and Monte Carlo simulation using the joint IM in one of the input matrix rows. This sequential algorithm, which is the Monte Carlo loop in this distributed framework, will be discussed in more detail in the next section.

The pseudo-code of this distributed algorithm (or MPI programming) is presented in Figure 2-2 and is explained as follows:

1- The code uses a conditional statement to differentiate between rank 0 and other ranks (ranks 1 to p-1). In MPI, rank 0 typically serves as the manager process, while others are worker processes that perform parallel computations. In this chapter of dissertation, the mpi4py module has been used for the distributed algorithm, which is a built-in Python library. At the request of this MPI code, a variable termed ClusterAdjuster is used for switching to another cluster (in case needed) to compute a part of fragility matrix after row number “n”.

2- For ranks other than 0 (workers), the code executes the Monte_Carlo_Loop function to calculate probabilities of failure for different damage states related to the given Structure

ID, based on the RNK - 1 (adjusted rank), MF value corresponding to the current rank, Sa value corresponding to the current rank, Width_of_Building, Height_of_Building, Num_GM (total number of GMs) and some other input parameters for Monte Carlo loop. The results, denoted as R, are then sent to rank 0 (the manager process) using comm.send (). This is the sending protocol of mpi4py module as discussed earlier. Using this protocol, a Monte Carlo simulation would be performed in each of the CPUs assigned to workers.

3- For rank 0 (manager process), the fragility matrix R0 is initialized as a zero matrix with dimensions (len (Sa) * len (MF), 5). This matrix will store the final results of this parallel processing.

4- The manager process then collects the results (Nd) sent by other processes (ranks 1 to p-1) using the comm.recv () function of mpi4py, and adds them to the R0 matrix. This aggregation process that is accomplished by receiving protocol of the MPI programming allows the manager process to combine results from all worker processes and obtain the final fragility matrix.

```
Algorithm MainSimulation()

  // Controlling parameters of the Simulation
  ClusterAdjuster = n                // This helps to use another cluster to compute fragility matrix after row "n"
  filename = str (ClusterAdjuster)

  // Axis points (from input matrix) and uncertainty configurations
  AX = axes (Structure ID)           // Discretization information of both IM axes (for earthquake and tsunami) is transferred here
  MF = AX [0]                        // A vector for MF values from input matrix
  Sa = AX [1]                        // A vector for MF values from input matrix
  Width_of_Building = AX [2]
  Heigh_of_Building = AX [3]
  Num_GM = AX [4]                    // Total number of ground motions being applied to the structure of interest
  Num_Uncertainty = AX [5]           // Total sets of uncertainty modeling (K)
  Column_Discretization = AX [6]     // Number of discretization points for the seaward columns of the structure

  // Initialize MPI environment
  comm = MPI.COMM_WORLD              // The function of MPI can be inserted to this simulation by mpi4py library of Python
  rank = comm.Get_rank()
  p = comm.Get_size()
  RNK = rank + ClusterAdjuster - 1

  if rank != 0 then
    // Each process (except rank 0) calculates Monte_Carlo_Loop for its specific data
    R = Monte_Carlo_Loop (Structure ID, RNK -1, MF [RNK -1, 0], Sa [RNK -1, 1],
    Width_of_Building, Heigh_of_Building, NumGM, Num_Uncertainty, Column_Discretization)
    comm.send (R, dest=0)
  else
    // Rank 0 initializes the fragility matrix for final results
    R0 = zeros ((len(Sa) * len(MF), 5))

    // Collect results from other processes (rank 1 to p-1)
    for procid in range (1, p) do
      Nd = comm.recv (source=procid)
      R0 = R0 + Nd
```

Figure 2-3. Pseudo-code description of the distributed framework

Therefore, the final fragility matrix, which has the exceedance probability failures for all damage states and all combinations of joint IM, is compiled by the manager node and saved in a single file using all the date of failure probabilities computed independently within each core. After this step, a surface fitting function suggested by Kern et al. (2004) is applied to the data for the fragility matrix obtained from this MPI-based framework:

$$P(Sa, MF) = \frac{E.(\frac{Sa}{C1}+\frac{MF}{C2}+\alpha.\left(\frac{Sa}{C1}\right).\left(\frac{MF}{C2}\right))^n}{(\left(\frac{Sa}{C1}+\frac{MF}{C2}+\alpha.\left(\frac{Sa}{C1}\right).\left(\frac{MF}{C2}\right)\right)^n+1)} \tag{2-2}$$

Where Kern et al. (2004) determined that the parameter *E* should have a value of 1.01. But in this study, the values of the tuning parameters *C1* and *C2*, as well as *E*, *α* and *n*, are obtained through an optimization procedure that is recommended by Kern et al. (2004). There are, therefore, five tuning parameters required for defining a fragility surface. In this way, the governing equation of the fragility surface for each damage state can be derived with a desired level of accuracy. It is possible that the number of rows in the input matrix (N) can significantly affect the accuracy level of the surface equations.

2.3.2 Sequential Analysis within a Single Core

In each single core of the cluster, a Monte Carlo simulation is performed over numerous successive analyses. Each Monte Carlo simulation is executed using a given pair of IMs as input parameters, i.e., the joint IM with one Sa and an MF value. In this sequential algorithm, the first loop index is designated for 44 GMs from the Federal Emergency Management Agency (FEMA) P-695 (2009) selected records for the NTHA procedure. After selecting the first GM, random parameters are generated for the structural modeling procedure and the characteristics related to the computation of the equivalent tsunami forces (based on Eq (2-1)) in the next loop which are termed as the uncertainty modeling box hereafter. From this loop, K sampling points are created for each random variable. From a previous study by Attary et al. (2021) which used 100 samples for generating random structural models (K in this study), a parametric study in this research revealed that 50 iterations for K also works well for having a reliable simulation.

Utilizing the randomly generated coefficients C_o and C_d, the flow velocity of the tsunami wave is calculated corresponding to varying inundation depths. These depths incrementally increase in each loop iteration, up to the maximum value outlined in the section detailing the successive analysis procedure. The study calculates tsunami flow velocity based on inundation depth by using MF as the tsunami IM. This IM is integrated into the algorithm as a part of the joint IM. For a given inundation depth (h), the tsunami velocity (u) is determined using the momentum flux equation, hu^2, with emphasis on considering only the positive root of the velocity.

In each iteration of the loop, the realized flow velocity is evaluated against a predetermined threshold dictated by the Froude number (Fr), requiring it to be ≤ 2. This benchmark stems from empirical observations of historical tsunamis, where Fr numbers characteristically fall below 2.0, as highlighted by other researchers (Iwai and Goto, 2021; Matsutomi and Okamoto, 2010), marking it as a plausible threshold for regions along the US West Coast. Nevertheless, instances of higher Fr values have been documented in various locations (e.g., McFall and Fritz, 2016) but this is rare and thus not included herein. If the calculated flow velocity is evaluated as realistic, the total tsunami force (F_h) is computed using the determined values of C_o and C_d. Subsequently, both the total tsunami force (F_h) and the iterated inundation depth (h_i) are forwarded to the successive analysis function of the algorithm, namely, the successive analysis procedure.

By comparing the predefined damage states with the outcomes of successive analyses (failure or non-failure cases), the status of each randomly generated multi-hazard scenario can be numerically assessed. This process, as illustrated in the algorithm in Figure 2-4, involves generating several pieces of information for each of the K samples from the uncertainty modeling box, including probable tsunami loading profiles characterized by varying tsunami heights while maintaining a constant resultant force. Central to this analysis is the use of the tsunami's momentum flux as the tsunami IM, a key part of the joint IM in the algorithm. This IM is instrumental in guiding the variation of the tsunami's inundation depth (h), enabling the creation of varied tsunami loading profiles at different depths. For each depth h, the flow velocity is calculated from the provided MF and evaluated against the Froude number threshold to ensure it does not exceed 2. Upon meeting this criterion, the total tsunami force is computed using Eq (2-1) and distributed proportionally along the structure's height, correlating with the hi for each scenario, thus providing a detailed assessment of tsunami impact under diverse conditions. For each set of the outputs from the uncertainty modeling loop, several structural models would be created such that each one would have a distinct value of h_i while the value of MF or the total tsunami force (F_h) remains constant for all these generated models. This sampling procedure is accomplished for all selected GMs. Finally, the probability of failure for each damage state is found using Monte Carlo simulation.

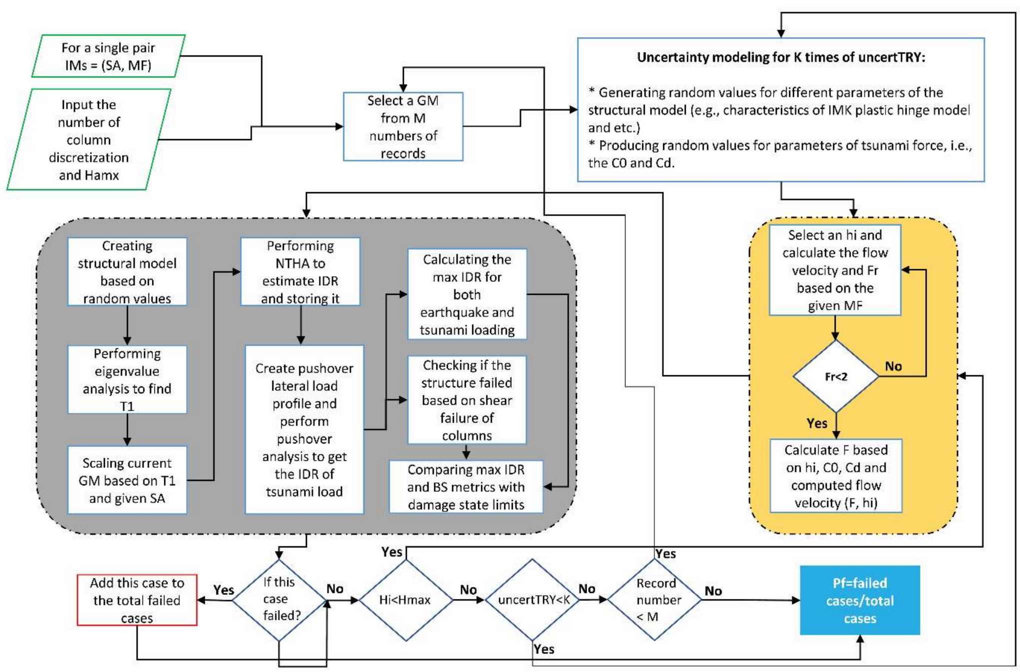

Figure 2-4. The algorithm controlling the computational procedure for each discrete point on the 3D fragility functions/surfaces for earthquake and tsunami; these computations are executed on a single core/CPU

2.4 Structural Modeling

2.4.1 Illustrative Building

The structural model introduced by Haselton et al. (2011) has been selected as the illustrative building example in this chapter of dissertation. More specifically, it is similar to a typical RC MRF system in terms of its design procedure and architectural geometric characteristics, which was assumed to be located at a site in Los Angeles. In their study, it is a 4-story building RC moment frame building with a plan area of 60 by 60 ft (18.29 by 18.29 m) in square shape. It has four frames in each direction, crossing each other orthogonally. Each of the four frames in each direction (along the x- or y-axis) is equally spaced, forming a bay width of 6.1 m (20 ft).

The structure was designed using capacity-based design, and the seismic characteristics and detailing of the members are based on the provisions of the International Building Code [International Code Council (ICC) 2003], ASCE 7-02 (ASCE 2002), and ACI 318 (ACI 2002). The building was seismically designed and detailed based on a design spectrum constructed for a site with a soil class D and the spectrum acceleration coordinates of S_S = 1.5 g and S_1 = 0.6 g.

2.4.2 Nonlinear Modeling Procedure

The OpenSeesPy software (Zhu, 2021) is employed in this study to model the nonlinear structural system. As seen in Figure 2-5, a 2D structural frame was created to represent the building described earlier. In this modeling approach, the stiffness and strength of the gravity systems are not considered directly in the structural model, but the destabilizing effects of the gravity loads are included in the model by adding leaning columns connected to the structure using truss-based link elements.

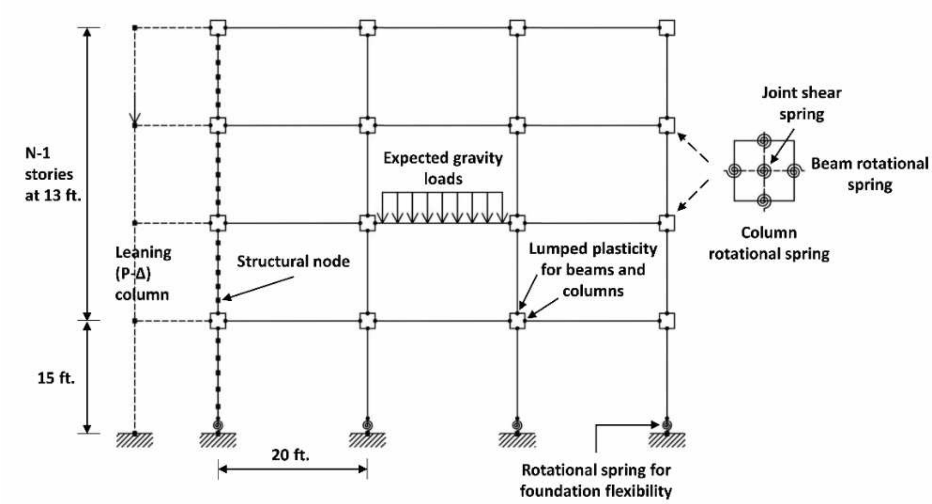

Figure 2-5. The schematic of the FEM model for the case study building

Figure 2-5 illustrates the 2D structural model used for simulating successive hazard events, contrasting two methods: the fiber and concentrated plasticity approaches, for modeling structures under tsunami or earthquake impacts. The fiber method is key for representing inelastic behaviors throughout a structure, especially beyond column ends, vital for managing distributed tsunami loads. However, a significant concern is the potential for shear failure in columns, especially at lower inundation levels where shear demands are heightened, risking failure before reaching the first floor. To account for variations in beam and column shear capacities dependent on axial loading during different earthquake-tsunami phases, either explicit simulation or post-processing is necessary for shear failure analysis. Force-or-displacement-based distributed plasticity elements prove effective here, allowing for interactions between moment, axial, and shear forces, thus offering a comprehensive view of structural responses to multi-hazard events. This method, as demonstrated in previous studies (e.g., Alam et al., 2019, Alam et al., 2018, Carey et al., 2019, Petrone et al., 2020, Rossetto et al., 2019, Rossetto et al., 2019) includes both flexural and shear failures, incorporating adjusted shear links or post-processing shear failure checks, thereby providing a robust assessment framework for such scenarios.

Conversely, several studies (e.g., Attary et al., 2021, Attary et al., 2017b, Attary et al., 2017a; Haselton, 2006; Haselton et al., 2011; Liel et al., 2011) have adopted the concentrated plastic hinge method. This approach employs lumped plasticity elements and finite joint shear springs, selected for their effectiveness in capturing strain softening due to rebar buckling and spalling, crucial for simulating the collapse of RC frames. Based on empirical data from extensive testing on both ductile and nonductile RC columns, this method ensures accurate modeling. However, it primarily focuses on calibrating model parameters to axial compression levels in columns due to gravity loads and may not fully encompass axial-flexure-shear interaction during the analysis, a critical factor for taller structures. While the fiber-spring model offers an alternative, it shows less numerical stability in dynamic analysis and struggles with simulating severe strain softening, a key failure mechanism in collapse scenarios. In contrast, the lumped-plasticity model effectively captures severe strain softening at a roof drift ratio of approximately 3% or higher, making it more suitable for seismic load simulations.

It is important to note that the concentrated plastic hinge method might not fully simulate tsunami responses, as it could fail to model inelasticity development away from seaward column ends under distributed loading. However, structures initially sustain earthquake-induced damage in simulations, forming a basis for further analysis. Therefore, accurately modeling collapse or near-collapse responses is essential. To overcome limitations in simulating tsunami impacts, a post-processing procedure is employed to account for shear failure of seaward columns, thus balancing trade-off errors and enhancing the overall accuracy in representing multi-hazard scenarios.

In this study, for modeling the 2D structure depicted in Figure 2-5, the shear panel of the joints is represented using the Joint2D Element within the OpenSeesPy framework. There are five nodes in beam-column joint element, including four edge nodes connecting to structural members and foundation using rotational springs and the other node at the center to incorporate the shear deformation of the joints. Elastic beam-column elements are connected to these five-node joints to function as beams and columns using the modified Ibarra-Medina-Krawinkler (IMK) deterioration model (Ibarra et al., 2005; Lignos and Krawinkler, 2011) as the nonlinear rotational springs. The IMK nonlinear hinge model (Figure 2-6) can control the degrading behavior of elements in terms of strength and stiffness. Additionally, the shear behavior of the beam-column joints is controlled by utilizing a nonlinear uniaxial material, as suggested by Celik and Ellingwood (2010). A calibrated linear spring is used to model the foundation rotation stiffness based on the grade-beam design and soil stiffness properties. Finally, to include viscous damping on the structural level simulation, the Rayleigh damping method with a random damping ratio (mean value=0.065) is applied to the beam and column elements of the whole structural system.

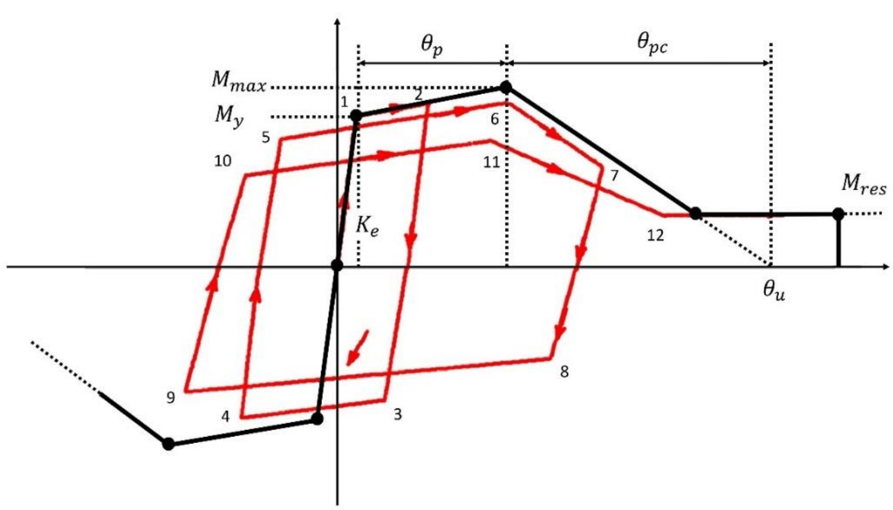

Figure 2 6. Modified Ibarra-Medina-Krawinkler (IMK) deterioration model with bilinear hysteretic response used for the modeling of plastic hinges of beams of columns of the case study structure (After Ibarra et al., 2005; Lignos and Krawinkler, 2011)

Utilizing six segments, the seaward edge columns of the building, as depicted in Figure 2-7, are discretely partitioned. This segmentation enables the formation and evolution of tsunami loading profiles along the building's height. Sequentially, h_i progresses through incrementally increasing heights (or indexed joints), thereby establishing a uniform loading profile. This profile extends uniformly from the base level to an elevation corresponding to h in Eq (2-1), ensuring consistent load distribution. To further refine this approach and develop a variable tsunami loading profile, the building's bay length (B), set at 6.1 meters, is factored into the total load calculation for the tsunami as outlined in Eq (2-1). This consideration of bay length is crucial for accurately determining the tsunami's impact across different sections of the building, contributing to a more detailed and realistic simulation of tsunami forces. In this way, after conducting a NTHA procedure under a scaled GM at a specific earthquake IM (Sa(T1)), a series of single-cycle tsunami flows are generated from the same value of tsunami IM, here the MF. These tsunami flow profiles are based on incrementally increasing inundation depth (h_i). As mentioned earlier, it is important to note that only those tsunami profiles with acceptable tsunami flow velocity (Fr<=2) are applied to structures. this approach, previously utilized in studies such as Attary et al. (2021, 2017b, 2017a), involving multiple single-cycle tsunami flows for the second phase of successive simulation, aligns with the requirements outlined in Chapter 6 of the ASCE Standard 7-22. According to this standard, structural designs to mitigate tsunami effects must encompass at least two tsunami inflow and outflow cycles. The first cycle is to be predicated on an inundation depth at 80% of the Maximum Considered Tsunami (MCT), with the subsequent cycle reflecting the MCT inundation depth at the site.

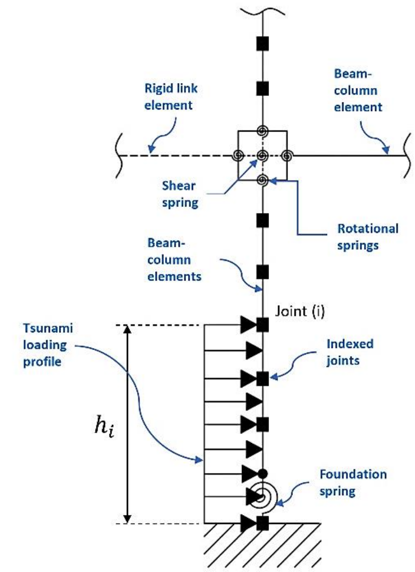

Figure 2-7. The variable tsunami lateral loading profile, which is applied to the seaward columns of the structure with a height of hi ranging from base level up to an indexed joint.

The pushover curve for the model created in this study and that reported by Haselton et al. (2011) is shown in Figure 2-8. As can be seen from Figure 2-8, there is a good agreement between these two pushover curves. The pushover results of both studies are based on median values of the input parameters in structural modeling procedure. However, this structural model used in this study is based on the modified IMK model (Lignos and Krawinkler, 2011), but Haselton et al. (2011) created their model based on the earlier version of the IMK plastic hinge element (Ibarra et al., 2005).

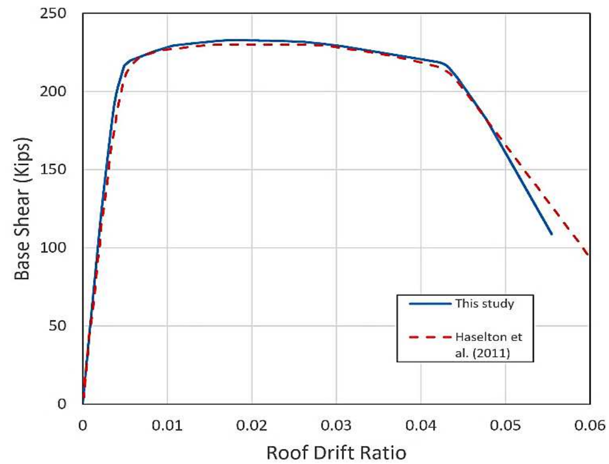

Figure 2-8. The pushover curve obtained from this study using modified IMK plastic hinges compared to that reported by Haselton et al. (2011)

The structural model presented here does not directly consider the local shear failure mechanism for beam and column elements. However, the shear capacity of the columns on the seaward side of the building are checked in a post-processing routine as a part of the failure criterion in each analysis. Due to this, the global collapse mode of the system resulting from the shear failure of the column caused by the tsunami is not directly included in this structural analysis simulation. Therefore, only the sidesway collapse of the structural system can be analytically predicted with this structural modeling procedure.

2.5 Uncertainty Modeling in the Simulation

The uncertainty of the input GM required for the NTHA of the MSA procedure is included by using a suite of far-field GMs recommended by FEMA P-695 (2009). The uncertainty quantification for the input parameters associated with the near-field tsunami forces is also incorporated into this simulation by modeling C_o and C_d factors as random variables using uniform distributions. The lower and the upper bounds of these uniform distributions are provided in Table 2-2. In addition, several other parameters in the structural analysis function are also modeled as the random variables herein.

To quantify and propagate the uncertainties associated with the structural modeling procedure, several input values are considered as random variables. As shown in Table 2-2, these random variables include those related to the modeling procedure for plastic hinges, dead loads and seismic mass, stiffness of column-to-foundation joints, hysteresis behavior beam-column joints, and the damping ratio of the Rayleigh damping method.

Table 2-2. The characteristics of the random variables used to model the structural system as well as the tsunami lateral loading profiles

Random Variable	Distribution type	Mean	COV	Reference(s)
C_o	Uniform (0.35-1)	-	-	(Alam et al., 2018a)
C_d	Uniform (1.25-2)	-	-	(Attary et al., 2021)
Dead load and seismic mass	Log-normal	1.05 ×(computed)	0.1	(Ellingwood, 1980)
Damping ratio	Log-normal	0.065	0.60	(Porter et al., 2002)
Element strength	Log-normal	1.0 × (computed)	0.12	(Panagiotakos and Fardis, 2001)
Element initial stiffness	Log-normal	1.0 × (computed)	0.36	(Fardis and Biskinis, 2003)
Element hardening stiffness	Log-normal	0.5 × (computed)	0.50	(Wang et al., 1978)
Plastic rotation capacity	Log-normal	1.0 × (computed)	0.60	(Panagiotakos and Fardis, 2001)
Post-capping stiffness	Log-normal	0.08 × (-Kelastic)	0.60	(Ibarra and Krawinkler, 2005)
Column footing rotational stiffness	Log-normal	1.0 × (computed)	0.3	(Haselton et al., 2008)
Joint shear strength	Log-normal	1.40	0.1	(Altoontash, 2004)

2.6 Numerical Results

The multi-distributed framework proposed in this research is applied to a building as an illustrative example. The data for the fragility matrix is in a 3D format, and for each pair of IMs related to the earthquake and tsunami hazards on the x-y plane, a probability of failure is computed and shown on the z-axis for each pre-defined damage state. As shown in Figure 2-9, the earthquake-tsunami fragility surface for the complete damage state is presented in 3-axis form (surface) using the discrete data for a fragility matrix composed of 400 joint-IM points. In order to find a smooth and continuous surface over the discrete data, a surface fitting procedure, as mentioned in the Methodology section, is utilized. It should be mentioned that two different and independent fragility curves, an earthquake-only and a tsunami-only fragility curve, can appear on the edges of the developed fragility surface as illustrated in Figure 2-9.

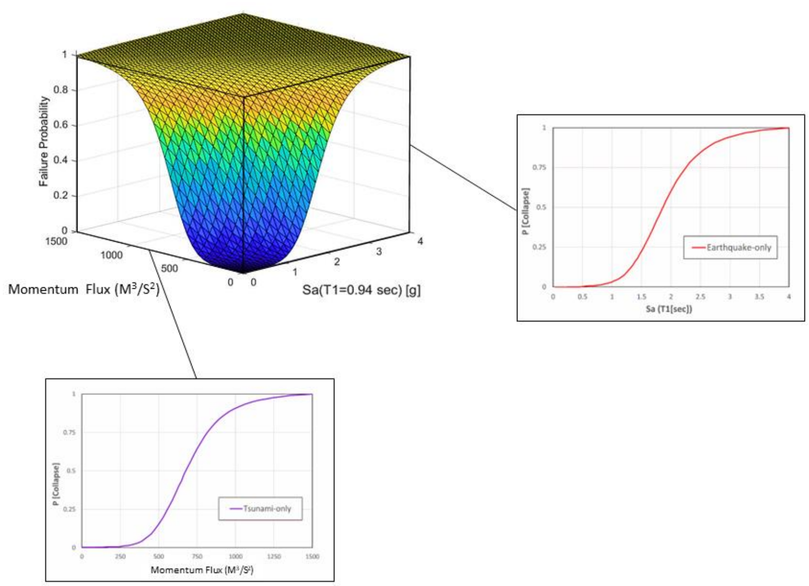

Figure 2-9. The three-dimensional fragility surface of earthquake and tsunami is at complete damage state, which can incorporate two separated fragility curves – the earthquake-only and tsunami-only fragility curves.

As mentioned, the fragility surfaces shown in Figure 2-9 are computed using 400 points for the joint IMs (N=400). However, as stated in the methodology section, the number of IM points (N) in the fragility matrix can control the surface fitting accuracy level. In this regard, a parametric study is performed based on a K of 50 (number of realizations for uncertainty modeling) using different IM points (N) and the equivalent number of CPUs to find the optimal case that leads to a fitted surface with appropriate quality. Four different values of N or joint IMs, including N=100, N=225, N=400, and N=900, are selected for this parametric study. As noticed in Figure 2-10, the accuracy level of the fitted surfaces entirely depends on the selected value of N. Although the accuracy level of the surface fitting is normally increased with an increase in the value of N, it should be noted that the quality of the final fragility surfaces is not considerably improved after a specific value of N. The fragility surfaces obtained from N=400 and N=900 are almost indistinguishable; This is more pronounced for the fragility surfaces on slight and moderate damage states/levels since the number of discrete points of the failure probabilities on these damage levels may be highly limited and insufficient in case simulation is carried out with small values of N. For example, it should be noted that the fragility surface for the slight damage state cannot be successfully determined using an N equal to 100 or 225.

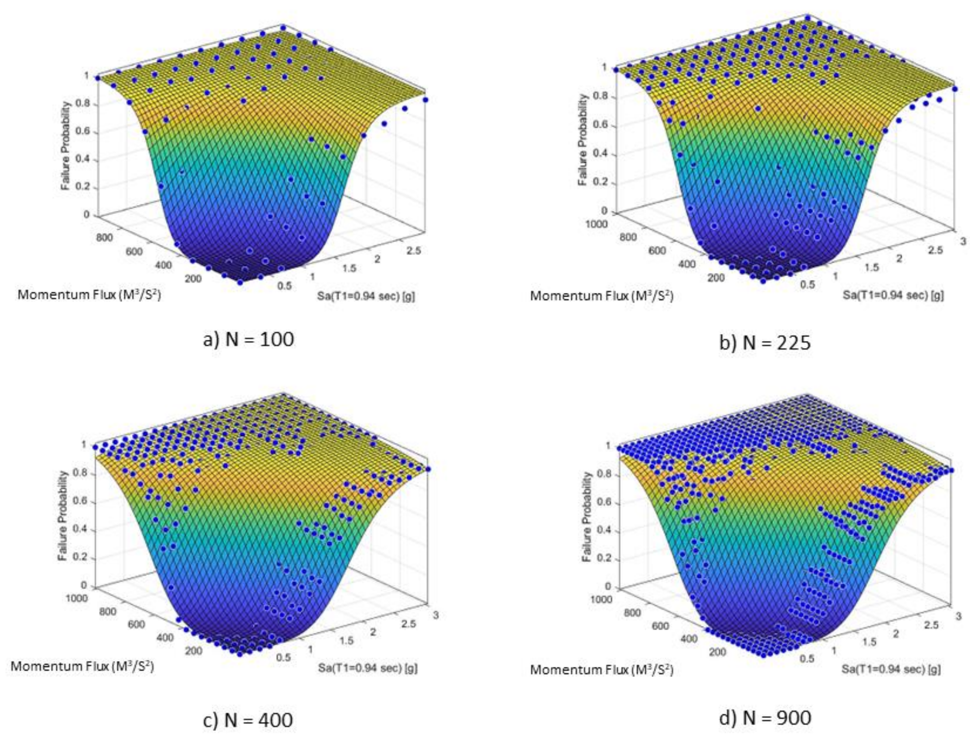

Figure 2-10. Earthquake-tsunami fragility surfaces using different numbers of discrete points (N) computed parallelly with N number of CPUs simultaneously.

Figure 2-11 displays the 3D fragility surfaces computed for different damage states, i.e., namely slight, moderate, and complete damage state, for the considered case study building.

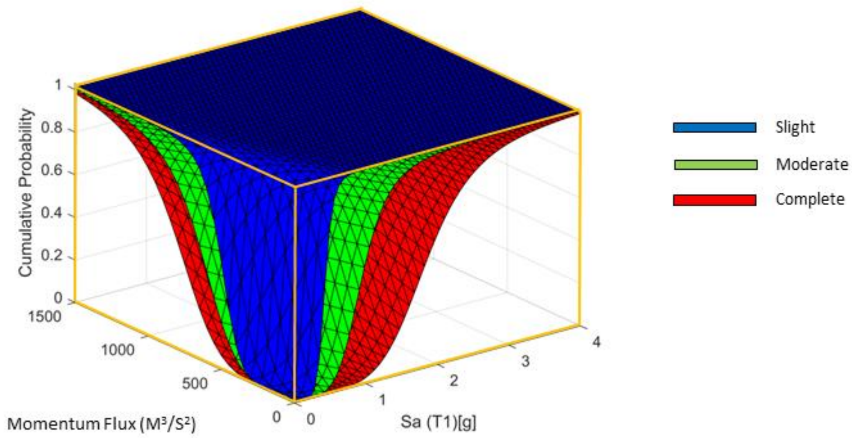

Figure 2-11. Earthquake-tsunami fragility surfaces for different damage states, i.e., slight, moderate, and complete damage states.

In Table 2-3, the parameters for Eq (2-2) are presented, namely *E*, *C1*, *C2*, *α*, and *n*. These parameters can be used to generate the earthquake-tsunami fragility surfaces for the target RC structure at different damage states. A multi-hazard community resilience analysis for earthquakes and tsunamis in a coastal community can utilize the parameters derived in Table 2-3, assuming the target community exclusively comprises this building typology. However, it is essential to generate multi-hazard fragility surfaces for various building archetypes to enable comprehensive community-level modeling and analysis. By obtaining the joint IM (Sa, MF) from hazard modeling, damage and subsequent resiliency-related assessments can be conducted for the target community effectively.

Table 2-3. Equation parameters of the earthquake-tsunami fragility surfaces of the considered RC structure at different damage states

PARAMETERS	DS1	DS2	DS3
E	0.9982	0.9982	0.9982
$C1$	0.4158	0.9054	1.6147
$C2$	516.6436	630.4792	724.6698
α	0.3683	0.5087	0.6414
n	7.7202	7.4998	7.6486

In Figure 2-12, the 2D earthquake fragility curve on the complete damage (DS3) state obtained from the 3D fragility surfaces of this study is shown by the red line. While this red line curve is extracted from the governing equation of the fitted surface, the black curve represents the earthquake fragility determined using the lognormal CDF fitted over the raw data of the fragility matrix. The fragility curve displayed with the dashed blue line is obtained considering the record-to-record (RTR) variability of earthquake motions while another fragility curve from Haselton et al. (2011) is presented with a solid blue line taking into account the RTR and the structural uncertainties in the FE modeling procedure. As seen in Figure 2-12, these earthquake fragility curves are in good agreement generally, but there are some differences in some sections, which is related to the various assumptions and the methodology taken throughout their development process. Even though the fragility curves obtained in this study are based on the presented methodology through the use of MSA and Monte Carlo simulation, Haselton et al. (2011) determined the earthquake fragility based on Incremental Dynamic Analysis (IDA) and the concept of dynamic instability. This type of difference has been documented ed by other studies as well (e.g., Baker, 2015; Pang and Wang, 2021).

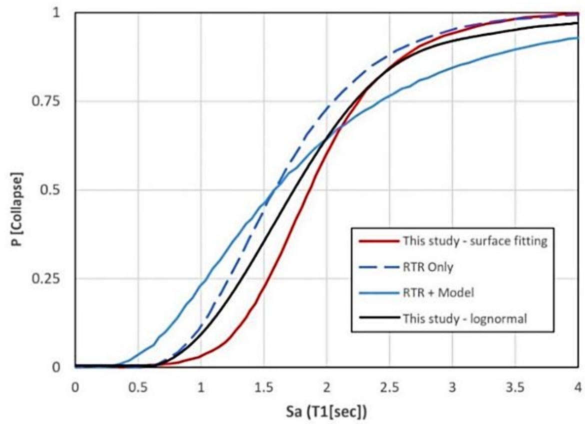

Figure 2-12. The earthquake-only fragility curve in this study at complete or collapse damage state versus the fragility curves reported by Haselton et al. (2011) for the same structure

In Figure 2-13, the tsunami-only fragility curves for different damage states are generated considering the prior structural damage (as the initial condition) imposed by the earthquakes at different intensity levels. These fragility curves are generated for two tsunami IMs (i.e., MF and Inundation Depth) using a moving average over the raw data of the fragility surface with N equal to 900 points. For a given level of Sa (e.g., Sa=1g), the same 2D tsunami curves can be equivalently obtained from Eq (2-2) for each of damage states whose parameters are reported in Table 2-3. Once the earthquake IM level, the Sa at the first vibration period, is increased, the overall pattern of tsunami-only fragility curves remains almost identical. However, these fragility curves are vertically reduced, starting from a larger value of exceedance probability for small values of tsunami IM when following earthquakes with higher Sa levels. Figure 2-13 reveals an increase in the failure probability for a structure if the direct impact of the earthquakes is incorporated in the generation procedure of the tsunami fragility functions. More specifically, this vertical reduction is occurring more rapidly for DS1 and DS2, meaning that structures can lose their capacity to resist tsunami waves even for smaller values of Sa. Park et al. (2012) also reported this cascading effect and the influence of the source earthquake on the near-field tsunami fragility curves using a simple nonlinear SDOF model with discrete and limited number of Sa points thus the final result assembled in the manager node of the cluster (outputs of Figure 2-13) will be entirely identical to the output of a single computer. In essence the number of simulations is unrealistic without parallelization, and thus this theoretical exploration underscores the promising potential of cluster computing in engineering applications, presenting the engineering community with the opportunity for substantial time savings without compromising the accuracy of results.

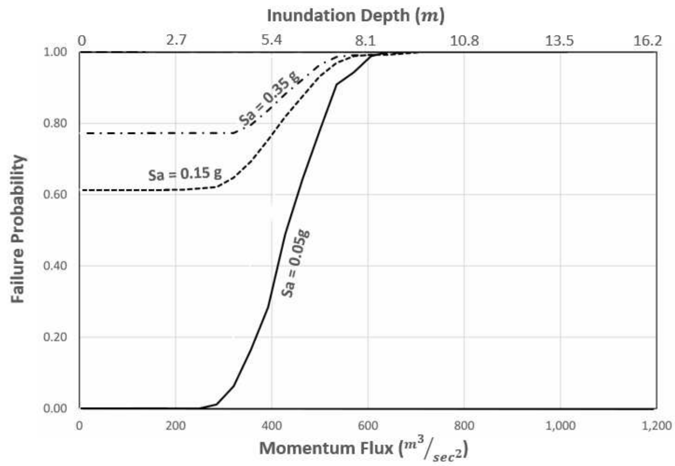

a) DS1

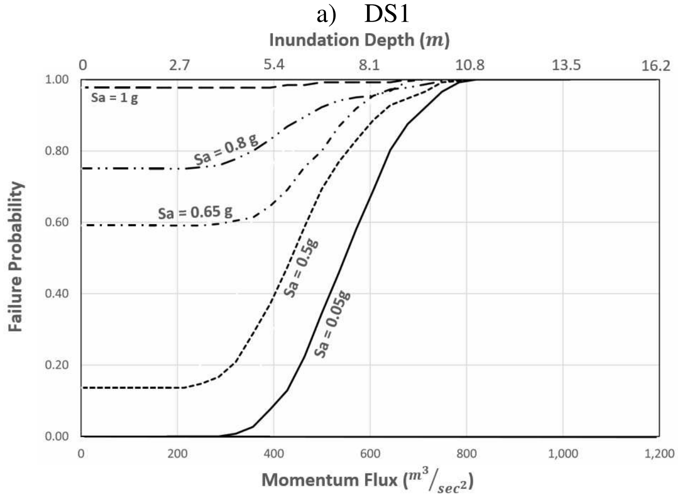

b) DS2

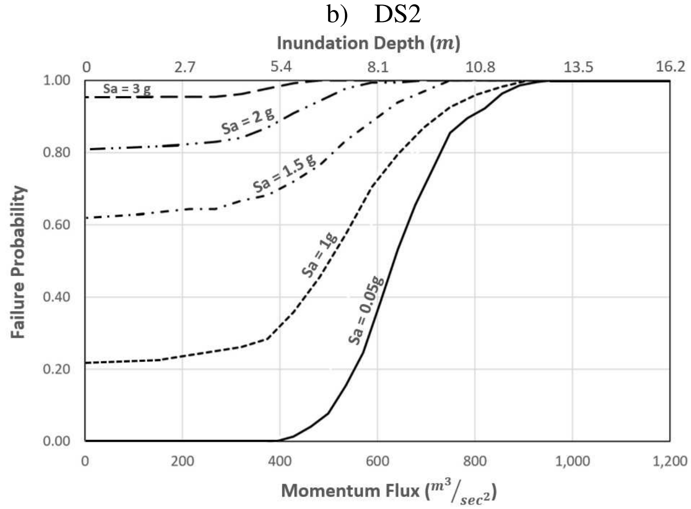

c) DS3

Figure 2-13. Tsunami-only fragility curves at different damage states conditioned on different values of spectral accelerations, Sa(T1[sec]), of the source earthquake

2.7 Computational Efficiency of the Framework

Figure 2-14 presents the framework performance and required computational time when the number of requested cores/CPUs is increased on the x-axis for two computational cases developing fragility surfaces with N equal to 225 and 400. This means that when the number of CPUs is set to 120, the parallel processing is performed with 120 CPUs only. In general, the required computational time is significantly reduced once the number of CPUs is increased to more than 80 for both cases. In Figure 2-14, the number of CPUs equal to unity represents the computational ability of a single machine or a basic personal computer running these analyses with sequential programming. As shown in Figure 2-14, a single machine needs 203 and 101 days to complete the required computational analysis of the fragility matrix for cases with N=400 and N=225, respectively.

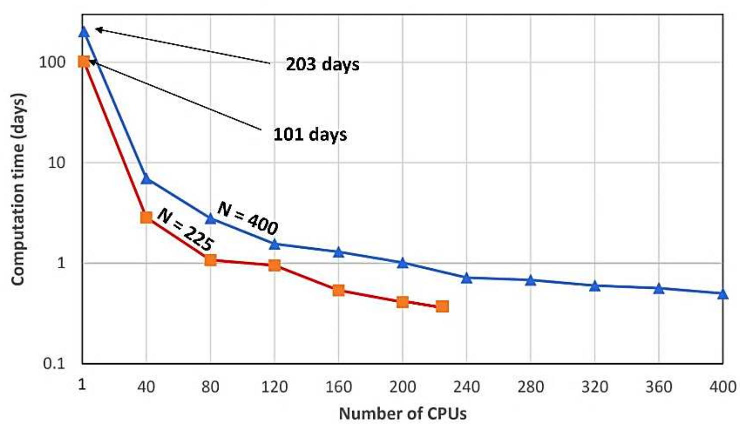

Figure 2-14. The computation time required for the generation of 3D fragility surfaces with N values equal to 225 and 400 shown for a single machine versus multi-distributed systems with increasing numbers of CPUs

Figure 2-15 also demonstrates the total required computation time of the analyses accomplished with different values of parameter N when the number of requested CPUs is the same as N value (fully distributed analysis). As seen in Figure 2-15, the required computational time for different cases remains almost the same. The differences are mainly due to the performance of the requested CPUs during the analysis, which is affected by several factors like CPU overheating, the temperature variation of the network, and the processing power of each CPU/node unit within the cluster.

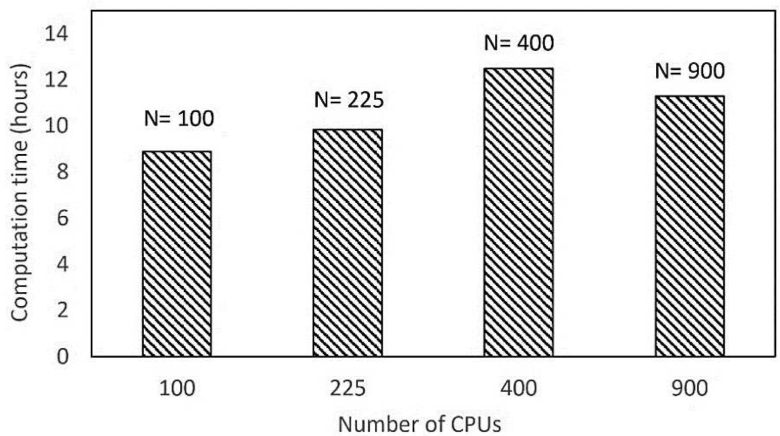

Figure 2-15. The computational time required to complete the successive analysis within the proposed MPI-based framework for different values of parameter N, namely for the N equal to 100, 225, 400 and 900.

CHAPTER 3: FRAGILITY FUNCTION PORTFOLIO OF REINFORCED CONCRETE AND WOODFRAME BUILDINGS[2]

3.1 Introduction

The impacts of natural hazards on the built environment can be mitigated by using community resilience as an analytical tool to manage, absorb, and adjust to the abrupt changes within the community and to return to the former (or improved) community condition in a reasonable timeframe following a natural hazard such as a tsunami and the source earthquake (Koliou et al., 2020). After an event, the recovery process of a community depends on the degree of infrastructure damage (Wang and van de Lindt, 2021) and on a number of other non-physical conditions. In other words, the initial damage to the infrastructure significantly impacts the functionality and recovery path of complex socioeconomic institutions within a community (Wang et al., 2021; Wang and van de Lindt, 2022; Watson et al., 2020; Zhang and Peacock, 2009). Regardless, community resilience frameworks require an appropriate estimate of the initial damage—through the development of fragility functions for a portfolio of building systems—to a community's infrastructure following a natural hazard to serve as initial conditions for recovery modeling.

This chapter develops earthquake-tsunami fragility surfaces for a portfolio of woodframe systems and RC buildings with various typologies and sizes, ranging from single-story to twenty-story structures, utilizing the methodology proposed by Harati and van de Lindt (2024) in Chapter 2 of this dissertation. The selected RC frame archetypes, encompassing both ductile and non-ductile systems, offer a representative sample typical in community settings. These models are instrumental for community-level studies to evaluate compound damage from earthquakes,

[2] This chapter is mainly based on the paper: Harati, M., and van de Lindt, J.W. (2024). "Fragility Function Development of RC Building Portfolio for Use in Earthquake-Tsunami Community Resilience Studies." Journal of Performance of Constructed Facilities, (Under Re-review).

tsunamis, or successive earthquake-tsunami events, enhancing the understanding of cascading effects on community-level spatial damage analyses. Diverging from previous computational-focused research, this work emphasizes the sequential probabilistic analysis and structural modeling process, contributing significantly to the scalability of fragility surface development and high-fidelity modeling for multi-hazard fragility functions, particularly in the contexts of multi-hazard community resilience analysis.

3.2 Development of Building Portfolio

3.2.1 Reinforced Concrete Buildings

The RC building portfolio in this study included ductile and non-ductile RC Moment Resisting Frames (MRFs), varying in structural height, configuration, and, more specifically, in design details. These MRF systems represent old and modern RC frames in California, which can be considered for a coastal region prone to both earthquake and tsunami hazards. Six RC ductile frames and four RC non-ductile frames with space frame lateral resisting systems were selected from previous studies by Haselton et al. (2011) and Liel et al. (2011), respectively.

All 10 RC buildings are assumed to be office buildings with a 20.3mm (8in) flat-slab floor system. In the RC ductile frames, the lateral force resisting systems (LFRS) have different bay lengths than their non-ductile counterparts and range from one- to twenty-stories. On the other hand, the non-ductile RC frames are designed to range from two- to twelve-stories. The general geometric properties and configurations of these LFRS are summarized in Figure 3-1, where bay length, the height of the first story, and the height of other stories above the first floor are denoted with L_1, L_2, and L_3, respectively. Table 3-1 summarizes some essential information along with those parameters depicted in Figure 3-1.

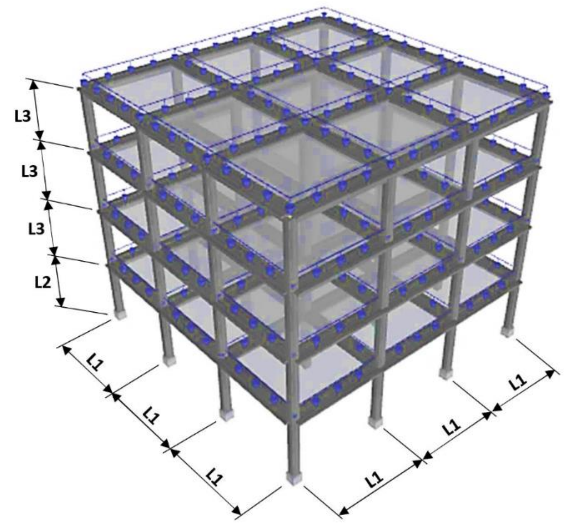

Figure 3-1. The frame configuration of a typical RC building used for numerical simulation in this study.

Table 3-1. General characteristics of the ductile and non-ductile RC frames (Haselton et al. 2011; Liel et al. 2011)

Structure ID	Number of stories	Ductility status	Seismic code	L_1 (ft.)	Base shear Coefficient	L_2 (ft.)	L_3 (ft.)
RC1	1	Ductile	ASCE 7-02	20	0.121	15	13
RC2	2	Ductile	ASCE 7-02	20	0.125	15	13
RC3	4	Ductile	ASCE 7-02	20	0.092	15	13
RC4	8	Ductile	ASCE 7-02	20	0.050	15	13
RC5	12	Ductile	ASCE 7-02	20	0.044	15	13
RC6	20	Ductile	ASCE 7-02	20	0.044	15	13
RC7	12	Non-ductile	UBC (1967)	25	0.047	15	13
RC8	8	Non-ductile	UBC (1967)	25	0.054	15	13
RC9	4	Non-ductile	UBC (1967)	25	0.068	15	13
RC10	2	Non-ductile	UBC (1967)	25	0.086	15	13

Liel et al. (2011) reported that the general structural configuration and geometric properties of non-ductile RC frames are based on the original structural drawings of RC buildings constructed before 1960. These MRF systems, as seen in Figure 3-1, are regular in elevation and plan, and have no strength or stiffness laterally irregularities. The non-ductile RC frames were seismically designed according to the highest seismic zone in California at the time, which was Zone 3 of the 1967 UBC code. In this regard, the design procedure for the non-ductile MRFs followed the essential building code requirement of that time, including maximum and minimum reinforcement ratio, stirrup design, and maximum spacing, to name a few. Readers are referred to the work conducted by Liel and Deierlein (2008) for more information on the structural details of the employed non-ductile LFRS in this study.

The study by Haselton et al. (2011) used the International Building Code (ICC 2003), ASCE 7 (ASCE 2002), and ACI 318 (ACI 2005) to design structural members for ductile RC frames. A special moment frame design procedure was employed to meet applicable code requirements for strength, stiffness, design capacity, as well as the dimensional details of the structural members. The current seismic design guidelines provide more ductility for structural members through provisions such as strong column-weak beam ratios, enhanced joint shear capacities, and regulations related to transverse confinement in plastic hinge zones. These ductile frames were designed for a typical high seismic location in Los Angeles was reported to be utilized, characterized by the S_D soil classification category. From Table 3-1, it can be seen that the design of both ductile and non-ductile frames was carried out in such a way that the base shear coefficients of two equivalent frames (e.g., eight-story RC frames with ductile and non-ductile systems) are adequately normalized, resulting in nearly identical base shear coefficients for both systems of the same height.

3.2.2 Woodframe Buildings

Although woodframe buildings are typically destroyed by a tsunami of more than a meter, they are prevalent in U.S. coastal communities and need to be represented in the community model. Thus, the methodology offered by Harati and van de Lindt (2024) presented in Chapter 2 has been used in this chapter to develop earthquake-tsunami fragility surfaces for woodframe structures. Laboratory tests have uncovered pronounced pinching in the hysteretic response of WSPs, suggesting that the in-plane strength and stiffness of these panels are primarily influenced and governed by their nailing patterns to vertical and horizontal studs, as elaborated in Bahmani et al. (2016).

This research provides detailed depictions of two-story woodframe structures, drawing on Amini (2012), as demonstrated in Figure 3-2, and includes the geometry and layout of the lower floor for simulating single-story structures with a story height of 2.74 meters. The exterior walls of both woodframe archetype structures comprise a layer of 12 mm thick sheathing-rated plywood with 10d nails, an external 19×184 mm horizontal wood siding (HWS) attached with two 8d nails per stud, and an interior layer of 12.7-mm gypsum wall board (GWB) fastened with #6 screws. Interior walls follow the same setup, excluding HWS. For the single-story structure, the configuration of the exterior walls remains the same except 6d nails were used for the nailing of HWS and GWB panels.

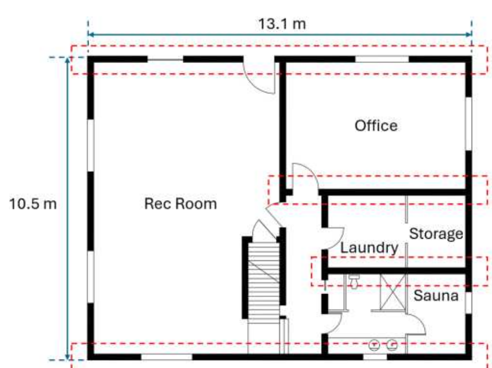

a) Lower floor

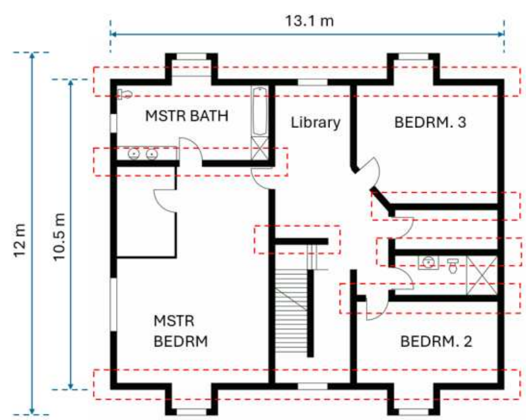

b) Upper floor

Figure 3-2. The geometry plan of one- and two-story woodframe buildings considered for the nonlinear modeling procedure (after Amini, 2012).

Although the structural system modeling remains consistent across designs (discussed later in this chapter), variations in the models arise from differing nail spacings in the WSP, which afford the structures varying ductility capacities. Specifically, three edge nailing spacings

(51 mm (2 in), 102 mm (4 in), and 153mm (6 in) cm) have been implemented for the WSPs, categorizing the structures from low-code to high-code design levels, in ascending order. Moreover, the study differentiates structures by employing the peak inter-story drift ratio (IDR) as the engineering demand parameter (EDP) acceptance criterion for various damage states, in line with HAZUS (2020) guidelines for different design levels (low, moderate, high). Structural identifiers such as W13 and W21 denote design levels and number of stories: W13 corresponds to a single-story building with a low design level, and W21 to a two-story building with a high design level, where the first digit signifies the number of stories and the second indicates the design level (3 for low, 2 for moderate, 1 for high). Consequently, the study models six distinct woodframe archetypes (W11, W12, W13, W21, W22, and W23) to develop earthquake-tsunami fragility surfaces for woodframe structures.

3.3 Earthquake and Tsunami Modeling

Earthquakes and tsunamis are closely linked hazards, where the structural damage caused by an earthquake can significantly increase the vulnerability of buildings to subsequent tsunami impacts. In this study, a successive analysis approach (introduced in Chapter 2) is used to develop fragility functions for both earthquake and tsunami hazards. The earthquake loading is analyzed using Multiple Strip Analysis (MSA), which helps predict structural responses at various seismic intensity levels. For the tsunami loading, a Nonlinear Static Procedure (NSP) is employed, incorporating a variable-height load pattern (VHLP) to account for the dynamic nature of tsunami waves. Additionally, the method considers the effects of building openings on the hydrodynamic forces, providing a more accurate representation of potential structural damage. Readers are referred to Chapter 2 of this dissertation for more details.

3.4 Structural Modeling Procedure
3.4.1 Modeling of RC Buildings

The nonlinear modeling of the selected structural systems was developed in OpenSeesPy (Zhu, 2021), as discussed in Chapter 2. As discussed in the previous chapter, beams and columns of considered RC buildings are considered to behave elastically while having nonlinear rotational springs at endpoints serve as the regions for concentrated plasticity. Modified Ibarra-Medina-Krawinkler (IMK) element (Ibarra et al. 2005; Lignos and Krawinkler 2011) was employed as the nonlinear rotational springs for both beams and columns (Figure 3-3) for all RC structures in this study. The modified IMK plastic hinge models are devised in such a way that they are capable of incorporating the strength and stiffness reduction of the element as it is damaged during the analysis. The modified IMK model provides hysteresis behavior for nonsymmetric degrading elements, such as RC beams with concrete slabs. In short, the beams and columns are modeled collectively by assembling an elastic beam-column element to two IMK hinges located at two extreme endpoints.

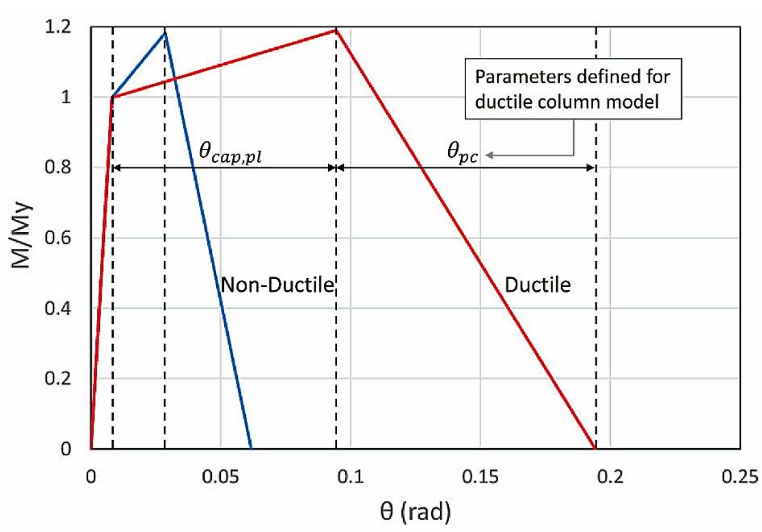

Figure 3-3. The column monotonic backbone curve based on Ibarra-Medina-Krawinkler (IMK) deterioration model (Liel et al. 2011).

The nonlinear structural behavior of beam-column joints was incorporated in this FE modeling procedure, where Joint2D elements with five nodes in OpenSeesPy are utilized for this purpose. As explained in the previous chapter, the surrounding nodes serve as the connection points between the beam-column joint and the beam or column elements. The node located at the center of the element is included to account for the linear or nonlinear shear deformation behavior of the joint. In the case of modeling an RC ductile frame, a linear uniaxial material is assigned to the central node of the Joint2D, as suggested by Haselton et al. (2011). But a non-linear uniaxial material, as recommended by Celik and Ellingwood (2008), is employed for the central node of the Joint2D element of the non-ductile RC frames. Hence, the brittle failure mode of the beam-column joints in a non-ductile RC frame can also be taken into account in this structural modeling approach.

Recall that for the tsunami loading phase in the successive analysis procedure, an NSP analysis with a VHLP loading profile was selected in this dissertation. Columns at the seaward side of the structural model have been discretized to make possible the formation of the VHLP tsunami lateral loading profile that can potentially increase along the height of the building (see Chapter 2 for more details). It should also be mentioned that the modeling approach herein does not incorporate the local shear failure mechanism in both beams and especially for columns that may be exposed to the shear demand of the tsunami flows. However, the shear capacity of the columns at the seaward side of the buildings was checked against the accepted shear failure criteria through a postprocessing procedure. The acceptance criteria for the column shear failure (CSF) is recommended by Biskinis et al. (2004), which allows for the implementation of the non-drift (shear force) damage state defined for columns in the second phase of the analysis. Consequently, the nonlinear structural models developed in this study can just incorporate a sidesway collapse mode directly. Nevertheless, if the shear demand in a seaward column exceeds the precalculated shear capacity, the analysis is stopped before reaching the terminal point in the sideway collapse mode and a failure is recorded.

The modeling choice, focusing on collapse simulation for DS3, involved using concentrated plasticity with modified IMK plastic hinges for structural elements. This approach effectively models the dominant flexural failure mode in RC structures, but makes including interface shear springs challenging, often causing nonconvergence issues in nonlinear analysis. Thus, shear capacity of the columns at the seaward side was considered as additional EDP along with peak SDR, as per the recommendation of studies such as Petrone et al. (2017). The shear failure model for columns at DS3 utilized equation (8) from Biskinis et al. (2004).

Implementing interface shear springs is more feasible in nonlinear modeling using the fiber section approach. However, this method was found less effective for accurately modeling the deterioration of RC members during the softening branch of the hysteretic response. Moreover, it is important to recognize that omitting joint shear panels in the modeling impacts the response of non-ductile systems, as corroborated by previous studies such as Celik and Ellingwood (2008). Due to this reason, joint shear panels have been incorporated into the structural modeling of non-ductile frames in this research.

3.4.2 Modeling of Woodframe Buildings

The pinching characteristic of WSPs in woodframe buildings of this study is simulated using the CUREe 10-parameter hysteretic model, also referred to as the SAWS model (Folz and Filiatrault, 2001), and available in the OpenSeesPy software (Zhu, 2021). Although empirical studies indicate a reduction in strength and stiffness of 30 to 50 percent for WSPs with openings (Anil et al., 2018), this analysis conservatively focuses solely on unperforated WSPs, excluding any panels with openings.

The SAWS hysteresis model with parameters sourced from Bahmani (2015) and Roohi et al. (2019) for WSPs (for different structural archetypes) aligned along the x-axis in Figure 3-3. It is worth mentioning that both exterior and interior wall layers are modeled using parallel 2-node link elements in OpenSeesPy. The WSPs and other wall elements featuring openings are linked to main WSPs through rigid connections rather than being directly modeled in the hysteresis analysis.

3.5 Methodology to Develop Earthquake-tsunami Fragility Surfaces

The method proposed by Harati and van de Lindt (2024), presented in Chapter 2, was selected to generate earthquake-tsunami fragility surfaces for a portfolio of woodframe and RC buildings for use in community-level damage and resilience analysis. This method employs a multiprocessing distributed framework to conduct millions of successive analyses. The process begins with a Monte Carlo loop that selects and scales ground motions (GMs) using the earthquake intensity measure (IM) as input, then generates uncertain parameters for the finite element (FE) nonlinear structural model and the equivalent tsunami force calculation. The structural model considers random variables for parameters such as plastic hinge development. The equivalent tsunami force is calculated using random values for C_0 and C_d, along with momentum flux (MF_i) as the tsunami IM. The flow velocity and other variables are adjusted incrementally to account for variability in water depth and velocity. This comprehensive approach ensures accurate modeling of the effects of successive earthquake and tsunami events on building structures. Readers are referred to Chapter 2 of this dissertation for more details.

Once the successive analysis procedure is complete, the recorded EDPs from the first and second phases of the analysis are evaluated against predefined damage states. If the analysis indicates that the structure or system cannot meet a particular damage state under the specific hazard scenario being examined, it is regarded as a failure for that realization of the MCS. The acceptance criteria for various damage states of buildings are detailed in Table 3-2, where peak SDRs for DS1 to DS3 are sourced from HAZUS, and the collapse failure capacity of seaward columns is the criterion for DS3 only.

It is worth mentioning that the HAZUS framework considers ductile RC archetypes in this research as High-Code structures. While HAZUS was revolutionary when developed, it has not had significant updates, though OpenHAZUS improvements are underway. Therefore, buildings designed with the most recent seismic design codes are assumed to represent High-Code structures for this analysis and research. Additionally, seismic codes and design guidelines (e.g., ASCE-7 and ACI codes) have been updated multiple times since ASCE 7-02, with changes in the minimum loads as a function of changes in ASCE 7. Consequently, it is logical to consider room for structural upgrading and retrofitting, allowing these frames to be classified as High-Code systems.

Furthermore, another assumption for the structural classification of the RC archetypes is based on building height:

- RC structural systems from 1-4 stories are considered low-rise RC buildings.
- Structural systems with 8 stories are considered mid-rise RC buildings.
- Structural frames with 12 and 20 stories are considered high-rise RC buildings.

Table 3-2. Damage limits considered for both earthquake and tsunami hazards

Structure ID	Hazard	EDPs	DS1	DS2	DS3
RC1	Earthquake	SDR (%)	0.9 %	2.3 %	6%
	Tsunami	*SDR (%) + CSF*	*0.9 %*	*2.3 %*	*6% or CSF*
RC2	Earthquake	SDR (%)	0.9 %	2.3 %	6%
	Tsunami	*SDR (%) + CSF*	*0.9 %*	*2.3 %*	*6% or CSF*
RC3	Earthquake	SDR (%)	0.9 %	2.3 %	6%
	Tsunami	*SDR (%) + CSF*	*0.9 %*	*2.3 %*	*6% or CSF*
RC4	Earthquake	SDR (%)	0.6 %	1.5 %	4%
	Tsunami	*SDR (%) + CSF*	*0.6 %*	*1.5 %*	*4% or CSF*
RC5	Earthquake	SDR (%)	0.45 %	1.15 %	3%
	Tsunami	*SDR (%) + CSF*	*0.45 %*	*1.15 %*	*3% or CSF*
RC6	Earthquake	SDR (%)	0.45 %	1.15 %	3%
	Tsunami	*SDR (%) + CSF*	*0.45 %*	*1.15 %*	*3% or CSF*
RC7	Earthquake	SDR (%)	0.4 %	1 %	2.5%
	Tsunami	*SDR (%) + CSF*	*0.4 %*	*1 %*	*2.5% or CSF*
RC8	Earthquake	SDR (%)	0.53 %	1.32 %	3.3%
	Tsunami	*SDR (%) + CSF*	*0.53 %*	*1.32 %*	*3.3% or CSF*
RC9	Earthquake	SDR (%)	0.8 %	2 %	5%
	Tsunami	*SDR (%) + CSF*	*0.8 %*	*2 %*	*5% or CSF*
RC10	Earthquake	SDR (%)	0.8 %	2 %	5%
	Tsunami	*SDR (%) + CSF*	*0.8 %*	*2 %*	*5% or CSF*

To account for the uncertainty in the simulation, the procedure is repeated K times, with the same GM and joint IM used for each round. Past sensitivity analyses suggested that an initial value of K (*K_initial*) should be 10 for preliminary uncertainty quantification. This approach involved conducting pilot Monte Carlo Simulations (MCS) for each of the N joint IMs at damage state j, which then informed the calculation of the total number of samplings ($n_{t,i}$) for the entire MCS analysis at the individual IM level. The required sample size for each IM was determined using the formula: $n_r = ((Z^2 \sigma^2) / Er^2)$, where Z is the Z-score corresponding to a 95% confidence level, σ^2 is the variance from the pilot run, and Er is the margin of error. This iterative refinement aimed at achieving an average error below 1% across the dataset, while maintaining a 95% confidence interval.

As part of this comprehensive assessment, *K_final*, the maximum value among all K values calculated for different IMs and damage states, was determined. *K_final* represents the number of iterations required to ensure the robustness of the MCS methodology. This number was found to be 100 for the study, providing sufficient sampling points for uncertainty propagation. The empirical verification of this *K_final* value across all structures in the fragility simulations confirmed that K=100 sufficed for the scope and requirements of the analyses.

Furthermore, in alignment with established practices in literature, it was assumed that all random variables in the simulations were perfectly uncorrelated. This assumption, foundational to the methodological approach, influenced the interpretation and application of the simulation results, and it is compatible with previous research (Liel et al. 2009). The same computational process should be followed for all GM records for a given joint IM, enabling the calculation of the exceedance probability of failure on each damage state through the MCS. Therefore, the exceedance probability of failures is obtained on all damage states through this sequential algorithm using a joint IM as the primary input parameter.

When a fragility matrix is created using the methodology outlined earlier, the raw data collected in a discrete format is subjected to a surface fitting procedure. This procedure, recommended by previous research (Chou and Talalay, 2005; Greco et al., 1995; Kern et al., 2004), is used to produce a near-continuous function that represents the earthquake-tsunami fragility surface at a specified damage state. The raw data for the fragility points is recorded in a three-dimensional coordinate system, enabling the creation of a fitted 3D surface over the collected data. The independent variables for these discrete data are *Sa* and *MF*, the selected IMs for earthquake and tsunami. The equation that can control the 3D fragility surfaces at different damage states is as follows:

$$P(Sa, MF) = \frac{E(\frac{Sa}{C1} + \frac{MF}{C2} + \alpha\left(\frac{Sa}{C1}\right)\left(\frac{MF}{C2}\right))^n}{(\left(\frac{Sa}{C1} + \frac{MF}{C2} + \alpha\left(\frac{Sa}{C1}\right)\left(\frac{MF}{C2}\right)\right)^n + 1)} \tag{3-1}$$

where the parameter E, along with the tuning parameters $C1$, $C2$, α, and n for the fragility surface over each desired damage state, were optimized using a nonlinear least squares method. While Kern et al. (2004) found E to be 1.01, in this study, it is treated as one of the target variables for optimization, alongside the other parameters. This method was selected for its proficiency in fine-tuning parameters to closely align with observed data, aiming to minimize the sum of squared differences between observed fragility data and model predictions. The optimization process involved iterative refinement of parameter values from initial estimates for the most accurate fit.

Additionally, a comprehensive sensitivity analysis was conducted to evaluate the impact of various optimization algorithms on solving the Nonlinear Least Squares (NLS) problem for our fragility function. Algorithms like Levenberg-Marquardt, Nelder-Mead, BFGS, and Conjugate Gradient were systematically compared under consistent initial conditions and datasets. This process involved monitoring each algorithm's convergence behavior, stability, and sensitivity to initial parameter estimates, as well as assessing their robustness and computational efficiency.

The findings revealed that the Levenberg-Marquardt algorithm, a hybrid of the Gauss-Newton algorithm and gradient descent, was most effective for this NLS problem. Its ability to interpolate between the Gauss-Newton approach and gradient descent, adapting based on the problem nature and residual sum of squares behavior, was especially advantageous for the complexity of our fragility function. This sensitivity analysis was instrumental in guiding the choice of optimization algorithm, ensuring the reliability and precision of the model in predicting structural fragility under multi-hazard scenarios. Therefore, in this study, five tuning parameters, including E, are required for the fragility surface over each damage state. The projection onto each 2D plane provides the earthquake-only or tsunami-only fragility (or scalar fragility function) when one IM is set to zero, which can be expressed as:

$$Frg(IM) = \emptyset(\frac{\ln(IM) - \mu}{\sigma}) \tag{3-2}$$

where IM represents a variable for a preferred range of intensity levels used to characterize hazards involved, i.e., both the earthquake and tsunami events; μ and σ refer to the mean and standard deviation of the logarithmically transformed IM for the dataset corresponding to the failure of the structural system. These parameters are derived from log-transformed data, emphasizing their relevance in a logarithmic context rather than in their original scale. The function Φ typically represents the cumulative distribution function of the standard normal distribution. To achieve this, a function representing the lognormal CDF is defined, and the Nelder-Mead algorithm is used to identify the optimal parameters (mean and standard deviation) that provide the best fit. This process is applied across different data sets, each representing varying earthquake-only or tsunami-only hazard scenarios, ensuring a nuanced fitting of the lognormal CDF to the extracted edge data and accurately reflecting the statistical properties. The Nelder-Mead simplex algorithm is particularly well-suited for handling nonlinear optimization problems where derivatives of the objective function are not available or difficult to compute. Recognized as a well-established technique in the realm of unconstrained optimization, the Nelder-Mead method is especially known for its application in multidimensional optimization problems. Its primary advantage in this context is its ability to navigate complex, nonlinear spaces without necessitating the gradient of the objective function. The goal of the optimization is to minimize the discrepancy between empirical data and the theoretical lognormal CDF.

The optimized parameters μ and σ, obtained through the Nelder-Mead method, can be readily utilized to reproduce the scalar fragility curves for earthquake-only or tsunami-only hazards. This precision in parameter optimization, achieved through the effective use of the Nelder-Mead algorithm, ensures a more accurate and reliable representation of the scalar fragility curves, critical for assessing structural vulnerability in single-hazard scenarios.

3.6 Fragility Surfaces for the RC Portfolio

The fragility matrix of a 4-story RC ductile frame is explained in detail to illustrate the results using a 30 × 30 matrix for the joint IM (i.e., Sa for earthquake IM and MF for the tsunami). However, through a parametric study, it was found that the 400 points for the joint IM results in an appropriate level of accuracy when developing earthquake-tsunami fragility surfaces. Figure 3-4(a) shows these discrete data points obtained for the complete damage state (collapse) of the 4-story RC ductile frame. Figure 3-4(b) illustrates the final governing earthquake-tsunami fragility surface for the illustrative building, with the x and y axis on the horizontal plane representing the IM of earthquake and tsunami, respectively. The values along the z-axis indicate the exceedance probability for the damage state, which in this figure is collapse.

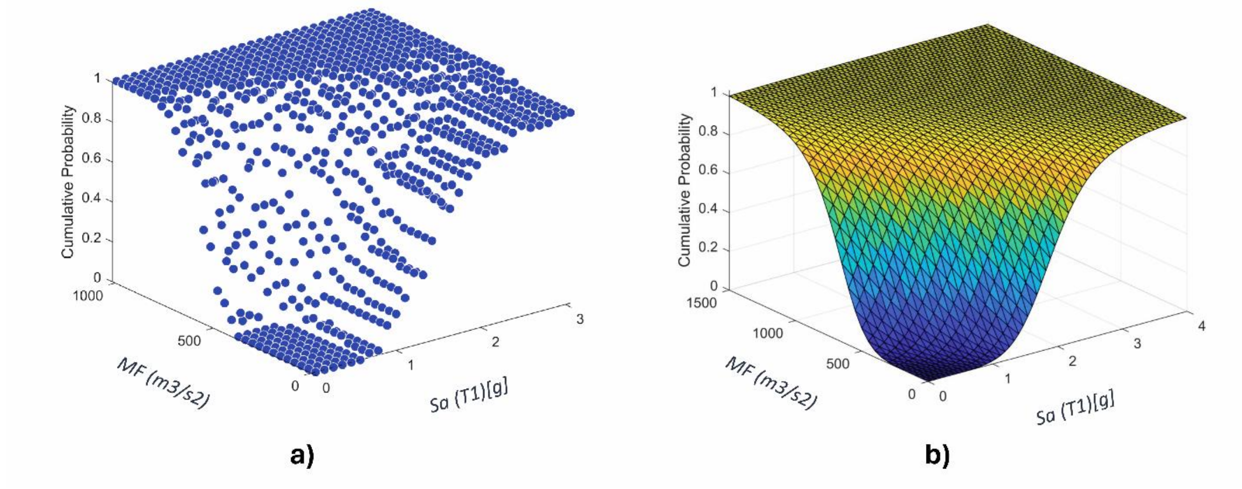

Figure 3-4. Fragility function of Earthquake and Tsunami for the 4-story building with ductile frames: a) points of raw data points; b) the fit fragility surface.

Figure 3-5 displays the earthquake-tsunami fragility surfaces for the 4-story RC ductile system across all considered damage states, including the slight, moderate, and complete damage state levels. Each edge of these fragility surfaces features three 2D fragility curves. For example, in the plane defined by the Sa and z-axis, 2D fragility curves for the earthquake-only hazard are derived for various damage states. Similarly, on the other edge of the fragility surfaces, along the MF axis, 2D fragility curves for the tsunami-only hazard across different damage states can be produced. Figs 3-5(b) and 3-5(c) depict the 2D fragility curves for earthquake-only and tsunami-only hazards, respectively.

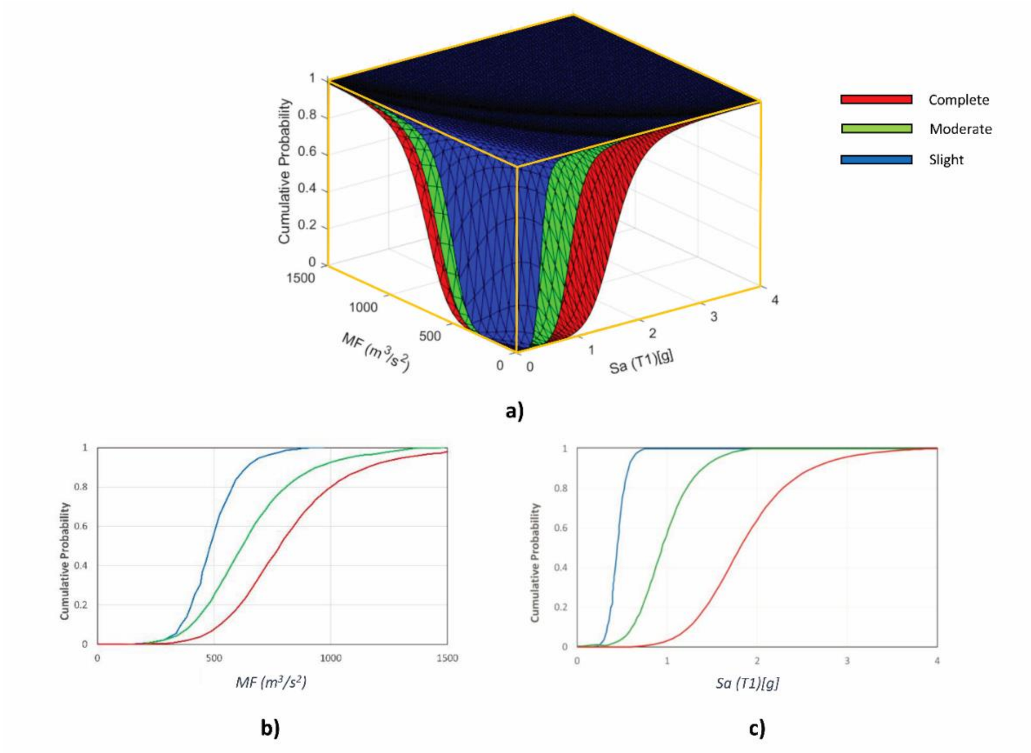

Figure 3-5. Fragility function of Earthquake and Tsunami at different damage states for a 4-story ductile system: a) earthquake-tsunami fragility surfaces; b) tsunami-only fragility curves; c) earthquake-only fragility curves.

Figure 3-6 compares the earthquake-tsunami fragility surfaces of the ductile and non-ductile frames for the 4-story RC building. As seen in Figure 3-6, for a Sa(T_1) of 1.2 and MF of zero, DS3 (complete damage state) is exceeded in the non-ductile system, while just DS1 is fully exceeded in the equivalent ductile system. It should also be noted that the ductile system is far from DS3, meaning that the damaged ductile system in this earthquake intensity level may still withstand the potential incoming tsunami.

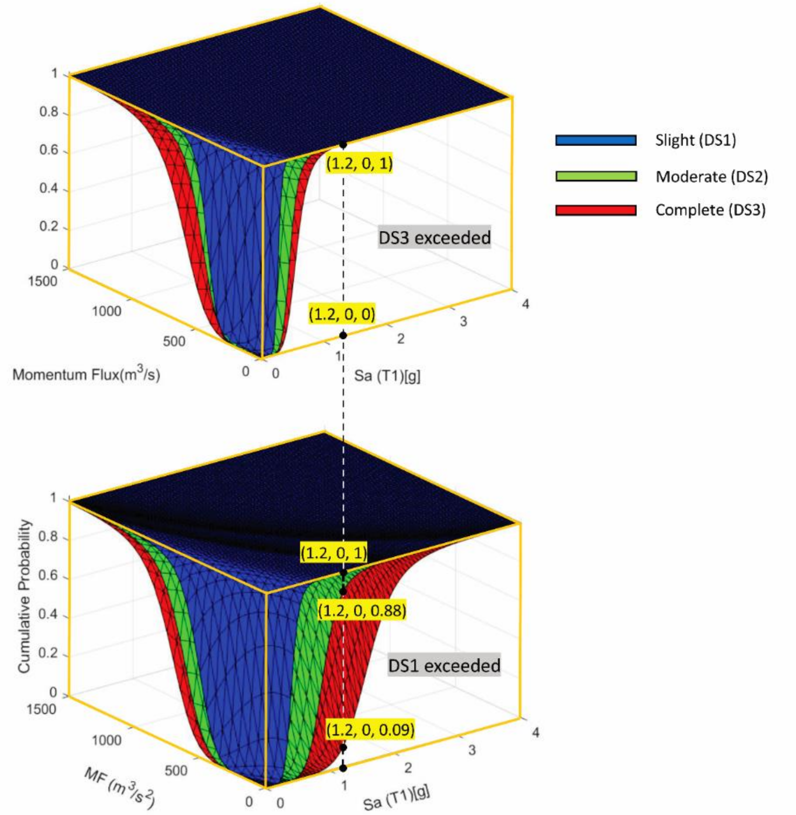

Figure 3-6. Comparison of fragility surfaces for four-story ductile and non-ductile RC frames

Fragility surfaces for all RC ductile frames were generated for all damage states using the method described earlier and are depicted in Figure 3-7(a) - (f).

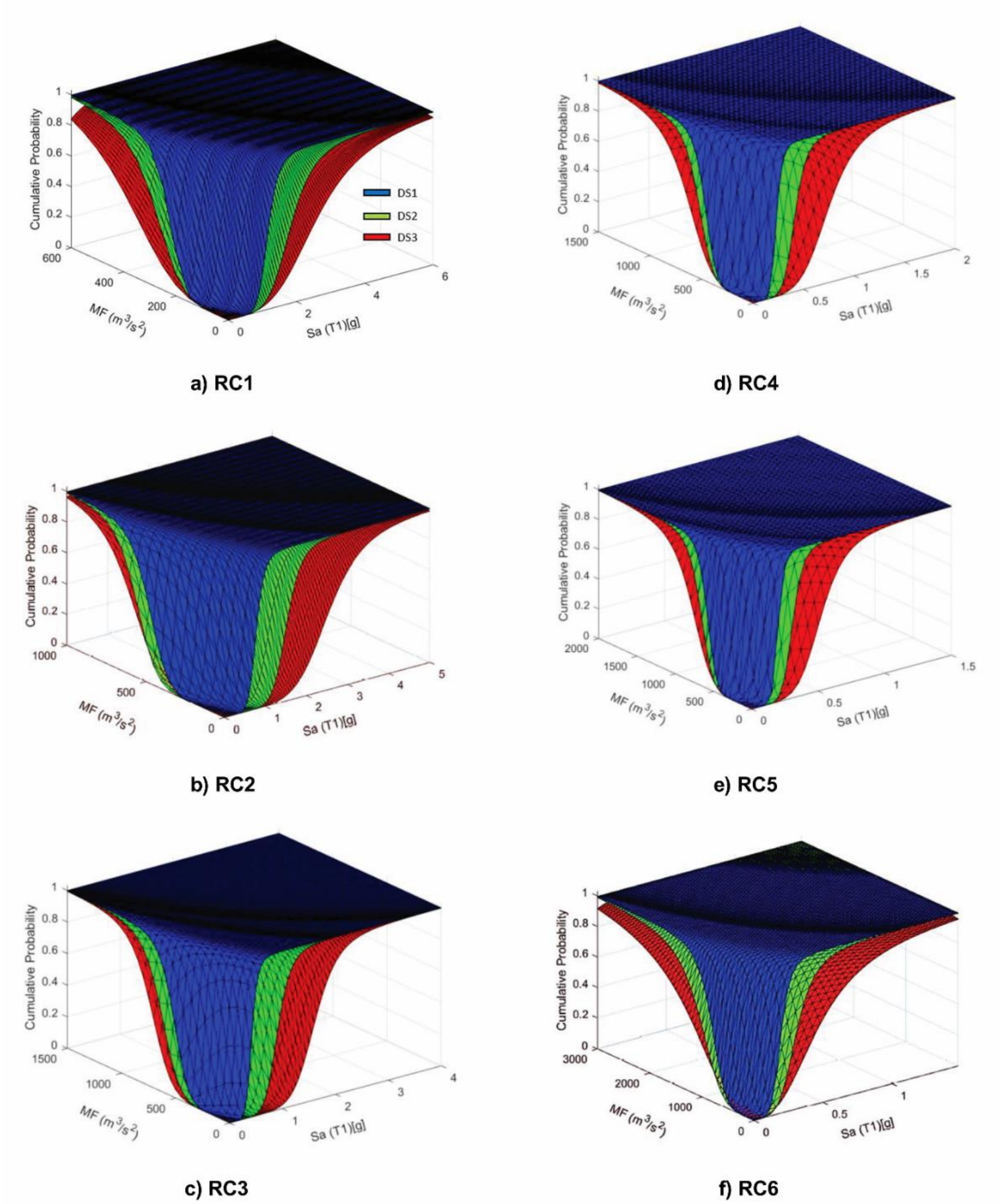

Figure 3-7. Earthquake-tsunami fragility surfaces at different damage states for ductile RC structures.

For all considered non-ductile frames within the archetypes, the earthquake-tsunami fragility surfaces on different damage states are shown in Figure 3-8(a) - (d).

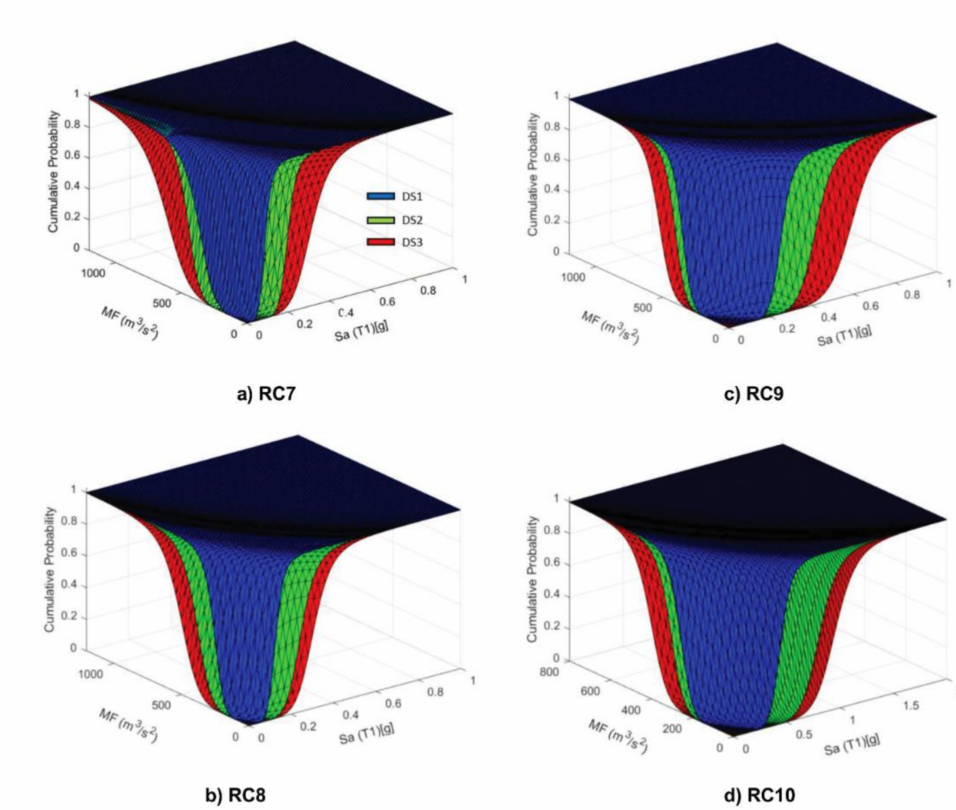

Figure 3-8. Earthquake-tsunami fragility surfaces at different damage states for non-ductile RC structures.

Table 3-3 shows the parameters for Eq (3-1)—including *C1, C2, α, n* and *E*—which can be used for the reproduction of earthquake-tsunami fragility surfaces for the ductile RC structures (RC1 to RC6) at different damage states. The same parameters have also been derived for generating 3D fragility surfaces for the non-ductile RC frames (RC7 to RC10), which are presented in Table 3-4.

Table 3-3. Equation parameters of the Earthquake-tsunami fragility surfaces of ductile RC structures at different damage states

Structure ID	Parameters	DS1	DS2	DS3
RC1	*E*	0.9973	0.9973	0.9973
	C1	1.1601	1.8230	2.5744
	C2	225.4266	276.9641	388.1996
	α	0.4329	0.4932	0.4586
	n	7.6751	5.4427	3.8462
RC2	*E*	0.9960	0.9960	0.9960
	C1	0.7755	1.5139	2.5297
	C2	478.1557	557.5409	588.6952
	α	0.5236	0.6407	0.6680
	n	8.1705	8.7889	6.2539
RC3	*E*	0.9982	0.9982	0.9982
	C1	0.4158	0.9054	1.6147
	C2	516.6436	630.4792	724.6698
	α	0.3683	0.5087	0.6414
	n	7.7202	7.4998	7.6486
RC4	*E*	0.9984	0.9984	0.9984
	C1	0.2281	0.4110	0.7479
	C2	464.9751	527.5779	636.9152
	α	0.4493	0.5253	0.5477
	n	8.6275	7.4997	5.2587
RC5	*E*	0.9980	0.9980	0.9980
	C1	0.1978	0.3062	0.5210
	C2	580.4954	664.4953	776.5700
	α	0.5265	0.5880	0.6023
	n	9.5770	8.3665	5.8722
RC6	*E*	0.9967	0.9967	0.9967
	C1	0.1932	0.3054	0.4681
	C2	809.1049	1025.8409	1251.3973
	α	0.4593	0.4977	0.5375
	n	5.8857	4.6346	2.7752

Table 3-4. Equation parameters of the earthquake-tsunami fragility surfaces of non-ductile RC structures at different damage states

Structure ID	Parameters	DS1	DS2	DS3
RC7	E	0.9993	0.9993	0.9993
	$C1$	0.0875	0.1979	0.3120
	$C2$	367.8088	452.2027	627.1102
	α	0.3065	0.4388	0.5580
	n	6.0108	9.9658	6.7042
RC8	E	1.0001	1.0001	1.0001
	$C1$	0.1262	0.2461	0.3063
	$C2$	258.1447	386.6487	506.4890
	α	0.2974	0.4433	0.5472
	n	7.0755	7.2128	7.5200
RC9	E	0.9964	0.9964	0.9964
	$C1$	0.2527	0.4205	0.5993
	$C2$	352.2990	406.6396	528.6192
	α	0.5169	0.6347	0.7235
	n	9.6303	10.1855	10.6232
RC10	E	0.9967	0.9967	0.9967
	$C1$	0.4441	0.8086	0.9575
	$C2$	258.6707	308.3039	404.2588
	α	0.4900	0.6305	0.7312
	n	9.1335	9.6257	10.0400

Tables 3-5 and 3-6 present the parameters for Eq (3-2) that have been derived to replicate the 2D fragility curves for earthquake-only and tsunami-only hazards, respectively. These tables provide the CDF lognormal parameters (μ, σ) for all structures within the minimum portfolio across three defined damage states (DS1-DS3). The log CDF functions, fitted to the data at the edges of these surfaces, yield an S-shaped curve that slightly differs from the one extracted directly from the fragility surfaces. This difference arises due to the distinct functions used. However, these log CDF functions serve as a viable approximation for the edges of the surfaces, especially in resilience frameworks that incorporate log CDF functions for 2D fragility curves.

Table 3-5. Equation parameters for the 2D fragility curves of earthquake-only hazard

Structure ID	Parameters	DS1	DS2	DS3
RC1	μ	-0.0893	0.3395	0.6701
	σ	0.3476	0.5862	0.7206
RC2	μ	-0.4546	0.2452	0.7234
	σ	0.1930	0.2510	0.4520
RC3	μ	-1.2171	-0.3036	0.3374
	σ	0.5722	0.3201	0.3933
RC4	μ	-1.6596	-1.0579	-0.5356
	σ	0.2281	0.3709	0.6133
RC5	μ	-1.8184	-1.3213	-0.8181
	σ	0.2256	0.3607	0.5799
RC6	μ	-1.8043	-1.4206	-1.0465
	σ	0.4469	0.6177	0.7603
RC7	μ	-2.0712	-1.7584	-1.3606
	σ	0.3138	0.2928	0.4760
RC8	μ	-2.1929	-1.5074	-1.3325
	σ	0.5266	0.3137	0.3950
RC9	μ	-1.5329	-0.9993	-0.8328
	σ	0.1421	0.2183	0.2983
RC10	μ	-0.9903	-0.3669	-0.1745
	σ	0.1603	0.2265	0.2377

Table 3-6. Equation parameters for the 2D fragility curves of tsunami-only hazard

Structure ID	Parameters	DS1	DS2	DS3
RC1	μ	5.2687	5.5930	5.9295
	σ	0.1907	0.1764	0.1605
RC2	μ	5.9923	6.1523	6.2917
	σ	0.1896	0.1887	0.1471
RC3	μ	6.0807	6.2821	6.5174
	σ	0.1814	0.1769	0.1743
RC4	μ	5.8794	6.1350	6.4179
	σ	0.1706	0.2122	0.2022
RC5	μ	6.1467	6.3874	6.6136
	σ	0.1712	0.1926	0.1757
RC6	μ	6.5222	6.8849	7.1218
	σ	0.2738	0.2162	0.1782
RC7	μ	5.2153	5.9160	6.2901
	σ	0.4822	0.2408	0.1942
RC8	μ	5.1703	5.7789	6.0769
	σ	0.2094	0.1759	0.2090
RC9	μ	5.5567	5.8509	6.1068
	σ	0.1284	0.1666	0.1761
RC10	μ	5.3008	5.5734	5.8858
	σ	0.1887	0.2211	0.1957

For consistency with the edge function of fragility surfaces, it is important to use the same surface equation for creating a 2D fragility curve for either a tsunami or an earthquake. In such cases, the IM value for the non-targeted hazard (e.g., setting the tsunami IM to zero when creating an earthquake 2D fragility curve) should be zero. This method ensures a more consistent and accurate representation in the development of these curves.

The 3D fragility surfaces for the earthquake and tsunami presented herein can be utilized in risk and damage assessments of the coastal communities using frameworks incorporating both events successively. The information related to the development of 2D fragility curves—the one for earthquake or tsunami hazards only, provides fragility functions that can be used in assessing a community exposed to one hazard or if a simplified approach of combining the two hazards is employed.

3.7 Fragility Surfaces for the Woodframe Buildings

The essential parameters for the earthquake-tsunami fragility surfaces, specifically for regular-duration earthquakes, are listed in Table 3-7. These parameters—E, $C1$, $C2$, α, and n—dictate the behavior of the equation for surface function ($h = P(Sa, MF)$) and are instrumental for reproducing the fragility surfaces of buildings categorized under these woodframe archetypes in community-level modeling.

Table 3-7. Equation parameters of the earthquake-tsunami fragility surfaces of light-frame wood structures subjected to regular-duration earthquakes for different damage states.

Structure ID	Parameters	DS1	DS2	DS3
W11	*E*	0.98	0.99	1.02
	C1	1.47	3.415	4.677
	C2	48.84	95.06	118.4
	α	0.54	0.56	0.59
	n	5.804	6.789	6.926
W12	*E*	0.97	1.00	1.03
	C1	1.437	3.118	4.288
	C2	44.01	87.15	112.5
	α	0.4161	0.45	0.49
	n	6.361	7.345	6.805
W13	*E*	0.98	0.99	0.97
	C1	1.148	2.208	4.162
	C2	40.71	65.63	106.9
	α	0.46	0.48	0.52
	n	8.425	5.903	6.876
W21	*E*	0.96	0.98	0.97
	C1	1.524	3.142	4.236
	C2	75.84	108.7	137.3
	α	0.43	0.46	0.49
	n	7.031	8.394	6.394
W22	*E*	0.96	0.97	1.02
	C1	1.352	2.672	4.093
	C2	71.5	104.5	127.4
	α	0.52	0.57	0.59
	n	6.825	7.622	7.046
W23	*E*	1.03	1.02	0.99
	C1	1.442	2.415	3.737
	C2	72.25	95.13	122.2
	α	0.45	0.49	0.54
	n	7.829	8.106	7.639

Tables 3-8 and 3-9 show the parameters for constructing 2D fragility curves for isolated regular-duration earthquakes and tsunami hazards, respectively, based on the lognormal CDF parameters (μ and σ). The lognormal CDF function is fundamental for assessing the vulnerability of lightweight wood structures to earthquake-only and tsunami-only hazards. These curves are imperative for modeling and assessing the vulnerability of lightweight wood structures in regions prone exclusively to long-duration earthquakes, such as Zone D (discussed in the next chapter), which is distant from coastal areas.

Table 3-8. Parameters of equation for the 2D fragility curves of earthquake-only hazard with regular strong motion duration

Structure ID	Parameters	DS1	DS2	DS3
W11	μ	0.3103	1.1279	1.4994
	σ	0.5346	0.4249	0.4745
W12	μ	0.2169	1.0277	1.3873
	σ	0.4910	0.4237	0.4618
W13	μ	0.0953	0.6622	1.3227
	σ	0.3688	0.4328	0.4587
W21	μ	0.1628	0.8295	1.2263
	σ	0.2963	0.3645	0.5119
W22	μ	0.0754	0.7402	1.1281
	σ	0.2738	0.4070	0.4454
W23	μ	0.1133	0.5735	1.0708
	σ	0.3029	0.3641	0.4296

Table 3-9. Parameters of equation for the 2D fragility curves of tsunami-only hazard with regular strong motion duration

Structure ID	Parameters	DS1	DS2	DS3
W11	μ	3.8474	4.5311	4.7592
	σ	0.2024	0.1943	0.1446
W12	μ	3.7158	4.3901	4.6906
	σ	0.1997	0.1680	0.1806
W13	μ	3.6476	4.0899	4.6262
	σ	0.1636	0.1803	0.1922
W21	μ	4.2038	4.6449	4.8990
	σ	0.1496	0.1629	0.1251
W22	μ	4.1328	4.5575	4.8094
	σ	0.1549	0.1600	0.1459
W23	μ	4.1334	4.4602	4.7424
	σ	0.1547	0.1348	0.1415

CHAPTER 4: IMPACT OF LONG-DURATION EARTHQUAKES ON SUCCESSIVE EARTHQUAKE-TSUNAMI FRAGILITIES[3]

4.1 Introduction

In contrast to previous studies that focused on far-field tsunamis, several investigations (Alam et al., 2019; Attary et al., 2021; Carey et al., 2019; Park et al., 2012; Petrone et al., 2020; Rossetto et al., 2019; Xu et al., 2021) have developed near-field tsunami fragility functions that can capture the cascading damage effects between earthquake and tsunami by taking into account loadings from both hazards. These studies typically utilized a two-phase successive analysis procedure consisting of a nonlinear time history analysis (NLTHA) for the earthquake loading, followed by a force-based NSP analysis for the tsunami hazard. However, these studies did not incorporate long-duration earthquakes in the NLTHA part of the successive simulation. Evidence from previous studies (Ando and Nakamura, 2013; Carvajal et al., 2017) revealed that earthquakes with a large moment magnitude (M) are more likely to cause tsunami events, which were found to have a high positive correlation with the significant ground motion (GM) duration (Kempton and Stewart, 2006; Mashayekhi et al., 2020a; Salmon et al., 1992).

Previous research on the effect of earthquake strong motion duration across different structural systems, including RC structures (Belejo et al., 2017; Hancock and Bommer, 2007; Li et al., 2022), masonry (Bommer et al., 2004), dams (B. Xu et al., 2018; Zhang et al., 2013), steel frames (Barbosa et al., 2017; Chandramohan et al., 2016; Wang and Li, 2022), and bridges (Su et al., 2023; Todorov and Billah, 2021), has identified a marked positive correlation between

[3] This chapter is mainly based on the paper: Harati, M., and van de Lindt, J.W. (2024). "Impact of long-duration earthquakes on successive earthquake-tsunami fragilities for reinforced concrete frame archetypes." Journal of Structural Engineering, DOI: 10.1061/JSENDH.STENG-1301

earthquake duration and structural damage or collapse probability (Chandramohan et al., 2016). Furthermore, structures exhibiting deteriorative responses to seismic shaking, notably RC and masonry structures, have been shown to be more adversely affected by strong duration of earthquake motions, which aligns with the highest correlations observed in structural damage (Mashayekhi et al., 2019). The degree of this correlation is significantly influenced by the chosen engineering demand parameter (EDP) in these studies, encompassing both local and global damage indices. Local indices covered cumulative damage metrics such as the Park-Ang damage index (Park and Ang, 1985), patterns of element cracks (Zhang et al., 2013), and hysteresis strength reduction (Bommer et al., 2004). Global indices incorporated measures like horizontal dam displacement (B. Xu et al., 2018), peak inter-story drift ratio (Belejo et al., 2017; Chandramohan et al., 2016), and floor acceleration (Li et al., 2022). While local indices, especially cumulative damage metrics, have shown a more pronounced correlation with the duration of strong earthquake motions (Hancock and Bommer, 2007; Mashayekhi et al., 2019), peak inter-story drift ratio (Belejo et al., 2017; Chandramohan et al., 2016) has been effectively employed in collapse and fragility assessments for higher earthquake intensity levels as an EDP, adeptly quantifying the impact of earthquake strong motion duration. It is important to note that these studies employed spectral matching to isolate the effect of earthquake strong motion duration from other amplitude-based earthquake parameters, aiming to solely quantify the impact of earthquake duration. This process involves adjusting or manipulating the frequency content of the original acceleration time series using spectral matching methods to match their response spectra to a target spectrum across all or a range of considered natural periods of vibration (Harati et al., 2021).

This study employs a methodology proposed by Harati and van de Lindt (2024), presented in Chapter 2, to quantify the impact of long-duration earthquakes on the fragility surfaces of successive earthquake and tsunami hazards. The approach considers uncertainty characterization associated with the structural modeling procedure, input GMs for the NLTHA procedure, and NSP analysis for the equivalent tsunami force and its distribution for the lateral loading profiles. In this chapter of dissertation, we investigate and quantify the impact of long-duration earthquakes on the topological behavior of earthquake-tsunami fragility surfaces by applying both long-duration and regular-duration earthquake motions to a portfolio of RC frames, including both ductile and non-ductile structures. The RC frame archetypes used in this study represent an RC building portfolio that could be used to populate a community-level model for a coastal community in areas exposed to tsunami and long-duration source earthquake risk.

4.2 Strong Motion Duration

There are various definitions in the literature for the strong motion duration of earthquake records. This study has selected significant duration for the definition of motion duration. Significant duration is based on a well-known integration-based relationship called Arias Intensity (AI), which provides a good representation of the earthquake input energy imparted to a structure. For a given earthquake motion, the AI can be calculated as:

$$AI = \frac{\pi}{2g} \int_0^t [a(t)]^2 dt \tag{4-1}$$

where the AI of a motion is calculated using the acceleration time history of an earthquake record, denoted as *a(t)*, and a time window for the earthquake signal [0-*t*], where *t* is less than or equal to the total duration of motion. The AI of an earthquake record is a function of time, which can be calculated based on the *a(t)* for the entire motion duration. Figure 4-1 demonstrates the normalized AI of the 1989 Loma Prieta earthquake that has been calculated and plotted against motion duration.

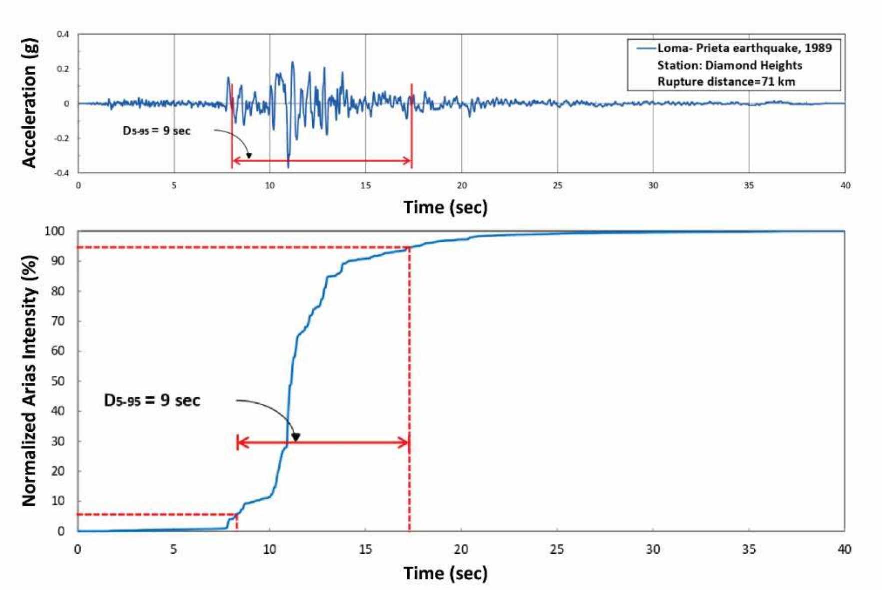

Figure 4-1. Significant strong motion duration, D5-95, and the associated curve of normalized arias intensity of a record from Loma-Prieta earthquake of 1989 (after Harati et al. (2020))

As illustrated in Figure 4-1, significant duration is typically denoted as DX-Y, where X and Y represent the lower and upper bounds defined on the AI function of an earthquake motion, respectively (e.g., 5% and 95% in this figure). In this case, the duration between 5% and 95% of the AI plot of an earthquake record is considered as the significant duration (referred to as D5-95 hereafter). While other forms of significant duration (e.g., D5-75) exist in the literature (Bommer and Martínez-Pereira, 1999), the D5-95 is more commonly used in the GM selection procedure (e.g., Afshari and Stewart (2016)), so it has been selected as the duration-related metric for this study.

4.3 Earthquake and Tsunami Loads

The method proposed by Harati and van de Lindt (2024), presented in Chapter 2 of this dissertation, generates earthquake-tsunami fragility surfaces buildings, crucial for community-level damage and resilience analysis. This method uses a multiprocessing distributed framework to conduct successive analyses. Initially, ground motions (GMs) are scaled, and nonlinear structural models incorporate random variables for parameters such as plastic hinge development. An equivalent tsunami force is calculated, incorporating variables like the drag coefficient (C_d) and tsunami momentum flux (MF), and a Nonlinear Static Procedure (NSP) is used to simulate tsunami impacts, accounting for variable-height load patterns. The combined effects of earthquake and tsunami loads are analyzed sequentially, ensuring that structural responses and potential cascading failures are accurately assessed. For more detailed information, readers are referred to Chapter 2 of this dissertation.

4.4 Structural Frame Archetypes

This study focuses on a suite of RC buildings, including both ductile and non-ductile RC moment-resisting frames (MRFs) with varying heights, configurations, and design details, representing typical structures in a U.S. west coast coastal community vulnerable to seismic hazards. Specifically, six ductile RC frames ranging from one to twenty stories and four non-ductile RC frames ranging from two to twelve stories were analyzed, designed as office buildings with flat-surface floors. The non-ductile frames, assumed to be constructed before 1960 and designed according to the 1967 UBC code, were contrasted with ductile frames designed per modern codes such as ASCE 7-02 and ACI 318, incorporating provisions for improved ductility like strong column-weak beam ratios. While base shear coefficients for these frames are generally similar, some differences exist, particularly for shorter structures. Readers can refer to Chapter 3 of this dissertation for more detailed information on the design and characteristics of these RC frames.

Woodframe buildings, despite typically being destroyed by tsunamis over a meter high, are common in U.S. coastal communities and thus must be represented in community models.

The methodology by Harati and van de Lindt (2024), as detailed in Chapter 2, has been used to develop earthquake-tsunami fragility surfaces for these structures. Laboratory tests, as described by Bahmani et al. (2016), indicate that the in-plane strength and stiffness of wood structural panels (WSPs) are significantly influenced by their nailing patterns. This research draws on Amini (2012) for detailed depictions of two-story woodframe structures and their geometries, including single-story structures with a 2.74-meter story height. The structural system modeling maintains consistency across designs but varies based on nail spacings, leading to different ductility capacities. The study categorizes woodframe structures into six archetypes (W11, W12, W13, W21, W22, W23) using peak inter-story drift ratio (IDR) as the engineering demand parameter (EDP) for damage states, aligning with HAZUS (2020) guidelines. For more information, readers are referred to Chapter 3.

4.5 Structural Modeling Procedure

In this study, RC frames were numerically modeled using OpenSeesPy, a Python library adapted from the TCL programming language, facilitating structural analysis scripts integration for parallel computations and post-processing tasks. To manage computational demands, the 3D structural systems were transformed into 2D finite element (FE) models, implying that earthquakes and tsunamis are applied in the same direction.

Two primary modeling approaches were considered in the past for the structural modeling of buildings under seismic forces; it contrasts two methods: the fiber and concentrated plasticity approaches, for modeling structures under tsunami or earthquake impacts. The fiber method is crucial for depicting inelastic behaviors along a structure, especially beyond column ends, essential for handling distributed tsunami loads. However, a major concern is shear failure in columns, particularly under lower inundation levels where shear demands are high, potentially leading to failure before reaching the first floor. Beam and column shear capacities, dependent on axial loading, vary across earthquake-tsunami phases, necessitating explicit simulation or post-processing for shear failure analysis. Force-or-displacement-based distributed plasticity elements are effective here, allowing for moment-axial-shear interactions and a comprehensive view of structural responses to multi-hazard events. This method, demonstrated in prior studies (e.g., Alam et al., 2019, 2018; Carey et al., 2019; Petrone et al., 2020, 2017; Rossetto et al., 2019), incorporates both flexural and shear failures, using adjusted shear links or shear failure checks in post-processing, providing a robust assessment framework for this multi-hazard scenario.

Conversely, other studies (e.g., Attary et al., 2021, 2017a, 2017b; Haselton, 2006; Haselton et al., 2011; Liel et al., 2011) have utilized the concentrated plastic hinge method. This technique involves lumped plasticity elements and finite joint shear springs, selected for their superior performance in capturing strain softening due to rebar buckling and spalling, essential for simulating the collapse of RC frames (Haselton, 2006; Haselton et al., 2011). Based on empirical data from extensive testing on both ductile and nonductile RC columns, this method ensures accurate modeling. However, it primarily calibrates model parameters to axial compression levels in columns due to gravity loads and does not fully account for axial-flexure-shear interaction during the analysis, a factor that may be important in taller structures (Liel et al., 2011). While the fiber-spring model offers an alternative, it demonstrates less numerical stability in dynamic analysis and struggles with simulating severe strain softening, a critical failure mechanism in collapse scenarios (Haselton, 2006; Haselton et al., 2011). In contrast, the lumped-plasticity model effectively captures this aspect, exhibiting severe strain softening at a roof drift ratio of approximately 3% or higher (Haselton, 2006), thus proving more fit for seismic load simulations.

It is important to recognize that the concentrated plastic hinge method may not adequately simulate tsunami responses due to the development of inelasticity away from the seaward column ends under distributed loading. However, in the simulations, structures first undergo earthquake-induced damage, serving as an initial damage condition for subsequent analysis. This necessitates accurate modeling of the collapse or near-collapse response of the system. To address the limitations in simulating tsunami impacts, a post-processing procedure is employed to incorporate the shear failure of seaward columns, thereby mitigating the trade-off errors, and enhancing the model's overall accuracy in representing this multi-hazard scenario.

As discussed in Chapter 3, the structural elements for beams and columns are created using a linear elastic element connected to two nonlinear rotational springs at the endpoints. The nonlinear rotational springs provide regions with concentrated plasticity for these elements, allowing the formation of plastic hinges at the endpoints throughout the analysis. The seismic mass mounted to linear beam elements is calculated according to the guidelines provided by *ASCE07 (2022)* regulations. Additionally, the shear behavior of beam-column joints was modeled, and shear demands on seaward columns were post-processed to check against shear capacity. This comprehensive modeling approach aims to accurately represent the structural responses to sequential seismic and tsunami hazards, acknowledging the need for further research on the role of infill walls. For more details, readers are referred to Chapter 3 of this dissertation.

The pinching characteristic of WSPs in woodframe systems is simulated using the CUREe 10-parameter hysteretic model, also known as the SAWS model (Folz and Filiatrault, 2001), available in OpenSeesPy (Zhu 2021). Although empirical studies indicate a 30 to 50 percent reduction in strength and stiffness for WSPs with openings (Anil et al. 2018), this analysis conservatively focuses solely on unperforated WSPs. The SAWS hysteresis model parameters are sourced from Bahmani (2015) and Roohi et al. (2019). Both exterior and interior wall layers are modeled using parallel 2-node link elements in OpenSeesPy, with WSPs and other wall elements linked through rigid connections. For more details, refer to Chapter 3.

4.6 Ground Motion Selection

As previously discussed, earthquakes with large moment magnitudes can generate tsunamis when they occur in seas or oceans. As illustrated in Figure 4-2, produced through millions of GM simulations by using the relationship developed by Mashayekhi et al. (2020), earthquakes with longer motion durations can contribute to such multi-hazard events triggered by source earthquakes with larger moment magnitudes. Figure 4-2 shows that the median value of strong motion durations of earthquakes varies exponentially with their moment magnitude in different soil types, indicating that larger significant durations (i.e., D5-75) should be expected from earthquakes with larger moment magnitudes. Therefore, selecting source earthquakes with long motion durations appears to be a more rational approach for numerical simulations of fragility functions in multi-hazard events, such as tsunamis. In this study, two different GM suits were selected: long-duration earthquakes and regular-duration earthquakes.

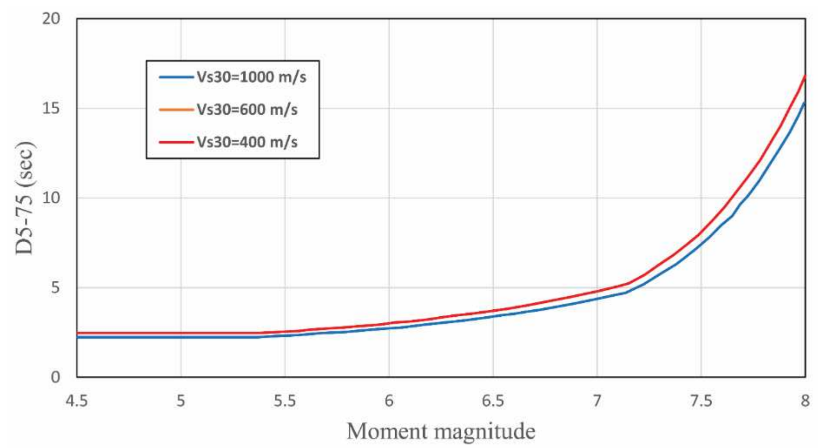

Figure 4-2. Simulation-based relationship between earthquake moment magnitude and significant duration, i.e., D5-75, of non-pulse-like (long-duration) earthquakes (Mashayekhi et al., 2020b)

In this study, a set of synthetic GMs (referred to as the M9 Project records hereafter) generated for a variety of earthquake rupture scenarios on the Cascadia subduction zone (megathrust) approaching magnitude 9.0 have been chosen specifically for long-duration earthquakes (Frankel et al. 2018). For regular-duration earthquakes, the far-field ground motions recommended by FEMA P-695 (*2011*) have also been selected as the reference earthquake motions in this investigation.

Spectral matching techniques (Hancock and Bommer, 2007; Harati et al., 2021) were not implemented for GM records in this study to avoid altering earthquake time series to match a predefined response spectrum. It is important to recognize that response spectra are not the only critical intensity measure of earthquakes. Modifying earthquake records to conform to a single response spectrum can inadvertently affect other vital earthquake characteristics, such as frequency content and the displacement and velocity time series of ground motions (Harati et al., 2021). Other investigations (Chandramohan et al., 2016; Hancock and Bommer, 2007; Harati et al., 2019) aimed to separate strong motion duration from other earthquake characteristics to determine its independent effect on structural damage. As noted by Mashayekhi et al. (2019), amplitude-based earthquake parameters (like PGA or SA) and strong motion duration (e.g., D5-75) are interrelated. Separating the duration component can alter the earthquake's frequency content and modify the amplitude-based characteristics. Isolating the duration allows for assessing its sole impact on structural response metrics. However, this approach alters the final outcome, such as fragility functions. These modified vulnerability functions, having adjusted GMs in terms of frequency content and amplitude-based parameters, may not be reliable for use in risk and community resilience analysis due to potential inaccuracies in representing real earthquake characteristics. Figure 4-3 presents the earthquake response spectra for the selected ground motions.

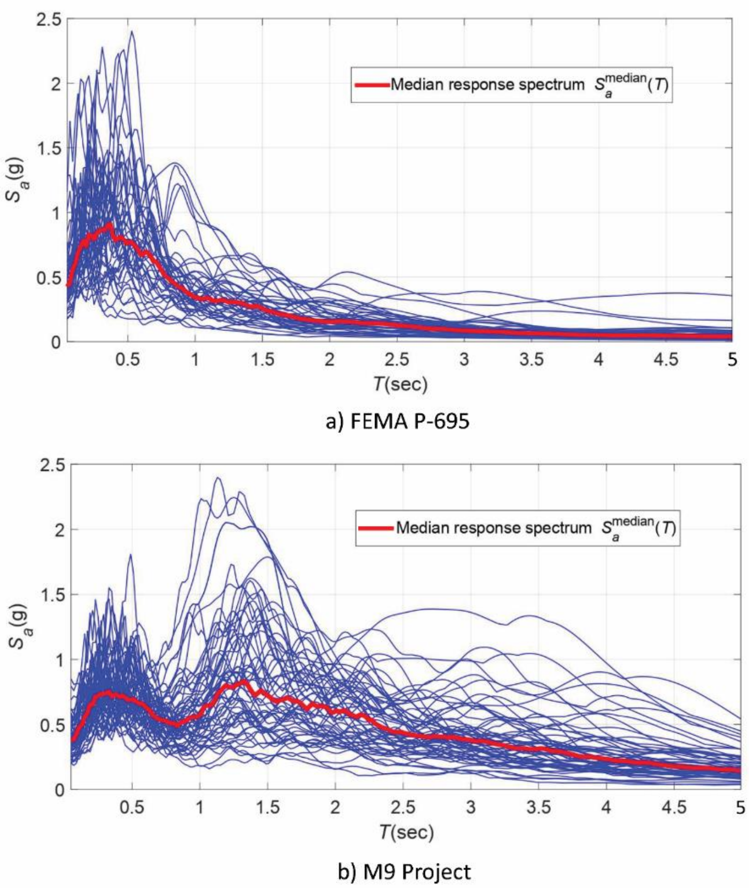

Figure 4-3. Earthquake response spectra for selected ground motions: a) records from FEMA P-695; and b) earthquake motions from the M9 Project

Two distinct categories for earthquake selection were utilized in this study: ground motions with long duration (M9 Project) and those with regular duration (FEMA P-695). In other words, the study investigates the impact of long-duration earthquakes (not the duration parameter of these motions) with their duration-based and amplitude-based characteristics against a set of regular-duration motions (and keeping all of its parameters) being employed as a reference GM set for developing fragility functions in the Western United States. The normalized AI plots for the two selected GM suites are shown in Figure 4-4, revealing two distinct patterns of input earthquake energy between the GMs from FEMA P-695 and the M9 Project.

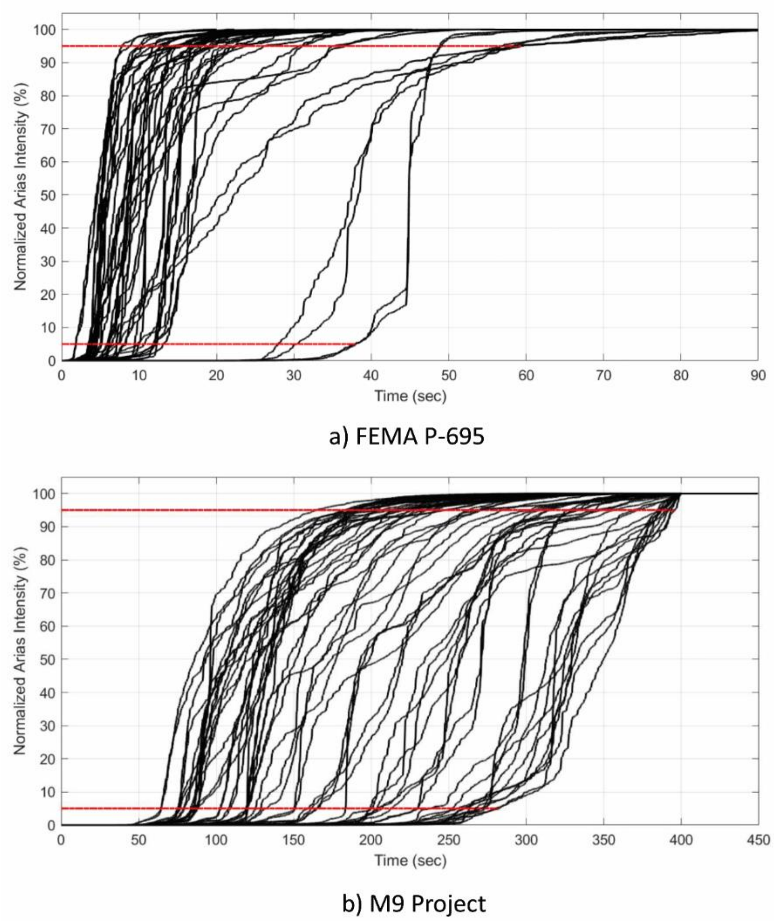

Figure 4-4. Increasing earthquake energy curves defined with the function of normalized arias intensity for both employed sets of earthquake records: a) ground motions from the FEMA P-695; and b) ground motions from the M9 Project

Figure 4-5(b) presents a scatter plot illustrating the relationship between significant durations (D5-95) and the PGA values of the records in both GM sets (long and non-long suits) selected for this study. It is clear from both Figures 4-5(a) and 10(b) that these two record sets are distinctly separated in the vicinity of the D5-95 equal to 60 sec, through inspection of the fitted lognormal distributions for their data in Figure 4-5(b).

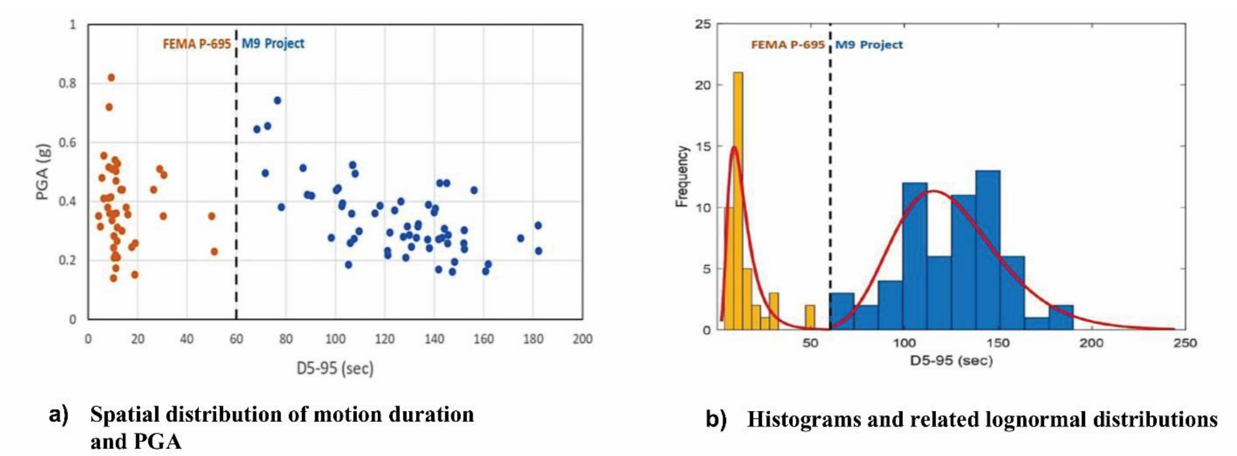

Figure 4-5. Comparison between the characteristics of long-duration earthquakes and the regular- duration earthquakes: a) spatial distribution of D5-95 and PGA; and b) Histograms and the corresponding lognormal distributions fitted to the D5-95 data for the motions

4.7 Methodology

This study uses the methodology proposed by Harati and van de Lindt (2024) discussed in Chapter 2 to develop earthquake-tsunami fragility surfaces for representative RC frame and woodframe archetypes exposed to long-duration earthquakes and subsequent tsunami loading. A two-phase, probabilistic successive analysis approach, grounded in the Monte Carlo Simulation (MCS), is used to determine joint failure probabilities for specific damage states, represented as discrete data points. Initially, MCS selects and scales a GM based on a joint IM, where the spectral acceleration (Sa_i) serves as the earthquake IM. The method involves generating uncertain parameters for both the finite element (FE) nonlinear structural model and the calculation of equivalent tsunami forces. The FE integrates random variables, including those relevant to the development of plastic hinges, dead and live loads, damping ratios, and beam-column joint modeling, as specified in Chapter 2. This uncertainty propagation ensures a realistic representation of structural behavior under varying conditions. Alam et al. (2018) and Attary et al. (2021) identified two primary variables for the equivalent tsunami force calculation, which are probabilistically modeled using uniform distribution as thoroughly discussed in Chapter 2.

Next, a nonlinear structural model is developed using the distribution functions defined earlier in this dissertation, and the equivalent tsunami force is calculated using Eq (4-1) of Chapter 2. This equation considers random variables C_0 and Cd, along with the momentum flux (MF_i) - the tsunami IM in this study. The bay length (B) in that Eq (4-1) is constant, representing the structural system's bay length perpendicular to the 2D building model. The fluid density parameter ρ_s, accounting for water density with sediments in tsunami scenarios, is conservatively set at 1.2 g/cm^3 (Hashimoto et al., 2023). The uncertainty in parameters like inundation depth (h) and velocity (u) in Eq (4-3) is incorporated in the second phase of the simulation. The algorithm calculates flow velocity from MF_i and checks the Froude number (Fr) to ensure velocity is within acceptable limits (Fr $\leq$ 2). If Fr is $\leq$ 2, the algorithm calculates the equivalent tsunami force for creating a lateral tsunami load profile. Successive analyses incrementally increase the tsunami flow depth (h), starting from zero or the water depth above the foundation, up to the building's maximum height (Hmax). The flow depth's initial and increment values are based on the columns' discretization on the seaward side at each story, resulting in various VH profiles with different tsunami flow depths but identical MF_i values.

After the successive analysis, the EDPs from both phases are compared against predefined damage states. Failure is declared for any MCS realization where the structure does not meet the damage state under the hazard scenario. Acceptance criteria for different building damage states are outlined in Chapter 3. To obtain a near-continuous function that governs the earthquake-tsunami fragility surface, a surface fitting procedure is performed on discrete data points of the joint failure probabilities. In this framework, surface fitting is carried out using an equation suggested by Kern et al (2004), Eq (3-1) of Chapter 3.

Meanwhile, the employed methodology can indirectly generate two independent scalar fragility functions at the boundaries of the surface, one fragility curve for earthquake hazard and the other for tsunami hazard. These scalar curves appear on the edges of the horizontal plane composed of the relevant IM axes. A repetitive optimization-based procedure is used to extract the controlling parameters of the lognormal CDF, as detailed in Eq (3-2) of Chapter 3.

4.8 Fragility Surfaces for the RC Building Portfolio Subjected to Long-duration Earthquake

The methodology outlined in this chapter has been utilized to assess the earthquake-tsunami fragility surface of a 4-story ductile RC frame, which is one of the RC buildings included in this study. This is achieved by generating earthquake-tsunami fragility surfaces for complete damage state using two different sets of GMs: the M9 Project for long-duration earthquakes, and the records from the FEMA P-695 for non-long duration earthquakes. Figure 4-6 displays the discrete data points of failure probabilities, along with the corresponding fitted surfaces for both sets of GMs.

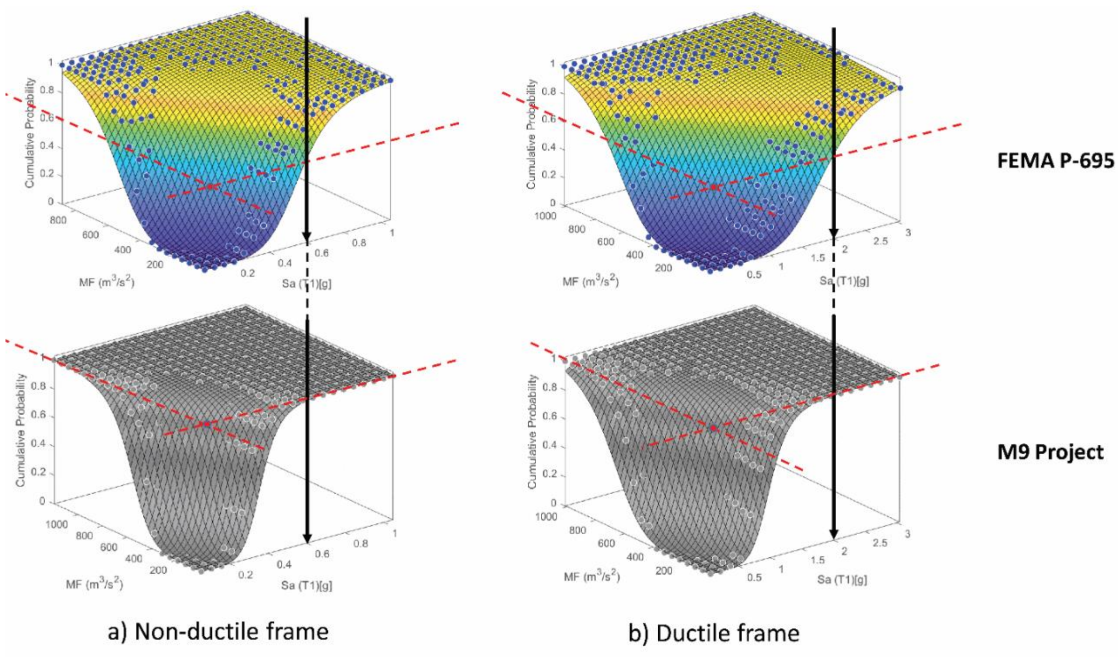

Figure 4-6. The earthquake-tsunami fragility surfaces and raw discrete data obtained for the complete damage state using input GMs from M9 Project and FEMA P-695: a) non-ductile frame of RC3 building b) Ductile frame of RC9 building

As evident from Figure 4-6, the fragility surfaces obtained from the two sets of GMs for 4-story RC buildings (ductile and non-ductile frames) exhibit a noticeable difference, indicating a shift in the fragility surface towards the vertical or z-axis when derived based on the M9 Project ground motions. This shift implies a higher probability of complete damage to the structure for a given joint IM of an earthquake-tsunami event when long-duration earthquakes are selected for the simulation procedure. For example, following the vertical black line with the arrow downward in Figure 4-6(b) for a Sa of 2g in this structure, the intensity of the tsunami event would have to be very large to have an exceedance probability approaching unity when exposed to regular-duration earthquakes. However, when subjected to long-duration earthquakes, the RC frame building reaches this failure probability with any value of the tsunami IM, indicating that it collapses before facing the incoming tsunami waves simply from the long-duration earthquake. This pattern of failure is also observed for the non-ductile frame (RC9) depicted in Figure 4-6(a), which exhibits a higher failure probability for lower earthquake IMs compared to its ductile counterpart, highlighting the critical influence of structural ductility on seismic resilience.

The earthquake-tsunami fragility surfaces for the 4-story RC ductile system at different considered damage states—slight, moderate, and complete—are derived for both sets of GMs selected in this study, as shown in Figures 4-7(a) and 4-7(b). These fragility surfaces are accompanied by governing equations that enable analysts to calculate exceedance failure probabilities for a desired joint IM under each considered damage state enabling researchers to populate a database for community-level modeling with a portfolio of RC buildings. The surfaces in Figure 4-7 include damage state exceedance probability calculations for the joint IM of (1.95, 0) as a demonstration. As shown on the fragility surfaces, the structures exposed to long-duration earthquakes have significantly higher failure probabilities compared to their regular-duration earthquake.

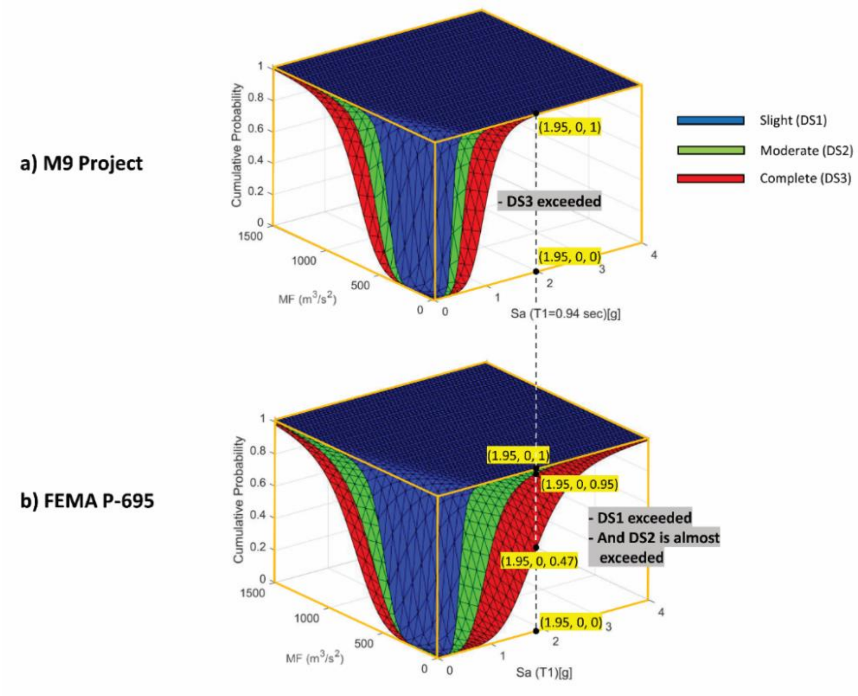

Figure 4-7. Earthquake-tsunami fragility surfaces derived for different defined damage states of RC3 building using long and non-long earthquakes: a) records from the M9 Project as long-duration earthquakes; and b) ground motions from the FEMA P-695 for regular-duration

The earthquake-tsunami fragility surfaces for both sets of GMs for the complete damage state (DS3) are presented side-by-side in Figure 4-8. The scalar fragility functions for tsunami-only and earthquake-only hazards are extracted from the edges of these fragility surfaces and displayed in Figures 4-8(b) and 4-8(c), respectively.

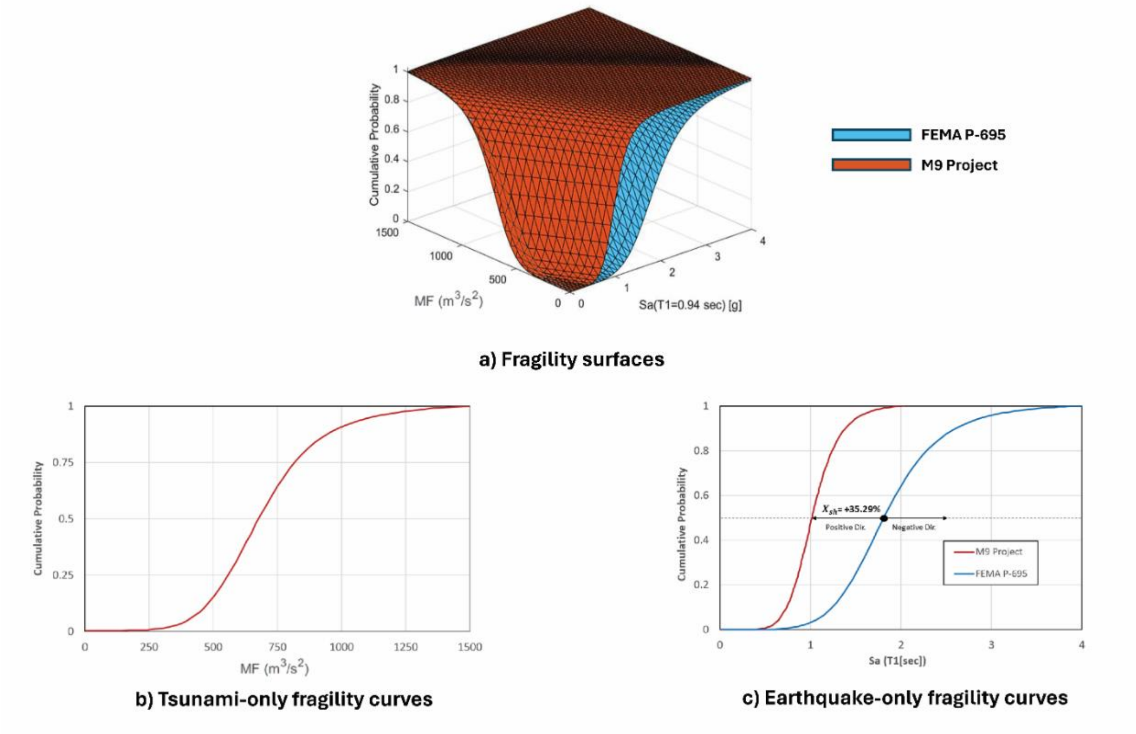

Figure 4-8. Comparison of fragility functions at the complete damage state of RC3 building derived with long-duration earthquakes and those developed based on regular-duration earthquakes: a) fragility surfaces for earthquake and tsunami; b) earthquake-only fragility curves

As shown in Figure 4-8(b), the scalar fragility curves for the tsunami-only hazard for both GM sets are closely aligned and share overlapping data points, indicating that the structures have a similar vulnerability to different levels of tsunami IM when prior seismic damage from the source earthquake is not taken into account. Since no earthquake is run for the tsunami-only analysis one can see that the two surfaces converge in the three-dimensional surface plot for both earthquake sets to form the tsunami-only fragility. But as is seen in Figure 4-8(c), the scalar earthquake fragility curve of the long-duration set is shifted to the left side, indicating that more structural damage can be expected from long-duration earthquakes.

The degree of the fragility curve shift (X_{sh}) has been quantified as a percentage, using the 50% cumulative probability of exceedance reference point for $Sa(T_1)$ for regular-duration motions. A positive shift is defined if the fragility curve generated using the long-duration motions is shifted to the left side compared to the reference point, demonstrating more initial seismic damage from the earthquake phase in this successive simulation. For example, in the four-story ductile RC frame illustrated in Figure 4-8, the positive shift is approximately 35%. This shift could be attributed to several factors, such as longer shaking duration leading to more cumulative damage to the structure or different spectral contents and their interaction with higher vibration modes in the structure of interest. This initial earthquake damage would affect the structural response for the tsunami in the second phase of the simulation, as demonstrated by the earthquake-tsunami fragility surface derived from long-duration motions.

Figure 4-9 displays the shift in fragility (Xsh) between long-duration and regular-duration earthquakes for both ductile and non-ductile systems. As previously noted, an Xsh of zero suggests a negligible shift in response due to long-duration earthquakes, implying almost identical responses for both sets of GM records. The impact on low- to mid-rise RC frames, irrespective of their design ductility levels, is more significant from long-duration earthquakes, showing a shift by more than 40%, compared to their response under regular-duration earthquakes. In contrast, high-rise RC structural systems show minimal shifting when subjected to long-duration motions, indicating that their fragility behavior is relatively similar when exposed to earthquake sets from both the FEMA P-695 and the M9 Project. This pattern suggests that in taller structures, long-duration earthquakes do not notably alter the structural response compared to regular-duration earthquakes, likely due to their specific dynamic characteristics or the seismic input's nature at higher modes. Moreover, the Xsh values are directly influenced by the initial damage each structure endures, as depicted in Figure 4-9. This figure clearly demonstrates that non-ductile frames are inherently more susceptible to earthquake damage, regardless of the type. Consequently, the variance observed in fragility shifts for ductile versus non-ductile frames should be interpreted based on the initial and reference damage states (based on regular-duration earthquakes) and inherent vulnerabilities of the considered structural systems, rather than as an indication of the direct structural responses of the buildings being examined under different seismic events.

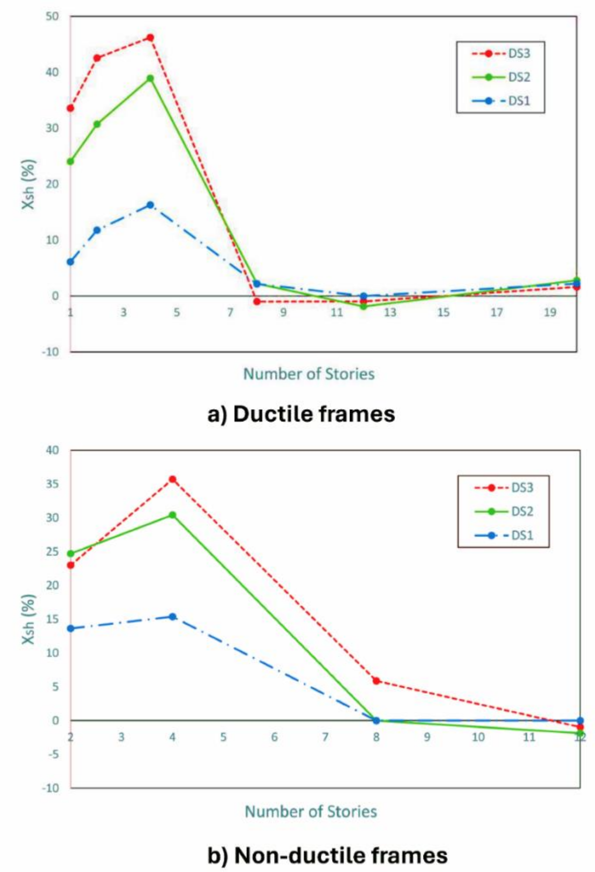

Figure 4-9. The degree of shift between long-duration earthquakes and regular-duration earthquakes in all (a) ductile and (b) non-ductile systems

Figure 4-10 shows scalar tsunami fragility functions for collapse or complete DS, conditioned on earthquake IMs for two distinct GM categories: FEMA P-695 and the M9 Project. These fragility functions are illustrated across various earthquake intensity levels, with specific focus on Sa values of 0.5g, 1.0g, and 1.5g. Each section of the figure demonstrates the changes in fragility functions corresponding to different Sa values, highlighting how these variations are key in determining the likelihood of varying levels of structural damage under tsunami loading post-earthquake. The comparative analysis of the two GM categories at each intensity level sheds light on the impact of different GM characteristics on structural vulnerability during tsunamis following earthquakes. Notably, the fragility curves for tsunamis, conditioned on each Sa value, exhibit a vertical compression and initiate from a higher cumulative probability in scenarios where a near-field tsunami follows a long-duration earthquake.

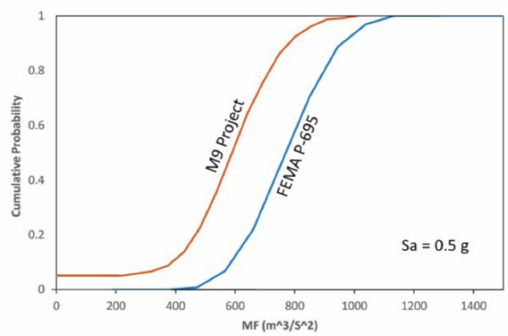

a) Sa = 0.5 g

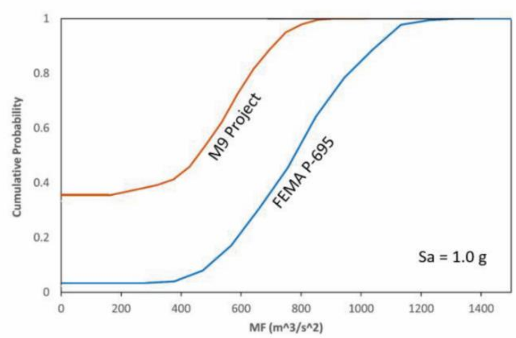

b) Sa = 1.0 g

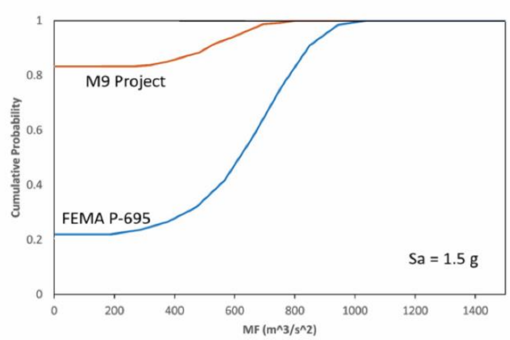

c) Sa = 1.5 g

Figure 4-10. Scalar tsunami fragility functions conditioned on earthquake IMs for both GM categories (FEMA P-695 and M9 Project) for building RC3 at different earthquake intensity levels: (a) Sa = 0.5g, (b) Sa = 1.0g and c) Sa = 1.5g

This vertical shift is evident at the beginning of each tsunami fragility curve under long-duration GM sets. Therefore, for this specific building archetype (RC3), the probability of collapse following a near-field tsunami event is generally higher when the structure experiences a seismic event characterized by a long-duration earthquake. However, it is essential to acknowledge that these observed vertical shifts in the fragility curves occur when there is a positive horizontal shift (Xsh) in earthquake fragility curves. In cases where Xsh is zero or minimal, such vertical shifts in the scalar tsunami fragility (conditioned on Sa) would not be observed. Furthermore, the rate of change in this vertical shifting tends to accelerate with larger Xsh values, indicating a direct correlation between the magnitude of horizontal shift and the rate of vertical shift in the fragility curves.

The key parameters of the long-duration earthquake-tsunami fragility surfaces for ductile RC structures, have been extracted and presented in Table 4-1. These parameters (*E, C1*, *C2*, α, and n) govern the surface equation presented in Chapter 2 and can be utilized to replicate the fragility surfaces for buildings assigned these archetypes for community-level modeling. Additionally, Table 4-2 contains the controlling parameters of the governing equations of near-continuous surfaces of non-ductile RC structures.

Table 4-1. Equation parameters of the earthquake-tsunami fragility surfaces for the ductile RC structures subjected to long-duration earthquakes for different damage states

Structure ID	Parameters	DS1	DS2	DS3
RC1	*E*	0.9940	0.9940	0.9940
	C1	1.1862	1.4549	1.6663
	C2	222.1572	293.0203	418.8514
	α	0.5183	0.6065	0.7210
	n	8.6144	7.6151	8.7140
RC2	*E*	1.0695	1.0695	1.0695
	C1	0.5255	1.0043	1.4251
	C2	475.1265	540.6804	614.5086
	α	0.5187	0.5885	0.6545
	n	8.1644	8.2881	7.9010
RC3	*E*	0.9990	0.9990	0.9990
	C1	0.3516	0.5274	0.8871
	C2	460.4590	546.6160	625.0746
	α	0.5037	0.5957	0.6849
	n	11.1587	10.7195	9.8662
RC4	*E*	0.9977	0.9977	0.9977
	C1	0.2439	0.3933	0.8008
	C2	463.0644	549.4345	648.6586
	α	0.4556	0.5416	0.6254
	n	8.4877	7.7198	6.2002
RC5	*E*	0.9980	0.9980	0.9980
	C1	0.2039	0.3153	0.5767
	C2	580.5488	664.6450	761.6400
	α	0.5261	0.5879	0.6519
	n	9.5713	8.3730	7.8906
RC6	*E*	0.9967	0.9967	0.9967
	C1	0.1783	0.2811	0.4307
	C2	808.9316	1026.1764	1251.7859
	α	0.4595	0.4977	0.2927
	n	5.8915	4.6345	2.7773

Table 4-2. Equation parameters of the earthquake-tsunami fragility surfaces for the non-ductile RC structures subjected to long-duration earthquakes at different damage states

Structure ID	Parameters	DS1	DS2	DS3
RC7	*E*	0.9995	0.9995	0.9995
	C1	0.1314	0.2124	0.3530
	C2	428.0241	462.7721	618.5010
	α	0.4436	0.5040	0.6295
	n	12.4349	8.8843	7.0898
RC8	*E*	0.9996	0.9996	0.9996
	C1	0.1489	0.2367	0.2896
	C2	371.4985	407.5319	519.4316
	α	0.3963	0.4588	0.5544
	n	11.8137	8.2911	8.6633
RC9	*E*	0.9985	0.9985	0.9985
	C1	0.2143	0.3001	0.3292
	C2	370.6026	442.1421	562.5499
	α	0.4333	0.5169	0.6046
	n	10.1249	8.3911	9.9739
RC10	*E*	0.9987	0.9987	0.9987
	C1	0.4168	0.6155	0.7284
	C2	264.0658	306.6170	417.7384
	α	0.3899	0.4784	0.5775
	n	8.7944	7.8252	8.0893

Table 4-3. Parameters of equation for the scalar fragility curves for the earthquake-only hazard with long-duration earthquakes

Structure ID	Parameters	DS1	DS2	DS3
RC1	μ	-0.0054	0.1696	0.3793
	σ	0.2728	0.3925	0.3060
RC2	μ	-0.5457	-0.1881	0.1957
	σ	0.1767	0.2727	0.3503
RC3	μ	-1.1319	-0.7962	-0.2561
	σ	0.1984	0.1845	0.2655
RC4	μ	-1.5710	-1.1042	-0.4232
	σ	0.2204	0.3613	0.5010
RC5	μ	-1.7879	-1.2922	-0.7890
	σ	0.2250	0.3607	0.5803
RC6	μ	-1.8847	-1.5756	-1.1202
	σ	0.4446	0.6648	0.7286
RC7	μ	-2.1600	-1.6953	-1.2430
	σ	0.1211	0.2979	0.4408
RC8	μ	-1.9697	-1.6098	-1.3877
	σ	0.1641	0.3058	0.2238
RC9	μ	-1.6105	-1.3708	-1.2688
	σ	0.1722	0.2383	0.1993
RC10	μ	-1.0424	-0.6596	-0.5012
	σ	0.1565	0.2053	0.2761

Table 4-4. Equation parameters for the scalar fragility curves for the tsunami-only hazard

Structure ID	Parameters	DS1	DS2	DS3
RC1	μ	5.2687	5.5930	5.9295
	σ	0.1907	0.1764	0.1605
RC2	μ	5.9923	6.1523	6.2917
	σ	0.1896	0.1887	0.1471
RC3	μ	6.0807	6.2821	6.5174
	σ	0.1814	0.1769	0.1743
RC4	μ	5.8794	6.1350	6.4179
	σ	0.1706	0.2122	0.2022
RC5	μ	6.1467	6.3874	6.6136
	σ	0.1712	0.1926	0.1757
RC6	μ	6.5222	6.8849	7.1218
	σ	0.2738	0.2162	0.1782
RC7	μ	5.2153	5.9160	6.2901
	σ	0.4822	0.2408	0.1942
RC8	μ	5.1703	5.7789	6.0769
	σ	0.2094	0.1759	0.2090
RC9	μ	5.5567	5.8509	6.1068
	σ	0.1284	0.1666	0.1761
RC10	μ	5.3008	5.5734	5.8858
	σ	0.1887	0.2211	0.1957

The parameters governing the scalar fragility curves for earthquake-only and tsunami-only hazards have been extracted and presented in Tables 4-3 and 4-4, respectively. These tables contain the parameters controlling the lognormal CDF function, which plays a critical role in determining the vulnerability of RC structures to earthquake-only and tsunami-only hazards. It is worth noting that the scalar earthquake fragilities for the RC frames when subjected to long-duration earthquakes can be constructed using the parameters presented in Table 4-3. The scalar earthquake fragility curves developed in this study can be utilized to model and assess the vulnerability of RC structures in a region anticipated to be exposed to long-duration earthquakes only, i.e., not near the coast, which can aid in community-level planning and decision-making for seismic risk reduction.

4.9 Fragility Surfaces for the Woodframe Buildings Subjected to Long-duration Earthquakes

The essential parameters for the earthquake-tsunami fragility surfaces, specifically for long-duration earthquakes, are listed in Table 4-5. These parameters—E, $C1$, $C2$, α, and n—dictate the behavior of the equation for surface function $(h = P(Sa, MF))$ and are instrumental for reproducing the fragility surfaces of buildings categorized under these woodframe archetypes in community-level modeling.

Table 4-5. Equation parameters of the earthquake-tsunami fragility surfaces of light-frame wood structures subjected to long-duration earthquakes for different damage states.

Structure ID	Parameters	DS1	DS2	DS3
W11	E	0.99	0.97	1.02
	$C1$	1.403	2.528	2.854
	$C2$	53.57	101.1	135.7
	α	0.46	0.52	0.57
	n	7.417	7.373	5.866
W12	E	1.03	0.97	0.98
	$C1$	1.318	2.36	2.899
	$C2$	43.19	91.78	123.6
	α	0.43	0.47	0.51
	n	7.343	7.47	6.691
W13	E	1.03	0.98	0.98
	$C1$	1.187	1.806	2.746
	$C2$	40.51	64.52	114.2
	α	0.53	0.54	0.56
	n	7.637	7.393	6.511
W21	E	0.99	0.98	0.96
	$C1$	1.28	1.875	2.069
	$C2$	83.95	123.6	152.7
	α	0.48	0.54	0.59
	n	6.867	6.287	5.484
W22	E	0.97	1.03	0.98
	$C1$	1.113	1.728	2.004
	$C2$	70.04	110.1	141.9
	α	0.52	0.55	0.59
	n	5.566	6.227	5.236
W23	E	0.96	0.99	1.02
	$C1$	1.222	1.729	2.004
	$C2$	74.24	98.78	136
	α	0.41	0.45	0.56
	n	6.237	6.954	6.337

Tables 4-6 and 4-7 show the parameters for constructing 2D fragility curves for isolated long-duration earthquakes and tsunami hazards, respectively, based on the lognormal CDF parameters (μ and σ). The lognormal CDF function is fundamental for assessing the vulnerability of lightweight wood structures to earthquake-only and tsunami-only hazards. These curves are imperative for modeling and assessing the vulnerability of lightweight wood structures in regions prone exclusively to long-duration earthquakes, such as Zone D (discussed in Chapter 5), which is distant from coastal areas.

Table 4-6. Parameters of equation for the 2D fragility curves of earthquake-only hazard with long strong motion duration

Structure ID	Parameters	DS1	DS2	DS3
W11	μ	0.2824	0.7417	0.8516
	σ	0.3104	0.2906	0.3457
W12	μ	0.2021	0.7200	0.8267
	σ	0.3166	0.3592	0.3789
W13	μ	0.0191	0.5289	0.8273
	σ	0.3542	0.2953	0.3632
W21	μ	0.0225	0.3381	0.4486
	σ	0.3206	0.3761	0.3638
W22	μ	-0.0840	0.2054	0.3829
	σ	0.3342	0.3358	0.4044
W23	μ	-0.0338	0.2813	0.4062
	σ	0.3172	0.3291	0.3926

Table 4-7. Parameters of equation for the 2D fragility curves of tsunami-only hazard with regular strong motion duration

Structure ID	Parameters	DS1	DS2	DS3
W11	μ	3.8474	4.5311	4.7592
	σ	0.2024	0.1943	0.1446
W12	μ	3.7158	4.3901	4.6906
	σ	0.1997	0.1680	0.1806
W13	μ	3.6476	4.0899	4.6262
	σ	0.1636	0.1803	0.1922
W21	μ	4.2038	4.6449	4.8990
	σ	0.1496	0.1629	0.1251
W22	μ	4.1328	4.5575	4.8094
	σ	0.1549	0.1600	0.1459
W23	μ	4.1334	4.4602	4.7424
	σ	0.1547	0.1348	0.1415

CHAPTER 5: COMMUNITY RESILIENCE ANALYSIS USING EARTHQUAKE-TSUNAMI FRAGILITIES4

5.1 Introduction

Approaches to community resilience analysis and performance-based tsunami design methods typically use separate and independent fragility curves for the earthquake and tsunami damage analysis of each facility within a community-level model (Burns et al., 2021; Capozzo et al., 2019; Goda, 2020; Goda et al., 2021; Ishibashi et al., 2021). This approach, while practical, can lead to a segmented understanding of damage prediction on a structural level. By treating these hazards in isolation, that approach neglects the direct cascading effects of both earthquake and subsequent tsunami damage on coastal communities and may result in an underestimation of the cumulative impact of multi-hazard events, as the interdependencies and compounded vulnerabilities are not fully captured. This is because the earthquake can critically soften structures, making them more susceptible to subsequent near-field tsunami damage (Harati and van de Lindt, 2024a). There is a growing realization within the disaster risk reduction and engineering communities that integrated modeling, which considers the interplay and sequential nature of these hazards, is essential for a more accurate assessment of risk and resilience in coastal areas (Jiang et al., 2022; Jojok Widodo et al., 2021).

Some studies have begun to integrate both earthquake and tsunami impacts in tsunami fragility function generation, employing two-phase successive analyses for the sequential impacts of the source earthquake and subsequent near-field tsunami (Alam et al., 2019; Attary et al., 2021; Carey et al., 2019; Park et al., 2012; Petrone et al., 2020; Rossetto et al., 2019; Xu et al., 2021).

[4] This chapter is based on the paper: Harati, M., and van de Lindt, J.W. (2024). "Community-Level resilience analysis using earthquake-tsunami fragility surfaces." Resilient Cities and Structures, DOI: 10.1016/j.rcns.2024.07.006

For example, Attary et al. (2021) proposed a probabilistic methodology combining Nonlinear Time History Analysis (NTHA) for earthquake loading with Nonlinear Static Pushover (NSP) for tsunami forces to generate earthquake-tsunami fragility surfaces. This methodology, offering a more realistic performance estimation than previous models, has been further enhanced by Harati and van de Lindt (2024a) through a multi-distributed parallel processing algorithm. This approach enables the generation of near-continuous fragility surfaces for both hazard intensity measures in a time-efficient manner. Building on this advancement, Harati and van de Lindt (2024b, 2024c) developed earthquake-tsunami fragility surfaces for a portfolio of reinforced concrete (RC) structures under regular- and long-duration earthquakes, ranging from one- to twenty-story buildings and including ductile and non-ductile RC buildings.

To date, no studies have applied earthquake-tsunami fragility surfaces at the community level, which is the focus of this chapter. This study presents a multi-hazard community resilience approach aimed at addressing the sequential damage resulting from earthquake and tsunami hazards at a community level utilizing a suite of archetypes and introduces a unique methodology for evaluating the combined impacts of these hazards on coastal communities. This methodology enables direct economic loss evaluation, and damage distribution analysis within a custom-designed testbed community, termed the Pseudo Seaside testbed. Advanced machine learning techniques have been utilized to create this testbed community, serving as an optimal instrument for examining the impact of the combined earthquake-tsunami successive loading on a coastal community, the city of Seaside, Oregon in the US Pacific Northwest which has been the subject of past investigations (see e.g. Cox et al., 2022).

This multi-hazard community resilience analysis focuses on the comprehensive development and explanation of fragility surfaces and curves for earthquake and tsunami events, specifically targeting light-frame woodframe buildings common in U.S. coastal communities, as well as reference to the RC structures based on existing literature (Harati and van de Lindt (2024b, 2024c))—which were developed as a portfolio of fragility functions in Chapter 3. These fragility suites are necessary for a community-level analysis. Integrating these advanced fragility models with others that assess water inundation-induced damage (contents of buildings) to building contents provides a holistic assessment of both structural and non-structural damage to buildings in coastal communities. This methodology is expected to effectively delineate the sequential impacts of earthquakes, tsunamis, and subsequent inundation from the tsunami, thereby offering a complete view of potential effects in such multi-hazard scenarios. This integrated approach aims to significantly improve the understanding of community performance, resilience, and post-disaster recovery in coastal environments.

5.2 FEMA Statistical Relationships

In assessing the vulnerability of structures to natural hazards, it is critical to account for the combined effects of multiple events. The FEMA statistical relationships (*FEMA, 2022*) provide a methodological framework to quantify the joint probability of damage states arising from the interplay of earthquake and tsunami forces. This approach is particularly pertinent in regions such as the Pacific Northwest, where the proximity to the Cascadia Subduction Zone presents a significant risk of concurrent seismic and tsunami events. According to FEMA's statistical relationships, the probability of a building reaching a specific damage state due to both earthquake (EQ) and tsunami (TS) is calculated by considering the individual probabilities of that damage state due to each hazard, as well as the overlap between them. For complete damage (DS3), this involves summing the individual probabilities and then subtracting their product to correct for the overlap. An additional term accounts for buildings that might experience extensive damage (DS2) from an earthquake and then progress to complete damage due to a subsequent tsunami. Mathematically, this is represented as:

$$P(DS3|EQ \cap TS) = P(DS3|EQ) + P(DS3|TS) - P(DS3|EQ)\,P(DS3|TS) + [P(DS2|EQ) - P(DS3|EQ)]\,[P(DS2|TS) - P(DS3|TS)] \quad (5\text{-}1)$$

Extending this approach to other damage states, the FEMA rule includes similar calculations for extensive (DS2), moderate (DS1), and slight (DS0) damage probabilities:

$$P(DS2|EQ \cap TS) = P(DS2|EQ) + P(DS2|TS) - P(DS2|EQ)\,P(DS2|TS) + [P(DS1|EQ) - P(DS2|EQ)]\,[P(DS1|TS) - P(DS2|TS)] \quad (5\text{-}2)$$

$$P(DS1|EQ \cap TS) = P(DS1|EQ) + P(DS1|TS) - P(DS1|EQ)\,P(DS1|TS) \quad (5\text{-}3)$$

$$P(DS0|EQ \cap TS) = P(DS0|EQ) + P(DS0|TS) - P(DS0|EQ)\,P(DS0|TS) \quad (5\text{-}4)$$

Each equation comprises several components that contribute to the overall damage assessment:

- $P(X|Y)$: Represents the probability of a damage state X given a single hazard Y, where X can be complete, extensive, moderate, or slight damage, and Y is either an earthquake (EQ) or a tsunami (TS) event.
- $P(X|EQ \cap TS)$: Represents the joint probability of damage state X due to both earthquake and tsunami.
- $P(X|EQ) + P(X|TS)$: The sum of the probabilities of a damage state X due to each hazard independently.
- $- P(X|EQ)\,P(X|TS)$: The subtracted product of the individual probabilities, which corrects for the overlap when both hazards occur independently.

As can be understood from these statistical equations, direct interaction and cascading effects between the source earthquake and tsunami damage have not been considered through this superposition-based relationship. Accordingly, in the next section of this chapter, a methodology to incorporate the direct cascading damage of the earthquake and tsunami hazards is presented, which are based on physics-based multi-hazard fragility functions/surfaces for the joint failure probability and damage state exceedance of earthquake and subsequent tsunami events.

5.3 Technical Description of Approach

Resilience and Performance-Based Design (PBD) frameworks for single- and multi-hazard events have been developed, as documented in the literature (Amini et al., 2023; Attary et al., 2017; Attary et al., 2021; Barbato et al., 2013; González-Dueñas and Padgett, 2021; Spence and Arunachalam, 2022). These frameworks, initially inspired by the successful application of PBD in earthquake engineering and related seismic standards (Günay and Mosalam, 2013; Hamburger et al., 2009), enable community-scale studies. At the core of these PBD frameworks lies the concept of uncertainty propagation, which emerges from numerous fundamental components. This propagation is typically addressed by disaggregating the failure risk probability into several elements using the total probability theorem (Barbato et al., 2013). While minor variations exist in these fundamental components across different PBD frameworks for various natural hazards, the risk of system or community block failure generally breaks down into key categories: hazard analysis, characterization of structural systems, structural analysis, damage assessment, and economic loss estimation combined with risk analysis.

As shown in Figure 5-1, this study uses mean damage factors that correlate with varying levels of structural damage severity. These factors are derived from documentation of the MAEviz software (McLaren et al., 2008), which are essential for accurately assessing the extent of damage herein. Additionally, the study examines a spectrum of hazard event frequencies, a critical step in understanding the recurrence and severity of these events. Central to the analysis is the valuation of each structure, with a focus on determining the costs associated with replacement or repair, thereby enabling a comprehensive evaluation of potential direct economic losses.

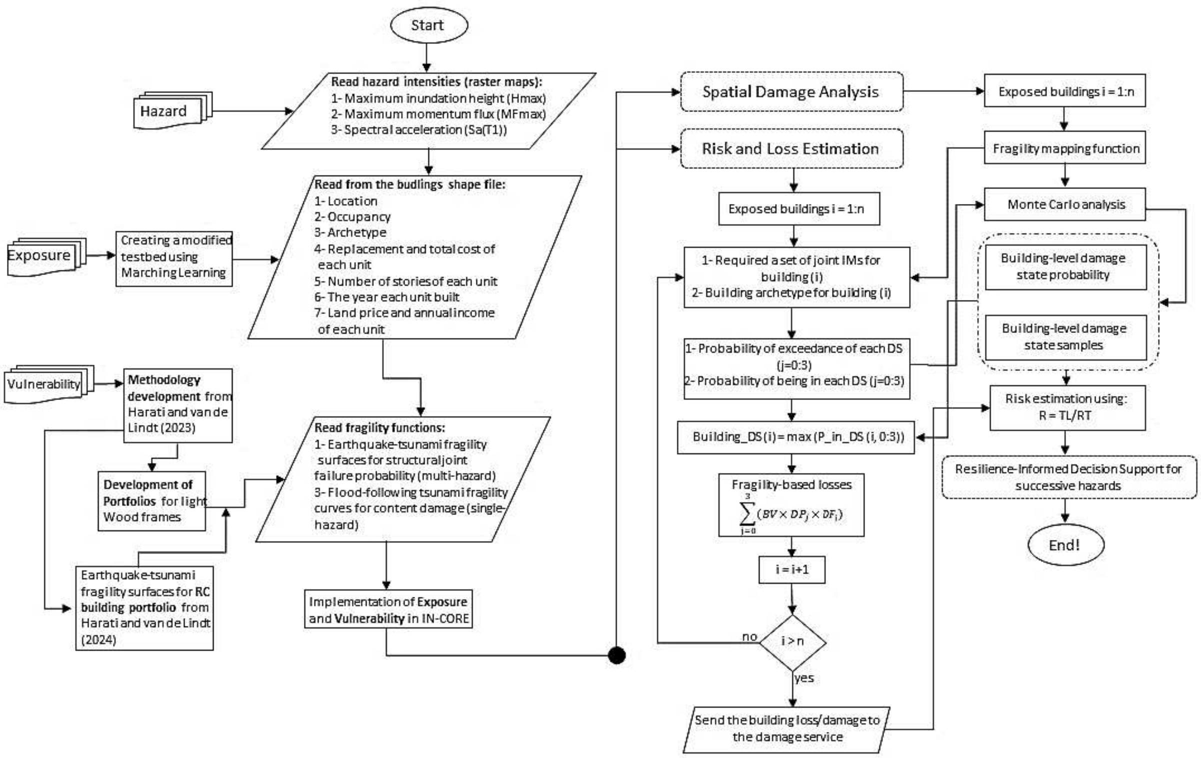

Figure 5-1. The proposed methodology for community resilience analysis under combined effects of earthquake and tsunami hazards.

The study adopts a well-known approach to estimate total losses (*HAZUS*, 2020), which effectively combines the structural valuation with the probability of damage occurrence and respective damage factors as:

$$Total\ Loss = \sum_{i=0}^{3} (BV \times DP_i \times DF_i) \quad (5\text{-}5)$$

where *BV* indicates the building value, which corresponds to the replacement or repair cost of each structure. And *DP* refers to the damage probability for each specific damage state obtained from a Monte Carlo simulation over the percent of being in each damage state. *DF*, the damage factor, is assigned based on a set of established mean values from MAEviz. This study considers four damage states: insignificant damage (DS0), slight damage (DS1), moderate damage (DS2), and extensive damage (DS3). The application of this formula spans various hazard types and scenarios, encompassing both individual and combined impacts of earthquakes and tsunamis. The study calculates total economic losses for each hazard scenario by aggregating the outcomes. The aggregated analyses are instrumental in quantifying the economic impact of each hazard type, providing essential insights for risk management and mitigation planning in areas prone to such natural disasters.

The approach described here has recently been implemented in the IN-CORE system as part of this research, and its Python package, pyIncore, with a focus on assessing damage and economic losses, particularly for structures affected by single and multi-hazards scenarios and their cumulative effects. IN-CORE stands for the Interdependent Networked Community Resilience Modeling Environment (van de Lindt et al., 2023), an open-source computational platform designed for community resilience analysis. It facilitates the modeling of natural hazard impacts on communities and assesses their resilience. This environment seeks to integrate risk analysis with the decision-making process, enabling a quantitative comparison of different resilience strategies (van de Lindt et al., 2023).

5.4 Development of Testbed Community

The "Pseudo Seaside" testbed was created to illustrate the earthquake and tsunami resilience response of a small coastal community located in a high seismic region. Informed by prior studies indicating a heightened tsunami risk for Seaside relative to other coastal Oregon towns in the Pacific Northwest of the U.S. (Park et al., 2017a), this testbed has a population of 7115 residents, which swells considerably due to seasonal tourism. The original testbed leverages machine learning (ML) to model Seaside's potential urban development, using initial building data from Clatsop County, augmented with Google Street View confirmations and targeted field inspections (Park et al., 2017b). Illustrated in Figure 5-2, the "Pseudo Seaside" testbed employs machine learning to project an altered building inventory (shown in gray) and its fluctuating population, influenced by seasonal tourism.

Figure 5-2. The new Pseudo Seaside testbed used as a target coastal community in this study

This comprehensive machine learning analysis incorporates evaluations of construction materials (including concrete and wood), design standards, building ages, and the number of floors to predict scenarios such as fluctuations in property values. It maintains the same structural systems found in the Seaside area, encompassing woodframe construction as well as ductile and non-ductile RC buildings. The machine learning algorithm was trained with the most recent data available from the town of Seaside (Park et al., 2017a). Figure 5-3 presents a feature importance analysis using this dataset, highlighting key factors such as building footprint geometry and land value that significantly influence the model’s forecasts for target variable, the building replacement cost.

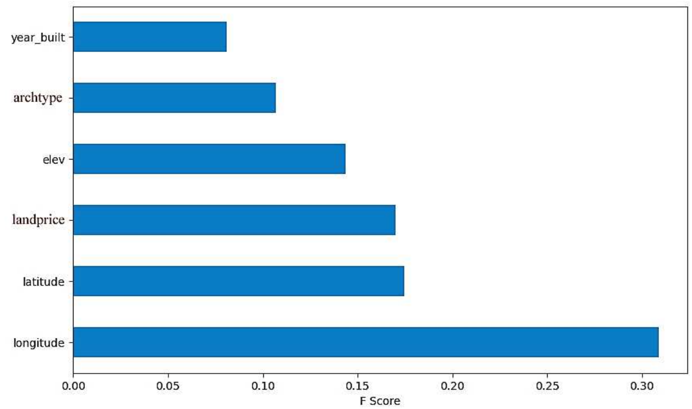

Figure 5-3. The feature importance analysis from the existing data of the Seaside town extracted for the building replacement cost as the target variable

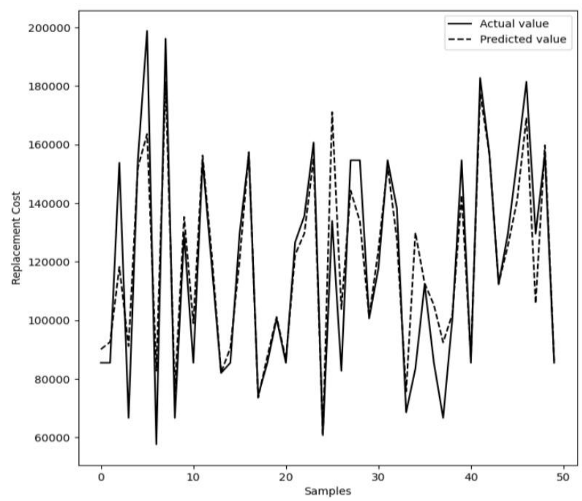

Figure 5-4. Temporal variation of the predicted values of building replacement cost versus the actual equivalent values.

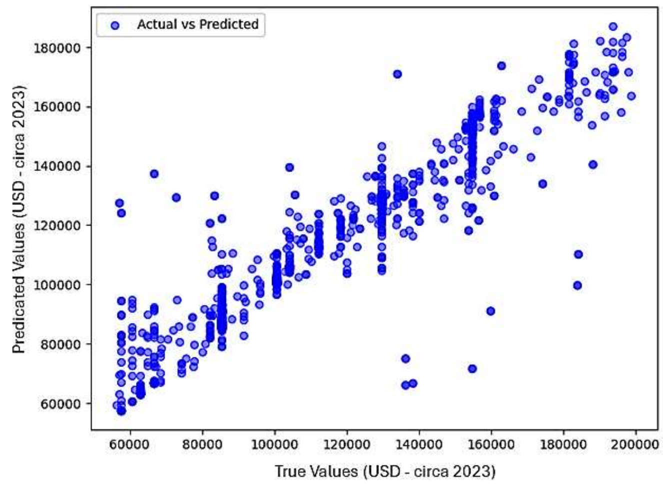

Figure 5-5. Correlation pattern between predicted building replacement costs and their actual equivalent values.

After training and validating a Random Forest regressor ML model, the algorithm is employed to forecast key variables, notably the replacement costs for individual building units. As shown in Figure 5-4 and 5-5, the developed model demonstrated a good temporal variation and correlation pattern (with an R^2 of 83%) compared to the actual observed data. The model predicts changes in the number of stories for buildings in downtown Seaside (Park et al., 2017a), broadening its scope to include other urban sectors. The objective is to forecast Seaside's economic and infrastructural developments, with a focus on urban expansion.

The resulting "Pseudo Seaside" testbed delineates Seaside into distinct hazard zones based on proximity to the coastline and the ensuing risk profile. Zone A, the coastal hazard zone, bears the highest risk of earthquake and tsunami effects. Zone B acts as a transitional hazard area, still at risk for tsunami effects but to a lesser extent, and thus calls for design for tsunami inundation, i.e. flooding. Zone C, situated inland, prioritizes earthquake resilience, focusing on seismic mitigation and performance. Finally, Zone D, insulated from tsunami hazards, centers on preparing for only seismic events. This strategic zoning allows for tailored resilience planning and analysis, ensuring that preparedness measures are appropriate for the specific risks of each zone.

5.5 Fragility Functions

5.5.1 Earthquake-tsunami Fragility Surfaces

The impact of some of the earthquake-induced hazards on buildings in each zone of coastal communities like the Pseudo Seaside testbed is compound. In zone A, B and C, the combined impact of earthquake and tsunami hazards for the structural systems of the buildings would require a multi-variate vulnerability function using a 3D fragility surface. However, the impact of inundation following tsunami is considered independent and can be computed separately using a single-variable vulnerability function. In zone D, the impact of inundation from tsunami hazard on buildings of inland communities can be neglected and structures are considered only to be exposed to earthquake shaking.

Building damage caused by earthquakes and subsequent tsunamis can be categorized into two primary components: structural damage and content damage. Structural damage further delineates into damage arising from earthquake-induced loading and damage stemming from tsunami-induced loading. In this study, an algorithm developed by Harati and van de Lindt (2024a), which was presented in Chapter 2, is used to generate earthquake-tsunami fragility functions of the building structures for zones A-C. These fragility functions are based on surface equations, where they used a two-phase probability-based successive analysis procedure. In this way, the joint failure probabilities at specified damage states can be computed in the form of discrete data points. To obtain a near-continuous function that governs the earthquake-tsunami fragility surface, a surface fitting procedure is performed on these data points. The fragility surface is formulated through an equation, which is based on a mathematical model $h(E, C1, C2, \alpha, n, Sa, MF)$ as introduced by Kern et al. (2004). This model incorporates five unknown parameters that are essential for calculating the joint failure probability $P(Sa, MF)$. For more information about this surface equation and its relevant five parameters, readers are referred to a study by Harati and van de Lindt (2024a) or Chapters 2 to 4 of this dissertation.

5.5.2 Fragility Surfaces for RC Building Frames

Harati and van de Lindt (2024b, 2024c)—presented in Chapter 3 and Chapter 4—reported fragility surface parameters for a portfolio of RC structures (both ductile and non-ductile) exposed to regular- and long-duration earthquakes. They used two earthquake sets: FEMA P-695 records (*2011*) for regular-duration earthquakes and M9 Project records (Frankel et al., 2018) for long-duration earthquakes. The earthquake-tsunami fragility surfaces for both sets of ground motions (GMs) for the complete damage state (DS3) are presented side-by-side in Figure 5-6. The 2D fragility curves for tsunami-only and earthquake-only hazards can be extracted from the edges at the boundaries of these fragility surfaces, respectively and appear on the edges of the horizontal plane composed of the relevant IM axes. A repetitive optimization-based procedure is used to extract the controlling parameters of the lognormal CDF (μ and σ for the mean and standard deviation). As shown in Figure 5-6, the fragility surfaces obtained from the two sets of GMs for 4-story RC buildings (ductile frames) exhibit a noticeable difference, indicating a shift in the fragility surface toward the vertical (z-axis) when derived from the M9 Project ground motions. This shift suggests a higher probability of complete damage to the structure for a given joint IM of an earthquake-tsunami event when long-duration earthquakes are selected for the simulation procedure.

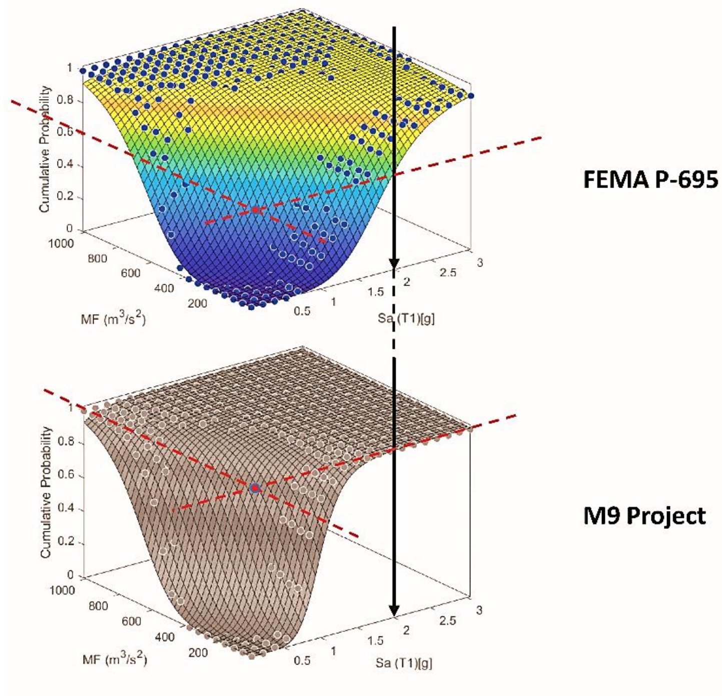

Figure 5-6. Comparative analysis of fragility functions of the 4-story RC ductile system (RC3) at DS3 for earthquake and tsunami scenarios derived from long-duration GMs versus regular-duration GMs.

5.5.3 Fragility Surfaces for Woodframe Buildings

Woodframe buildings, despite being typically destroyed by tsunamis over a meter high, are common in U.S. coastal communities and thus need representation in community models. This study utilizes the methodology by Harati and van de Lindt (2024a) in Chapter 2 of this dissertation to develop earthquake-tsunami fragility surfaces for woodframe structures. Laboratory tests revealed significant pinching in the hysteretic response of wood shear panels (WSPs), influenced by nailing patterns, simulated using the CUREe 10-parameter model (SAWS) in OpenSeesPy software. This analysis focuses on unperforated WSPs, with variations in ductility capacities across different designs due to differing nail spacings. The study categorizes woodframe structures by peak inter-story drift ratio (IDR) as the engineering demand parameter (EDP) across six archetypes, considering design levels from low to high. The specific details of the woodframe models and their parameters are elaborated in Chapter 3 and 4. For more details, readers are referred to Chapter 3 of this dissertation.

5.5.4 Fragility Functions for Inundation-following Tsunami

For assessing content damage from inundation of tsunami hazard in zones A to C, this research employs static flood fragility functions, as depicted in Figure 5-7, developed by Nofal and van de Lindt (2020). These functions form a fundamental part of the methodology to assess damage in buildings that experience inundation post-tsunami to quantify the content damage of the buildings from tsunami events based on maximum inundation depth (Hmax). They are tailored to evaluate content damage varying from no damage (DS0) to significant damage (DS3). In contrast, the DS4 limit state level in these vulnerability functions, indicative of structural damage due to foundation scour, represents a substantial deterioration in the structural integrity. Such damage is usually associated with prolonged flood events, typical of riverine and rainfall-induced flooding but can occur during tsunami drawdown where water flow back out to the ocean. However, this is felt to be beyond the scope for the present study and is omitted, focusing on the immediate seismic and tsunami related impacts to the superstructure. The exclusion is partially justified as the structural damage in this multi-hazard simulation is already incorporated through the earthquake-tsunami fragility surfaces, but the scour remains beyond scope.

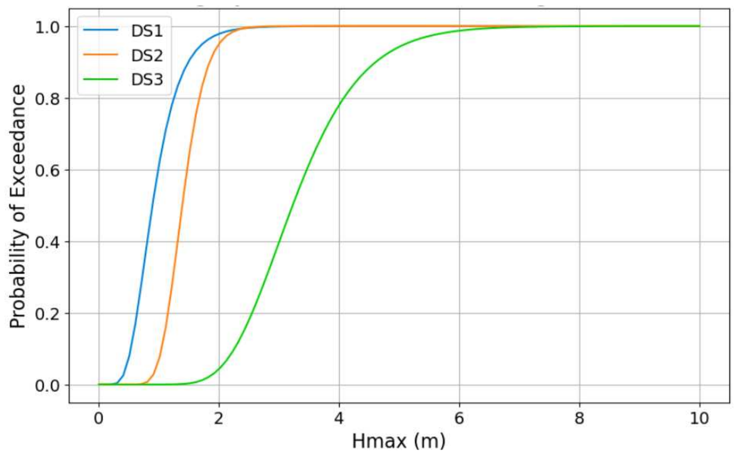

Figure 5-7. Static flood fragility curves for building content damage for archetype F3 of the study (after Nofal and van de Lindt, 2020).

The selection of static flood fragility functions for the content damage of building archetypes in this study is primarily based on the maximum expected inundation height (discussed in Chapter 2, 3 and 4 with more details) and the occupancy type of archetypes available in the inventory data of Pseudo Seaside. Tall RC buildings (structures with more than six stories) and W2 woodframes, assumed to serve commercial purposes, have been assigned the F7 archetype from Nofal and van de Lindt (2020). For RC buildings with fewer than six floors and W1 woodframes, the F2 and F4 archetypes from Nofal and van de Lindt (2020) are used. Low-rise RC buildings and woodframe systems (with two floors or fewer) are assigned the F2 archetype, while the F4 flood archetype is used for the remaining cases in the content damage analysis.

5.6 Hazard Simulation

This study extends the Probabilistic Seismic and Tsunami Hazard Analysis (PSTHA) framework introduced by Park et al. (2017a), which executed a hazard simulation for earthquake and tsunami events, specifically targeting Seaside, Oregon. Utilizing a logic-tree methodology, they evaluated the effects of a complete rupture along the Cascadia Subduction Zone (CSZ), incorporating essential elements such as an earthquake source model derived from a tapered Gutenberg-Richter distribution function for generating hazard values, and a ground motion prediction equation-based earthquake simulation model developed by Abrahamson et al. (2016). Additionally, they incorporated a tsunami simulation model based on the nonlinear shallow water equations introduced by Lynett et al. (2002) and Titov et al. (2011).

The analysis quantified site-specific annual exceedance probabilities for both earthquake and tsunami hazards by integrating parameters such as peak ground acceleration (PGA), elastic spectral acceleration (Sa) for various fundamental periods, Sa (Ti), aligned with different structural systems within the Seaside testbed area, along with H_{max}, maximum predicted tsunami wave velocity (Vmax), and maximum expected tsunami momentum flux (MF). This comprehensive delineation of seismic and tsunami hazards for mean recurrence intervals, particularly for the 100, 250, 500, and 1,000-year benchmarks, furnishes the necessary hazard values for an in-depth multi-hazard community resilience analysis. Emphasizing these recurrence intervals is important, as longer recurrence intervals correlate with severe damage, challenging emergency response and post-disaster recovery efforts.

5.7 Numerical Results of Illustrative Example: Pseudo Seaside

The Pseudo Seaside testbed was utilized for this analysis, employing both the 3D fragility surfaces for combined earthquake and tsunami hazards, and the 2D fragility curves for isolated earthquake or tsunami scenarios. These 2D curves, projections of the comprehensive 3D earthquake-tsunami fragility surfaces (for both regular- and long-duration GMs), were derived from 16 building archetypes that existed in the testbed. For scenarios focusing on either earthquake or tsunami hazards alone, FEMA's combination rules were used to calculate the cumulative structural damage from both hazards. Additionally, single-variable fragility curves, as formulated by Nofal and van de Lindt (2020), were incorporated to assess damage from tsunami inundation modeled as static flooding, further enriching the multi-hazard framework's capabilities.

As mentioned earlier, the Pseudo Seaside testbed was developed based on the original Seaside testbed (Park et al., 2017a) for an in-depth evaluation of the multi-hazard community resilience analysis, focusing on earthquake and tsunami events. This evaluation examined the effectiveness of the FEMA combination-rule methodology for community resilience analysis, comparing it to the method developed herein, the latter which is grounded in 3D earthquake-tsunami fragility surfaces. This critical assessment aimed to validate the precision of FEMA combination rules and their applicability to resilience studies. In this case, the potential of new perspectives introduced in the study and the importance of having the knowledge on how to employ statistical rules (such as FEMA formula) to combine damage assessments from multiple hazards were also considered.

Figure 5-8 illustrates the distribution of building types within the Pseudo Seaside testbed and categorizes the buildings into two primary structural systems: RC buildings and woodframe buildings. It should be noted that woodframe buildings are more prevalent than their RC counterparts, but typically much smaller often representing a single-family dwelling, but some woodframe buildings can be used for commercial applications. Specifically, the testbed includes two variations of woodframe structures, designated as W1 for residential buildings and W2 for commercial. Additionally, Figure 5-8(a) includes two types of design of RC structures: those with ductile designs and those without. Figure 5-8(b) comprehensively displays all building archetypes present in the testbed, encompassing both light woodframes with varied design (W11-W23) and RC structures, with a clear distinction between ductile and non-ductile RC designs (from RC1 to

RC10). This detailed presentation underscores the diversity of structural systems studied within the Pseudo Seaside testbed.

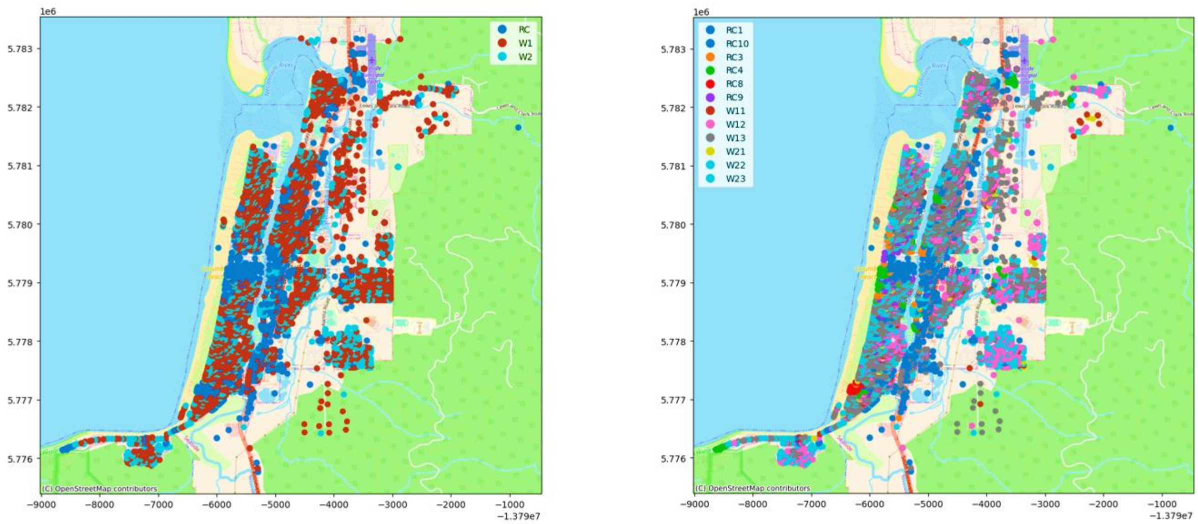

a) Main categories of the buildings

b) Building archetypes in detail

Figure 5-8. Distribution of the archetype buildings in the Pseudo Seaside testbed: a) the main categories of the buildings; and b) building archetypes in detail

Figure 5-9 showcases the results of failure probabilities on household level from a spatial damage analysis for the Pseudo Seaside testbed, focusing on a near-field tsunami event. This analysis is divided into structural damage from the tsunami alone (Figure 5-9(a)) and the augmented damage from subsequent inundation (Figure 5-9(b)), with the latter specifically examining content damage within buildings and basing assessments on tsunami inundation depth. A critical comparison reveals that inundation-related damage exceeds the initial structural impacts that were based on momentum flux as the intensity measure of the tsunami events. All analyses have been conducted with a mean recurrence interval (MRI) of 1000 years for the seismic source. Figure 5-9(c) illustrates the spatial dispersion of structural damage attributable to earthquake hazards alone, underscoring the propagation of seismic damage throughout the town rather than confinement to coastal vicinities. Additionally, Figure 5-9(d) explores the combined effects of earthquake and tsunami, using the methodology aligned with surface fragility equations (here for long-duration earthquakes) proposed in this study. It demonstrates that pre-existing earthquake damage significantly increases vulnerability to the tsunami, as depicted by the severe damage escalation compared to the tsunami-only scenario. This multi-hazard analysis emphasizes the importance of considering the successive effects of earthquakes and tsunamis in community vulnerability assessments, highlighting the application of surface fragility equations to understand the compounded damage dynamics on the Pseudo Seaside testbed.

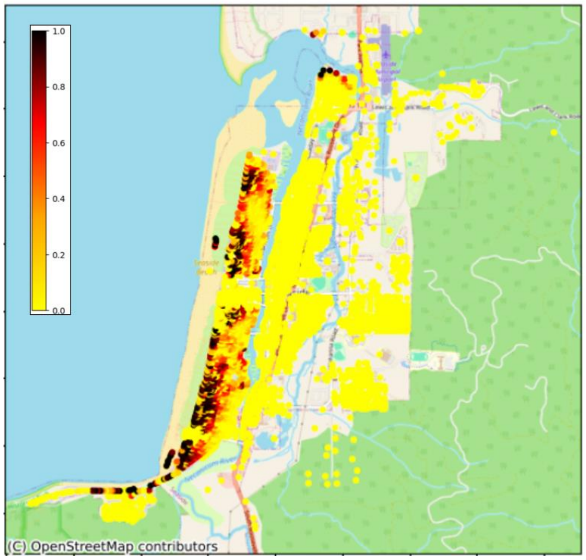

a) Tsunami-only (structural damage)

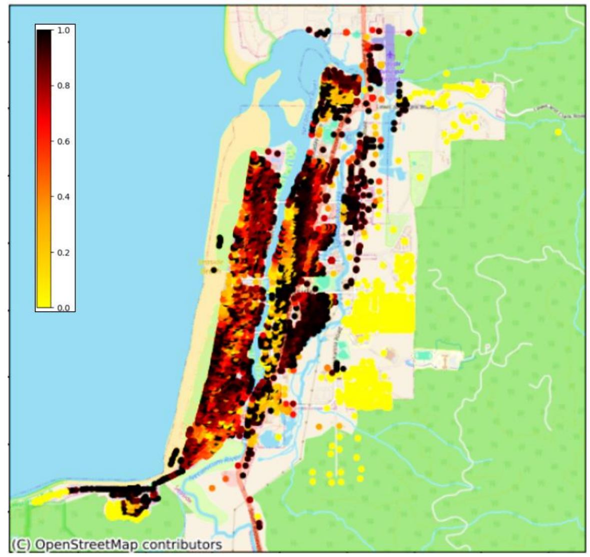

b) Inundation-following tsunami (contents damage)

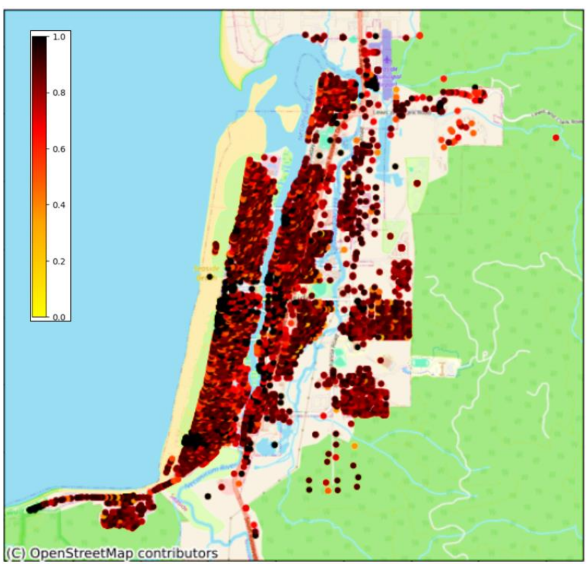

c) Earthquake-only (structural damage)

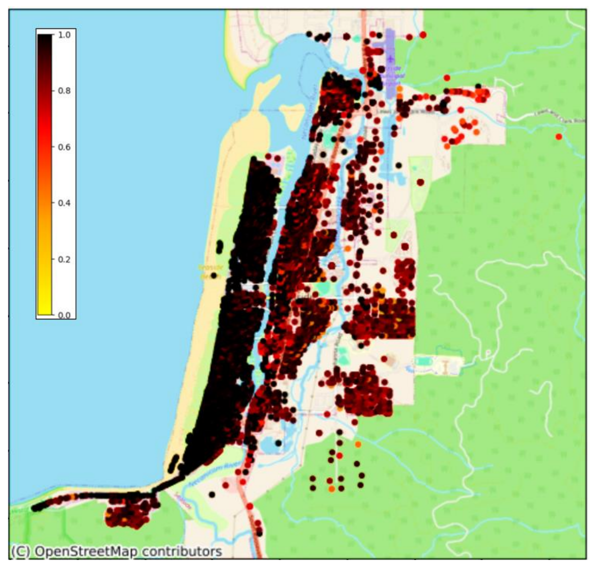

d) Cumulative damage of earthquake and tsunami (surface equation)

Figure 5-9. Spatial damage analyses for the Pseudo Seaside testbed for a near-field tsunami event: a) tsunami-only with the focus on structural damage, b) inundation-following tsunami considering contents damage, and c) cumulative damage from the source earthquake

Figure 5-10 illustrates the probability distributions for failure of archetype buildings under varied hazard scenarios across different MRIs of the source earthquake, specifically for MRIs of

500, 1000, and 2500 years. These probabilities for each household unit in the Pseudo Seaside testbed were calculated using the Monte Carlo simulation procedure described earlier, with 1000 realizations. Notably, the figures depict the count of buildings damaged, each assigned a failure probability value to form their distribution. The initial figures (first row) in Figure 5-10 represent failure probabilities due to earthquake-only hazards, utilizing 2D fragility curves derived from combined earthquake and tsunami surface fragilities (for long-duration earthquakes). This analysis reveals that, particularly for a 2500-year MRI earthquake, many buildings are at a failure probability approaching unity, indicating severe damage. As expected, an increase in earthquake MRI correlates with increased building damage in this analysis.

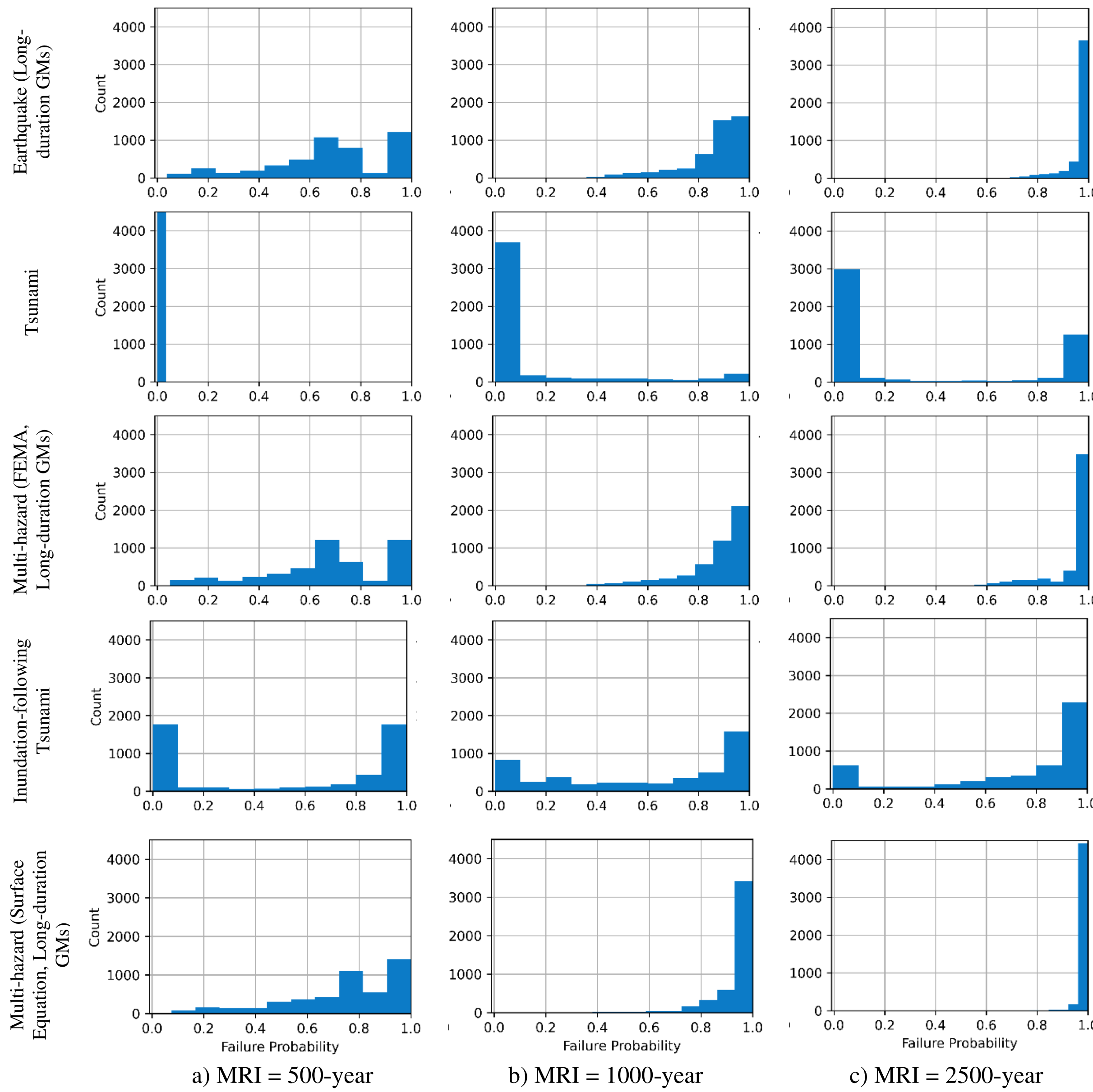

Figure 5-10. Distribution of the failure probability of the archetype buildings under different hazard scenarios for different earthquake recurrence intervals: a) MRI = 500-year, b) MRI = 1000-year, and c) MRI = 2500-year

For tsunami-only hazards, failure probabilities were determined using equivalent tsunami-only fragility curves derived from the earthquake-tsunami fragility surfaces. A comparative analysis of failure probabilities between earthquake-only and tsunami-only hazards, as shown in Figure 5-10, indicates significantly lesser structural damage from tsunamis alone if we assume that the occurrence of a far-field tsunami in this location was even possible theoretically. The third row of Figure 5-10 demonstrates the compounded structural damage from both hazards across various MRIs, employing FEMA's combinational rule and independent sets of 2D fragility curves for a multi-hazard scenario. This combination, especially for a 1000-year MRI, reveals more damage to buildings compared to earthquake-only hazard, showing over 2000 buildings with high failure probabilities.

The analysis of tsunami inundation hazards shows damage distributions similar to the structural damage from tsunami-only hazard, with increased damage due to the inclusion of tsunami inundation depth for assessing content damage, aligning with observations (from Figure 5-9) that areas near the shoreline are more susceptible to tsunami-induced inundation and MF-based damage.

The concluding figures in Figure 5-10 pertain to a multi-hazard damage assessment using earthquake-tsunami fragility surfaces (for long-duration earthquakes) developed in this study. The distributions closely resemble those derived from FEMA's rule for a 500-year MRI but show a shift towards higher failure probabilities for longer MRIs. This indicates that the FEMA combinational rule may underestimate cascading damage for higher MRIs, a gap addressed by incorporating direct cascading damage between earthquake and tsunami hazards using the proposed methodology. It should also be mentioned that the proposed approach is computationally more efficient than the FEMA rule, requiring significantly fewer computations by directly combining damages from both hazards through earthquake-tsunami fragility surfaces, thus suggesting a threefold reduction in computational time compared to separate analyses for each hazard followed by their combination. Of course, there is significant effort in the original development of the fragility surfaces themselves.

The insights from Figure 5-10 are substantiated by tracking the quantity of buildings within each damage state, as determined by both the FEMA combinational rule and the surface equation methodology. Figure 5-11 reveals that applying the surface equation to the Pseudo Seaside's infrastructure within a 1000-year MRI results in alterations to approximately 50 percent of the damage states. Figure 5-11 further illustrates that, under the stipulated multi-hazard scenario, there is a notable shift in the damage pattern, particularly affecting the damage state levels of DS2 and DS3.

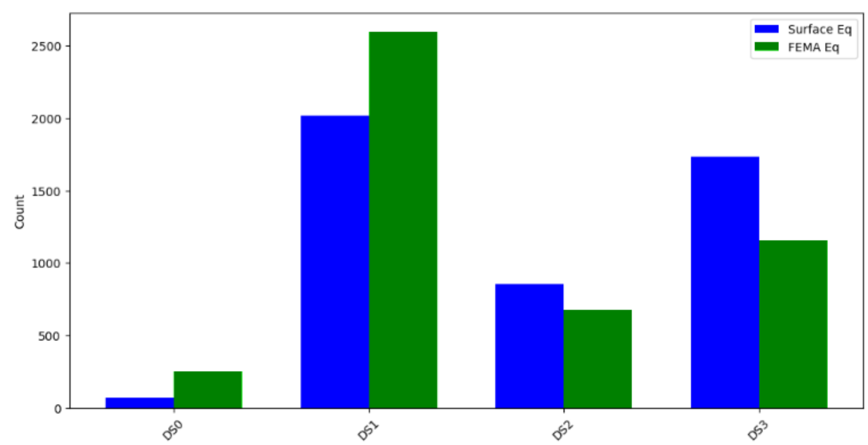

Figure 5-11. Damage states of Pseudo Seaside under a multi-hazard scenario of earthquake and near-field tsunami using both FEMA and surface equation method at a seismic intensity corresponding to a 1000-year MRI.

Figure 5-12 corroborates the findings depicted in Figure 5-11, illustrating the escalation of cumulative damage in Pseudo Seaside at a seismic intensity level with a 1000-year MRI. This intensification is evident when utilizing the surface equation method as opposed to the FEMA combination rule. Enhanced transition of damage from DS1 to DS2 and from DS2 to DS3 is detailed in Figure 5-12(b), indicating that the FEMA approach may underestimate the cumulative damage sustained by the infrastructure.

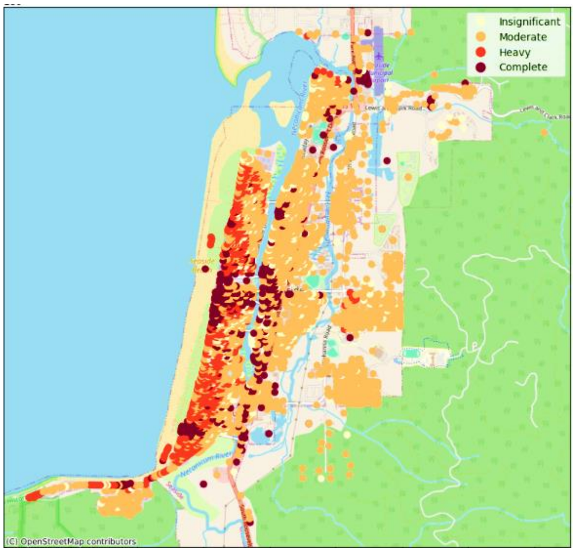

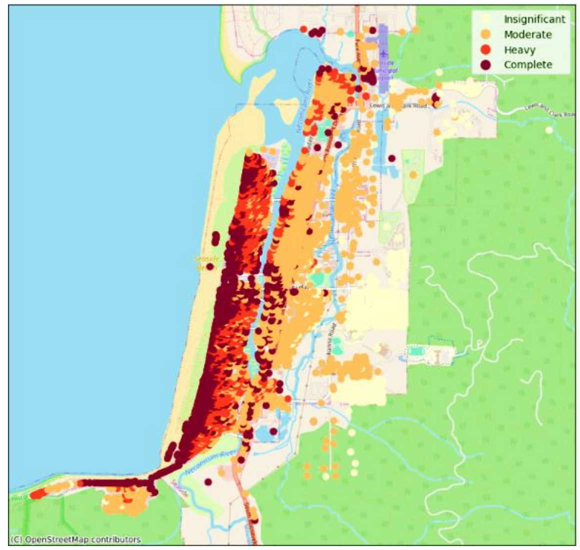

a) FEMA rule

b) Surface equation

Figure 5-12. Cumulative damage state pattern of Pseudo Seaside under a multi-hazard scenario of earthquake and near-field tsunami at an intensity level of a 1000-year MRI using different methods: a) FEMA approach; b) Surface equation methodology in this study.

Figure 5-13 presents the predicted direct economic losses against MRIs for the Pseudo Seaside community under varied earthquake and tsunami hazard scenarios. Figure 5-13(a) delineates the predicted direct economic losses for each hazard individually, plotted against the source earthquake's MRI. The economic losses calculated according to the proposed methodology encompass structural damage caused by earthquakes (for both regular- and long-duration earthquake sets) and tsunamis, as well as content damage due to inundation following a tsunami. Notably, structural damage attributable to tsunami-only hazards initiates at an MRI of 500 years, whereas content damage from post-tsunami inundation begins at an MRI of 250 years. This indicates that tsunami-induced content losses, driven by inundation depths, can impact coastal communities even during relatively minor tsunami events (with MRIs as low as 250 years).

Figure 5-13(b) aggregates the total direct economic losses from tsunami-only events—combining structural and content damages—with those from earthquake losses. Additionally, economic losses from the combined effects of earthquake and tsunami events are calculated using both the FEMA approach and the method proposed in this study and are displayed in Figure 5-13(b). In the FEMA approach, 2D fragility curves extracted from the developed fragility surfaces based on both regular- and long-duration GMs were utilized in this analysis. This choice was primarily because fragility curves associated with regular-duration GMs align more closely with FEMA's combinational approach. For MRIs below 250 years, the losses from earthquake-only scenarios and multi-hazard scenarios (calculated using both methods) appear to converge. Nonetheless, as the MRI surpasses 250 years, a stark divergence emerges between the earthquake-only and multi-hazard scenario losses, with this gap amplifying with increasing MRIs, peaking at a 25% disparity in the most severe cases. This is considerably narrower than the nearly 50% difference observed in the damage assessments between the two methods. This divergence underscores the significant impact of cascading seismic damage from earthquakes and the subsequent tsunami damage at higher earthquake MRIs. It highlights the critical need for a dependable methodology to accurately account for combined losses in coastal communities facing multi-hazard scenarios.

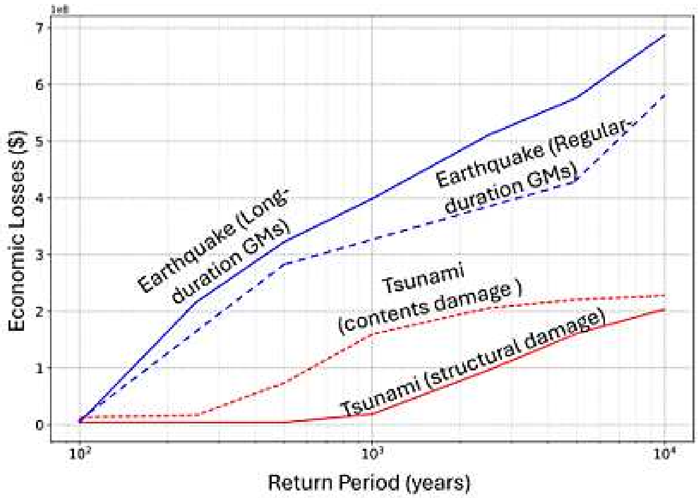

a) Induvial hazard components

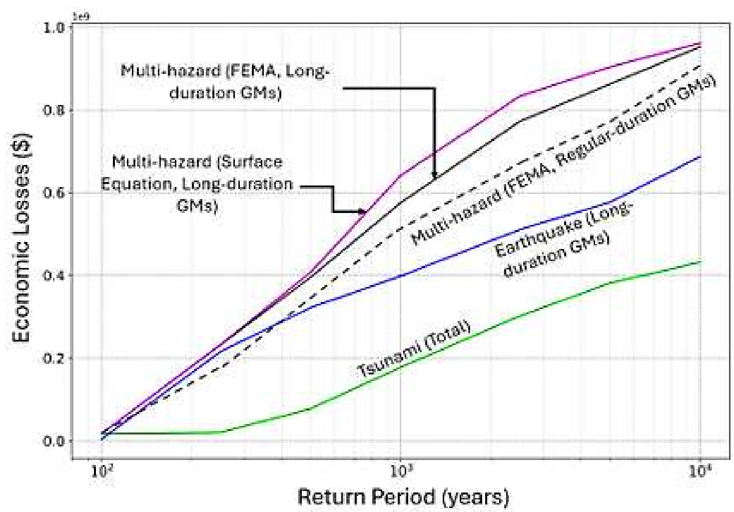

b) Cumulative effects of the hazards

Figure 5-13. Prediction of economic losses versus earthquake recurrence intervals for the Pseudo Seaside community under different earthquake and tsunami hazard scenarios: a) for each individual hazard components b) for the cumulative effects of the hazards based on FEMA combinational rule and fragility surface equations.

The findings detailed herein suggest that the FEMA combination rule's effectiveness is primarily constrained to lower seismic intensity levels (for MRIs below 500 years), with its accuracy diminishing at higher hazard intensities. The FEMA rule constitutes a significant advancement in multi-hazard risk assessment by providing a foundational framework for enhancing disaster preparedness and guiding resilient infrastructure development, but the limitations highlighted should be considered for future revisions of the rule. The successive model that produces the surfaces in this study can more precisely capture the interplay between seismic and tsunami hazards, thereby providing more accurate risk assessment and ultimately enabling decision-makers the ability to target key mitigation strategies for improved resilience.

CHAPTER 6: PHYSICS-INFORMED ML MULTI-HAZARD FRAGILITY SURFACES: AN EARTHQUAKE-TSUNAMI MITIGATION ANALYSIS[5]

6.1 Introduction

In recent developments for near-field tsunami fragility assessments, an integrated approach that simultaneously accounts for both earthquake and tsunami loadings has been pursued. Researchers such as Attary et al. (2021), Park et al. (2012), and Xu et al. (2021) have adopted a sequential analysis methodology, initiating with a nonlinear time history analysis (NTHA) to simulate earthquake effects, followed by a force-based NSP analysis for tsunami impacts. In this regard, Attary et al. (2021) used a more comprehensive probabilistic method for the generation of earthquake-tsunami fragility surfaces, which can incorporate the cascading damaging impacts of both hazards. This approach, although methodologically innovative, introduces complexities in developing a unified, continuous fragility function, complicating its integration into risk and resilience frameworks such as the Interdependent Networked Community Modeling Environment (IN-CORE) (van de Lindt et al. (2018, 2023)). In the Attary work, the uncertainty propagation model adopted utilized a set of 10 ground motion records for the NTHA procedure and limits uncertainty quantification to the yield strength (f_y) of steel within the structural model, indicating a narrowly focused exploration of uncertainty parameters critical to structural resilience in multi-hazard scenarios.

To enhance this approach, Harati and van de Lindt (2024) in Chapter 2 of this dissertation proposed a methodology based on parallel processing programming architecture. This enables

[5] This chapter is mainly based on the paper: Harati, M., and van de Lindt, J.W. (2024). "Physics-Informed ML Multi-Hazard Fragility Surfaces for use in Community Resilience Studies." Computer-Aided Civil and Infrastructure Engineering, (Under Re-review).

millions of nonlinear successive analyses to be performed in order to propagate uncertainty across all layers of the simulation, generating earthquake-tsunami surfaces that fully couple the cascading effects of both hazards. Additionally, these surfaces, due to their near-continuous nature, facilitate simpler implementation into resilience frameworks (e.g., IN-CORE) and applications. They also offer scalability crucial for developing fragility models for extensive building portfolios and community-level resilience analysis. However, while this method accurately models the successive cascading damage from earthquakes and tsunamis and improves the ease of fragility function application, it remains computationally demanding, requiring substantial high-performance computing (HPC) infrastructure. Additionally, it demonstrates limited flexibility, particularly in modifying fragility functions for tasks like seismic retrofitting at the community scale, which are essential for community-level mitigation analysis.

In seismic retrofitting, engineering solutions that essentially result in a horizontal shift of fragility functions is crucial for assessing and improving the earthquake resilience of structures and evaluating the impact of retrofitting on a community's overall resilience. The method adjusts fragility curves, which estimate the probability of a building exceeding different damage states under seismic loads, to reflect enhanced seismic performance post-retrofit (Aljawhari et al., 2022). By shifting these curves along the seismic intensity axis—often measured in spectral acceleration (Sa) for earthquakes or momentum flux (MF) for tsunami events—this method quantitatively demonstrates how retrofit plannings improve a structure's seismic resistance (Aljawhari et al., 2022; Jafari and Mahini, 2023; Park et al., 2017). Horizontal scaling effectively compares the resilience of structures before and after retrofitting, providing a measurable evaluation of retrofit efficacy. This technique assumes that retrofits primarily modify structural strength or stiffness, aiding decision-makers in evaluating retrofit investments. Engineers can determine the extent of curve shifting through parametric studies and detailed finite element (FE) modeling of structures before and after retrofitting (Jafari and Mahini, 2023).

This chapter presents a physics-informed machine learning (ML) algorithm designed to synthesize 3D earthquake-tsunami fragility functions without requiring HPC infrastructures or detailed FE modeling procedures, building upon the foundational work by Harati and van de Lindt (2024) presented in Chapter 2 of this dissertation. Unlike their approach, this ML-based method employs two distinct and randomly selected 2D fragility curves—one for earthquake and another for tsunami hazards—to develop these synthesized 3D fragility surfaces.

The structure of this chapter is as follows: it begins by defining the problem statement and research objectives; it then details the methodology, which includes the use of Extreme Gradient Boosting and Random Forest algorithms, extensive data preprocessing, hyperparameter tuning through grid search optimization, and a comprehensive suite of model evaluation metrics. The chapter proceeds with rigorous model validation and sensitivity analysis to ensure the robustness of the proposed ML model. It also introduces a methodology for the practical application of the ML models in mitigation planning and analysis using the multi-hazard fragility surfaces (both retrofitted and non-retrofitted).

This research aims to enhance multi-hazard risk assessment and resilience planning in communities vulnerable to combined natural hazards, such as earthquakes and tsunamis. This chapter of dissertation concludes with a detailed discussion on the limitations of the ML-based fragility generator and highlights the model's potential to synthesize multi-hazard fragility surfaces for various combinations, such as earthquakes and fire-following earthquakes, potentially replacing FEMA's combinational rule for calculating exceedance probabilities. Perhaps most notable is that this novel approach will provide a mechanism to combine 2D fragility curves for earthquake and tsunami for the same structure from any source. For example, both fragilities could be numerical, or both fragilities could be from post-even observation (empirical), or one fragility from numerical simulation and the other empirical.

6.2 Problem Statement

Originating from the same geophysical mechanisms, earthquakes and near-field tsunamis impact built structures in a sequential yet statistically independent manner, resulting in cascading structural and non-structural damage. Since these seismic hazards do not show statistical correlation in their effects on structural integrity, it is essential to consider the diminished seismic capacity of structures after an earthquake when assessing the potential effects of a subsequent near-field tsunami. Bayes' equation, as shown in Eq (6-1), offers a solid mathematical framework for updating the reliability assessments of structures subjected to these sequential hazards.

$$P(TS \mid EQ) = \frac{P(EQ \mid TS)\, P(TS)}{P(EQ)} \tag{6-1}$$

The primary objective of this chapter is to quantify the conditional failure probability *P(TS/EQ)*, which represents the likelihood of structural failure during a near-field tsunami following damage induced by the source earthquake. This probability is referred to as the near-field tsunami fragility function in the literature. Individual failure probabilities *P(TS)* for far-field tsunamis and *P(EQ)* for earthquakes can be derived from established 2D fragility functions. Examples of sources for earthquake fragility functions include Bandyopadhyay et al. (1990), Goda (2012), Li et al. (2014), and Paez-Ramirez et al. (2020). For far-field tsunami fragility functions, examples include Alam et al. (2018), Attary et al. (2017), and Zoppo et al. (2022). These references are illustrative, with numerous other studies also contributing to this domain of knowledge.

The equation theoretically requires *P(EQ|TS)*, a term that is computationally infeasible since tsunamis do not naturally precede earthquakes. To overcome this limitation, Harati and van de Lindt (2024)—proposed in Chapter 2—have developed a two-phase sequential analysis that calculates combined earthquake-tsunami fragility functions without the need for *P(EQ|TS)*, thereby providing a practical numerical framework for analyzing the complex interactions between these sequential hazards. They implemented a multi-distributed parallel processing architecture, utilizing hundreds to thousands of CPUs simultaneously via HPC clusters, to develop the earthquake-tsunami fragility surfaces depicted in Figure 6-1.

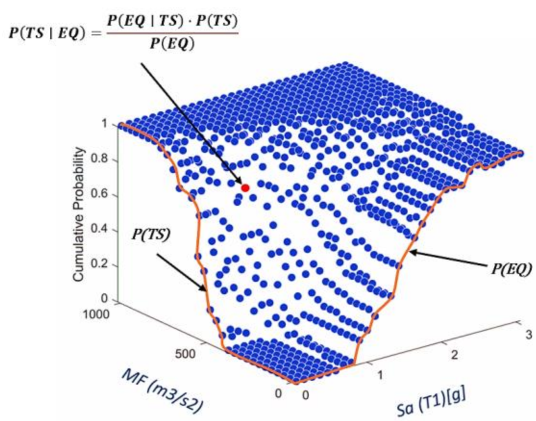

a) Discrete points for *P(TS|EQ)*

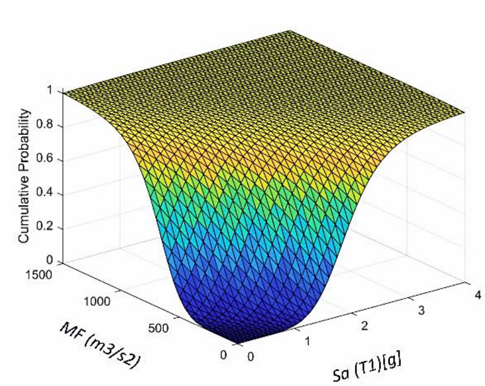

b) Near-continuous surface function for *P(TS|EQ)*

Figure 6-1. Failure probability values computed for the term *P(TS|EQ)* in a 4-story RC frame: a) discreate data points for the earthquake-tsunami fragility surface; b) surface fitting over the raw data points of *P(TS|EQ)*

Figure 6-1(a) from Harati and van de Lindt (2024) discussed in Chapter displays discrete data points on an earthquake-tsunami fragility surface, showcasing the failure probability on complete collapse damage level of a 4-story reinforced concrete (RC) frame. The x and y-axes represent earthquake and tsunami intensity measures (IM), respectively, with Sa and MF used as the related hazard IMs in this study. The z-axis indicates the exceedance probability of structural collapse. Notably, Figure 6-1(a) provides computed values for *P(TS|EQ)* derived from their methodology, thus eliminating the need for the otherwise unfeasible term *P(EQ|TS)*. Furthermore, on the boundaries of the surface, Figure 6-1(a) also presents the discrete points pertinent to the failure probability of the structure under each hazard individually, namely *P(TS)* and *P(EQ)*.

Figure 6-1(b) illustrates the earthquake-tsunami fragility surface for the same prototypical structure. Along each boundary of this fragility surface, a single 2D fragility curve is displayed. On the plane defined by the Sa and z-axis, a 2D fragility curve specific to earthquake-induced hazards (*P(EQ)*) is extracted and projected from the near-continuous fragility surface. Conversely, along the opposing MF axis, a 2D fragility curve representing far-field tsunami hazards (*P(TS)*) is presented.

The fragility surface is defined by Eq (6-2), based on the mathematical model $h(E, C1, C2, \alpha, n, Sa, MF)$ as introduced by Kern et al. (2004) and later adapted and adjusted for fragility assessments by Harati and van de Lindt (2024)—presented in details in Chapter 2 and Chapter 3. This model includes five unknown parameters needed for calculating the joint failure probability *P(Sa, MF)*, which corresponds to the earlier introduced term *P(TS|EQ):*

$$P(Sa, MF) = \frac{E(\frac{Sa}{C1} + \frac{MF}{C2} + \alpha\left(\frac{Sa}{C1}\right)\left(\frac{MF}{C2}\right))^n}{(\left(\frac{Sa}{C1} + \frac{MF}{C2} + \alpha\left(\frac{Sa}{C1}\right)\left(\frac{MF}{C2}\right)\right)^n + 1)} \tag{6-2}$$

The unknown parameters in this earthquake-tsunami fragility model can be identified through a surface-fitting optimization technique as recommended by Harati and van de Lindt (2024a)—readers are referred to Chapter 2 and Chapter 3 of this dissertation for more details. In the context of Eqs (1) and (2), the following relationships hold true:

$$P(TS \mid EQ) = P(Sa, MF) \tag{6-3}$$

$$P(EQ \mid TS) = h(E, C1, C2, \alpha, n, Sa, MF)(\frac{P(EQ)}{P(TS)}) \tag{6-4}$$

$$P(EQ \mid TS) = f(E, C1, C2, \alpha, n, Sa, MF) \tag{6-5}$$

From Eq (6-5), the term *P(EQ|TS)*, which is problematic in practical applications as outlined in Eq (6-1), can be substituted by parameters from Eq (6-2). This enables the approximation of the focal term *P(TS|EQ)* in Eq (6-1) as follows:

$$P(TS \mid EQ) = f(E, C1, C2, \alpha, n, Sa, MF)(\frac{P(TS)}{P(EQ)}) \tag{6-6}$$

As can be seen from Eq (6-6), the term *P(TS|EQ)* cannot be directly derived from two 2D fragility curves located at the boundaries of the earthquake-tsunami fragility surface because the function *f* depends on 5 unknown parameters. However, it is hypothetically possible to find a function, say function *f*, that can produce the surface when multiplied by a term shown in Eq (6-6), which is based on the two individual 2D fragility curves (*P(TS)/P(EQ)*). The central research inquiry aims to identify a new function that predicts *P(TS|EQ)* solely based on the individual failure probabilities *P(EQ)* and *P(TS)*, as stipulated in Eq (6-7):

$$P(TS \mid EQ) = g(P(EQ), P(TS)) \tag{6-7}$$

The function *g* is assumed to take 2D fragility functions for both earthquake (*P(EQ)*) and tsunami (*P(TS)*) as inputs. Its purpose is to directly compute the joint failure probability *P(TS/EQ)* or *P(Sa,MF)*, thereby eliminating the need for complex sequential or multi-distributed analyses, as introduced by Harati and van de Lindt (2024) in Chapter 2. Consequently, Eqs (1) through (7) can be reformulated into Eq (6-8), allowing the necessary parameters for Eq (6-2) to be determined directly from the existing 2D fragility functions for earthquake and tsunami hazards:

$$P(Sa, MF) = g(P(EQ), P(TS)) = h(E, C1, C2, \alpha, n, Sa, MF) \tag{6-8}$$

As shown in Eq (6-8), the function *g* cannot be derived through typical mathematical procedures since there are five unknown parameters in function *h* while having only two 2D fragility equations on the boundaries. Moving forward, the primary objective of this chapter is to engage in a comprehensive exploration aimed at accurately identifying the function *g(P(EQ), P(TS))*. This involves leveraging a blend of computational methodologies, including ML algorithms, statistical analyses, and physics-based simulations, especially because a purely analytical solution for the function is not attainable. The implications of this function for advancing current practices in multi-hazard structural reliability assessments will also be examined and discussed.

6.3 Methodological Approach

Given the complexity and computational challenges of determining the *g(P(EQ), P(TS))* function through conventional mathematical methods, this study adopts tree-based ML algorithms as a numerical approach to approximate the function. As shown in Figure 6-2, this physics-informed ML framework comprises three main phases: training, prediction, and validation. In the training phase, each selected ML algorithm is used to create a feature matrix aimed at potentially reducing the variables involved in the final ML model. The model is then tested using predefined performance metrics (to be discussed later in this section). Finally, the new ML model undergoes a thorough examination based on physics-based criteria to ascertain whether the selected ML algorithm meets the engineering and theoretical expectations. Should the ML algorithm fail the testing, an alternative will be selected and subjected to the same phases.

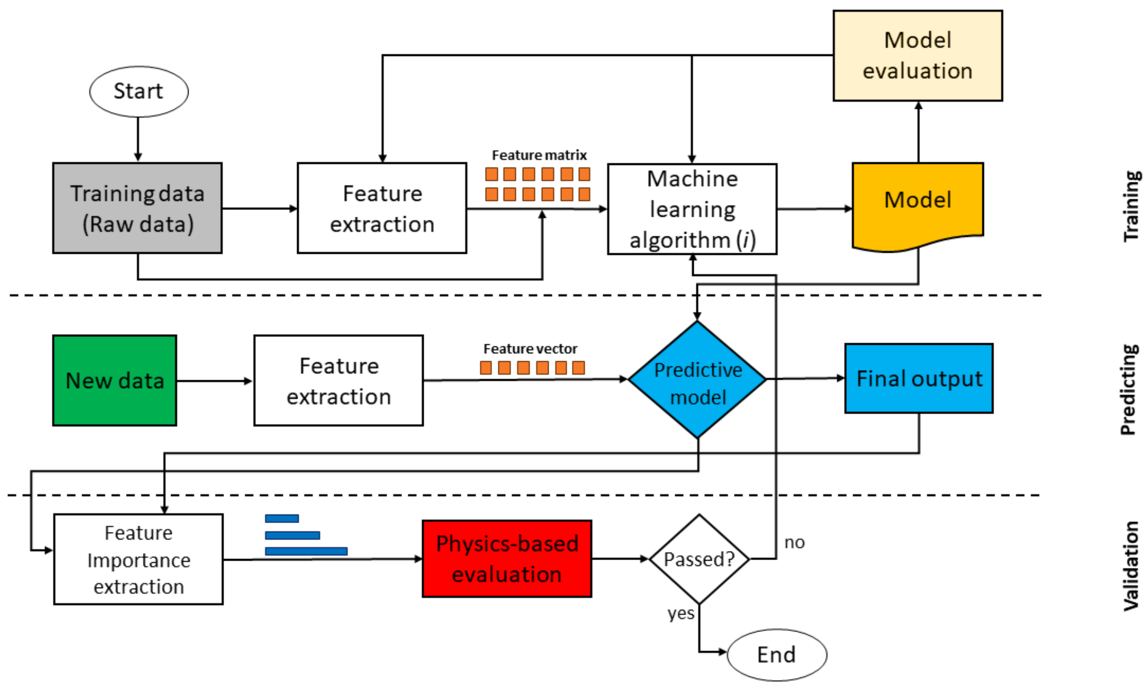

Figure 6-2. The proposed framework for the physics-based ML modeling for synthesized earthquake-tsunami fragility functions.

6.3.1 Tree-based Machine Learning Algorithms

In this chapter of dissertation, two well-established tree-based ML regressor algorithms are utilized. The Extreme Gradient Boosting (XGBoost) algorithm, refined by Chen and Guestrin

(2016), is a notable enhancement of the Gradient Boosted Decision Trees, integrating a regularization term to curtail overfitting and employing a second-order Taylor expansion for optimization, which has proven effective in various complex engineering settings. In contrast, the Random Forest (RF) algorithm, pioneered by Breiman (2001), utilizes an ensemble of decision trees to improve prediction accuracy and prevent overfitting through averaging and random subspace methods, making it suitable for high-dimensional datasets and complex applications. Both algorithms are distinguished in the ML community for their robustness and have been successfully applied across multiple predictive tasks. For further details on these ML algorithms, readers are encouraged to consult the papers by Chen and Guestrin (2016) and Breiman (2001).

6.3.2 Data Pre-processing and Construction of the Dataset

Data pre-processing initiates with a cleaning phase customized for tree-based ML algorithms like RF and XGBoost. To counter overfitting, outliers and noise are treated through either transformation techniques or statistical imputations. Primary continuous variables such as Sa and MF, which model hazard intensities, are discretized for computational efficacy. In this investigation, a minimum of 100 discretization points is chosen for each axis—whether x and y, or Sa and MF—yielding no fewer than 10,000 data points per specific fragility surface for a considered damage state. The dataset comprises a five-column matrix: x, y, $f(x)$, $f(y)$, and $f(x,y)$, where x and y act as independent variables denoting Sa and MF, the hazard IMs. The 2D fragility functions $f(x)$ and $f(y)$, initially labeled as $P(EQ)$ and $P(TS)$ for earthquake and tsunami hazards respectively, draw upon research by Harati and van de Lindt (2024a) in Chapter 2. The $f(x,y)$ column integrates the 3D fragility surface $P(TS|EQ)$, also based on Harati and van de Lindt (2024a), utilizing x and y as joint IMs for the involved hazards. The fragility functions used in this study cover 10 archetypes for RC frames, 6 vulnerability models for ductile systems, and several models for non-ductile structures. Notably, the vulnerability functions are earthquake-tsunami surfaces developed based on regular-duration earthquakes as outlined in FEMA P-695 (*2011)*.

As shown in Figure 6-2, the first four columns function as independent variables (or boundary conditions) for the ML model, while the last column, *f(x, y)*, is designated as the target variable for prediction, as outlined in Section 2. Figure 6-3 illustrates the distributions of the functions *f(x)* and *f(y)* within the dataset. These figures demonstrate that a broad range of earthquake and tsunami IM values have been included in the dataset creation. Specifically, the dataset covers Sa values from zero to 6g for the earthquake IM, and MF values from 0 to 3000 m^3/s^2 for the tsunami IM.

$$Dataset = \left\{ \begin{matrix} x & y & f(x) & f(y) & \boldsymbol{f(x,y)} \\ . & . & . & . & . \\ . & . & . & . & . \\ . & . & . & . & . \\ . & . & . & . & . \\ . & . & . & . & . \\ . & . & . & . & . \\ . & . & . & . & . \\ . & . & . & . & . \\ . & . & . & . & . \\ . & . & . & . & . \end{matrix} \right\} \text{“m” rows of data}$$

Figure 6-3. The configuration of the dataset containing independent and target variables for the fragility ML model.

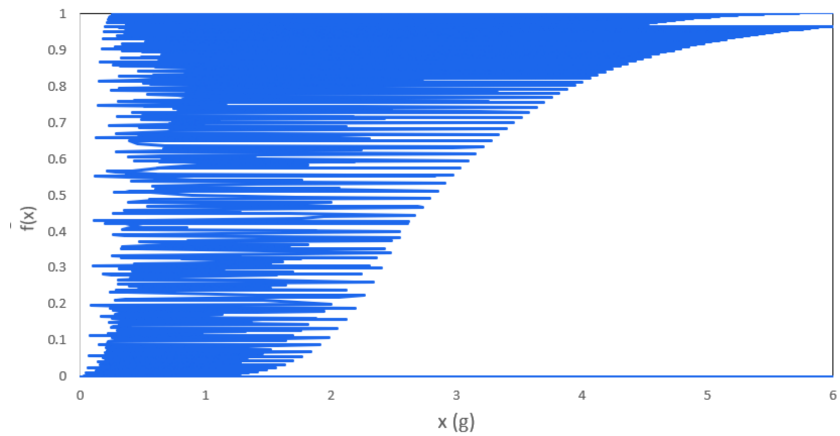

(a) Range of variables for *f(x)* versus *x*

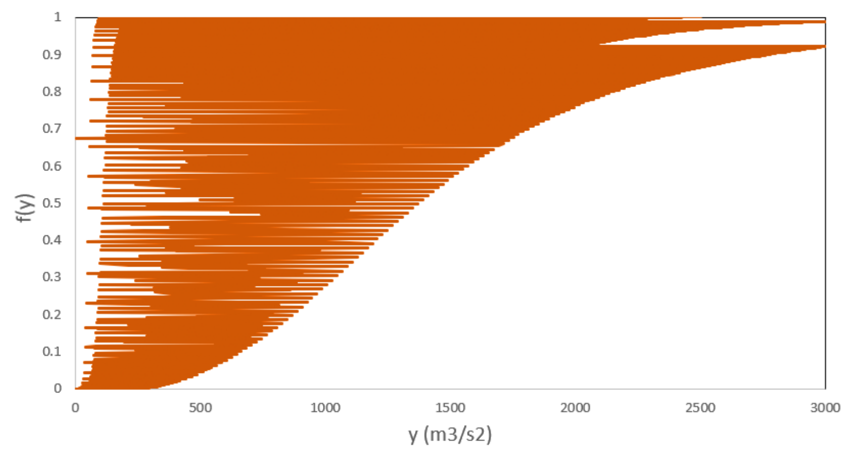

(b) Range of variables for *f(y)* versus *y*

Figure 6-4. The range of IM values for each individual hazard, earthquake and tsunami, for the 2D input fragility functions: a) data for input earthquake fragilities; b) data for input tsunami fragility functions.

In the construction of the dataset, partitioning the data into training and testing subsets constitutes a fundamental step. Seventy percent of the shuffled data is designated for training, while the remaining 30% serves as the testing set. This 70-30 ratio balances model training against testing adequacy, consistent with commonly employed standards. Collectively, half a million rows of data have been ultimately tried to be collected as the final size for the candidate dataset (later discussed). The use of k-fold cross-validation on the training set allows the evaluation of model performance, leading to a model that is not only reflective of the data but also generalizable.

6.3.3 Hyperparameters and Grid Search Optimization

Hyperparameter tuning is a significant phase in optimizing the predictive power of ML models, particularly focusing on hyperparameters essential for tree-based algorithms like RF and XGBoost in this study. For RF algorithm, key parameters include ‘n_estimators’, which sets the number of trees in the forest; ‘max_depth’, defining the maximum depth of the trees; ‘min_samples_split’, the minimum number of samples required to split an internal node; and ‘min_samples_leaf’, the minimum number needed for a leaf node. For XGBoost, adjustments are made for ‘learning_rate’ to control overfitting through step size shrinkage, ‘max_depth’ for the depth of decision trees, subsample for the fraction of data used in each boosting round, and ‘colsample_bytree’ for the fraction of features used in tree construction. Grid search optimization is employed to systematically explore various parameter combinations, using k-fold cross-validation on the training set to evaluate each. Performance is measured by the root mean square error (RMSE) metric, selecting the lowest RMSE scores to determine optimal settings, ensuring the model is accurate and generalizable to new data. The best hyperparameters found for RF algorithm include n_estimators at 300, min_samples_split at 2, min_samples_leaf at 1, max_features as None, max_depth at 20, and ‘bootstrap’ as True. For XGBoost, optimal parameters include learning_rate of 0.05, max_depth of 6, subsample of 0.8, and colsample_bytree of 0.8.

6.3.4 Model Evaluation Metrics

To comprehensively assess the performance of the RF and XGBoost regressor models, several metrics are utilized, each capturing different aspects of model efficacy. The Root Mean Square Error (RMSE) evaluates the average magnitude of residuals, with a lower RMSE indicating superior performance, calculated as $\sqrt{\frac{1}{n}\sum_{i=1}^{n}(y_i - \hat{y}_i)^2}$. The Mean Absolute Error (MAE) measures the average of the absolute differences between observed and predictions, less sensitive to outliers than RMSE, defined by $\frac{1}{n}\sum_{i=1}^{n}|y_i - \hat{y}_i|$. The R-Squared ($R^2$) quantifies the variance in the dependent variable explained by the independent variables, calculated as $1 - \frac{\sum_{i=1}^{n}(y_i - \hat{y}_i)^2}{\sum_{i=1}^{n}(y_i - \bar{y})^2}$, where $\hat{y}$ is the mean of observed values. Additionally, Feature Importance Engineering (FIE) assesses the contribution of each feature to model performance, especially relevant for tree-based models, ranking variables based on the proportion of splits they participate in. Both models are evaluated on these metrics using the same training and testing data subsets, allowing for a robust and comparative evaluation.

6.4 Model Validation and Sensitivity Analysis

In evaluating the ML models developed in this study, FIE emerges as a paramount performance criterion. It elucidates the contribution of each feature or independent variable within the model. As outlined in Section 2, the objective is to devise a physics-informed ML function, as described by Eq (6-7), capable of accurately predicting the probability of exceeding a prescribed damage state. This model is expected to primarily rely on the outputs of functions *f(x)* and *f(y)*, showing limited sensitivity to the parameters *x* and *y* (where Sa=*x*, MF=*y*). The premise is that the influence of *x* and *y* on the model's predictions diminishes as the dataset expands towards an infinitely large size. In this study, the dataset size has been progressively increased to a substantial number, aiding in validating this hypothesis.

As the dataset reached its final targeted size—a size deemed reasonable for this study—empirical findings, as depicted in Figure 6-3, reveal that the XGBoost algorithm does not effectively meet the FIE performance metric. In contrast, the RF algorithm significantly reduced the influence of variables *x* and *y*, with their combined contributions diminishing to less than 3.56%. This substantial reduction closely aligns the RF algorithm with the function *g(P(EQ),* *P(TS))*, thereby fulfilling the theoretical requirements specified in the study. Consequently, the RF algorithm has been selected as the primary regression model for subsequent analyses. This decision ensures a physics-informed approach to generating ML-assisted earthquake-tsunami fragility surfaces, aligning with engineering judgment and enhancing the credibility and applicability of the results within the fields of reliability and community resilience modeling.

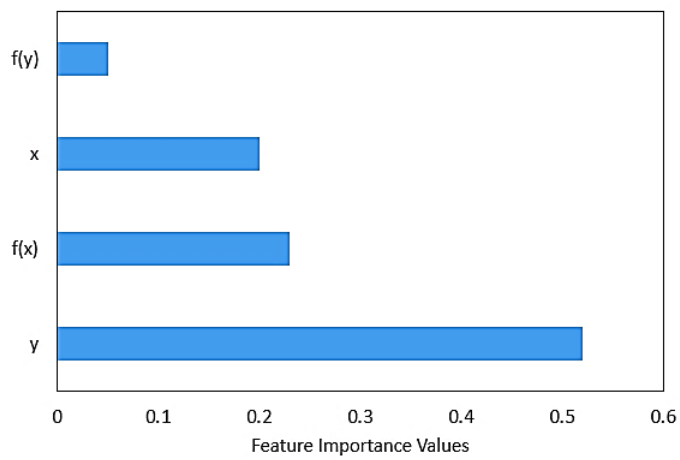

a) XGBoost algorithm

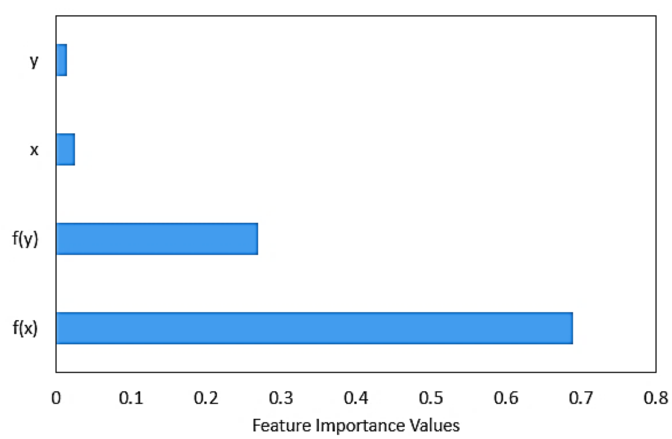

b) Random Forest algorithm

Figure 6-5. Results of feature importance analysis over the raw data of the composed dataset for different ML algorithms: a) XGBoost algorithm; and b) RF algorithm

In the assessment of a sophisticated ML framework developed for synthesizing earthquake-tsunami fragility surfaces, the analysis performed on 30% of unseen data, designated as the test dataset, demonstrates remarkable accuracy, vital for generating ML-assisted fragility surfaces for use in multi-hazard community resilience analysis in coastal regions. The MSE, remarkably low at 0.0001, and the MAE, at 0.0019, both reflect a strong correlation between the model's predictions and the actual observations. Figure 6-6 reveals the RMSE, measured at 0.0102, affirming the model's reliability in predictions.

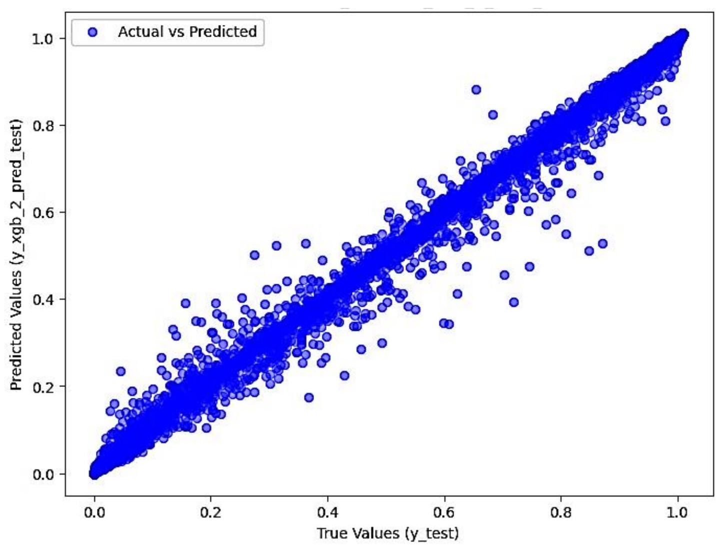

Figure 6-6. Correlation between the predictions of the ML model in this study and the actual observations.

The R-squared score of 0.997, detailed in Section 3.4 and illustrated in Figure 6-6, is particularly noteworthy for indicating an almost exact model fit. This high score, highlighted once more in Figure 6-7, underscores the model's clear ability to capture the variance within the dataset, including its capability to accurately trace temporal variations.

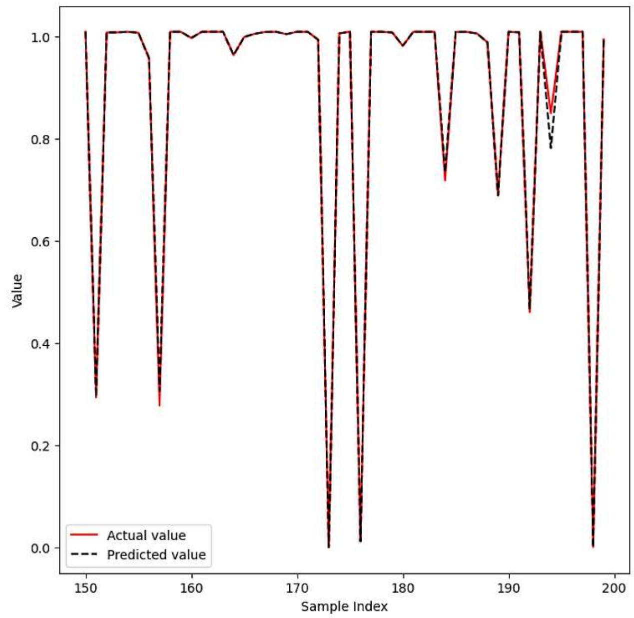

Figure 6-7. Temporal variations between the predictions of the developed ML model and the actual observations.

6.5 Illustrative Applications of the Predictive Model

In this section, two illustrative applications are provided to demonstrate the ability of this ML model to generate synthesized earthquake-tsunami fragility surfaces from two independent 2D fragility curves for earthquake and tsunami hazards. Following this, the proposed methodology for developing multi-hazard fragility surfaces is applied in a community-level mitigation analysis which would, in theory, later extend to a community resilience (e.g. IN-CORE) for a coastal community facing both hazards. This analysis involves creating retrofitted fragility surfaces synthesized for various archetypes representing buildings within a community-level analysis.

6.5.1 Synthesized Fragility Surfaces

The new ML model is applied to two independent 2D fragility curves for each individual hazard to generate a synthesized earthquake-tsunami fragility surface. It should be noted that these fragility curves are single-variable functions for each hazard, earthquake and tsunami. The fragility curves, used as input functions for the ML model representing the *g* function discussed in Section

2, should be appropriately discretized to create a sufficient number of discrete points required for the boundaries of the targeted fragility surface. In this way, sufficient points for the independent variables, including x, y, $f(x)$, and $f(y)$, are generated as the input dataset for the ML model to predict the target variable, the $f(x, y)$ function. By increasing the level of discretization for each fragility curve, the quality and accuracy of the final synthesized spatially distributed failure probability points for the target variable $f(x, y)$ would also improve. However, to maintain computational efficiency, the 2D fragility curves are discretized into 100 points each. With this level of discretization for each single-variable fragility curve, it takes the algorithm only 8 seconds to produce the spatially distributed values of the $f(x, y)$ function.

As the first example, the proposed ML model is applied to two related 2D fragility curves from past studies at complete damage state (DS3). Both curves pertain to the same structural system, a 3-story steel frame modeled using a high-resolution FE modeling procedure. However, the earthquake and tsunami fragility curves were generated through different simulation procedures in separate studies. As shown in Figure 6-8, the earthquake fragility curve from Attary et al. (2021) was first discretized in Figure 6-8(a), followed by the tsunami fragility curve from Attary et al. (2017) in Figure 6-8(b). Both serve as input functions for the ML model. These two 2D fragility curves were input into the developed ML model to generate the synthesized spatially distributed failure probability points, which are the primary outcome of the ML-based g function representing $f(x, y)$. The surface-fitting optimization technique suggested by Harati and van de Lindt (2024b), presented in Chapter 3, and mentioned in Section 2 was then employed to the points shown in Figure 6-8(c) to obtain the smooth synthesized fragility surface seen in Figure 6-8(d). The parameters required to reproduce this 3D fragility function can be readily obtained from the proposed algorithm, including E=1.02, $C1$=0.96, $C2$= 544.83, α=0.57, and n=7.84, from which this fragility surface can be used for this archetype in a community-level damage (and subsequent resilience analysis).

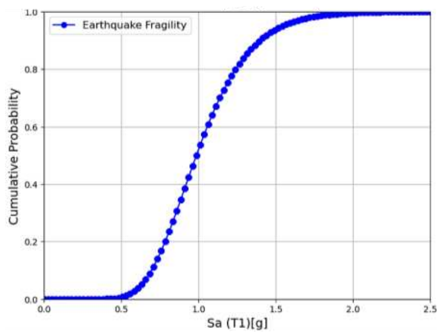

a) Discretized earthquake fragility

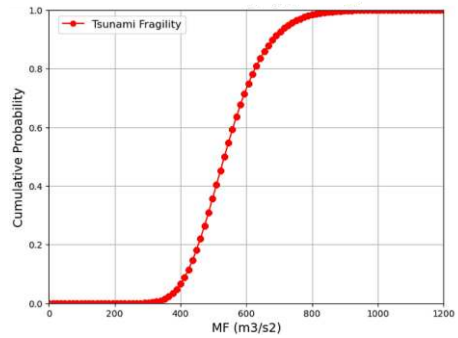

b) Discretized tsunami fragility

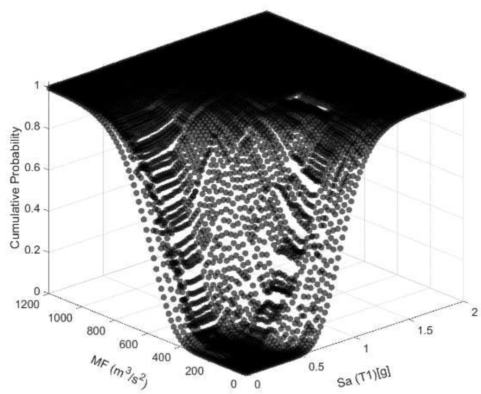

c) Discrete points of surface

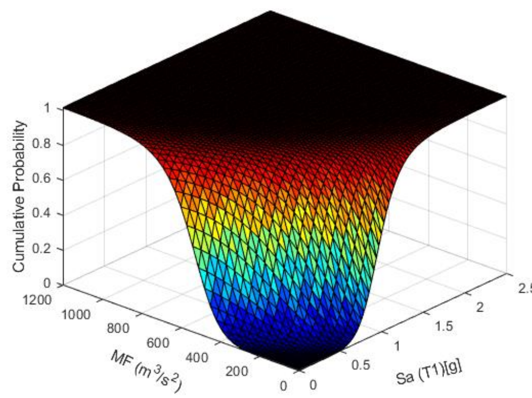

d) Fitted fragility surface

Figure 6-8. Synthesized earthquake-tsunami fragility surface computed based on 2D fragility curves of other studies: a) 2D fragility curve for earthquake from Attary et al. (2021); b) 2D fragility curve for tsunami from Attary et al., (2017); c) failure probability points computed from ML-assisted algorithm, and d) synthesized earthquake-tsunami fragility surface.

It is worth noting that the earthquake-tsunami fragility surface generated has two fragility curves at its boundaries that are consistent with the input functions used for the ML model. The earthquake-tsunami fragility surface for this structural system was generated without any information related to the FE model or two-phase simulations suggested by Harati and van de Lindt (2024a) in Chapter 2, nor any of the methods used in the studies discussed for deriving the

2D fragilities. More significantly, the ML model was trained and developed based on data from RC buildings, while the current structure is steel. Therefore, it appears that the developed ML model is not sensitive to the type of structural system for which its systemized fragility surface is of interest.

For the next example, one 2D fragility curve for tsunami hazard and two earthquake fragility curves for earthquake hazard, all for the same structural system—a 4-story RC ductile frame from Harati and van de Lindt (2024c) of Chapter 3—will be used to generate the synthesized fragility surface. These fragility curves have been extracted from the boundaries of simulated fragility surfaces obtained for two different earthquake sets: regular- (Harati and van de Lindt (2024a)) of Chapter 3 and long-duration (Harati and van de Lindt (2024c)) earthquakes of Chapter 4. As shown in Figure 6-9(a), there are two earthquake fragility curves at the DS3 damage level for the structure under regular- and long-duration earthquakes. As expected, both studies reported the same tsunami fragility curve shown in Figure 6-9(b). This example aims to use the tsunami fragility curve and the earthquake fragility curve for long-duration earthquakes as input functions for the new ML model to generate the synthesized fragility surface for long-duration earthquakes at DS3. The resulting surface will be compared with an equivalent one generated using the two-phase physics-based simulation reported by Harati and van de Lindt (2024c) in Chapter 4. Although the ML model was trained and developed based on data from physics-based fragility surfaces for RC structures under regular-duration earthquakes, comparing Figure 6-9(c) and (d) demonstrates that the methodology is successful in generating earthquake-tsunami fragility surfaces for long-duration earthquakes. Interestingly, using this ML-based fragility generator allows for altering or changing one or both 2D fragility functions for either earthquake or tsunami and then generating a new synthesized fragility surface. In this way, the procedure for earthquake-tsunami fragility generation has been decoupled into a new path where, instead of using the suggested two-phase simulation procedure by Harati and van de Lindt (2024) presented in Chapter 2 of this dissertation, the 2D fragility functions for earthquake and tsunami can be generated separately and then used as input functions for the ML-based fragility generator for the synthesized fragility surface, acting as a superposition procedure for these 2D fragility functions.

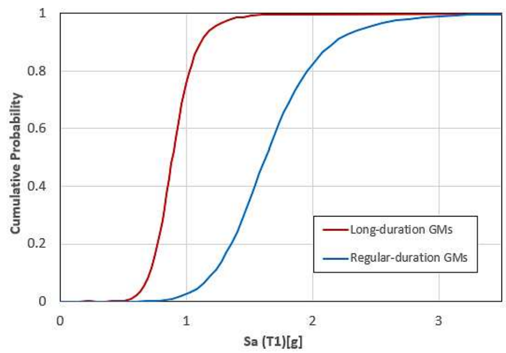

a) Earthquake fragilities

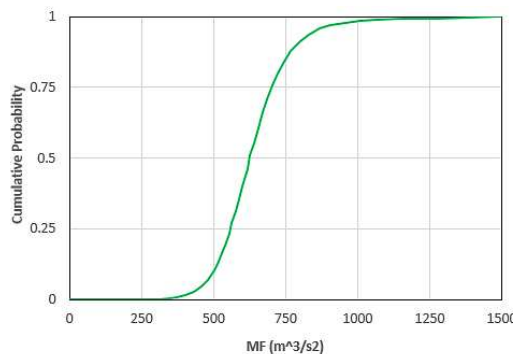

b) Tsunami fragility

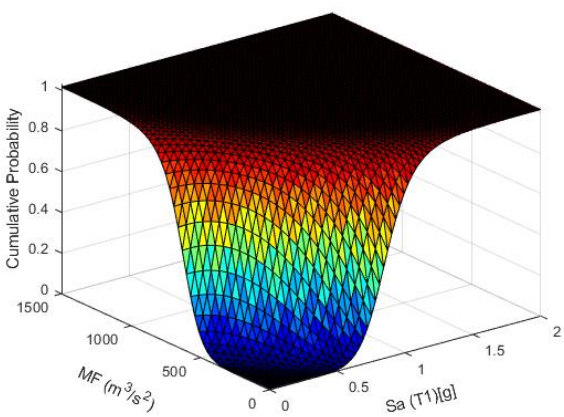

c) ML-assisted fragility surface

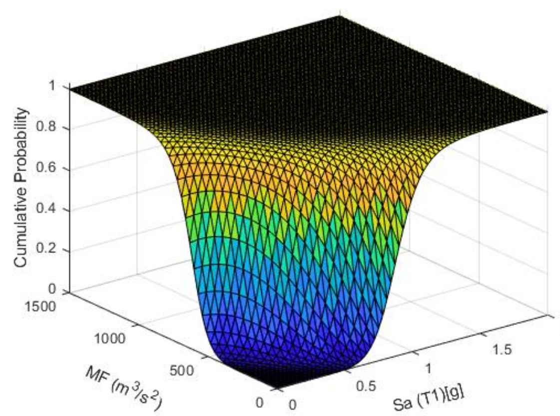

d) Physics-based fragility surface

Figure 6-9. Simulated earthquake-tsunami fragility surface versus synthesized fragility surface computed based on two simulated 2D fragility curves: a) earthquake fragility curves; b) tsunami fragility curve; c) synthesized earthquake-tsunami fragility surface, and d) simulated earthquake-tsunami fragility surface.

Following the examples provided here, it can be understood that the methodology developed in this study can take two randomly selected 2D fragility curves for earthquake and tsunami hazards and generate a synthesized multi-hazard fragility surface. The ML model appears to be sensitive only to the values of the functions *f(x)* and *f(y)*, as indicated by the FIE sensitivity analysis in Section 4. Consequently, it is not sensitive to the type of structural systems, the type of applied ground motions, or the method used to generate 2D fragility curves. Therefore, it appears that even empirical fragility functions or curves can be readily shaped into a synthesized earthquake-tsunami fragility surface.

6.5.2 Fragility-oriented Structural Retrofitting

As mentioned in the introduction section of this chapter, fragility-oriented structural retrofitting or mitigation analysis can be performed using the horizontal shifting of single-variable or 2D fragility curves, as shown in Figure 6-10. In Figure 6-10, non-retrofitted single-variable or single-hazard fragility curves can be shifted to the right to form a retrofitted fragility curve. The extent of this shifting typically depends on the type of retrofitting approach being employed for a specific structural system, which can be determined using an FE modeling procedure or extracted from existing guidelines (e.g., HAZUS *(2020)* and FEMA *(2022)*). This is intended to demonstrate how the ML approach herein can be used with retrofitted earthquake and tsunami fragilities.

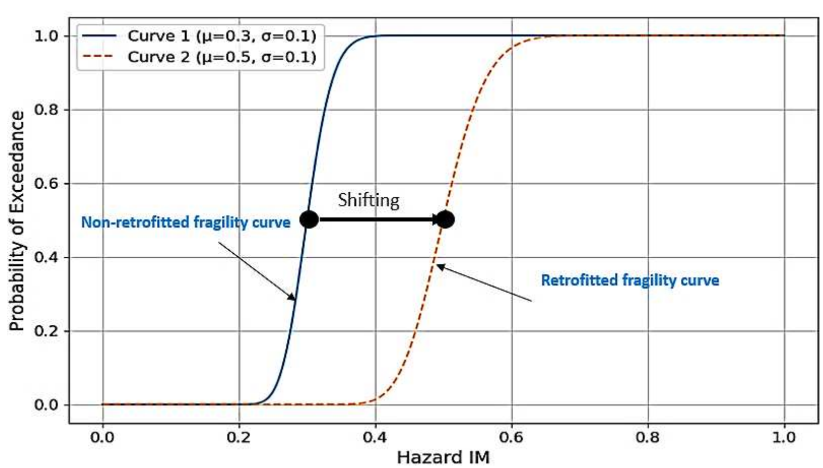

Figure 6-10. Shifting fragility curves horizontally for fragility-oriented structural retrofitting.

Although the fragility-oriented structural retrofitting approach is an established methodology in the literature for community risk and resilience analysis frameworks using single-variable fragility curves, the earthquake-tsunami fragility surfaces introduced by Harati and van de Lindt (2024) in Chapter 2 seem to be rigid and not horizontally shiftable since their five controlling parameters do not originally depend on the individual 2D fragility curves at the boundaries of these surfaces. In this case, the ML-based approach (*g* function) developed in this study will be used to decouple the earthquake-tsunami fragility surfaces into two independent 2D fragility curves for the horizontal shifting of each. After horizontally shifting of each fragility curve (for earthquake or tsunami or both hazards), the retrofitted earthquake-tsunami fragility surfaces at different damage states have been regenerated using the ML-based function introduced in this chapter.

The essential parameters that govern the behavior of retrofitting earthquake-tsunami fragility surfaces for various structural archetypes are thoroughly detailed across multiple tables. Table 6-1 outlines critical parameters—*E*, *C1*, *C2*, α, and *n*—specifically for long-duration earthquakes, crucial for reproducing fragility surfaces of ductile RC frame archetypes in community-level modeling. Table 6-2 expands on this by detailing near-continuous surfaces for non-ductile RC frames. Additionally, Table 6-3 presents the surface parameters necessary to define fragility surfaces for woodframe archetypes, ensuring comprehensive coverage of key structural variations.

Table 6-1. Equation parameters of the retrofitting earthquake-tsunami fragility surfaces for the ductile RC structures subjected to long-duration earthquakes for different damage states.

Structure ID	Parameters	DS1	DS2	DS3
RC1	*C1*	1.638	2.177	2.72
	C2	566.4	686.2	1057
	α	2.294e-14	2.231e-14	2.246e-14
	n	6.415	5.429	6.06
RC2	*C1*	0.9439	1.417	2.172
	C2	1227	1363	1481
	α	2.228e-14	2.337e-14	2.257e-14
	n	7.25	6.123	5.442
RC3	*C1*	0.5005	0.7909	1.428
	C2	1280	1603	1971
	α	2.337e-14	2.332e-14	2.337e-14
	n	6.65	6.858	6.062
RC4	*C1*	0.2859	0.5545	1.071
	C2	1066	1210	1430
	α	2.337e-14	2.332e-14	4.237e-14
	n	7.31	4.713	4.005
RC5	*C1*	0.2313	0.43	0.7166
	C2	1486	1640	1721
	α	2.337e-14	2.249e-14	0.1607
	n	7.521	4.343	3.063
RC6	*C1*	0.1571	0.2518	0.4719
	C2	1896	1880	2446
	α	2.254e-14	0.6078	0.3298
	n	4.243	2.193	2.349

Table 6-2. Equation parameters of the retrofitting earthquake-tsunami fragility surfaces for the non-ductile RC structures subjected to long-duration earthquakes at different damage states.

Structure ID	Parameters	DS1	DS2	DS3
RC7	*C1*	0.1679	0.3254	0.5456
	C2	1174	2063	2889
	α	2.337e-14	2.248e-14	2.227e-14
	n	4.997	4.905	3.896
RC8	*C1*	0.22	0.3604	0.5155
	C2	1151	1912	2645
	α	2.337e-14	2.323e-14	2.231e-14
	n	7.792	4.956	5.653
RC9	*C1*	0.3399	0.5048	0.6198
	C2	1658	2121	2867
	α	2.332e-14	2.337e-14	2.337e-14
	n	8.13	5.62	6.033
RC10	*C1*	0.6221	1.078	1.305
	C2	1244	1641	2101
	α	2.334e-14	2.337e-14	2.306e-14
	n	7.391	6.665	5.904

Table 6-3. Equation parameters of the retrofitting earthquake-tsunami fragility surfaces for the woodframe systems subjected to long-duration earthquakes at different damage states.

Structure ID	Parameters	DS1	DS2	DS3
W11	*C1*	2.743	4.177	4.553
	C2	126	246.7	315.2
	α	2.252e-14	2.31e-14	2.337e-14
	n	7.738	7.165	5.975
W12	*C1*	2.462	4.118	4.466
	C2	106.8	213	287
	α	2.337e-14	2.334e-14	2.333e-14
	n	7.743	6.824	5.827
W13	*C1*	2.111	3.541	4.53
	C2	99.79	163.6	262.1
	α	2.227e-14	2.337e-14	2.227e-14
	n	7.795	8.126	6.124
W21	*C1*	2.116	2.757	2.926
	C2	181.6	277.8	365.5
	α	2.227e-14	2.283e-14	2.337e-14
	n	8.096	6.02	5.417
W22	*C1*	1.783	2.255	2.607
	C2	328.9	501.6	616.6
	α	2.224e-14	2.245e-14	2.235e-14
	n	6.408	5.905	4.976
W23	*C1*	1.876	2.439	2.784
	C2	335.8	469.3	565.2
	α	2.249e-14	2.337e-14	2.292e-14
	n	6.527	5.943	5.091

A mitigation analysis for fragility-oriented structural retrofitting using ML-assisted fragility surfaces is proposed in this study (Figure 6-11). Retrofitted fragility surfaces can be created for different retrofitting scenarios, tested within this framework, and evaluated against community performance criteria. First, hazard-related information, specifically the intensity of joint earthquake and tsunami scenarios, is imported into the analysis. Next, GIS-based data of building units are inputted, including geometric location, land price, replacement cost, year of construction, and other parameters collectively referred to as exposure data, which are accessible through community level testbeds in computational environments for resilience analysis like IN-CORE (van de Lindt et al., 2023). Vulnerability functions are also a crucial part of community resilience analysis and should be available for different archetypes in the testbed.

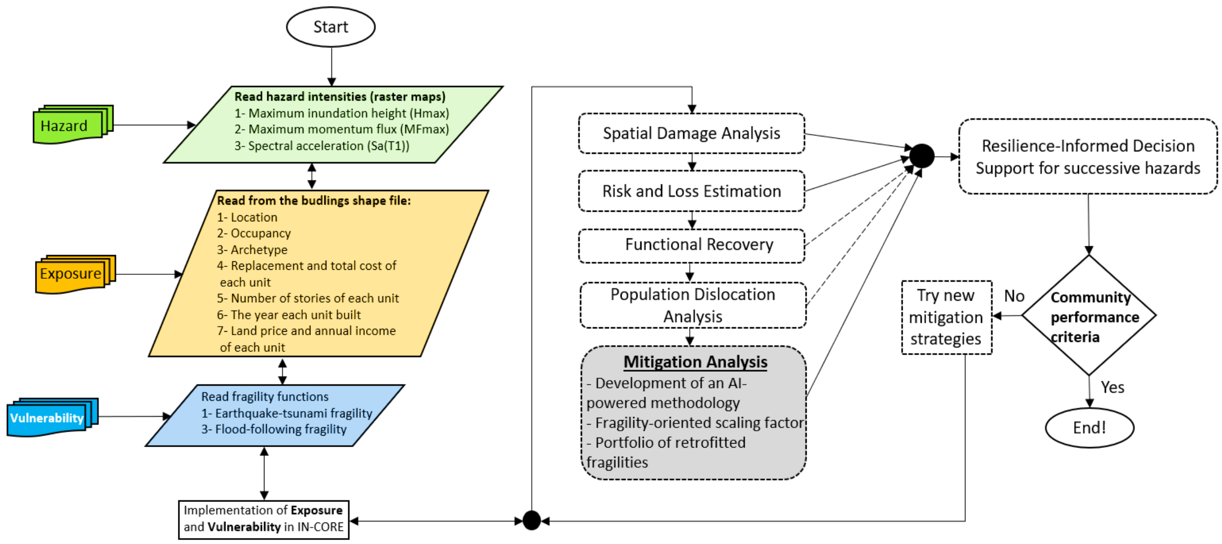

Figure 6-11. The algorithm proposed in this study to perform mitigation analysis for a community under a multi-hazard scenario of earthquake and near-field tsunami hazards.

The Pseudo Seaside testbed (Harati and van de Lindt, 2024a) will be used as an illustrative example for this proposed mitigation analysis (see Chapter 5 for more information). Figure 6-12 displays the variety of building types within the testbed, categorizing them into two primary structural categories: RC buildings and woodframe structures, with the latter being more prevalent. The testbed features two types of light woodframe constructions: W1 for residential purposes and W2 for industrial use. Additionally, Figure 6-12(a) distinguishes RC buildings by their design, differentiating between ductile and non-ductile constructions. Figure 6-12(b) comprehensively details all building archetypes in the testbed, ranging from various light woodframe designs (W11-W23) to RC structures, explicitly separating ductile (RC1 to RC6) from non-ductile designs (RC7 to RC10).

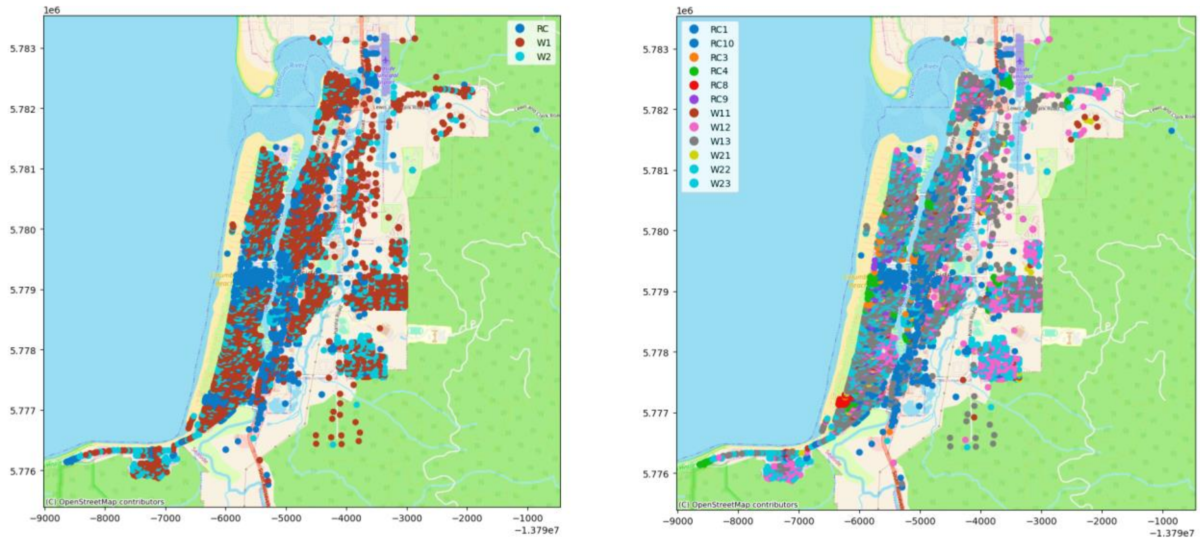

a) Main categories of the buildings

b) Building archetypes in detail

Figure 6-12. Distribution of the archetype buildings in the Pseudo Seaside testbed: a) the main categories of the buildings; and b) building archetypes in detail.

For the woodframe buildings, the first digit (e.g., W12) indicates the occupancy type, while the second digit signifies the level of ductility, ranging from low ductility or design level (1) to the highest design level (3). This classification underscores the diverse structural systems explored in the Pseudo Seaside testbed. The simulated earthquake-tsunami fragility surfaces, along with the 2D fragility curves for non-retrofitted vulnerability models under a scenario of a long-duration earthquake followed by a near-field tsunami, are sourced from Harati and van de Lindt (2024c) and Harati and van de Lindt (2024a) for RC frames and woodframe buildings, respectively (see Chapter 3 and 4 for more information). For modeling the joint hazard values on the community level, a hazard model recommended by Park et al. (2017) for the town of Seaside is employed in the mitigation analysis. It is noted that the hazard simulation utilized in this section is based on a mean recurrence interval (MRI) of 1000 years.

The retrofitted versions of the adopted multi-hazard vulnerability models in this mitigation analysis were developed by extracting 2D single-variable fragility curves from the boundaries of non-retrofitted earthquake-tsunami fragility surfaces and shifting them horizontally for each hazard separately. The scale factor for the horizontal shift of both hazards was calculated to elevate the design level of a specific non-retrofitted model to the highest possible level, in this case, high design level (3). To achieve this, the median value of the empirical fragility curves reported in relevant guidelines (e.g., HAZUS *(2020)* for earthquake and FEMA *(2022*) for tsunami hazard) was divided by the median value of the empirical fragility curves for the same design level as identified in a specific non-retrofitted fragility model. For example, the design level of a non-ductile RC frame in this study was labeled as low design. Therefore, to compute the scale factor, the median value of a fragility curve for a specific damage state at the highest design level was divided by that at the low design level, as outlined in the aforementioned guidelines. As previously demonstrated, the retrofitted 2D fragility curves can then serve as input functions for the new ML model to generate synthesized retrofitted fragility surfaces. The scale factors for the horizontal shifting of the 2D fragility curves for all the archetypes in this study have been reported in Harati (2024). The final parameters for reproducing the retrofitted earthquake-tsunami fragility surfaces have been provided earlier in this section.

For the mitigation analysis, only woodframe buildings have been structurally retrofitted as an assumed retrofitting plan for the entire Pseudo Seaside community. Information regarding the retrofitted earthquake-tsunami fragility surfaces for this building type is shown in Table 6-3 in Appendix A and used in the proposed mitigation algorithm shown in Figure 6-11. Figure 6-13 presents the results of the community level damage analysis with non-retrofitted and retrofitted fragility surfaces. As shown in Figure 6-13, spatial damage analysis reveals that this mitigation or structural retrofitting plan reduced damage levels from complete (DS3) and heavy (DS2) to moderate (DS1) and insignificant (DS0) in many woodframe buildings across the testbed.

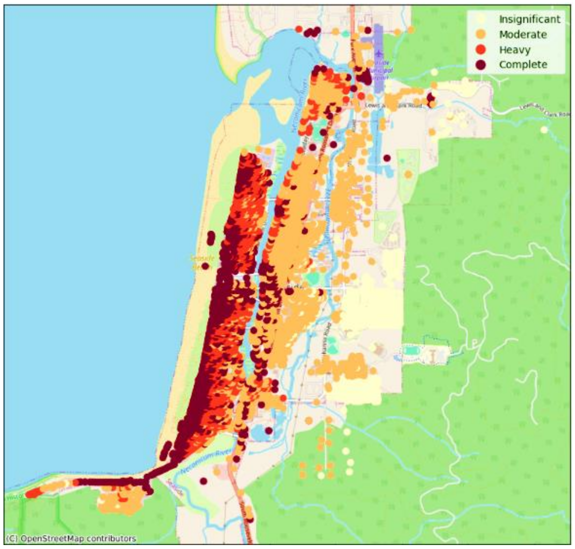

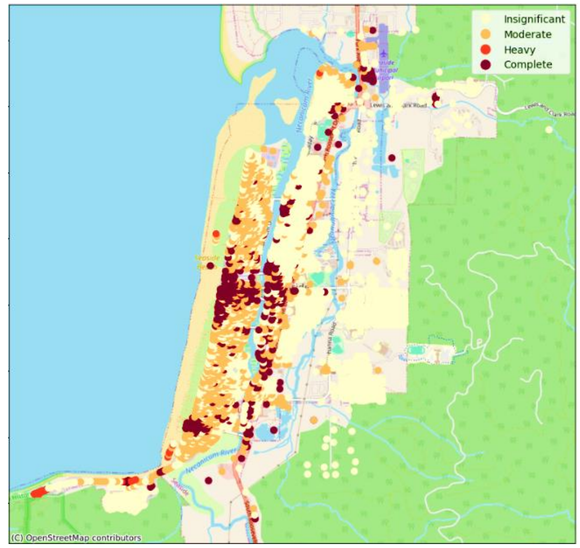

a) Non-retrofitted archetypes

b) Retrofitted archetypes

Figure 6-13. Damage state patterns of Pseudo Seaside under a multi-hazard scenario of earthquake and near-field tsunami hazards at an intensity level of a 1000-year MRI using two different fragility suites: a) based on non-retrofitted archetypes; and b) from retrofitted archetypes.

Figure 6-14 also displays the total number of buildings in each damage state for two different scenarios: with and without the retrofitting plan. As seen in Figure 6-14, damage states DS1 and DS3 have been most impacted, indicating that in more than 1,000 building units, the risk of collapse has been severely mitigated under this mitigation plan and for this hazard scenario.

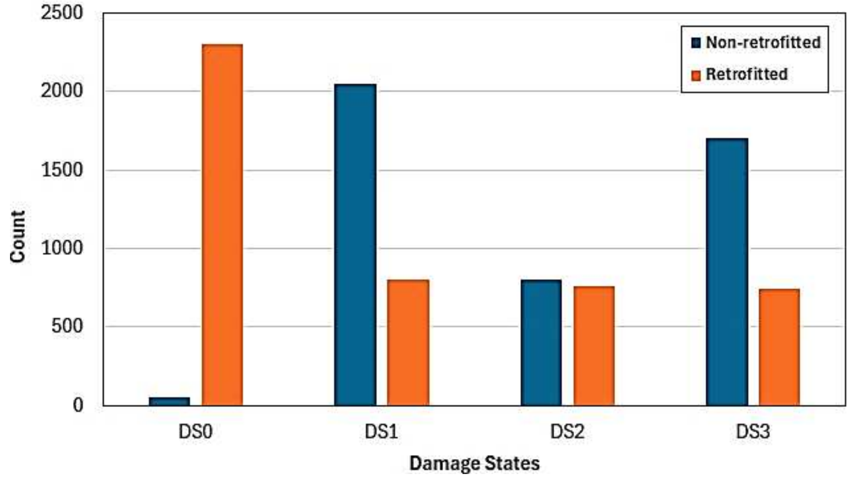

Figure 6-14. Damage state patterns of Pseudo Seaside under a multi-hazard scenario of earthquake and near-field tsunami at an intensity level of a 1000-year MRI using two different fragility suites: a) based on non-retrofitted archetypes; b) after using the retrofitted archetypes.

The research presented in this chapter demonstrated that the new ML model can reliably generate a synthesized earthquake-tsunami fragility surface based on two randomly selected 2D fragility curves for earthquake and tsunami separately. However, caution should be exercised when using this ML-based fragility generator, as it has been developed based on a specific dataset. The training data for this model is derived from simulated fragility surfaces of RC frames subjected to far-field regular-duration earthquakes. Although results for other structural systems under different types of earthquakes may vary, the model's performance is still anticipated to be reliable.

CHAPTER 7: MAINSHOCK-AFTERSHOCK BUILDING FRAGILITY METHODOLOGY AND ITS APPLICATION IN COMMUNITY RESILIENCE MODELING[6]

7.1 Introduction

The concept of seismic resilience has become increasingly prominent in the field of earthquake engineering, emphasizing the important role of buildings in community resilience and urban planning. Resilient buildings are a necessary (but not sufficient) condition for community resilience. The recent earthquakes in Turkey and Syria in February 2023, which were followed by thousands of aftershocks, including more than 30,000 in the three months post-mainshock, further underline the importance of this aspect. These events mirror the significant human and financial toll observed in earlier seismic sequences such as Chi-Chi (1999), Tohoku (2011), and central Italy (2016) among many others. The Turkey-Syria earthquakes, as reported by Dal Zilio and Ampuero (2023), exemplify the ongoing challenges in managing and mitigating the aftermath of complex mainshock-aftershock sequences (e.g., Kazama and Noda, 2012; Wang et al. 2022).

Resilience is defined in Presidential Policy Directive 21 (*PPD*, 2014) as the ability to prepare for, withstand, and rapidly recover from adverse events. This concept involves anticipating potential challenges, mitigating their impacts, and efficiently recovering from any resultant setbacks (Wang et al., 2021). Community resilience frameworks regularly incorporate fragility functions as a foundational step to estimate the initial damage a target community might incur following a single or compound hazard scenarios, such as source earthquakes and their subsequent impacts (Bruneau et al., 2003; Harati and van de Lindt, 2024a). These fragility

[6]This chapter is based on the paper: Harati, M., and van de Lindt, J.W. (2024). "Mainshock-Aftershock Building Fragility Methodology for Community Resilience Modeling." Structures, (Under Review).

functions, tailored to the specific structural typologies present in a community, utilize the output from hazard analyses for selected scenario events to assess initial damage. This initial risk-based damage assessment is crucial for scientists and engineers to evaluate a community post-event or, more generally, when performing “what if scenarios” to examine the effect of a potential policy at the community level during planning (Wang et al., 2021; Wang and van de Lindt, 2021). Furthermore, it aids in mapping the recovery trajectory of complex socioeconomic institutions within that community (Watson et al., 2020). Seismic resilience, therefore, is not just about the immediate structural integrity of buildings and infrastructure but also encompasses the broader ability of a community to anticipate, withstand, and bounce back from the compounded effects of seismic events (Hu et al., 2023; Kourehpaz et al., 2023; Bruneau et al, 2003).

FEMA P-2012 (2018) emphasizes the significance of advancements in nonlinear structural response simulations, notably Nonlinear Time History Analysis (NTHA), for creating earthquake fragility functions that accurately characterize structural performance. NTHA is crucial for assessing dynamic structural behavior under seismic forces, taking into account nonlinear material properties and structural dynamics vital for understanding the complex effects of seismic loading. Incremental Dynamic Analysis (IDA) and Multiple Strip Analysis (MSA) enhance these evaluations by testing structures under increasing seismic loads and estimating fragility across various intensity measures (IMs), respectively (Pang and Wang, 2021). MSA, combined with site-specific ground motion (GM) selection and Monte Carlo simulations, significantly improves the predictive accuracy of mainshock-aftershock fragility curves, despite high computational demands (Harati and van de Lindt, 2024a; Jalayer and Cornell, 2009). This approach offers substantial benefits for seismic engineering, allowing for a detailed assessment and prediction of structural fragility following mainshock and aftershock sequences.

In earthquake engineering research, the selection of GMs for mainshock-aftershock (MS-AS) sequences is guided by four principal methods, each tailored to specific seismic analysis needs. The mainshock-mainshock (MS-MS) approach (e.g., Hatzigeorgiou and Beskos 2009; Raghunandan et al. 2015) selects both sequence events from recorded mainshocks. In this method, the second GM may be a scaled or unscaled version of the first, or an entirely different mainshock motion, although it doesn't replicate the distinct characteristics of aftershocks. For a closer representation of aftershock scenarios, the targeted mainshock-mainshock (TG-MS-MS) method (e.g., Goda 2012; Hatzigeorgiou and Beskos 2009) chooses the second GM from a mainshock event, but with attributes more typical of aftershocks, such as lower magnitude and larger rupture distance. The same-sequence mainshock-aftershock (SS-MS-AS) approach (e.g., Ruiz-García and Negrete-Manriquez 2011; Wen et al. 2017) uses both events' records from the same earthquake sequence, effectively capturing the natural correlation between mainshocks and aftershocks. Conversely, the different-sequence mainshock-aftershock (DS-MS-AS) method, similar to SS-MS-AS in intent, selects records from different earthquake sequences, expanding the dataset but potentially missing specific correlations found in single-sequence events (Boore et al., 2014). These methodologies collectively underline the complexity and intricacies involved in accurately modeling earthquake sequences and their impact on structures, thereby emphasizing the need for nuanced approaches in seismic analysis to predict and understand structural behavior under sequential seismic events. The SS-MS-AS methodology is meticulously employed in this study for selecting mainshock-aftershock sequences, with a focused effort on identifying and choosing only one significant aftershock subsequent to the mainshock.

In this study, a comprehensive approach is adopted to generate fragility functions for mainshocks and mainshock-aftershock sequences, leveraging a two-phase multi-distributed framework as recommended by Harati and van de Lindt (2024a) presented in Chapter 2. Central to this mainshock-aftershock extension of the mentioned approach is the utilization of the MSA method along with the MCS procedure, effectively integrated into a parallel processing framework. This integration not only incorporates uncertainty propagation on the structural modeling and seismic input layers simultaneously but also aligns with the complex requirements of seismic resilience assessment of structures with high-resolution Finite Element (FE) modeling.

Furthermore, the study employs a portfolio of buildings to develop robust and detailed fragility models. This portfolio approach allows for a diverse and representative range of building typologies (often referred to as archetypes) and structural characteristics, which are crucial for accurate and comprehensive seismic risk assessments. The fragility models generated from this varied building portfolio are then utilized to conduct a community-level vulnerability analysis which can eventually propagate to a full resilience analysis.

7.2 Problem Statement and Research Methodology

The analysis is conducted in two distinct phases. In the first phase, the impact of the mainshock on the structural system is evaluated. Here, the state of the system post-mainshock, denoted as X, is determined through the function $X=f\ (M,\ S,\ \Theta)$. This function incorporates the characteristics of the mainshock record M, the intrinsic properties of the structure S, and a set of probabilistic parameters Θ. These parameters represent the uncertainties in structural behavior, including aspects such as dead load, damping ratio, and element strength, among other aspects that are discussed subsequently. This phase captures the initial damage and the changes in structural properties due to the mainshock, forming a critical foundation for the subsequent phase of the analysis. The second phase focuses on the aftershock's effects on the already damaged structure. The final state of the structure post-aftershock, represented as *Y*, is calculated using the function *Y=g (X, A, Φ).* In this expression, *X* is the damaged state from the mainshock, *A* describes the aftershock GM, and *Φ* includes aftershock-specific probabilistic parameters. These parameters account for the altered dynamic characteristics of the structure after the mainshock, such as changes in element hardening stiffness and post-capping stiffness.

At the core of the proposed methodology is the fragility function *F(d)*, which is derived through the integration over the distributions of mainshock and aftershock. This function effectively quantifies the probability of the structural system reaching or exceeding a particular damage state *d*. The integral in Eq (7-1) encompasses the conditional probability of surpassing various damage thresholds, thereby integrating the variabilities and uncertainties inherent in seismic events and structural responses:

$$F(d) = \int_{A}^{A} \int_{M}^{A} P(\, Y \geq d \mid M, A, S, \Theta, \Phi \,)\, p(M, A)\, dMdA \qquad (7\text{-}1)$$

In the upcoming 'Structural Modeling Procedure' section, a detailed exploration of the random variables *Θ* and *Φ* will be presented. This analysis is aimed at documenting their influences on fragility assessment, emphasizing the sensitivity of structural responses to the probabilistic nature of seismic events and structural parameters. However, the task of addressing thousands of uncertainties across multiple layers, including those related to GMs for both mainshocks and aftershocks, as well as structural realizations generated randomly from various input modeling parameters, presents considerable computational challenges. To address these challenges, this study adopts a two-phase successive computation procedure, as recommended by Harati and van de Lindt (2024a) in Chapter 2, which was originally developed to generate multi-hazard fragility functions for structures under the risk of earthquakes followed by tsunamis. This study refines their initial method to exclusively focus on a two-phase analytical process, beginning with a NTHA procedure of the mainshock, followed by a second phase concentrated on aftershocks. Furthermore, the discussion will extend to include detailed materials on the development of mainshock-aftershock fragility functions, the selection criteria for seismic GMs of the mainshock and aftershock, and the methodology for estimating losses at the community level.

7.2.1 Mainshock-aftershock Fragility Functions

As can be seen in Figure 7-1, a parallel processing scheme is utilized for mainshock-aftershock fragility development. In the initial step, increasing levels of spectral acceleration (Sa) are considered as the input to the algorithm. Each Sa level in the input matrix is assigned to an individual CPU or node. Within each CPU, a Monte Carlo simulation is conducted, starting with a level of seismic IM, specifically the spectral acceleration at the first mode of vibration, Sa (T1). The next step involves selecting a GM for the mainshock. Then the process progresses to generate a set of random parameters for structural modeling, which is discussed later in this chapter. Each realization is then subjected to the two-phase successive analysis, simulating structural responses for both the mainshock and aftershock scenarios. The analysis assesses the maximum peak inter-story drift ratio (PIDR) at each story level to determine if the structure meets or fails the acceptance criteria considered for prescribed damage states based on HAZUS (2020). For more information on the drift-based damage states considered for all structural systems in this study, readers are referred to the study conducted by Harati and van de Lindt (2024b)—discussed in Chapter 3 of this dissertation comprehensively.

In cases where the structure fails, it is added to the tally of failed cases; otherwise, the analysis continues with the next GM or pair of GMs in the set (if aftershocks are considered). At the end of the Monte Carlo simulation, the failure probability for each IM level is determined considering both mainshock and aftershock sequences. It should be noted that if the aftershock analysis is not considered in the analysis, then the second phase of the simulation is omitted automatically.

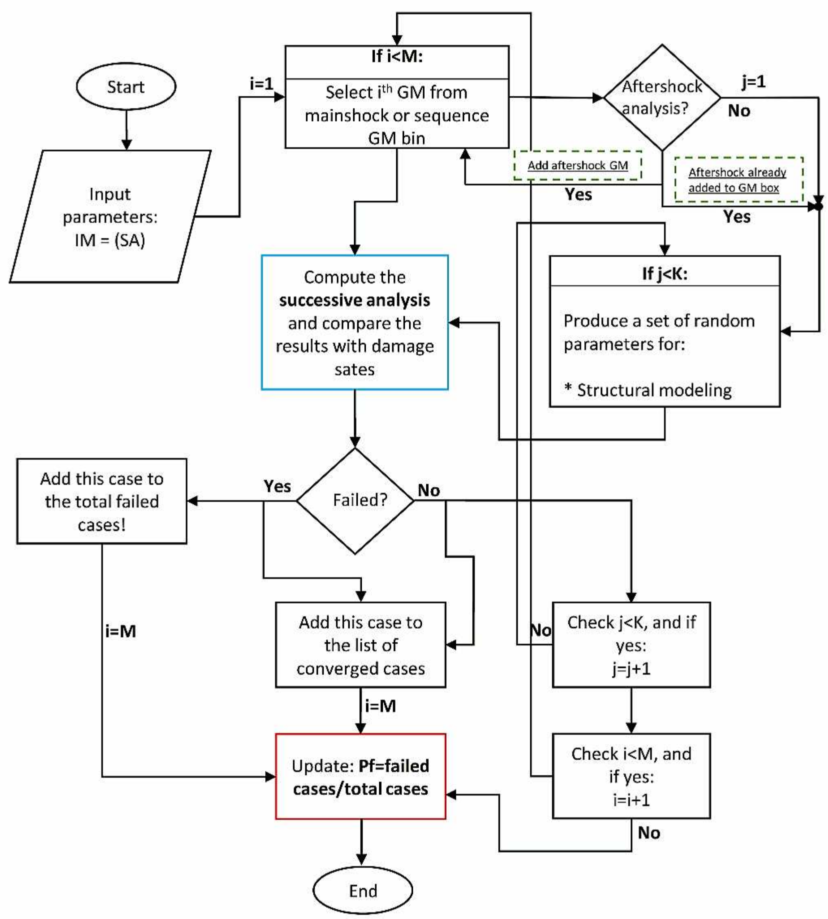

Figure 7-1. The sequential algorithm controlling the computational procedure of each discrete data point on the 2D successive fragility functions of mainshock-aftershock sequences.

The failure probabilities calculated at different levels of Sa, or within different CPU cells, are combined at the manager node to construct scattered failure probability points for the formation of the fragility curves for each damage state. Fragility curves for earthquake sequences are generated as:

$$Fr(IM) = \emptyset(\frac{\ln(IM) - \mu}{\sigma}) \quad (7\text{-}2)$$

In this equation, *IM* symbolizes the discrete data points reflecting failure probabilities for either mainshocks or mainshock-aftershock sequences under a given damage state. The terms μ and σ represent the mean and standard deviation, respectively, of the data vector *IM*.

7.2.2 Mainshock-aftershock Sequences

This study examines recorded sequences of mainshocks followed by aftershocks. Only the most significant aftershock, determined by its relative spectral amplitude, is paired with each mainshock, a method consistent with prior research (Abdollahzadeh et al., 2019; Han et al., 2014). This particular aftershock is selected based on its peak ground acceleration (PGA), to ensure it represents the most substantial seismic event following the mainshock. As shown in Figure 7-2, a 30-second pause with zero acceleration is incorporated between the seismic events to mimic a return to a static state of the structure after mainshocks. Thirty such real mainshock-aftershock sequences were derived from the PEER NGA Database (Ancheta et al., 2014). These sequences are from nine distinct earthquakes, with mainshock magnitudes ranging from M5.77 to M7.62 and aftershocks from M5.01 to M6.2 (Hu et al., 2021). Detailed data along with the RSN numbers of the records on these events is cataloged and reported by Hu et al. (2021).

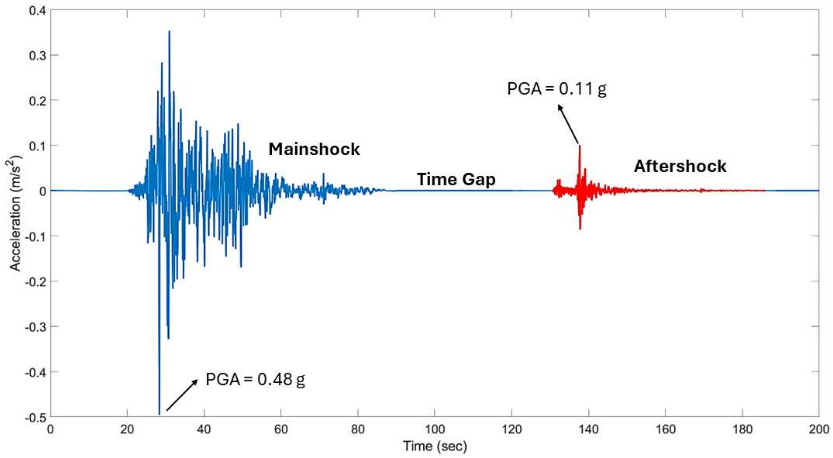

a) A mainshock-aftershock sequence with bigger PGA in the mainshock GM

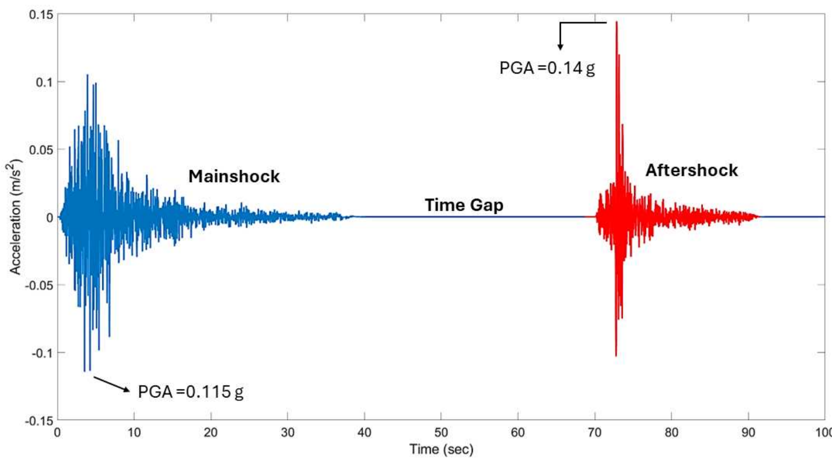

b) A mainshock-aftershock sequence with bigger PGA in the aftershock GM

Figure 7-2. Real mainshock-aftershock sequences having different types of aftershocks in terms of their PGA magnitudes: a) a sequence with smaller aftershocks; b) a sequence with bigger aftershocks.

Figures 7-3(a) and (b) showcase comparative response spectra for mainshocks and aftershocks, with aftershocks typically exhibiting reduced spectral accelerations, particularly for periods longer than 1 second. Despite mainshock PGAs generally exceeding those of aftershocks, there are exceptions in which aftershock sequences have higher PGA values, as can be seen in Figure 7-2. These anomalies, along with period-dependent variations in spectral accelerations shown in Figures 7-3(a) and (b), are indicative of the complex nature of seismic intensity contrasts between mainshocks and aftershocks. Such variations, attributable to factors like rupture mechanisms and propagation distances, are in agreement with findings by Han et al. (2014). For an in-depth examination of the earthquake records concerning these seismic events, the reader is directed to Hu et al. (2021) for further information.

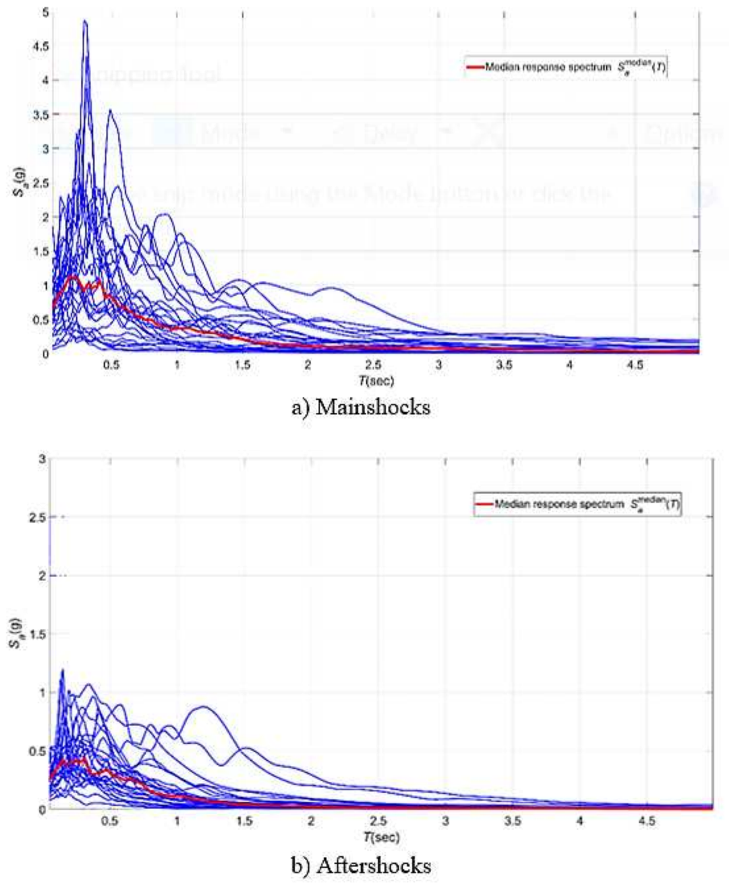

Figure 7-3. Response spectra of GM sequences: a) mainshock earthquakes; b) aftershock earthquakes

The FEMA P695 (*2009*) far-field earthquake records, frequently employed for creating fragility functions in the Western United States, were selected to facilitate a direct comparison of fragility curves obtained from the FEMA P695 set to those mainshock records derived from PEER NGA Database as previously discussed. Figure 7-4 and Figure 7-3(a) demonstrate a significant similarity between the response spectra and median response spectra of the two GM suites considered, particularly when FEMA P695 earthquakes are compared with the mainshock components of the selected mainshock-aftershock sequences in this study.

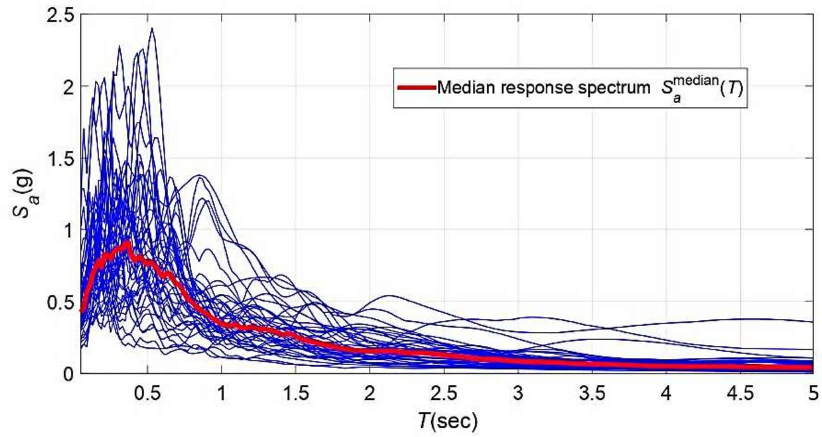

Figure 7-4. Response spectra and the median spectrum of FEMA P695 earthquake GMs.

Furthermore, Figure 7-5 displays the normalized Arias Intensity (AI) plots for the selected GM suites, which is a measure of the earthquake's energy content during the strong GM. The plots show analogous distribution patterns, especially in terms of their density and mean values, between the GMs from FEMA P695 and the mainshock GM records from Hu et al. (2021), suggesting a similarity in the seismic energy input profile and the range of strong motion duration of the two data sets.

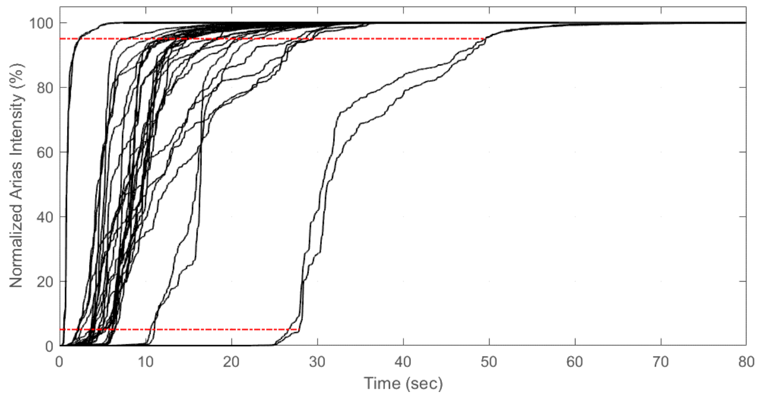

a) PEER GMs

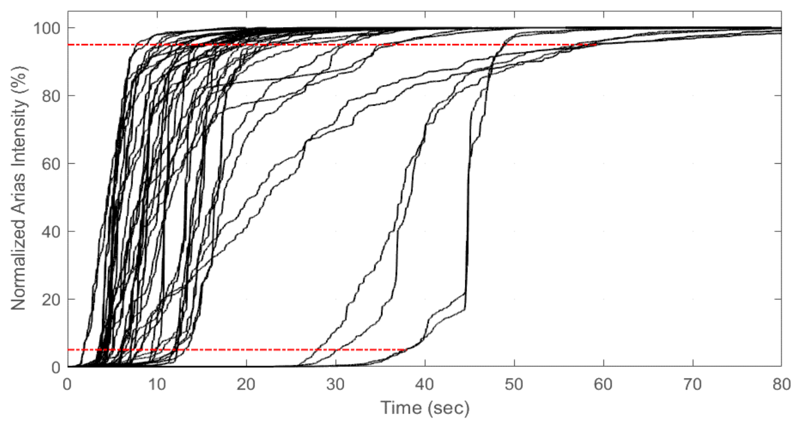

b) FEMA P695

Figure 7-5. Normalized arias intensity curves for earthquake GMs: a) selected GMs from PEER database; and b) GMs from FEMA P695.

7.2.3 Risk-based Loss Assessment

Here, the evaluation of the effects of sequential earthquakes, specifically mainshocks followed by aftershocks, for the community-level analysis are examined. By utilizing mean damage factors from HAZUS (*2020*), it quantifies structural damage across varying severity levels and analyzes hazard event frequencies to gauge their recurrence and impact. The approach prioritizes accurate structural valuation for determining costs associated with repairs or replacements, aiming for a comprehensive assessment of direct economic losses (Harati and van de Lindt, 2024d)—see more in Chapter 5.

The approach utilized herein is shown in Figure 7-6, integrating structural valuation with damage probabilities and damage factors to calculate total economic losses from mainshock-aftershock sequences, thus providing an understanding of their impact on buildings within a community.

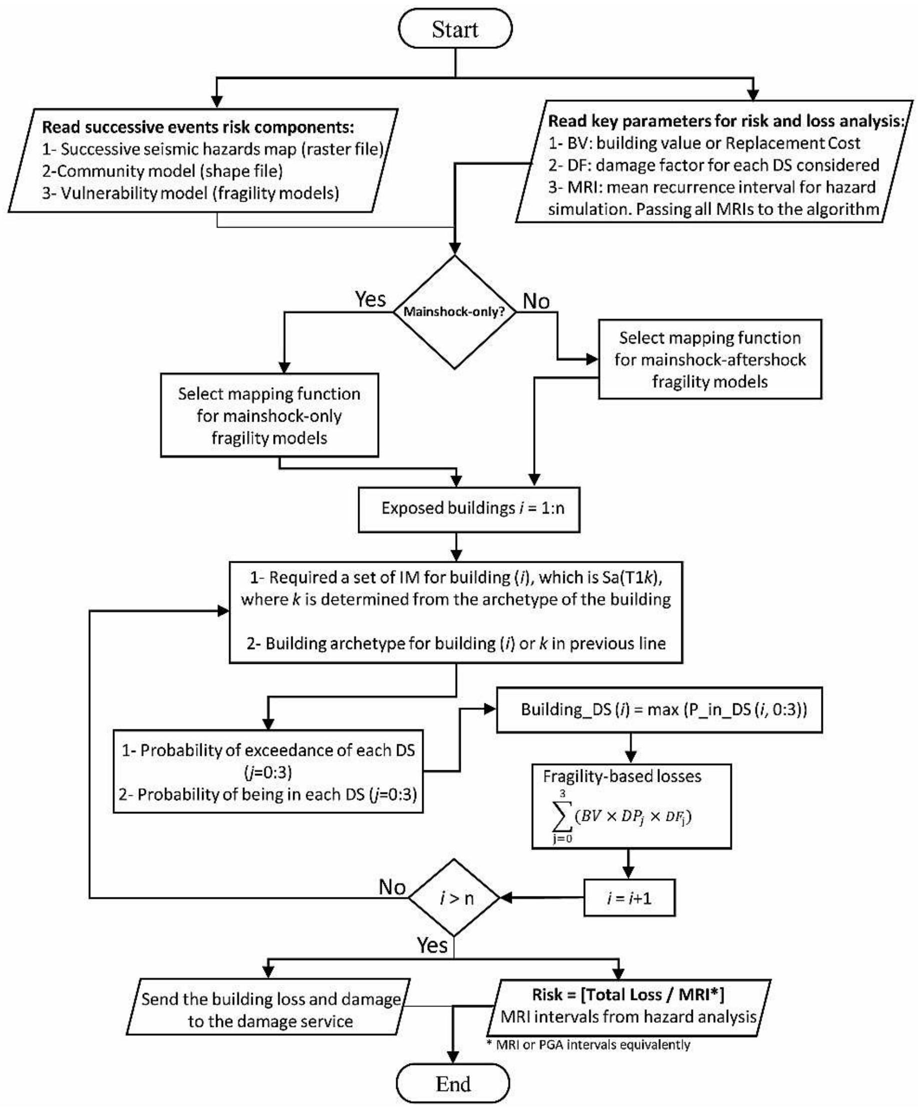

Figure 7-6. An algorithm developed for IN-CORE to process risk-based loss assessments for a target community under seismic hazards.

Then, the economic risk posed by each type of hazard event—be it mainshock, aftershock, or their combination—is computed by using a simple formula that relates total loss to the mean recurrence interval (MRI)—or PGA values equivalently—of these events. This calculation reveals variations in economic risk levels in accordance with the frequency of natural hazard occurrences. Implemented within the Interdependent Networked Community Resilience Modeling Environment (IN-CORE) system (van de Lindt et al., 2023) and its associated pyIncore package, this methodology supports the analysis of community resilience and the cumulative effects of single and multiple hazard events on structures. The IN-CORE system's comprehensive approach to modeling natural hazard impacts and assessing resilience strategies can provide insight for risk management and mitigation planning in areas vulnerable to such hazards, highlighting the importance of understanding economic impacts and risks associated with the sequential nature of natural hazards (van de Lindt et al., 2018; 2023).

7.3 Seismic Hazard Analysis

Ground-motion prediction equations (GMPEs) have become fundamental in probabilistic seismic hazard analysis (PSHA) due to their straightforward application and adaptability to various seismic scenarios. This study utilizes the GMPE developed by Abrahamson et al. (2016), based on a comprehensive dataset of subduction zone earthquakes. This GMPE methodically integrates critical parameters such as the closest distance to the rupture (Rrup), the shear wave velocity of the soil's upper 30 meters (Vs_{30}), and the median peak ground acceleration for a normalized Vs_{30} ($PGA_{1,000}$), alongside a total standard deviation (σ) that encapsulates both intra-event and inter-event variabilities. Focusing on the Cascadia Subduction Zone (CSZ), this study prioritizes intra-event variability. The GMPE also includes a refined magnitude scaling function and a site condition factor that differentiates responses based on forearc or backarc positions. These aspects, combined with the complete model coefficients from Abrahamson et al. (2016), form the foundation of the seismic hazard assessment presented herein, consistent with the approaches recommended by Park et al. (2017).

7.4 Structural Modeling Procedure

This study uses the methodology by Harati and van de Lindt (2024a), which discussed thoroughly in Chapter 3, for modeling the nonlinear behavior of RC and woodframe structures subjected to sequential natural events, utilizing OpenSeesPy for successive structural analysis. The RC frames include both ductile and non-ductile Moment Resisting Frames (MRFs), representing old and modern buildings in seismic regions, and are modeled using 2D finite element models with the Joint2D Element to simulate joint behavior and the IMK deterioration model for plastic hinges. Uncertainty in the models is addressed by considering various random variables, as discussed in Chapter 2 and Chapter 3. The woodframe systems, primarily constructed using Wood Structural Panels (WSPs), are modeled with the CUREe 10-parameter hysteresis model to simulate their response, focusing on unperforated WSPs to simplify the analysis. The study differentiates woodframe structures by nailing patterns and categorizes them by design levels, using PIDR as the engineering demand parameter (EDP) for evaluating damage states. For more detailed information, readers are referred to Chapter 3 of this dissertation.

7.5 Illustrative Example

The methodology presented in this chapter is illustrated using the Pseudo Seaside testbed at a community-level analysis, namely, to illustrate how the application of the developed mainshock-aftershock fragility functions impacts a community. The Pseudo Seaside testbed (Harati and van de Lindt, 2024d) of Chapter 5 is a sophisticated testbed framework designed to assess the resilience of a small coastal community in a seismically active region to earthquakes and its subsequent impacts such as tsunami or aftershocks, based on prior research that identified Seaside, Oregon, as particularly vulnerable to seismic hazards (Amini et al., 2023; Cox et al., 2022; Sanderson et al., 2021).

Figure 7-7 presents the assortment of building types in the Pseudo Seaside testbed, dividing them into two main structural categories: RC buildings and light woodframe structures. Notably, light woodframe buildings outnumber their RC counterparts. The testbed incorporates two variants of light woodframe constructions: W1 for residential purposes and W2 for commercial use. Moreover, Figure 7-7(a) differentiates RC buildings based on their design, distinguishing between those that are ductile and those that are non-ductile. Figure 7-7(b) thoroughly outlines all building archetypes in the testbed, including a variety of light woodframe designs (W11-W23) and RC structures, explicitly separating ductile from non-ductile RC designs (RC1 to RC10). This classification highlights the wide range of structural systems explored in the Pseudo Seaside testbed.

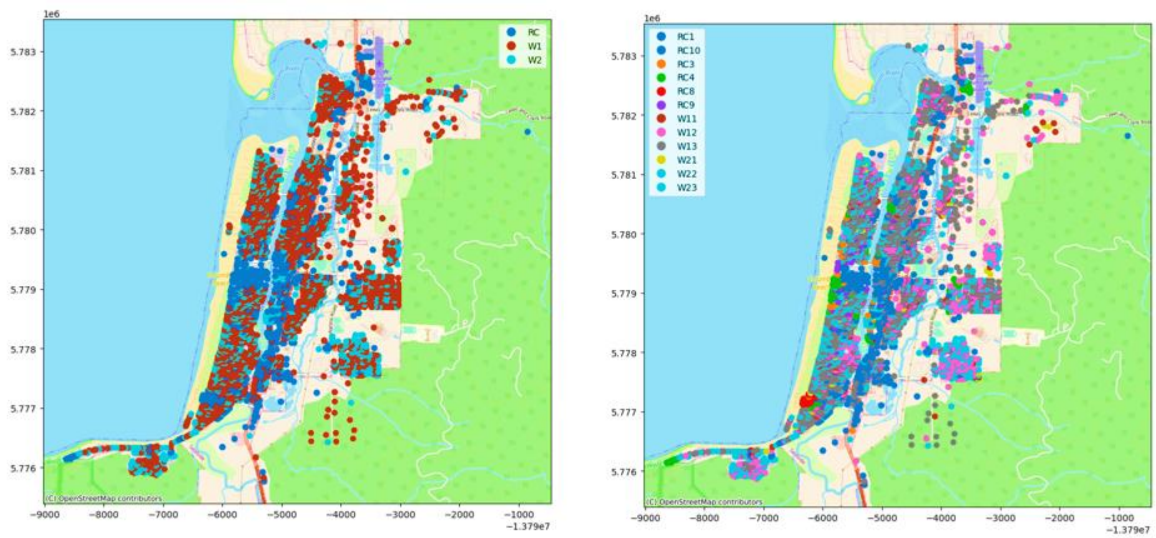

a) Main categories of the buildings

b) Building archetypes in detail

Figure 7-7. Distribution of the archetype buildings in the Pseudo Seaside testbed: a) the main categories of the buildings; and b) building archetypes in detail.

Following the categorization of building types in Pseudo Seaside testbed, the procedure for developing fragility functions for mainshock and mainshock-aftershock sequences is discussed in detail. The algorithm presented in Section 7.2.1 is utilized for this purpose, with parameters controlling the fragility functions of mainshock and mainshock-aftershock sequences reported for reproducibility and further use in community-level studies. Subsequently, the developed fragility functions are applied as input vulnerability functions for community resilience analysis using the methodology outlined in Section 7.2.3. This comprehensive approach aims to provide a robust framework for assessing and enhancing community resilience against sequential seismic events.

7.5.1 Development of Fragility Functions

Figure 7-8 illustrates the time history response of the top displacement (roof displacement) for a 4-story RC building designed as a ductile frame (RC3) across various growing earthquake intensity levels, from Sa (T1) of 0.5g to 3.5g. At lower earthquake IMs, within the elastic response range of the structure, the occurrence of a mainshock does not significantly affect the seismic response of the structural system, as anticipated. However, at higher seismic intensities, as depicted in Figure 7-8 (b) and (c), the aftershock sequence influences the building's time history response, altering its permanent displacement pattern or even leading to unlimited displacement responses, i.e. numerical (potential) collapse. Conversely, when the earthquake IM is sufficiently large to induce collapse during the mainshock, the subsequent aftershock sequence becomes negligible, as the structural system is already compromised beyond recovery (both analytically and realistically).

It is worth noting that the time gap between the mainshock and aftershock GMs causes a damped free vibration, numerically converging to a stable permanent displacement, as shown in Fig. 11(a), which has been reported by other studies as well (e.g., Shi et al. 2020). In addition, the time history responses in these figures have been derived from a structural model based on median values to simplify the uncertainty representation in the simulations. However, uncertainty propagation modeling has been thoroughly implemented in developing the fragility functions (reported later).

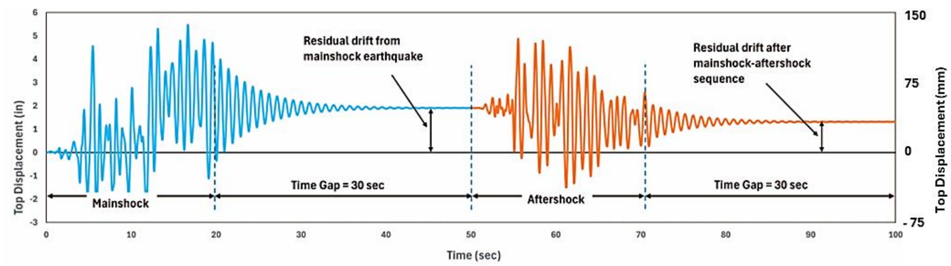

a) Sa (T1) = 0.5g

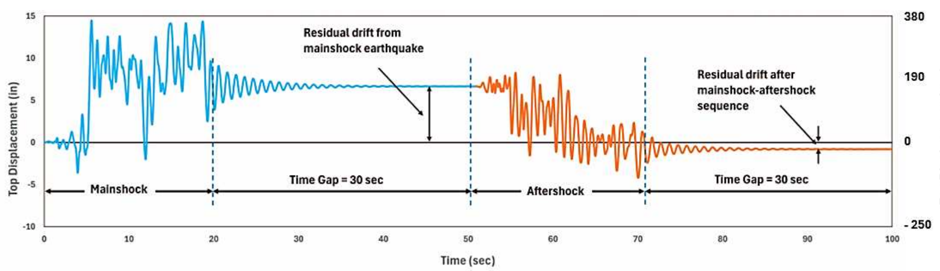

b) Sa (T1) = 1.5g

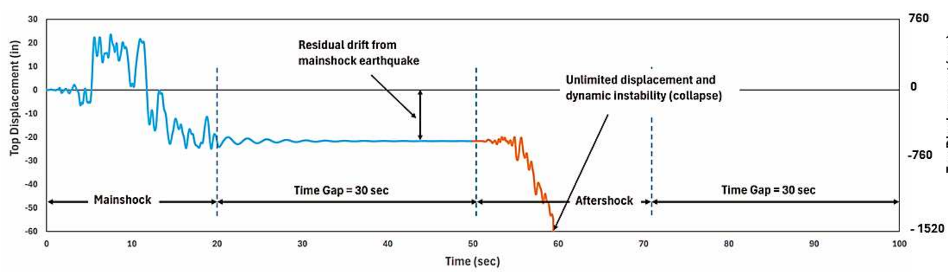

c) Sa (T1) = 2.5g

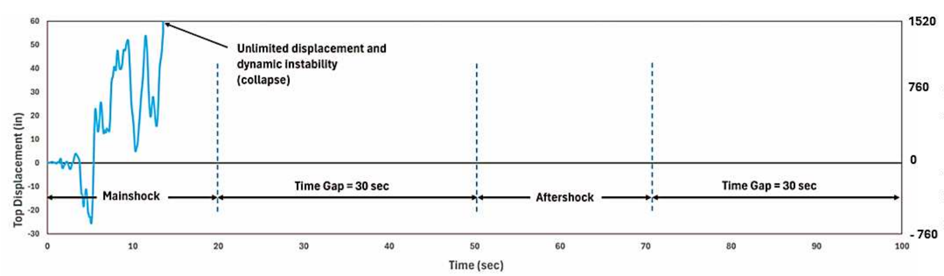

d) Sa (T1) = 3.5g

Figure 7-8. Top displacement time history of a 4-story RC structure (RC3) under a mainshock-aftershock sequence at different increasing earthquake IMs, here for Sa (T1): a) 0.5g; b) 1.5g; c) 2.5g, and d) 3.5g.

Figure 7-9 presents the earthquake fragility curves for the mainshock records, employing FEMA P695 and the selected mainshock GM records specific to this research. Given that far-field GMs from FEMA P695 are commonly utilized for developing earthquake fragility curves in Western United States regions, this study contrasts the fragility functions at the complete damage state (DS3) for a 4-story ductile RC structure, identified here as RC3, using both sets of records (i.e., mainshocks of FEMA P695 and the selected GMs from PEER NGA database in Section 7.2.2). As shown in Figure 7-9, there is good agreement between these two fragility curves, indicating that the final fragility curves produced by the mainshock records of these two GM sets are very similar to each other.

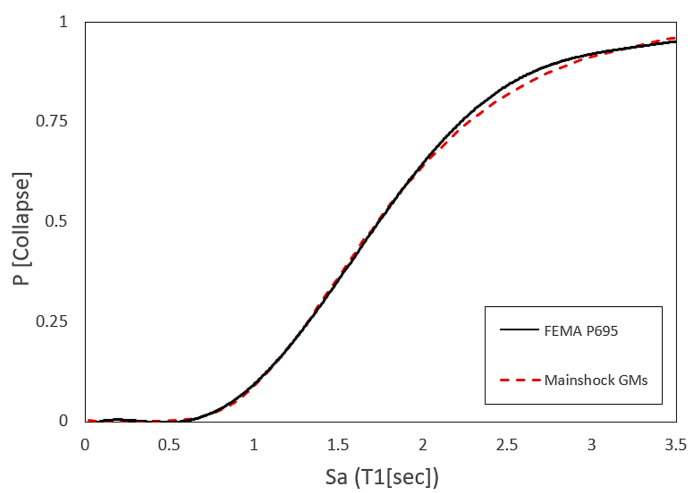

Figure 7-9. Earthquake fragility curves of this study computed using FEMA P695 and mainshock GMs for a 4-story ductile RC structure (RC3) at collapse level DS.

Figure 7-10 highlights fragility functions for certain ductile and non-ductile RC structures at different damage states covered in this research. These functions, created for both mainshock and mainshock-aftershock sequences using the methodology outlined in this chapter, showcase a portion of the structural archetypes analyzed. Aftershocks at median intensity levels notably increase the likelihood of failure across all damage states. However, the impact of this increase is significantly more pronounced for damage states DS2 and DS3 than for DS1, where the structure typically remains within its elastic response range.

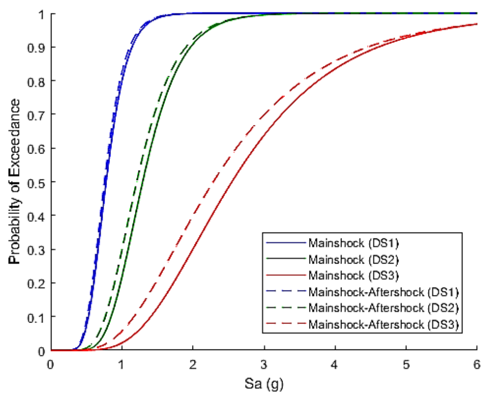

a) 2-story (ductile)

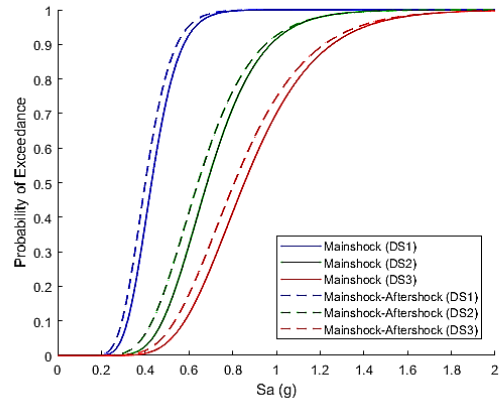

b) 2-story (non-ductile)

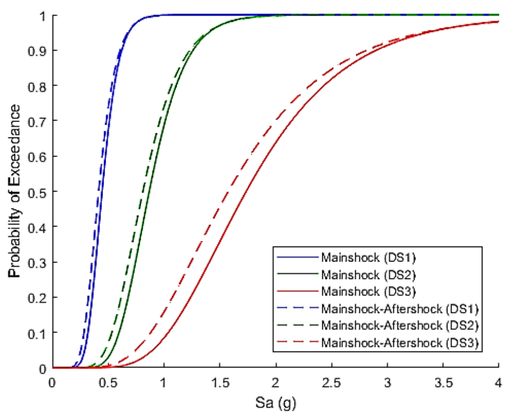

c) 4-story (ductile)

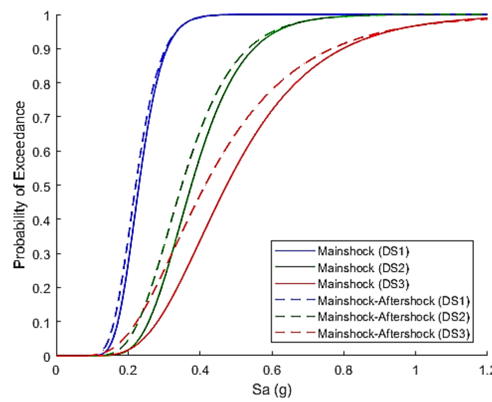

d) 4-story (non-ductile)

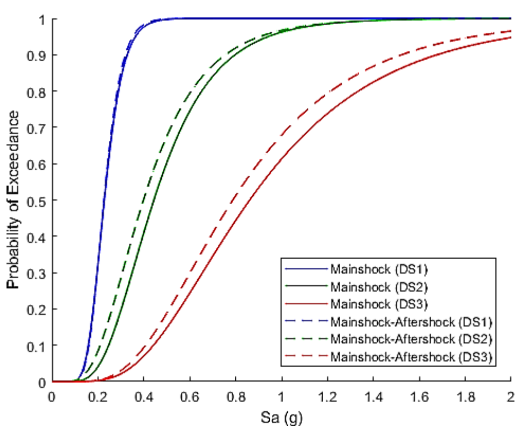

e) 8-story (ductile)

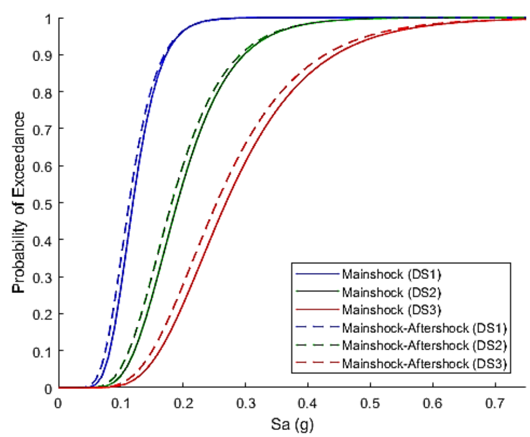

f) 8-story (non-ductile)

Figure 7-10. Fragility functions of mainshock and mainshock-aftershock sequences for RC structures: a) 2-story ductile system; b) 2-story non-ductile system; c) 4-story ductile system; d) 4-story non-ductile system; e) 8-story ductile system and f) 8-story non-ductile system.

While Figure 7-10 focuses on some RC structures, it is important to note that fragility functions for all archetypes discussed in this study, including woodframe systems, have been comprehensively developed. The critical parameters guiding these fragility functions—μ (mean) and σ (standard deviation)—are outlined in Tables 7-1 and 7-2, offering a quantitative foundation for assessing the seismic vulnerability of the RC structures under study.

Table 7-1. Equation parameters for the fragility curves of RC frames under mainshocks.

Structure ID	Parameters	DS1	DS2	DS3
RC1	μ	0.5580	0.9712	1.1292
	σ	0.3034	0.3760	0.4429
RC2	μ	-0.2489	0.2576	0.9357
	σ	0.2996	0.3275	0.4627
RC3	μ	-0.8089	-0.1418	0.5518
	σ	0.2612	0.2914	0.4011
RC4	μ	-1.4787	-0.8123	-0.1494
	σ	0.2834	0.4575	0.5203
RC5	μ	-1.6406	-1.0874	-0.3924
	σ	0.3845	0.3951	0.5425
RC6	μ	-1.5792	-1.0262	-0.4674
	σ	0.3204	0.4577	0.4211
RC7	μ	-2.2414	-1.7653	-1.1563
	σ	0.2147	0.3858	0.3719
RC8	μ	-2.1243	-1.6565	-1.3138
	σ	0.2870	0.3476	0.3917
RC9	μ	-1.4686	-0.9779	-0.7457
	σ	0.2283	0.2961	0.4056
RC10	μ	-0.8451	-0.3802	-0.1574
	σ	0.2302	0.2765	0.3003

Table 7-2. Equation parameters for the fragility curves of RC frames under mainshock-aftershock sequences.

Structure ID	Parameters	DS1	DS2	DS3
RC1	μ	0.5534	0.8485	0.9476
	σ	0.2941	0.4028	0.4965
RC2	μ	-0.2795	0.1906	0.8274
	σ	0.3017	0.3542	0.5216
RC3	μ	-0.8790	-0.2094	0.4548
	σ	0.2960	0.3267	0.4537
RC4	μ	-1.4847	-0.9203	-0.2387
	σ	0.2683	0.4994	0.5141
RC5	μ	-1.6545	-1.1281	-0.4714
	σ	0.3702	0.3467	0.5151
RC6	μ	-1.6166	-1.1066	-0.5391
	σ	0.3462	0.4711	0.4458
RC7	μ	-2.2821	-1.8464	-1.2213
	σ	0.2121	0.4163	0.4002
RC8	μ	-2.1760	-1.7050	-1.3707
	σ	0.3137	0.3690	0.4067
RC9	μ	-1.5077	-1.0513	-0.8803
	σ	0.2487	0.3308	0.4802
RC10	μ	-0.9140	-0.4437	-0.2128
	σ	0.2410	0.3071	0.3204

These parameters are crucial for delineating the vulnerability equations and for the precise modeling of the fragility of the building types discussed, facilitating community-level analysis. The development and detailing of fragility functions for woodframe structures, which are fundamental to the archetypes examined, are also included in Table 7-3 and 7-4, underscoring their significance in the overall assessment of community resilience.

Table 7-3. Parameters of equation for the earthquake fragility curves in woodframe structures under mainshocks.

Structure ID	Parameters	DS1	DS2	DS3
W11	μ	0.3103	1.1279	1.4994
	σ	0.5346	0.4249	0.4745
W12	μ	0.2169	1.0277	1.3873
	σ	0.4910	0.4237	0.4618
W13	μ	0.0953	0.6622	1.3227
	σ	0.3688	0.4328	0.4587
W21	μ	0.1628	0.8295	1.2263
	σ	0.2963	0.3645	0.5119
W22	μ	0.0754	0.7402	1.1281
	σ	0.2738	0.4070	0.4454
W23	μ	0.1133	0.5735	1.0708
	σ	0.3029	0.3641	0.4296

Table 7-4. Parameters of equation for the earthquake fragility curves in woodframe structures under mainshock-aftershock sequences.

Structure ID	Parameters	DS1	DS2	DS3
W11	μ	0.2660	1.0946	1.4674
	σ	0.4687	0.3874	0.4533
W12	μ	0.1930	0.9946	1.3422
	σ	0.4486	0.3811	0.4256
W13	μ	0.0773	0.6270	1.2769
	σ	0.3298	0.3841	0.4202
W21	μ	0.1466	0.8012	1.1707
	σ	0.2722	0.3278	0.4539
W22	μ	0.0604	0.7090	1.0814
	σ	0.2563	0.3676	0.3849
W23	μ	0.0984	0.5445	1.0262
	σ	0.2824	0.3270	0.3829

7.5.2 Community-level Analysis under Mainshock-aftershock Scenarios

The vulnerability functions developed for mainshocks, and mainshock-aftershock sequences were applied to the Pseudo Seaside testbed community to assess the potential seismic response and resilience of the area when subjected to a source earthquake and its subsequent aftershocks. To evaluate the resilience performance of the testbed community across different damage states, a community-level analysis was conducted. This analysis spanned various MRIs resulting in analyses with low to relatively high earthquake intensity levels. As depicted in Figure 7-11(b), a notable increase in the percentage of building units transitioning to a higher damage state occurs post-mainshock with an earthquake MRI exceeding 1000 years (or equivalently, a PGA of 0.65 or more), indicating that aftershock effects can exacerbate damage, potentially elevating the DS status for over 30% of buildings from DS1 to DS2 following a mainshock-aftershock sequence.

As shown in Figure 7-11(a), the maximum percentage of DS1 for the mainshock-only scenario decreases from 60% to about 30% at an earthquake IM of 0.85g when both mainshock and aftershock are considered in a community-level analysis. This decrease occurs because approximately 30% of the buildings are being reclassified into a higher damage category, namely DS2. This significant impact can be attributed to buildings in the Pseudo Seaside region typically experiencing moderate to significant structural softening at a PGA around 0.65, making them more vulnerable to additional damage from aftershocks. The analysis also subtly indicates an increase in buildings reaching damage state DS3, even though the hazard values, such as PGAs for the seismic scenario simulated in this study, are not exceedingly high. This underscores the complex impact of aftershocks on community damage analysis and subsequent resilience studies, highlighting the importance of incorporating these effects into seismic vulnerability assessments.

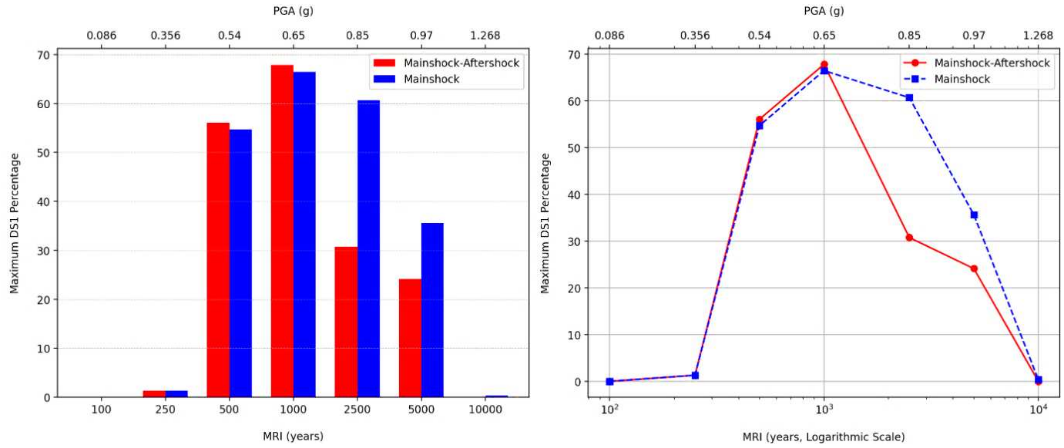

a) Max percentage of DS1

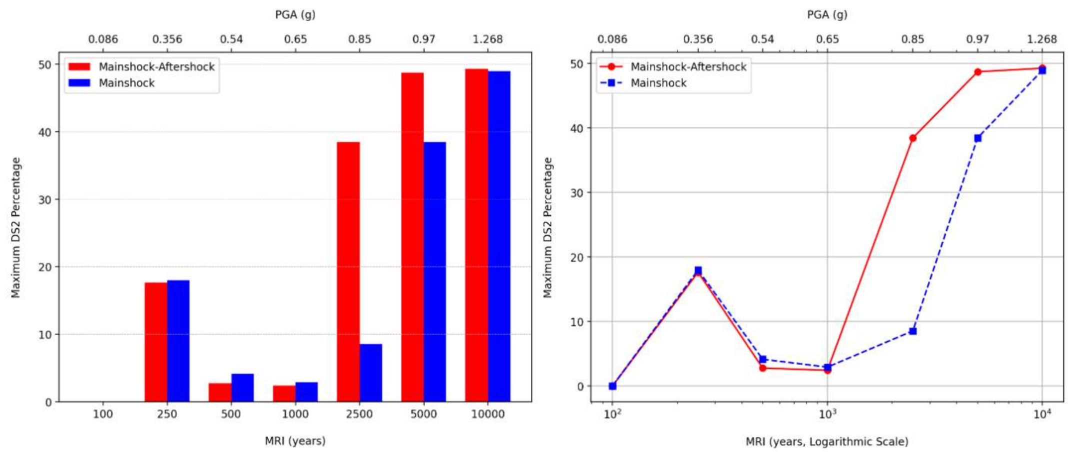

b) Max percentage of DS2

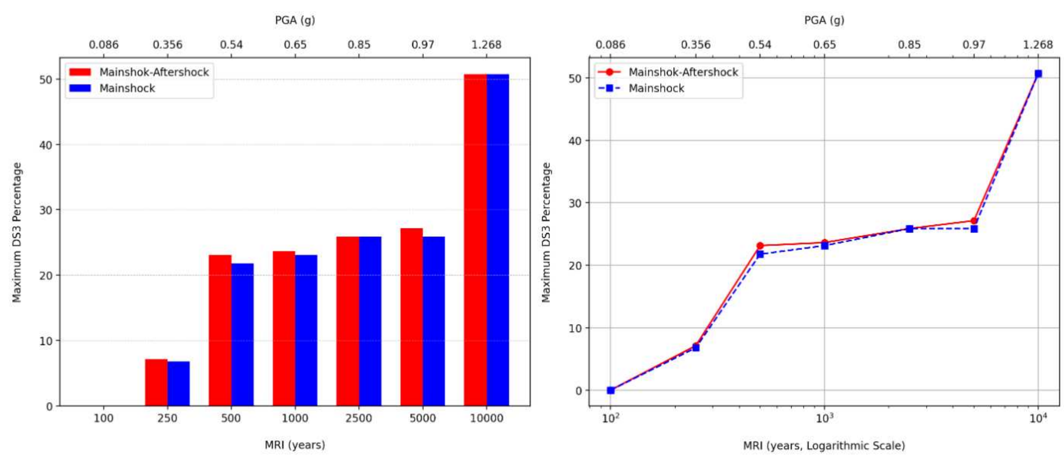

c) Max percentage of DS3

Figure 7-11. Maximum percentages of the considered DS versus the earthquake MRIs—or PGAs equivalently—for: a) DS1; b) DS2 and c) DS3.

The spatial damage analysis output from this community damage simulation, depicted in Figure 7-12, demonstrates a recurring damage pattern where a significant number of buildings escalate from moderate to heavy damage states due to the aftershock event in a hazard scenario featuring a PGA of 0.85g.

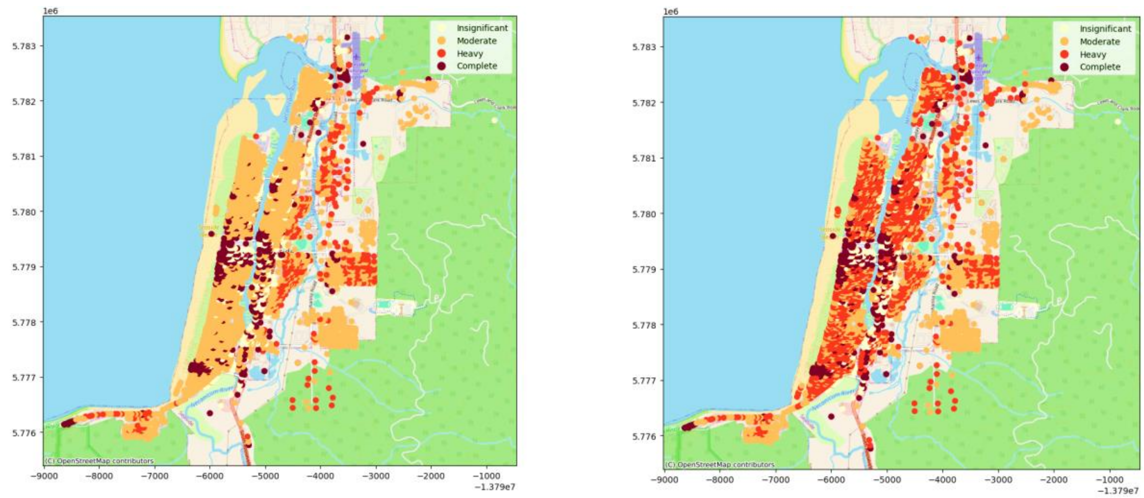

a) Mainshock senario

b) Mainshock-aftershock senraio

Figure 7-12. Spatial damage analysis for an earthquake event with PGA of 0.85g in different seismic scenarios considered: a) for mainshock sequence only, and b) in mainshock-aftershock sequences.

Moreover, Figure 7-13 validates that over 2000 building units in the target community have escalated to damage state DS2. Given that economic loss, risk, and recovery processes depend on the initial damage states of buildings, overlooking the impact of aftershock events could result in considerable inaccuracies in the vulnerability assessment of the region in question.

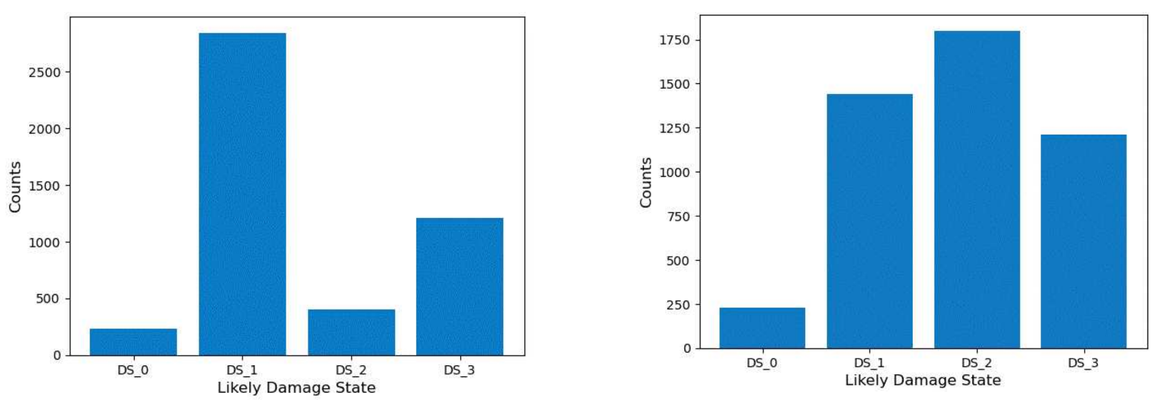

a) Mainshock scenario

b) Mainshock-aftershock senario

Figure 7-13. Damage state distribution for an earthquake event with PGA of 0.85 in different considered seismic scenarios: a) the mainshock sequence only; b) for mainshock-aftershock sequences.

The earthquake loss and risk differential in the region were analyzed by deducting the economic loss and risk values calculated for the mainshock-only event from those of the mainshock-aftershock sequence events across varying seismic intensity levels, as indicated by different MRIs or PGA values. As illustrated in Figure 7-14(a), the economic loss differential escalates with increasing PGA values of seismic hazards, reaching up to 30 million dollars for a PGA close to or around 0.97g (point F on Figure 7-14(a)). It should also be noted that the economic loss begins to intensify significantly after an MRI of 500 years or a PGA of 0.54g equivalently (point C on Figure 7-14(a)). It's important to highlight that this economic loss is supplementary to that anticipated from the mainshock alone. Hence, overlooking aftershocks can significantly underestimate the total economic losses.

Figure 7-14(b) presents the normalized risk differential, computed through the total economic risk algorithm outlined in section 7.2.3. In this methodology, the total economic loss differential is divided by the PGA values for different earthquake intensity levels to assess the risk differential attributable to aftershocks. The resulting risk differential values are then normalized by dividing them by the maximum observed risk differential, resulting in normalized values ranging between 0 and 1. Importantly, the analysis identifies the community's highest economic risk vulnerability occurs at a seismic hazard scenario having a PGA of approximately 0.36g (point B on Figure 7-14(b)), given the reduced probability of earthquakes with higher PGA values.

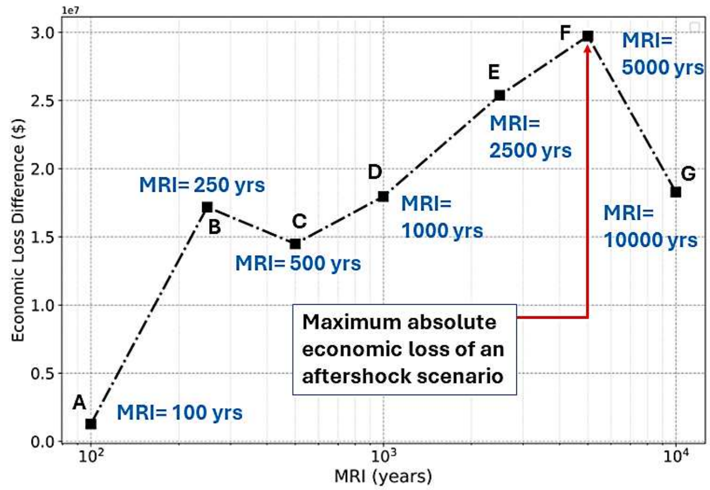

a) Economic loss difference

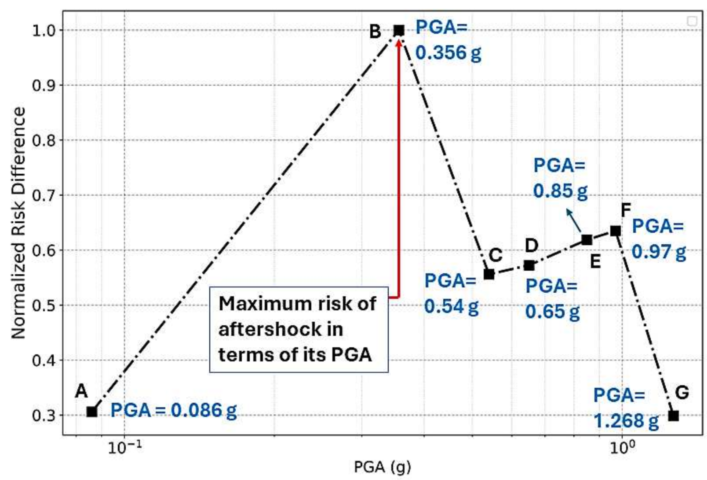

b) Normalized risk difference

Figure 7-14. Economic loss and risk difference computed for the impact of aftershock solely taking account the cumulative damage from mainshock earthquake.

CHAPTER 8: MODELING POPULATION DISLOCATION AND BUILDING FUNCTIONAL RECOVERY IN COMMUNITIES AFFECTED BY SUCCESSIVE SEISMIC EVENTS S

8.1 Introduction

This chapter introduces an approach for modeling the functional recovery of buildings post-event, using the method developed by Wang and van de Lindt (2021) for residential building units and another study by Wang et al. (2023) focused on commercial buildings. The methodology for residential buildings employs a probabilistic Monte Carlo simulation (MCS) divided into two main sections: immediate building repair downtime and delays induced by the disaster. A critical aspect is the probabilistic, layered MCS, quantifying delay time based on initial building damage from specified hazards. The framework estimates delay time related to building damage using 'N1' scenarios and 'N2' realizations of repair time within the MCS procedure. The methodology also focuses on financial delays at the household level, significantly affecting the capacity to fund repairs or retrofitting post-disaster, integrated within the REDi framework (Arup, 2017). Additionally, this chapter introduces repair fragility functions for earthquake-related hazards, applying the Weibull distribution to model delay and recovery times. The methodology's limitation is the assumption that no outmigration of households occurs, implying all remain within the community throughout the repair process. This is a necessary assumption at this stage in the research due to the complexity of outmigration decision-making by households.

For commercial buildings, the study adopts the functional recovery model proposed by Wang et al. (2023)—as mentioned earlier—a modified version of the REDi Downtime Assessment Framework, highlighting the significance of federal programs and private financial institutions. The study employs high-fidelity multi-hazard and multi-event fragility functions (see Chapter 4 and Chapter 7) tailored to the Pseudo Seaside community, integrating socio-demographic and financial resources data.

8.2 Functional Recovery Modeling

This chapter outlines an approach for modeling post-disaster recovery of residential buildings, directly employing the method developed by Wang and van de Lindt (2021). The methodology, utilizing a probabilistic MCS framework, is divided into two principal sections. The first section focuses on downtime due to immediate building repair, while the second section centers on delays induced by the disaster. A critical aspect of this methodology is the probabilistic, layered Monte Carlo framework, which quantifies delay time as a function of the initial building damage from a specified hazard. This framework engages 'N1' scenarios to estimate delay time related to building damage, each coupled with 'N2' realizations of repair time within the MCS, thus facilitating a comprehensive analysis of both aspects.

As shown in Figure 8-1, an essential element of this method is the focus on financial delays at the household level, influenced by the availability of financial resources. This aspect significantly affects the capacity to fund repairs or retrofitting post-disaster. The study examines the potential for households to use available funds for rebuilding or retrofitting efforts. This financial delay assessment is integrated within the detailed REDi (the Resilience Based Earthquake Design Initiative) framework (Arup, 2017), with further elaboration to follow in subsequent sections. Additionally, this chapter introduces repair fragility functions, specifically formulated for earthquake-related hazards, to enhance understanding of repair-related downtime. The methodology concludes by applying the Weibull distribution to model MCS results, capturing delay and recovery times for individual building units. However, a limitation of this approach is the assumption that no out-migration of households occurs, implying all remain within the community throughout the repair process.

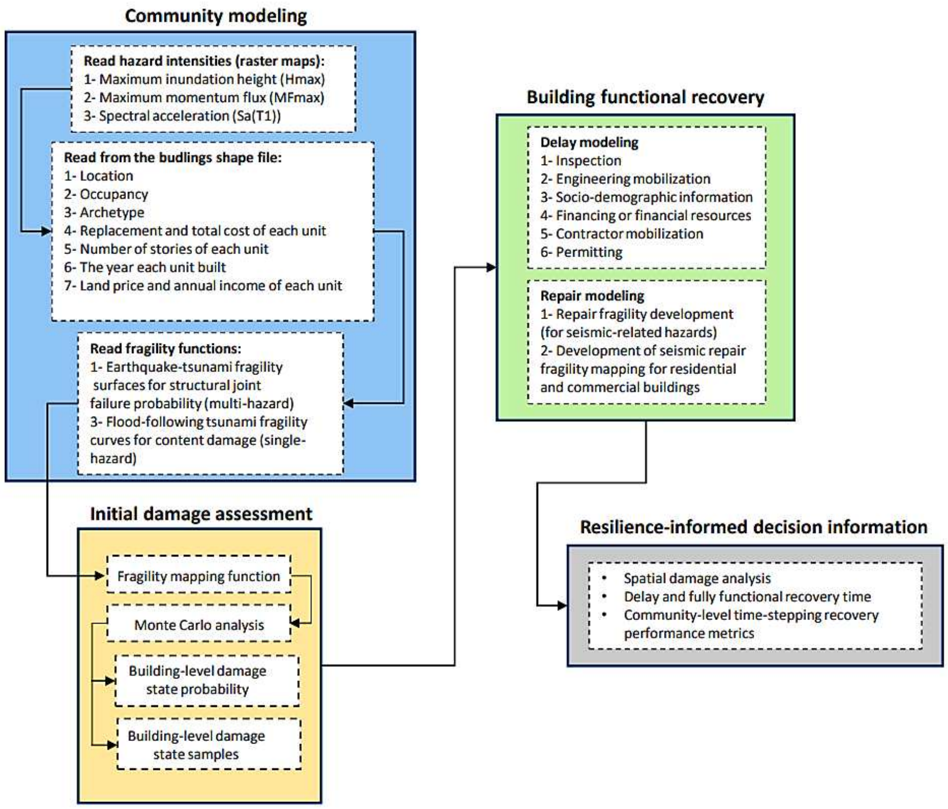

Figure 8-1. Algorithm of building level recovery analysis used for this seismic recovery modeling of successive events

For buildings identified as commercial entities, this study adopts the functional recovery model proposed by Wang et al. (2023). This model is a modified version of the REDi Downtime Assessment Framework. The framework differentiates the recovery pathways for residential and commercial buildings, with the latter involving more complex strategies encompassing personal savings, insurance, SBA loans, and various recovery programs. It underscores the significance of federal programs like the SBA's disaster assistance loans and other government-based funds, alongside contributions from private and local financial institutions.

A central aspect of Wang et al.'s (2023) study is the empirical simulation of financing resources and associated delays following hazard events. This involves constructing a detailed recovery resource portfolio based on federal program documentation, media reports, and government agency reviews. The approach illuminates the extent of support available to businesses, the fund disbursement timeline, and the overall financial impact of each program. Importantly, the study suggests that the financial recovery patterns observed post-Hurricane Ike could be indicative of similar scenarios in other hazard events, although this premise is distinct from other delay-inducing factors, such as inspection and permitting. The methodology of Wang et al. (2023) is therefore applied to the commercial buildings of the Pseudo Seaside coastal community in Oregon (see Chapter 5 for more information), utilizing data from the Galveston area post-Hurricane Ike to assess its applicability in similar coastal contexts.

The accuracy of the recovery analysis, applicable to both residential and commercial buildings, is considerably influenced by the initial building damage level. To this end, the study employs high-fidelity multi-hazard and multi-event fragility functions tailored to the Pseudo Seaside community, potentially vulnerable to a source earthquake, subsequent tsunami, and aftershocks. These high-fidelity vulnerability functions are integral to the initial building damage analysis. Another crucial aspect of this recovery analysis, developed within this chapter, is the formulation of repair fragility functions for seismic-related hazards. These functions are intended to be integrated with adjusted socio-demographic and financial resources data, and the delay factors of residential buildings in communities facing successive seismic hazards. The intricacies of this integration and its impact on the recovery process will be discussed in detail later in the chapter, offering a holistic perspective on recovery dynamics in hazard-prone communities. For detailed information on high-fidelity multi-hazard and multi-event fragility functions, readers are encouraged to refer to Chapters 3, 4, and 7 of this dissertation.

8.2.1 Fragility Functions for Assessing Building Damage and Recovery

The Bayesian probabilistic framework is crucial for community resilience analysis, particularly in evaluating multi-hazard risks, such as the compounded effects of sequential natural hazards like earthquakes and tsunamis. It allows for the assessment of increased vulnerability in structures when exposed to successive hazards, such as a tsunami following an earthquake. This method provides a comprehensive way to quantify the likelihood of structural failure under varying hazard intensities by integrating fragility functions for both hazards (see Chapter 6 for more information). Although modeling the effects of a tsunami followed by a source earthquake is unrealistic, it is relevant for aftershocks following a tsunami. Harati and van de Lindt (2024) proposed a two-phase probabilistic approach in Chapter 2 to address this challenge, enabling the computation of joint failure probabilities for earthquake-tsunami scenarios and fitting a near-continuous fragility surface to the data. This research applies these surfaces to 16 archetypes Chapter 3 and 4, covering RC and woodframe buildings. Additionally, the methodology presented in Chapter 2 has been extended to analyze the cumulative impacts of earthquakes and aftershocks, with fragility functions developed specifically for mainshock-aftershock sequences, which are further explored in Chapter 7.

8.2.2 Restoration Functions for Repair Time Analysis

The concept of building-level repair time fragility curves is integral to understanding the recovery process of structures following natural hazard events. Central to this concept is the relationship between a building's damage state and its level of functionality, a relationship that varies depending on the building's occupancy type. The aim of recent studies in this area has been to correlate these two aspects, though fully developing this relationship requires extensive field study and survey data, which often falls outside the scope of initial studies. Traditionally, fragility curves have focused on achieving 100% functionality post-event. However, this approach can limit the exploration of various recovery scenarios and optimization processes at the community level. Consequently, recent methodologies have proposed considering multiple levels of functionality (100%, 75%, 50%, 25%, and <25%) to better address the different combinations of damage that can occur in both structural and nonstructural components of a building (Koliou and van de Lindt, 2020). This relationship can be represented as:

$$F(D) = \begin{cases} 100\% & \text{if } D \leq D_{min} \\ 75\% & \text{if } D_{min} < D \leq D_1 \\ 50\% & \text{if } D_1 < D \leq D_2 \\ 25\% & \text{if } D_2 < D \leq D_3 \\ < 25\% & \text{if } D \leq D_3 \end{cases} \tag{8-1}$$

where *F(D)* denotes the functionality level, and *D* represents the damage state, with D_{min}, *D1, D2* , *D3* being specific damage thresholds.

The development of these repair fragility curves requires a detailed understanding of the estimated repair times for each component of a building (sourced from FEMA P-58). A hierarchical Bayesian model is employed to capture the complexity and variability of these estimates, where the repair time *T* for each component is a function of several parameters, including the type of damage, the extent of damage, and the repair techniques used, mathematically expressed as:

$$T|\theta, \lambda, \phi \sim Lognormal(\mu(\theta, \lambda), \sigma^2(\phi)) \tag{8-2}$$

In this model, θ represents parameters related to the building and damage characteristics, λ denotes parameters related to the repair process, and ϕ includes parameters that capture the uncertainty inherent in the repair process. This approach allows for a more adaptive and comprehensive modeling of repair times, considering the variability and complexity inherent in post-disaster repair processes.

A significant aspect of this methodology originally proposed by Koliou and van de Lindt (2020) is the use of an S-shaped repair time curve, inspired by logistic growth models. This curve is designed to reflect the real-world scenario where repair rates are initially slow following a disaster but increase over time. The curve is used to calculate the mean repair value for achieving specific functionality levels (e.g., 75%, 50%, 25%) based on the damage sustained by the building. The S-shaped curve can be mathematically defined using the logistic equation:

$$Q(t) = \frac{1}{1 + e^{-k(t-t_0)}} \tag{8-3}$$

where $Q(t)$ represents the repair level at time t, k is the growth rate, and t_0 is the midpoint of the curve.

The probability of reaching specified levels of functionality is assessed through a triple integration process, which considers the relationship between functionality, damage measure (DM), engineering demand parameter (EDP), and IM. This relationship is mathematically expressed as:

$$g[Q] = \iiint p[Q \mid DM] \cdot p[DM \mid EDP] \cdot p[EDP \mid IM] \cdot g[IM] dDMdEDPdIM \tag{8-4}$$

where $g[Q]$ represents the probability of achieving a functionality level Q, $p[Q|DM]$ is the probability of reaching Q given DM, $p[DM|EDP]$ is the probability of DM given EDP, and $p[EDP|IM]$ is the probability of EDP given IM. This comprehensive approach involves using MCS procedures with a large number of samples (100,000 in this case) to accurately evaluate the post-disaster repair time distributions. These repair functions are essential in predicting the probability of a building achieving different levels of functionality based on the severity of the hazard impact. This method provides a more detailed and probabilistic understanding of the building's recovery trajectory, crucial for effective community-level resilience planning and decision-making in post-disaster scenarios. It is important to note that repair fragility functions in this dissertation have been developed to estimate the probability of achieving full functionality (100%).

8.2.3 Delay Factors for Housing Recovery

In the realm of disaster risk reduction and community resilience, a comprehensive analysis of delay factors in post-disaster recovery is essential for both residential and commercial buildings. This study, recognizing the importance of such analysis for commercial buildings, integrates the data-driven model from the Galveston area, as utilized in the recovery model of Wang et al. (2023). These delay factors are crucial in determining the recovery timeline and cover a spectrum of elements, including the duration needed for post-disaster inspections, the challenges of securing engineering and contractor services, the procedures to access financial assistance, and the complexities inherent in the building permit process. The innovative adaptation of the REDi framework, originally tailored for seismic-related hazards like earthquakes, to encompass these delay factors, represents a significant advancement. This adaptation not only broadens the framework's application to a wider range of disaster types but also deepens its utility in guiding community resilience and recovery strategies. Central to this enhanced approach is Eq (7-5) from the referenced study, which precisely quantifies the delay factors. The equation is presented as:

$$T_{Delay}=T_{INSP} + T_{ENGM} + T_{FINA} + T_{CONM} + T_{PERM} \tag{8-5}$$

In this formulation, T_{Delay} denotes the total modeled delay time. The components of the equation represent various critical phases: T_{INSP} for the duration of post-event inspection, T_{FINA} for the time to secure engineer/contractor services, T_{CONM} for the period of financial assistance processing, T_{PERM} for construction management time, and T_{PERM} for the time taken to acquire a building permit. This equation is a cornerstone within the MCS framework of the study, providing an intricate and detailed assessment of the various elements that contribute to the delay in residential building recovery following diverse disaster events. Such a detailed quantification is essential for policymakers and planners in devising targeted strategies that effectively address these delay factors, thereby enhancing the speed and efficiency of community recovery post-disaster.

8.2.4 Potential Fundings for Seismic-related Hazards

In the context of seismic-related hazards, the potential fundings for housing recovery are significantly influenced by household income, a critical factor that determines the financial resources available to households during the recovery process. This relationship becomes evident when examining the distribution of funding sources such as insurance, SBA-backed loans, private loans, and savings/others across various income groups (Wang et al. 2023). The data demonstrates a distinct trend wherein lower-income groups, particularly those earning less than $15,000 annually, primarily rely on savings or alternative means, often due to limited access to formal lending or insurance options. As household income increases, there is a noticeable shift towards greater dependence on formal funding sources like insurance and SBA-backed loans, underscoring the relationship between income and financial resilience in the face of seismic events.

In California (a region susceptible to seismic-related hazards), earthquake insurance coverage remains surprisingly low despite the state's high seismic risk. Only 13% of homeowners currently have earthquake insurance, a figure that has not significantly increased over time (NPR, 2019). Among renters, the situation is even more stark, with just 5.24% carrying earthquake insurance (Los Angeles Times, 2017), a sharp decline from nearly 10% a decade ago. This disparity highlights a significant vulnerability, particularly among renters, whose coverage rate is only about 40% of that of homeowners. The recent earthquakes in Mexico have sparked a renewed interest in earthquake insurance, yet the overall uptake remains limited, leaving many Californians exposed to potential financial losses in the event of a major quake.

The situation in Oregon presents a noteworthy contrast to California, with approximately 20% of homeowners carrying earthquake insurance. In Oregon, earthquake insurance must be bought separately because standard homeowner, mobile home, condo, and renter insurance policies usually don't cover earthquake damage (State of Oregon, 2017). This separate purchase requirement likely contributes to the relatively low coverage rates. However, the 20% coverage among homeowners is still significantly higher than what is observed in many other earthquake-prone areas, reflecting a greater awareness or concern for seismic risks among Oregon residents.

Given that renters in California have a coverage rate that is about 40% of homeowners, a similar trend in Oregon suggests that approximately 8.06% of renters might have earthquake insurance coverage. While this figure may seem small, it is a critical factor in mitigating the financial devastation that could follow a major seismic event. Earthquake insurance is especially important for protecting significant investments, particularly for homeowners, whose properties often represent their most valuable asset.

On average, it is assumed that 20% of homeowners (HH4 and HH5) have insurance, while only 8.06% of other categories, primarily renters, have earthquake insurance in the state of Oregon—where the target community of this study, Pseudo Seaside, is located. With this distribution reflected in the insurance column of Table 8-1, the data provides insight into how different income groups rely on various funding sources—such as insurance, SBA-backed loans, private loans, and savings/others—during the recovery process. The numbers in the other columns have been assumed based on a previous study by Wang and van de Lindt (2021). For lower-income groups, particularly those earning less than $15,000 annually (HH1), there is an overwhelming dependence on savings or other informal means (92.8%), with no reliance on insurance or private loans. As household income increases, there is a noticeable shift towards formal funding sources, with higher-income groups (HH4 and HH5) exhibiting greater reliance on insurance (17.9% and 22.1%, respectively) and SBA-backed loans (80.8% and 77.4%, respectively). This trend underscores the intricate relationship between income levels and financial resilience in the face of seismic events, highlighting that higher-income households are better positioned to secure formal financial aid, while lower-income households remain vulnerable due to limited access to such resources.

Table 8-1. Income-based distribution of disaster recovery resources and insurance coverage

Household Income Group	Insurance	SBA-Backed Loans	Private Loan	Savings/Others
HH1 (Less Than $15,000)	0 %	7.2 %	0 %	92.8 %
HH2 ($15,000 To $24,999)	2.5 %	8.6 %	8.6 %	72.6 %
HH3 ($25,000 To $74,999)	5.6 %	40.9 %	40.9 %	0 %
HH4 ($75,000 To $99,999)	17.9 %	80.8 %	0 %	0 %
HH5 (More Than $100,000)	22.1 %	77.4 %	0 %	0 %

8.2.5 Socio-demographic Information

By incorporating annual household income as a key socio-demographic indicator, recovery models can effectively predict the funding options available to households for residential building repairs. Making this connection is essential in functional recovery analysis as it provides a realistic view of the economic capabilities and constraints of affected households. Understanding the financial dynamics of affected communities is crucial for accurately estimating recovery times. Policymakers and planners can utilize this information to develop more effective, targeted support strategies. Tailoring these strategies to address the specific financial needs and constraints of different households ensures that financial aid and resources are appropriately distributed, facilitating a more efficient recovery process. Such strategies are instrumental in reducing recovery periods, thereby significantly enhancing the resilience of communities to bounce back more efficiently from future hazards. This comprehensive approach to integrating socio-demographic data, particularly household income, into recovery models marks a significant advancement in disaster resilience planning and policy development.

The methodology for obtaining annual household income data, as described in a study by Wang and van de Lindt (2021) with more details, employs a detailed process crucial for analyzing financial resources available to households during the recovery process post-disaster. This data was acquired by merging information at the housing unit level from the ACS (2012) 5-year survey, utilizing tables B19001 and B19101. The approach involves a housing unit allocation algorithm, as detailed by Rosenheim et al. (2021), to predict household income. This is pivotal for understanding the socio-economic dynamics of the community affected by the disaster.

The dataset, developed for the Joplin testbed in IN-CORE (van de Lindt et al., 2023) through a study by Wang and van de Lindt (2021), provides a foundation for validation and includes data from 7,201 housing units in 5,327 buildings. However, this study faced significant challenges, notably a 10.5% rate of missing household income information, due to discrepancies in characteristics like race/ethnicity between the Census and ACS data. While the allocation process was comprehensive, it acknowledged potential inaccuracies, particularly in cases of vacant housing units and group quarters like nursing homes. The methodology attempted to mitigate these issues by de-aggregating housing units to the census block level for more precise prediction of missing income data. In multi-family buildings, income groups were aggregated from the household to the building level (Rosenheim, 2021; Rosenheim et al., 2021), based on the assumption that units with the highest income have the best financial resources for restoration. Although this nuanced approach to data collection and analysis is fundamental for modeling the recovery process, the persistent challenge of missing data highlights a significant gap in this area. Resolving this issue is critical to ensuring accurate representations of economic capabilities and constraints within communities, which is essential for developing effective recovery strategies. Addressing the missing data problem remains a key priority to advance the accuracy and reliability of socio-demographic analyses in disaster resilience planning.

In analyzing annual household income data for the designated study area, referred to as the Pseudo Seaside in this dissertation, a comprehensive approach is employed to address missing income values and ensure robust analysis. It is assumed that the household income distribution at the census block level in the Pseudo Seaside remains consistent with the original Seaside testbed, meaning the modifications introduced in Chapter 5 do not alter the annual household income distribution across census blocks.

The methodology begins with an extensive data-gathering phase, involving detailed research to compile a balanced and representative distribution of income data at the census block level. This is illustrated in Figure 8-2(a), which draws from trusted and credible sources (Best Neighborhood, 2023). Following the compilation of the initial data, the next step involves refining and cleaning the image data, as depicted in Figure 8-2(b). This process entails removing any texts, labels, or extraneous elements that could distract from the analysis, thereby ensuring that the image is clear and focused solely on the income data. This step is essential for preparing the image for further processing.

Once the image has been thoroughly cleaned, advanced image processing techniques are employed to transform the visual income maps into an analyzable grayscale raster format, as shown in Figure 8-2(c). This conversion is a critical step that allows for the quantitative analysis of the income distribution across the study area. The process includes several key steps: data normalization, contrast enhancement, and noise reduction, all of which are essential for improving the clarity and precision of the income distribution representation. To further refine the grayscale image, Gaussian filtering is applied, which helps to smooth the data and reduce any remaining noise that might interfere with the analysis. Additionally, the RGB scaling is reversed as shown in Figure 8-2(d) to align the grayscale values with the known extremities of income ranges, ensuring that the final image is precisely calibrated. This alignment is crucial for accurately mapping income levels to specific geographic areas, allowing for a detailed and accurate analysis of income distribution within the study area.

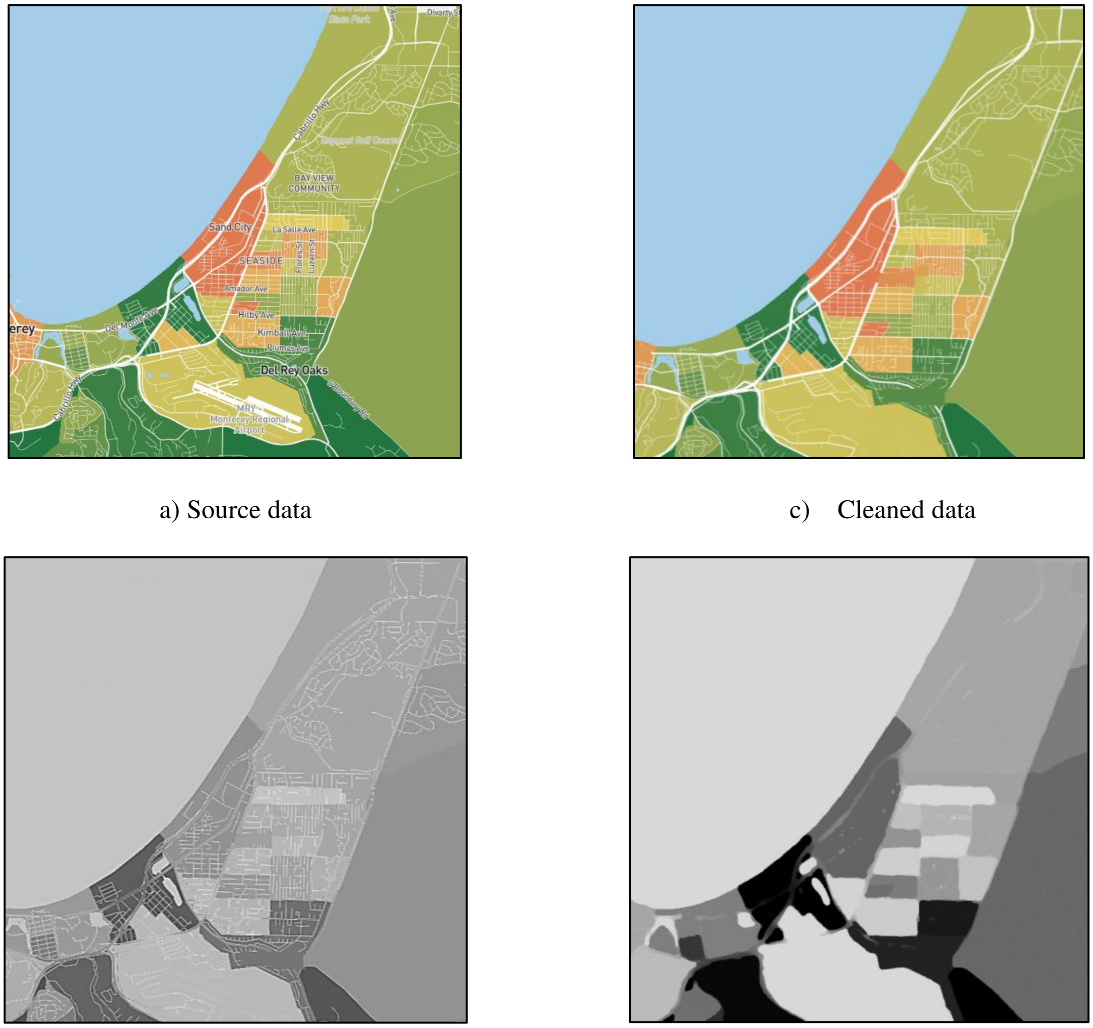

a) Source data

c) Cleaned data

c) Grayscale RGB raster

d) Reversed grayscale raster without missing data

Figure 8-2. Image processing workflow for income data analysis: a) source data, b) cleaned data, c) grayscale RGB raster, d) reversed grayscale raster RGB without missing data.

To maintain data consistency and reliability, values below a minimum income threshold were discarded. The XGBoost machine learning algorithm (Chen and Guestrin, 2016) was employed to estimate missing income data that had been identified through the Rosenheim et al. (2021) approach, with a target accuracy threshold exceeding 90%. Additionally, sophisticated data augmentation techniques were utilized to enhance the overall quality of the dataset. This comprehensive approach culminated in the construction of a block-level income distribution model, which serves as foundational data for the community recovery model, drawing on methodologies suggested by Wang and van de Lindt (2021, 2023).

8.3 Population Dislocation Modeling

The Population Dislocation Algorithm (PDA), an integral tool in the field of community resilience analysis, is particularly critical following natural hazard events. It synergizes data from building damage assessments with detailed socio-demographic information, enabling the prediction of population dislocation probabilities. These predictions are invaluable for effective emergency planning and recovery strategies. The PDA employs logistic regression to estimate the probability of binary outcomes, specifically predicting post-disaster household relocations. This model incorporates constants (c_1 to c_5) and key variables representing factors like property value loss and building types (single-family or multi-family). Additionally, it integrates neighborhood characteristics, such as the proportions of black and Hispanic populations. This consideration acknowledges the disparate impacts of disasters on various communities, emphasizing that vulnerability transcends physical aspects to include socio-economic factors.

Drawing upon seminal research (Peacock et al., 1997; Rosenheim et al., 2021, 2019; Zhang and Peacock, 2009), the PDA adopts a holistic approach in predicting dislocation. The model differentiates probabilities across damage states, reflecting the substantial role of damage severity in influencing relocation decisions. The logistic regression formula applied within the PDA is:

$$P_{\mathrm{dis;i;m}}^{K} = \frac{1}{1 + e^{-(c_1 + c_2.ploss_{i,m}^{k} + c_3.dsf_m^{k} + c_4.pblack_m + c_5.phisp_m)}} \tag{8-6}$$

This expression delineates the dislocation probability for each building *(k)* in a given census group *(m)* and damage state *(i)*, incorporating variables such as property loss, dwelling type, and demographic percentages. Slight or no damage (state 1) is assessed separately from more severe damage states (2 to 4), consistent with building functionality assessments, demonstrating the interplay between physical damage and social impact. Moreover, the PDA features an equation to aggregate dislocation probabilities across varying damage states:

$$P^{\mathrm{k}}_{\mathrm{dis;m}} = P^{\mathrm{k}}_{\mathrm{dis;1;m}} \times P^{\mathrm{k}}_{\mathrm{damage;1}} + \sum_{i=2}^{4} P^{\mathrm{k}}_{\mathrm{dis;i;m}} \times (P^{\mathrm{k}}_{\mathrm{damage;i}} - P^{\mathrm{k}}_{\mathrm{damage;i-1}}) \qquad (8\text{-}7)$$

This equation calculates the comprehensive dislocation probability for each building in a census group, integrating probabilities from the least severe (state 1) to more severe damage states.

The efficacy of the PDA is contingent on the accuracy of the input data. Variables such as property value loss, building type, and demographic attributes must be meticulously assessed and updated for precise predictions. The use of non-specific logistic regression constants may limit the algorithm's local applicability. Thus, the PDA should be regarded as a dynamic instrument within disaster risk management, necessitating continuous refinement and validation to keep pace with evolving community profiles and building norms. Its advancement is imperative for examining dislocation patterns and improving community resilience to natural hazards.

In this dislocation model, the categorization of race and ethnicity plays a crucial role in understanding the differential impacts of hazards on various demographic groups within the community. The categories used in the model are as follows:

- **Vacant Housing Units (HU) No Race Ethnicity Data (G1)**: This category includes housing units that are vacant, and therefore, no race or ethnicity data is available for these units.

- **White alone, Not Hispanic (G2)**: This category represents individuals who identify solely as White and are not of Hispanic or Latino origin.
- **Black alone, Not Hispanic (G3)**: This category includes individuals who identify solely as Black or African American and are not of Hispanic or Latino origin.
- **Other Race, Not Hispanic (G4)**: This category encompasses individuals who identify with any race other than White or Black and are not of Hispanic or Latino origin. This may include, but is not limited to, those identifying as Asian, Native American, or Pacific Islander.
- **Any Race, Hispanic (G5)**: This category includes individuals of any racial background who identify as Hispanic or Latino, reflecting the ethnic diversity within the Hispanic or Latino community.
- **Group Quarters no Race Ethnicity Data (G6)**: This category refers to individuals living in group quarters (such as dormitories, nursing homes, or correctional facilities) where specific race or ethnicity data is not available.

These categories allow for analysis of dislocation and recovery dynamics, ensuring that the varied experiences of different racial and ethnic groups are appropriately captured and addressed in the model.

8.4 Illustrative Examples

8.4.1 Testbed Community Information

The "Pseudo Seaside" testbed was presented in Chapter 5 to model the earthquake and tsunami resilience of a small coastal community, informed by studies highlighting the elevated tsunami risk for Seaside, Oregon. The testbed uses machine learning to project urban development, incorporating building data, seasonal population changes, and construction characteristics. The

Random Forest regressor model predicts building replacement costs with strong accuracy (R^2 = 83%), considering factors like building footprint geometry. The testbed's strategic zoning categorizes areas based on proximity to the coast and associated risks, guiding tailored resilience planning for seismic and tsunami hazards. By delineating specific hazard zones, this testbed enables targeted analysis and planning, making it an essential tool for understanding community resilience. This comprehensive testbed will serve as the benchmark in this chapter of the dissertation, providing a robust framework for evaluating resilience strategies in high-risk coastal areas.

8.4.2 Initial Building Damage under Successive Seismic Events

Two different sets of multi-hazard fragility functions, developed in Chapters 3 and 4 for regular- and long-duration earthquakes, were applied to the Pseudo Seaside testbed community to analyze the damage patterns at the community level. This analysis was conducted using the community-level damage assessment framework developed in Chapter 5 of this dissertation. Additionally, it is important to note that the hazard mean recurrence interval (MRI) considered in this analysis is 1,000 years; for more information on this, readers are encouraged to refer to Chapter 5.

Figure 8-3 compares the initial damage assessment under these two seismic scenarios: regular-duration ground motions (GMs) and long-duration GMs. The fragility surfaces in Figure 8-3(a) (regular-duration GMs) and Figure 8-3(b) (long-duration GMs) demonstrate how the duration of an earthquake influences the vulnerability of structures to subsequent tsunami damage. It is apparent that the community under long-duration earthquakes experiences exacerbated damage patterns, with many building units reaching a complete damage state, particularly those near the coastline. This indicates that long-duration motions can significantly soften the structural systems in this area, making them more vulnerable to the tsunami waves in this joint hazard scenario.

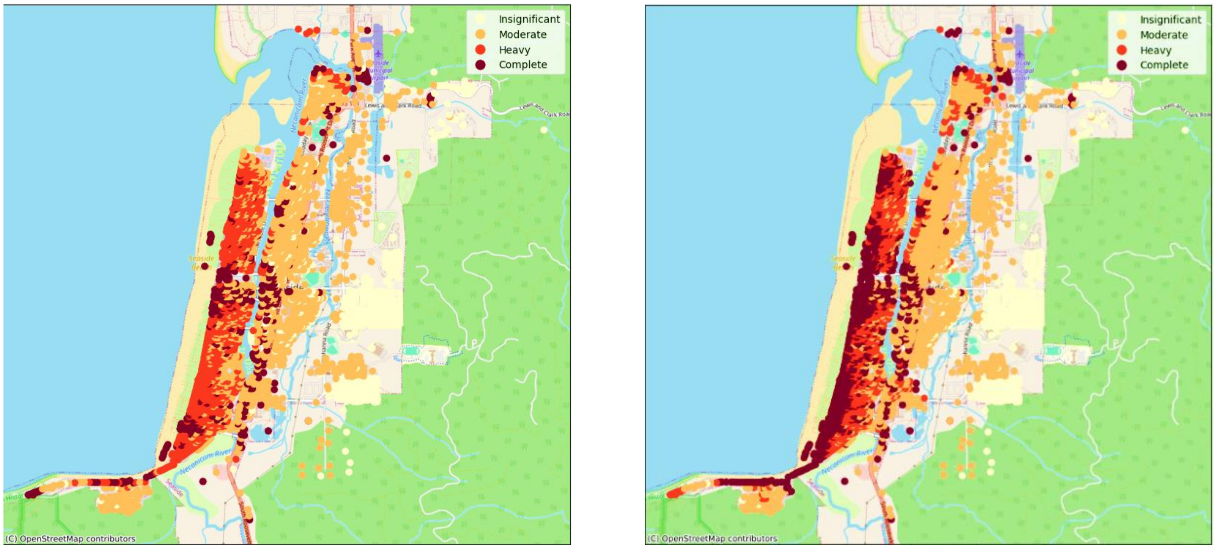

a) Regular-duration earthquakes

b) Long-duration earthquakes

Figure 8-3. Initial damage assessment in Pseudo Seaside under successive seismic hazards of the earthquake and tsunami using multi-hazard fragility surface: a) earthquake-tsunami fragility surfaces developed under regular-duration GMs b) earthquake-tsunami fragility surfaces developed based on long-duration GMs

Figure 8-4 illustrates the number of buildings in the Pseudo Seaside community that fall into each damage state when subjected to combined earthquake and tsunami hazard scenarios, as analyzed using the two different sets of multi-hazard vulnerability functions. The figure compares the distribution of damage states under regular-duration and long-duration ground motions (GMs). The data reveals that buildings exposed to long-duration earthquakes tend to suffer more severe damage, with a 41% increase in the number of buildings reaching the complete damage state (DS3). This finding suggests that long-duration seismic events can significantly weaken structural systems, making them more vulnerable to subsequent tsunami impacts in this joint hazard scenario. Consequently, for the remainder of the recovery modeling analyses in this dissertation, the multi-hazard earthquake-tsunami vulnerability functions developed under long-duration earthquakes, as presented in Chapter 4, will be utilized.

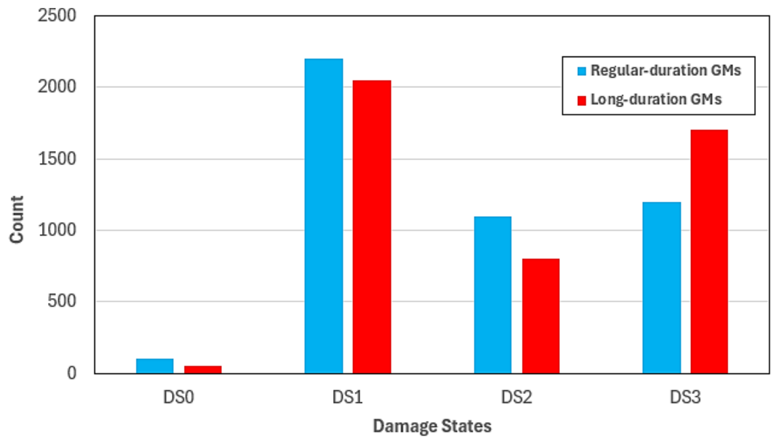

Figure 8-4. Number of buildings in Pseudo Seaside community being on each damage state in an earthquake and tsunami hazard scenarios analyzed using two different sets of multi-hazard vulnerability functions

The vulnerability functions for mainshocks and mainshock-aftershock sequences developed in Chapter 7 were applied to the Pseudo Seaside testbed community to assess its seismic response and resilience. A community-level analysis across various MRIs revealed that aftershock effects can significantly exacerbate damage, especially when the earthquake MRI exceeds 1000 years (PGA ≥ 0.65), causing over 30% of buildings to shift from DS1 to DS2. As depicted in Figure 7-11 in Chapter 7, the combined impact of mainshock and aftershock sequences reduces the percentage of buildings remaining in DS1 while increasing those in DS2 and DS3, underscoring the importance of including aftershocks in seismic vulnerability assessments. The hazard simulations and modeling procedures used here for recovery modeling under the mainshock and aftershock scenarios follow the same methodologies applied in the previous chapter. The spatial damage analysis (Figure 7-12 in Chapter 7) and economic loss differential (Figure 7-14 in Chapter 7) further demonstrate the heightened vulnerability and economic risk associated with aftershocks, which, if overlooked, could lead to significant underestimation of total economic losses. For a more detailed discussion, please refer to Chapter 7, Section 7.5.2.

8.4.3 Recovery and Population Dislocation Results

This section presents the recovery and population dislocation results following different seismic scenarios, specifically focusing on earthquake and tsunami events, as well as mainshock and aftershock sequences. The analysis provides insights into how these hazards impact the recovery trajectory of the Pseudo Seaside community and the displacement of its population. By examining the outcomes under these distinct scenarios, a comprehensive understanding of the community's resilience and the challenges faced during the recovery process is achieved.

8.4.3.1 Earthquake and Tsunami

Understanding recovery dynamics in response to different hazard types is crucial for improving community resilience. Figure 8-5 presents a comparative analysis of the building recovery process under earthquake-only, tsunami-only, and combined earthquake-tsunami scenarios at the community level. The figure illustrates the time-stepped recovery process, showing the percentage of recovery for all building categories (both residential and commercial) over time for each hazard type. To generate these recovery curves, the recovery paths of individual buildings were aggregated at the community level. The recovery modeling used a 1,000-year mean recurrence interval (MRI), consistent with the hazard simulations applied in the initial damage assessment. This ensures uniformity in the hazard simulations for all scenarios, including earthquake-only, tsunami-only, and combined earthquake and tsunami events. The figure demonstrates how each scenario uniquely affects the recovery trajectory, with the combined hazard scenario leading to the most prolonged and challenging recovery. Specifically, the recovery time for the community to reach 80% recovery is nearly twice as long in the combined hazard scenario compared to the tsunami-only scenario. However, the recovery time difference between the earthquake-only and combined hazard scenarios is less pronounced, especially for recovery percentages above 50%. Overall, the combined effects of an earthquake followed by a tsunami result in greater damage and slower recovery compared to single-hazard scenarios, underscoring the increased complexity and severity of recovery efforts in the presence of multiple hazards.

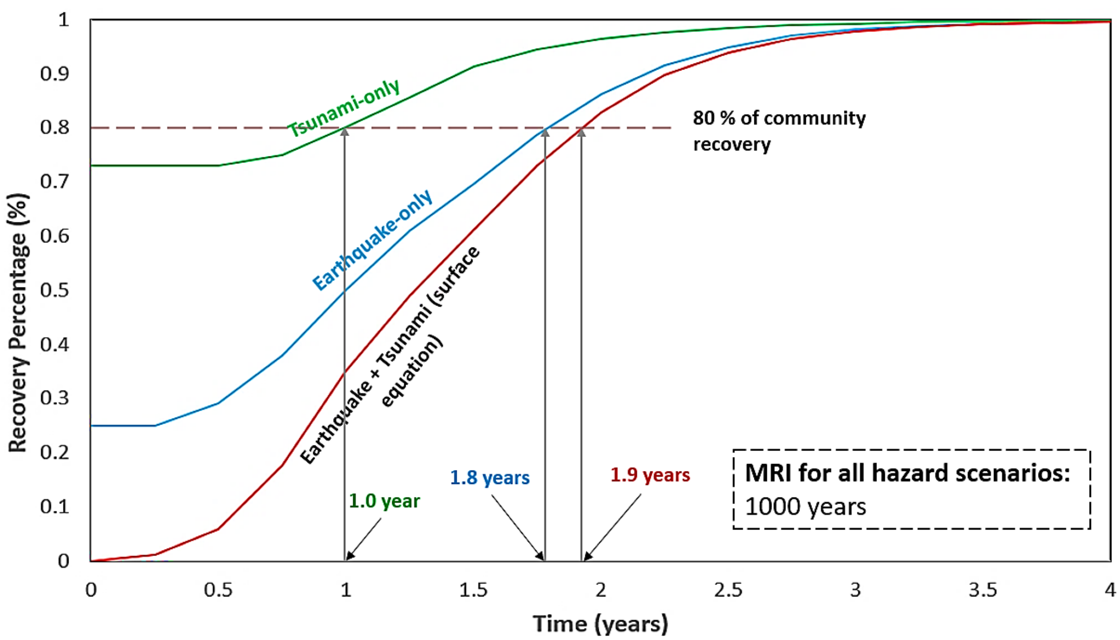

Figure 8-5. Time-stepping building recovery on the community level for different hazard types, including earthquake-only, tsunami-only, and the combined earthquake-tsunami joint hazard scenario.

This comparison offers valuable insights into community resilience under various disaster scenarios, underscoring the importance of comprehensive recovery planning that accounts for the compounded effects of multiple hazards. The recovery curves obtained through this analysis appear to be compatible with the initial damage assessments discussed in the previous section, illustrating how the precision of initial building damage analysis and the accuracy of developed fragility functions can significantly influence the uncertainties in recovery modeling and analysis.

Figure 8-6 utilizes the dislocation model introduced earlier in this chapter to analyze population dislocation within the target community, Pseudo Seaside, based on an MRI of 1,000 years. This approach ensures compatibility with the previous community-level analyses conducted in this chapter. The bar chart in Figure 8-6 features two axes: the first horizontal axis represents the different race and ethnicity groups defined earlier (G1 to G6), while the second axis illustrates the percentage of displaced people within each of these groups. The chart reveals that dislocation impacts vary significantly depending on both the hazard type and the demographic group. The tsunami-only scenario consistently shows the lowest dislocation percentages across all groups, with a total community impact of 8.52%. In contrast, the earthquake-only scenario results in much higher dislocation percentages, particularly for the G2 (White alone, Not Hispanic), G3 (Black alone, Not Hispanic), and G5 (Any Race, Hispanic) categories, where the dislocation percentages are 45.09%, 54.17%, and 46.79%, respectively. The combined hazards scenario, which considers the compounded effects of both an earthquake and a tsunami, leads to slightly higher dislocation percentages than the earthquake-only scenario, particularly for the G3 and G5 groups, with dislocation rates reaching 58.33% and 51.20%, respectively.

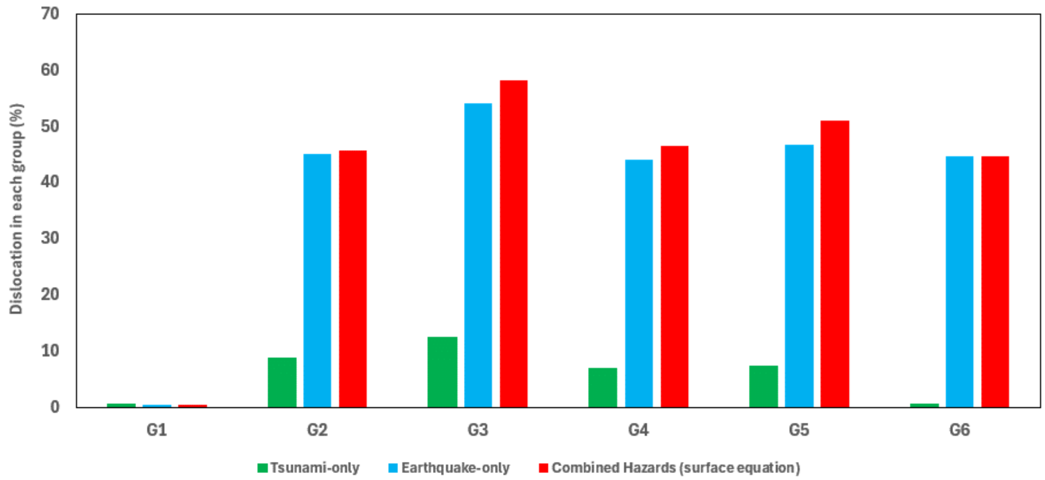

Figure 8-6. Population dislocation percentages by race and ethnicity (G1-G6) in Pseudo Seaside under tsunami-only, earthquake-only, and combined hazards scenarios

The G3 (Black alone, Not Hispanic) group is the most impacted across all scenarios, particularly under the earthquake-only and combined hazards scenarios. In contrast, G1 (Vacant HU No Race Ethnicity Data) and G6 (Group Quarters no Race Ethnicity Data) exhibit minimal variation across scenarios, with dislocation percentages remaining stable. Compared to the damage models and recovery model presented in this chapter, it appears that the results of population dislocation in each of the defined groups (G1-G6) have not been compounded as significantly as in the two other community-level resilience analyses—the damage assessment and building recovery modeling. The relatively smaller compounding effect observed in the population dislocation model, compared to the damage and recovery models, may be attributed to several factors. First, the population dislocation model might be less sensitive to the physical intensity of hazards that significantly influence building damage and recovery. While structural damage and recovery are directly affected by the severity of the earthquake and tsunami, population dislocation could be more influenced by socio-economic factors, such as mobility, access to resources, and individual or household decisions about whether to relocate. These factors may not compound in the same way that physical damage does under multiple hazards.

Additionally, a saturation effect might be occurring, where severe damage or slow recovery in a single hazard scenario (such as an earthquake) already results in high dislocation rates. As a result, adding a second hazard (such as a tsunami) may not significantly increase the already high displacement rates. Furthermore, some demographic groups, like G1 (Vacant HU No Race Ethnicity Data) and G6 (Group Quarters no Race Ethnicity Data), may be inherently more stable or less vulnerable to displacement, regardless of the hazard scenario. These groups might be less affected by the compounding effects that more directly impact physical infrastructure. Lastly, the assumptions and limitations inherent in the dislocation model could also play a role, potentially underestimating the interactions between multiple hazards or not fully capturing cumulative impacts. This suggests that while the dislocation model provides valuable insights, its dynamics differ from those driving damage and recovery, emphasizing the need for targeted strategies that consider the unique vulnerabilities of different demographic groups. Overall, Figure 8-6 highlights the importance of understanding how different hazards affect various demographic groups, emphasizing the need for targeted resilience strategies that consider the compounded effects of multiple hazards on vulnerable communities.

8.4.3.2 Mainshock and Aftershocks

In this section, the focus shifts to analyzing the recovery and population dislocation outcomes following a mainshock event and subsequent aftershocks. Building on the earlier discussions in Section 8.4.3.2, this analysis delves into how the compounded effects of aftershocks influence the overall recovery process and displacement patterns within the affected community, offering a deeper understanding of the extended challenges posed by aftershocks in the context of community resilience and recovery.

Figure 8-7 provides a detailed illustration of these dynamics under two different scenarios: a mainshock event and a mainshock-aftershock sequence, both modeled with a hazard MRI of 1,000 years to ensure compatibility with the previous sections of this chapter. Part (a) of Figure 8-7 presents the recovery data, organized by time intervals and building categories, with average recovery times calculated for each building within specific recovery ranges. This initial analysis offers a clear depiction of the recovery trajectories under both scenarios, highlighting differences in recovery progress over time.

Building on this, Part (b) of Figure 8-7 compares the recovery curves from the two scenarios, highlighting the delays caused by aftershocks. By calculating and averaging these positive differences, the analysis quantifies the overall impact of aftershocks on the recovery process. To ensure accuracy, the data is further refined through a cumulative sum, smoothing the recovery values over time. The final visualizations in Figure 8-7(b) illustrate the percentage of recovery over time and the extent to which aftershocks have delayed recovery, offering valuable insights into how different hazard scenarios affect the community's recovery trajectory. As shown in Figure 8-7(b), the delays caused by aftershock effects can average around 3 months for recovery percentages below 90%, extending to nearly 150 days for the final stages of the recovery process, where recovery exceeds 90%.

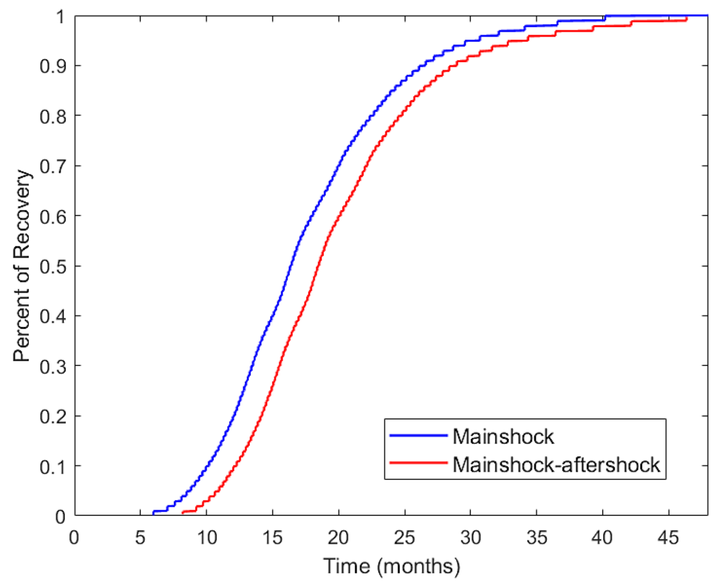

a) Community-level recovery curve

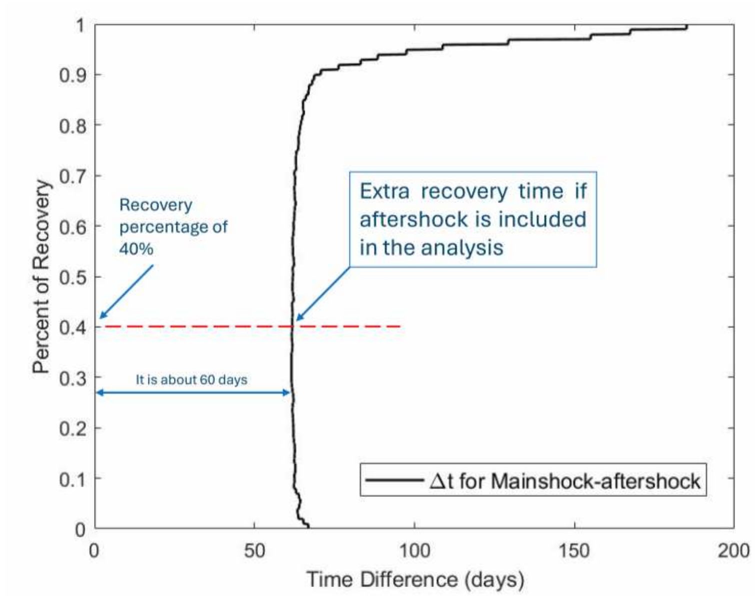

b) Recovery time difference between mainshock and aftershock

Figure 8-7. Community recovery dynamics and the effect of aftershocks on recovery times: (a) community-level recovery curve for mainshock and mainshock-aftershock scenarios, and (b) recovery time difference between mainshock and aftershock events

The observed delays in recovery, as shown in Figure 8-7(b), occur because aftershocks exacerbate the damage caused by the mainshock, slow down the repair process, and strain already limited recovery resources. In the early stages of recovery, when damage is widespread but less severe, the community may still recover relatively quickly despite the occurrence of aftershocks, resulting in an average delay of around 3 months for recovery percentages below 90%. However, in the later stages of recovery, where the focus shifts to restoring the final 10% of the community to pre-disaster conditions, aftershocks can significantly hinder progress. This is due to the fact that the remaining recovery tasks often involve more complex repairs or rebuilding efforts, which are more vulnerable to disruptions from aftershocks. As a result, the recovery delay extends to nearly 150 days during these final stages, reflecting the cumulative impact of aftershocks on a community already weakened by the initial mainshock.

The bar chart in Figure 8-8 compares dislocation percentages across different race and ethnicity groups under two scenarios: the mainshock and mainshock with aftershocks. This analysis, conducted for a PGA value of 0.85g, revealed in Chapter 7 that the percentage of buildings in the DS2 damage state increased by approximately 30% in the mainshock scenario compared to the mainshock-aftershock hazard scenario. The horizontal axis represents the various race and ethnicity groups (G1 to G6), while the vertical axis indicates the percentage of dislocation within each group. The chart shows that while there is a slight increase in dislocation percentages for certain groups, such as G2 (White alone, Not Hispanic) and G5 (Any Race, Hispanic) when aftershocks are considered, the overall difference is negligible. The total dislocation percentage rises from 49.25% to 50.48%, indicating that aftershocks have little to no meaningful effect on dislocation.

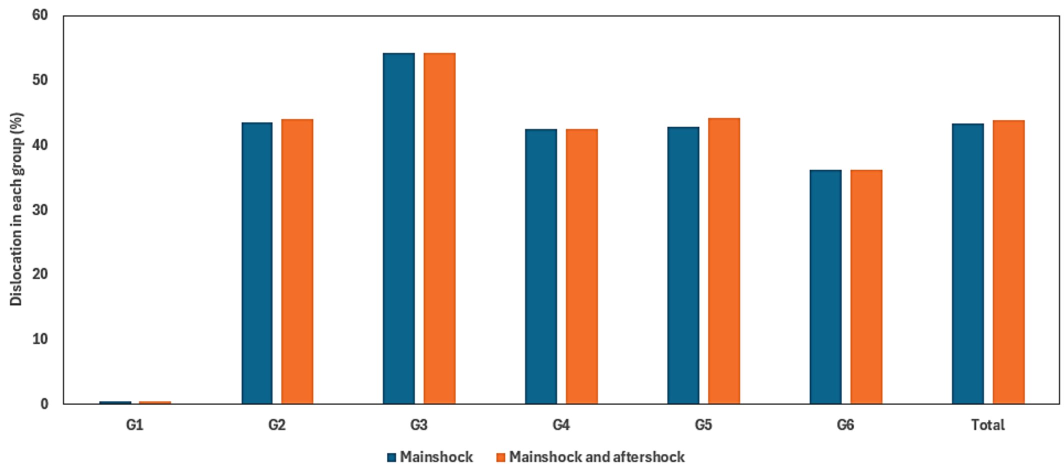

Figure 8-8. Dislocation percentages across race and ethnicity groups under mainshock and mainshock-aftershock scenarios at a PGA of 0.85g, showing slight increases in dislocation for certain groups and a minor overall rise in total dislocation.

The data from Chapter 7, along with the recovery analysis presented in this section, showed that the aftershock did cause additional damage, resulting in further delays in the community's overall recovery time. However, the community's initial displacement and damage from the mainshock might have reached a threshold where further displacement was limited, despite the increased damage. Additionally, the socio-economic factors influencing dislocation, such as access to resources and residents' decision-making processes, may not have been as sensitive to the aftershocks, leading to the observed minor effects on overall dislocation percentages. A similar pattern was observed in the dislocation analysis of the community under successive hazards of earthquake and tsunami in the previous section.

In conclusion, the analysis in this section underscores the significant impact that aftershocks can have on the recovery process, yet a marginal impact on population dislocation within a community. By comparing recovery dynamics between a mainshock event and a mainshock-aftershock sequence, the findings reveal how aftershocks can further delay recovery, intensifying the challenges faced by affected communities. However, the impact on population dislocation remains relatively minor. The detailed examination of recovery trajectories and the quantification of these delays provide essential insights into the need to account for aftershocks in resilience planning. These insights are critical for developing more robust recovery strategies that address the prolonged effects of aftershocks, ultimately fostering more resilient communities in the face of successive seismic events.

8.5 Discussion

In this section, the broader applicability and limitations of the restoration functions developed in the preceding analyses are discussed. These restoration functions, originally designed for earthquake scenarios, have the potential to be extended to other seismic-related hazards, such as tsunamis and aftershocks. The flexibility of these functions allows them to be adapted for use in various hazard contexts, offering valuable insights into recovery dynamics across different types of seismic events. By applying these functions to a wider range of scenarios, researchers and planners can better understand and predict the recovery trajectories of communities facing successive or compound hazards. However, it is important to acknowledge that the accuracy of these recovery models may decrease at very high seismic intensity levels. In such extreme cases, the complexity of damage and the intricacies of the recovery process may introduce uncertainties that the current models do not fully capture. This limitation is particularly relevant for scenarios involving intense seismic activity, where the restoration functions might struggle to account for the more severe and widespread damage, leading to potential inaccuracies in predicting recovery times.

A similar concern arises with the dislocation models used in this research. While these models are effective in estimating population displacement under moderate to high seismic intensities, they may also exhibit some level of inaccuracy when applied to extremely severe events. At very high seismic intensities, the factors influencing dislocation—such as structural failures, access to resources, and socio-economic variables—become more complex and may not be fully represented in the current model framework. This could lead to underestimations or overestimations of dislocation rates, particularly in communities facing catastrophic damage.

These considerations underscore the need for further refinement of both recovery and dislocation models, particularly when applied to scenarios involving very high seismic intensities. Improving these models to account for the complexities of extreme seismic events will enhance their reliability and utility in resilience planning, ultimately contributing to more effective strategies for managing recovery and population displacement in the aftermath of severe disasters.

CHAPTER 9: SUMMARY, CONTRIBUTIONS, AND RECOMMENDATIONS

9.1 Summary and Conclusions

In summary, this dissertation presents a comprehensive study aimed at advancing the methodologies for assessing and enhancing community resilience against multi-hazard events, with a particular focus on earthquakes and tsunamis. By employing advanced computational techniques, structural modeling, and machine learning algorithms, the research provides high-resolution, probabilistic assessments that significantly contribute to resilience planning and mitigation strategies. Each chapter systematically addresses various facets of multi-hazard resilience, including the compounded impacts of successive hazards, the effects of long-duration earthquakes, integrated risk assessments, and the development of innovative fragility modeling approaches. The findings demonstrate the effectiveness of these advanced methodologies in achieving accurate risk assessments and improving community resilience planning.

This research offers substantial contributions to the field by integrating long-duration seismic events into multi-hazard analyses and utilizing machine learning for fragility surface generation. The innovative approaches presented not only enhance the accuracy of risk assessments but also provide practical tools for resilience planning, such as the synthesized fragility surfaces for different building typologies and the comprehensive recovery trajectory framework. These advancements equip engineers and scientists with essential insights and methodologies for improving community resilience against the growing threats of natural hazards. Overall, this dissertation underscores the critical need for refined multi-hazard resilience planning and provides valuable recommendations for future research directions. The methodology has been included in IN-CORE to provide proper access to the models along with an IN-CORE example Jupyter notebook.

Chapter 2 presents a multi-distributed parallel processing framework that can be used to produce 3D fragility surfaces of near-field tsunamis and the source earthquake events. Uncertainty within the problem is disaggregated into three significant parts, including the uncertainties associated with the structural model as well as the uncertainties that exist in earthquake and tsunami loadings themselves. A RC moment frame was selected in Chapter 2 as the illustrative building example to examine the performance of the proposed framework for 3D fragility surface development. Furthermore, based on a parametric study performed in this chapter, it was demonstrated that the controlling parameters of the 3D fragility surfaces can be reliably obtained using 50 sets of random variables for uncertain parameters and 400 reference points over the joint IM space distributed over 400 cores/CPUs. It was shown that the proposed method is highly efficient in reducing the computational demands needed for developing these multi-hazard fragility surfaces, so this framework can be used as a time-efficient and scalable technique to develop the earthquake-tsunami fragility surfaces for a portfolio of building structures within a community. As a result, the final earthquake-tsunami fragility surfaces obtained for different damage states have smooth and near-continuous functions that can be easily implemented and employed in platforms like IN-CORE, focusing on risk and reliability analysis at the structure or community levels. In this regard, the governing surface equation and the controlling parameters of the presented fragility surfaces have been detailed in Chapter 2. It was also demonstrated in this chapter that the earthquake-only fragility curve at the complete collapse level of this study is in good agreement with equivalent IDA-based fragility curves developed in prior research studies. While the results of the study in this chapter are limited to the assumptions considered in the proposed methodology, it is clear that the fragility curves for the tsunami-only hazard at different damage states are impacted by the prior imposed earthquake loading, especially for the tsunami loading following earthquakes with higher values of earthquake IM. While this is an expected result, the ability to quantify it is key for risk and resilience studies.

Chapter 3 produced earthquake-tsunami fragility surfaces using three damage states for a portfolio of RC building and woodframe system archetypes. As outlined in Chapter 2, the uncertainties related to structural modeling and both hazards were included in the simulation procedure using a fully probabilistic successive analysis with two phases, i.e., an NTHA procedure for earthquake and an NSP analysis for tsunami. The considered frame archetypes arguably can be used as a portfolio for implementation into risk and resilience models for a coastal community. Through these earthquake-tsunami fragility surfaces, this chapter reveals a critical difference between non-ductile and ductile systems: while non-ductile RC frames can collapse at moderate earthquake intensities before the tsunami wave arrives, the ductile frames may endure the tsunami wave even when partially damaged, highlighting their superior performance and the benefits of modern design. The fragility surfaces for the tsunami and the source earthquake, which can directly incorporate the damaging impacts of both hazards successively, also have two sets of 2D fragility curves on their edges. Furthermore, the 2D and 3D fragility functions generated in this study are near-continuous for both earthquake and tsunami IMs. The controlling parameters of the 2D and 3D fragility equations were extracted and reported in this chapter, providing a basis for damage analysis to serve as initial conditions for recovery, and community resilience analysis of coastal communities exposed to these hazards.

Chapter 4 utilized a fully probabilistic simulation within a two-phase successive analysis procedure, introduced in Chapter 2, to investigate the potential impact of long-duration earthquakes on RC frame buildings. This was accomplished through the investigation in the changes in earthquake-tsunami fragility surfaces for a selected suite of typical RC frame and woodframe buildings. The vector-valued fragility surfaces for the earthquake and tsunami for the suite of RC frame buildings, exposed to both long-duration and regular-duration earthquakes, were evaluated in this chapter. The information pertinent to the parameters of scalar fragility curves for earthquake-only (with long durations) or tsunami-only, can be extracted directly from the edges of the fragility surfaces in their respective planes. Parameters for both the surfaces and scalar fragilities are provided for community modeling purposes and can serve as a data set for this suite of 16 RC and woodframe buildings. Additionally, studies in this chapter have shown that initial seismic damage resulting from the source earthquake in low- to mid-rise structures increases the probability of failure by up to 40% when subjected to long-duration earthquakes. Specifically, RC buildings up to 8 stories in height, including both ductile and non-ductile RC frames, are at a higher risk of structural damage and failure (defined with DS1, DS2 or DS3) in the earthquake before the tsunami strikes. Furthermore, equivalent tsunami forces in the second phase of the simulation exacerbate the condition of structures with more initial earthquake damage as one would expect. This study indicates that the conclusions can potentially be applicable to a wide range of buildings facing strength and stiffness degradation, although their current scope is confined to RC frame buildings. Further research is essential to determine their generalizability to other types of structures.

Chapter 5 has presented a comprehensive community level damage and direct loss analysis employing a novel methodology that integrates 3D fragility surfaces for combined earthquake and tsunami hazards, alongside 2D fragility curves for individual hazard scenarios. Accurate damage assessment across a community is critical as it serves as the first major step in community resilience analysis. Applied to the Pseudo Seaside testbed, this approach allowed for an in-depth evaluation of spatial damage, economic loss, and risk under single and multi-hazard scenarios. The findings underscore the importance of considering the successive effects of earthquakes and tsunamis in resilience planning, especially given the significant disparities in damage and loss estimations between single-hazard and combined scenarios. The development and application of 3D fragility surfaces, derived from 16 building archetypes within the Pseudo Seaside community, marks a necessary advancement in multi-hazard community resilience assessment. This methodology not only facilitates a better understanding of structural vulnerabilities but also enhances the accuracy of economic loss and risk predictions. The community-level analysis conducted in this chapter highlights the need for resilience planning in coastal communities, even at lower seismic intensities, and reveals the compounded risk presented by multi-hazard scenarios, particularly beyond an MRI of 250 years. It provides a critical examination of the FEMA combinational rule within the context of multi-hazard exposure demonstrating its accuracies but also its limitations. This underscores the need to continue to refine methods that better account for the interdependencies between seismic and tsunami hazards, thereby improving the precision of risk assessments and the formulation of mitigation strategies. The observations from the Pseudo Seaside testbed—ranging from the distribution of building types and their respective vulnerabilities to the detailed damage assessments—offer valuable insights into the dynamics of multi-hazard impacts on community resilience. In conclusion, the results of this chapter contribute significantly to the field of multi-hazard engineering by providing a robust methodology with application at the community level for the assessment of earthquake and tsunami risks, highlighting the urgency of integrating comprehensive multi-hazard analyses into resilience planning and resilience strategies. Future studies should aim to refine and expand upon the methodologies introduced here in this chapter, exploring their applicability to a broader range of community settings and structural archetypes, as well as focusing on time to recovery and inclusion of additional physical infrastructure, as well as socio-economic models.

Chapter 6 presents a physics-informed ML model capable of synthesizing 3D earthquake-tsunami fragility surfaces with high accuracy using (essentially any) two 2D fragility curves for earthquake and tsunami hazards. The ML model integrates comprehensive data preprocessing, hyperparameter tuning, and rigorous evaluation metrics. A sensitivity analysis conducted through FIE analysis between Extreme Gradient Boosting and Random Forest algorithms resulted in the final model being based on the Random Forest algorithm. This approach eliminates the need for HPC infrastructure and detailed FE modeling procedures, as it was required by the method presented in Chapter 2. Mitigation analysis using the Pseudo Seaside testbed showcased the practicality and effectiveness of this synthesized fragility surface approach in assessing and reducing multi-hazard risk at the community level. By horizontally shifting 2D fragility curves to represent retrofitted structural systems under a relevant hazard type, which served as input functions for the ML model, portfolios of retrofitted earthquake-tsunami fragility surfaces were generated and used as vulnerability models for the mitigation analysis. As an extension of the study presented in this chapter, the ML-based model can potentially be used for other multi-hazard fragility functions composed of two different 2D fragility curves from two distinct hazard types. For instance, multi-hazard fragilities such as earthquakes and fire-following earthquakes can be synthesized into a multi-hazard fragility surface using this proposed ML model. Moreover, it can be employed instead of FEMA's combinational rule—introduced in FEMA *(2022*)—to combine damage state exceedance probabilities from two different hazard types for fragility-related analyses or community resilience analysis using two separate (simulation-based or empirical) 2D fragility curves. More research is essential for these potential applications and extensions.

Chapter 7 has analyzed the seismic vulnerability and resilience of the Pseudo Seaside testbed community. By implementing a fully probabilistic methodology for the development of fragility functions applicable to both mainshock and mainshock-aftershock sequences, insights into the effect of including aftershocks in community level damage and loss analysis are illustrated. The findings reveal a critical elevation in risk and economic loss following aftershock sequences, particularly highlighted in scenarios with higher PGA values, demonstrating the essential consideration of aftershocks in seismic vulnerability assessment at the community level. By generating new fragility curves for mainshock and mainshock-aftershock sequences for the building archetypes required for the Pseudo Seaside testbed community and analyzing the differential effects of aftershocks on building damage states, this chapter highlights the need for incorporating comprehensive aftershock modeling in seismic vulnerability assessments. This is particularly important for communities similar to or larger than the Pseudo Seaside testbed to accurately estimate potential economic losses and enhance community resilience against sequential seismic events. Developing successive fragility functions for mainshock-aftershock sequences for a suite of representative building archetypes is critical to providing an accurate starting point for recovery analysis.

Chapter 8 presents an analysis of building recovery in communities exposed to successive events and hazards. The post-disaster recovery phase is crucial in community resilience modeling, as it addresses the wide-ranging effects of earthquake-induced hazards on a community's economy and social institutions. Quantifying losses across different community sectors delineates the recovery journey and plays a pivotal role in estimating damage at both building and community levels. These assessments aid in evaluating immediate post-event functionality and lay the foundation for probabilistic recovery analysis. By integrating advanced computational techniques and probabilistic methodologies, Chapter 8 provides a detailed framework for assessing and modeling the recovery trajectory of communities impacted by successive earthquake and tsunami events, equipping engineers and scientists with valuable insights into resilience enhancement strategies.

9.2 Contributions

The research contained in this dissertation offers the following contributions to the research communities, which are also highlighted in the flowchart displayed in Figure 9-1. While the flowchart provides context for how the work fits into the IN-CORE framework, it is important to emphasize that the primary contributions extend beyond just its integration into IN-CORE. Given this, the flowchart has been downplayed in the current revision to avoid overshadowing the broader impact of the research.

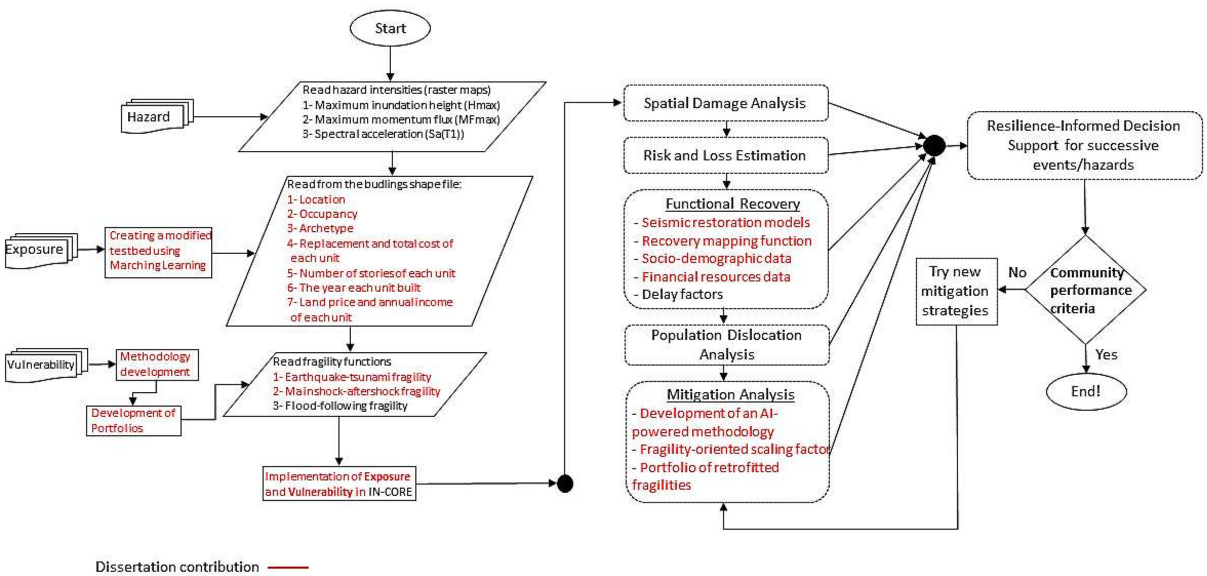

Figure 9-1. Contributions from this dissertation

- **Methodology for Successive Fragility Functions:** this dissertation presents a probabilistic multivariate/single-variable method to create fragility functions that consider successive events, including earthquakes, tsunamis, and the subsequent aftershocks following mainshocks.
- **Developing Earthquake-tsunami and Mainshock-aftershock Fragility Models:** this dissertation successfully generated fragility models for earthquake-tsunami scenarios and mainshock-aftershock sequences, concentrating on a diverse portfolio that includes both reinforced concrete (RC) and woodframe structures. These models play a pivotal role in evaluating building vulnerability to seismic and tsunami events, significantly enhancing the comprehension of the risks associated with these hazards.
- **Assessing the Influence of Long-duration Earthquakes on Earthquake-tsunami Fragility Surfaces:** This dissertation examines the influence of long-duration earthquakes on earthquake-tsunami fragility surfaces, with an emphasis on their overall impact rather than a detailed analysis of specific seismic characteristics. By assessing how long-duration ground shaking affects the vulnerability of structures to successive earthquake and tsunami events, the research offers a comprehensive understanding of the broader risks posed by these compound hazards. These findings contribute valuable insights into the development of more effective disaster resilience and mitigation strategies, helping to inform policies and practices aimed at reducing community vulnerability to earthquake-induced disasters.
- **Developing a High-resolution Community-level Tsunami Risk Analysis Framework:** this dissertation presents the development of an advanced, high-resolution framework aimed at conducting a comprehensive analysis of tsunami risk at the community level. The resulting robust tool is capable of assessing the complex and cumulative effects of

earthquakes and tsunamis on coastal communities. This tool enables precise and detailed assessments of damage and economic losses. The framework developed through this research is a valuable asset in strengthening preparedness and mitigation approaches for coastal regions susceptible to seismic and tsunami hazards.

- **Community Resilience Modeling for Mainshocks and Aftershocks:** this dissertation presents the creation of an adaptable community resilience model specifically designed to address the complexities presented by both mainshocks and their subsequent aftershock sequences. This model enables a comprehensive assessment of community resilience in the context of these seismic events, allowing exploration of the intricate interactions between the initial seismic occurrences and their subsequent aftershocks. It helps understand how the developed successive fragility functions influence community resilience metrics compared to a single event alone. The overarching objective is to deepen the understanding of the multifaceted risks associated with earthquake-induced hazards and actively contribute to the development of impactful resilience strategies.
- **Facilitating Resilience-Informed Decision-Making:** the results emerging from this research serve to inform decisions, primarily geared towards enhancing resilience for coastal communities susceptible to earthquake and tsunami. This encompasses identifying vulnerabilities linked to consecutive events and hazards within communities and crafting mitigation strategies to fortify their resilience. Moreover, the framework's flexibility enables seamless integration of pre-existing socio-economic models, creating a comprehensive decision-making resource. Additionally, the research delivers valuable insights through functional recovery analysis and population dislocation analysis, offering

a holistic understanding of communities' response and recovery capabilities in the face of successive events and hazards.

9.3 Recommendations

Based on the comprehensive studies and findings presented in this dissertation, several recommendations can be made for future research and practical applications in the field of multi-hazard community resilience. The integration of advanced computational techniques, structural modeling, and machine learning has opened new pathways for understanding and mitigating the risks associated with successive natural hazards. To build on these advancements and ensure their effective implementation, the following recommendations are proposed to guide future research endeavors and practical applications. By addressing gaps in current knowledge, expanding the scope of research, and promoting interdisciplinary collaboration, these recommendations will help pave the way for more comprehensive and impactful resilience strategies.

- **Expansion of Building Archetypes:** future research should expand the range of building archetypes to include a more diverse set of structural systems and materials, such as steel frames and masonry buildings. This will enhance the applicability of the developed fragility models to a broader range of community settings.
- **Incorporation of Additional Hazards:** the methodologies developed in this dissertation can be extended to include other natural hazards, such as hurricanes, floods, and wildfires. This will allow for a more comprehensive assessment of community resilience against multiple simultaneous or successive hazards.
- **Integration with Socio-Economic Models:** there is a need for further integration of the developed frameworks with detailed socio-economic models to better capture the impact of multi-hazard events on community recovery and resilience. This integration will provide

a more holistic understanding of the indirect effects of disasters on social and economic systems.

- **Development of Real-Time Assessment Tools:** future research should focus on developing real-time assessment tools based on the frameworks and models presented in this dissertation. These tools can be used by emergency managers and decision-makers to quickly evaluate the potential impacts of imminent natural hazards and to devise timely and effective response strategies.
- **Long-Duration Earthquake Studies:** Additional studies are needed to further explore the impacts of long-duration earthquakes on various types of structures and to refine the fragility models developed for these scenarios. This research will improve the accuracy of risk assessments and resilience planning for regions prone to long-duration seismic events.
- **Field Validation of Fragility Models:** Conducting field studies to validate the developed fragility models against observed data from past earthquakes and tsunamis will enhance the credibility and reliability of the models. Such validation efforts will also provide insights into the real-world performance of different structural systems under multi-hazard conditions.
- **Enhancement of Computational Techniques:** continuous improvement of the computational techniques used in this research, including the development of more efficient algorithms and the use of advanced hardware, will help manage the substantial computational demands associated with high-resolution, probabilistic assessments.
- **Community-Level Case Studies:** applying the developed methodologies to real-world communities, through detailed case studies, will provide practical insights and help refine

the models. These case studies can also demonstrate the effectiveness of the proposed frameworks in enhancing community resilience.

- **Education and Training:** it is recommended to develop educational programs and training workshops for engineers, urban planners, and emergency managers on the use of the developed tools and methodologies, i.e. within the context of IN-CORE. This will ensure that the knowledge and innovations from this research are effectively translated into practice.
- **Policy and Standards Development:** collaborating with policymakers and standard-setting organizations to incorporate the findings and methodologies of this dissertation into building codes and resilience planning guidelines will help institutionalize the advances made in multi-hazard resilience research.

By following these recommendations, future research can build on the foundations laid by this dissertation, further advancing the field of multi-hazard community resilience and contributing to safer, more resilient communities.

References

Abdollahzadeh, G., Mohammadgholipour, A., Omranian, E., 2019. Seismic Evaluation of Steel Moment Frames Under Mainshock–Aftershock Sequence Designed by Elastic Design and PBPD Methods. Journal of Earthquake Engineering 23, 1605–1628. https://doi.org/10.1080/13632469.2017.1387198

Abrahamson, N., Gregor, N., Addo, K., 2016. BC Hydro Ground Motion Prediction Equations for Subduction Earthquakes. Earthquake Spectra 32, 23–44. https://doi.org/10.1193/051712EQS188MR

Afshari, K., Stewart, J.P., 2016. Physically Parameterized Prediction Equations for Significant Duration in Active Crustal Regions. Earthquake Spectra 32, 2057–2081. https://doi.org/10.1193/063015EQS106M

Akhoondi, M.R., Behnamfar, F., 2021. Seismic fragility curves of steel structures including soil-structure interaction and variation of soil parameters. Soil Dynamics and Earthquake Engineering 143, 106609. https://doi.org/10.1016/j.soildyn.2021.106609

Alam, M.S., Barbosa, A.R., Scott, M.H., Cox, D.T., van de Lindt, J.W., 2019. Multi-hazard Earthquake-Tsunami Structural Fragility Assessment Framework, in: Proceedings of the 13th International Conference on Applications of Statistics and Probability in Civil Engineering (ICASP13). Korean Institute of Bridge and Structural Engineers, pp. 1318–1325. https://doi.org/10.22725/ICASP13.244

Alam, M.S., Barbosa, A.R., Scott, M.H., Cox, D.T., van de Lindt, J.W., 2018a. Development of Physics-Based Tsunami Fragility Functions Considering Structural Member Failures. J. Struct. Eng. 144, 04017221. https://doi.org/10.1061/(ASCE)ST.1943-541X.0001953

Alam, M.S., Barbosa, A.R., Scott, M.H., Cox, D.T., van de Lindt, J.W., 2018b. Development of Physics-Based Tsunami Fragility Functions Considering Structural Member Failures. J. Struct. Eng. 144, 04017221. https://doi.org/10.1061/(ASCE)ST.1943-541X.0001953

Aljawhari, K., Gentile, R., Galasso, C., 2022. A fragility-oriented approach for seismic retrofit design. Earthquake Spectra 38, 1813–1843. https://doi.org/10.1177/87552930221078324

Altoontash, A., 2004. SIMULATION AND DAMAGE MODELS FOR PERFORMANCE ASSESSMENT OF REINFORCED CONCRETE BEAM-COLUMN JOINTS 245.

America, J.F.P.J.F.P. covered nearly every aspect of national business news-including corporate, Street, W., Angeles, global economic matters-for more than 30 years in L., April 2020, N.Y.H. retired in, 2017. Few Californians have earthquake insurance, but interest has jumped since the Mexico quakes [WWW Document]. Los Angeles Times. URL https://www.latimes.com/business/la-fi-agenda-earthquake-insurance-20171002-story.html (accessed 8.22.24).

Amini, M., Jeon, H., Sanderson, D.R., Cox, D.T., Barbosa, A.R., Cutler, H., 2023a. Integrated Engineering–Economic Analysis for Multihazard Damage and Loss Assessment. J. Infrastruct. Syst. 29, 04023031. https://doi.org/10.1061/JITSE4.ISENG-2229

Amini, M., Sanderson, D.R., Cox, D.T., Barbosa, A.R., Rosenheim, N., 2023b. Methodology to incorporate seismic damage and debris to evaluate strategies to reduce life safety risk for multi-hazard earthquake and tsunami. Nat Hazards. https://doi.org/10.1007/s11069-023-05937-8

Amini, M.O., 2012. Determination of Seismic Performance Factors for Cross Laminated Timber Shear Wall System Based on FEMA P695 Methodology (Ph.D.). Colorado State University, United States -- Colorado.

Ancheta, T., Darragh, R., Stewart, J., Seyhan, E., Silva, W., Chiou, B., Wooddell, K., Graves, R., Kottke, A., Boore, D., Kishida, T., Donahue, J., 2014. NGA-West2 database. Earthquake Spectra 30. https://doi.org/10.1193/070913EQS197M

Ando, M., Nakamura, M., 2013. Seismological evidence for a tsunami earthquake recorded four centuries ago on historical documents. Geophysical Journal International 195, 1088–1101. https://doi.org/10.1093/gji/ggt270

Anil, Ö., Togay, A., Karagöz Işleyen, Ü., Döngel, N., Söğütlü, C., 2018. Effect of Timber Type and Nail Spacing on the Hysteretic Behavior of Timber-Framed Shear Walls with Openings. Int J Civ Eng 16, 629–646. https://doi.org/10.1007/s40999-016-0138-7

ASCE 7 standard | ASCE [WWW Document], 2002. URL https://www.asce.org/publications-and-news/asce-7 (accessed 11.30.22).

Assessing Seismic Performance of Buildings with Configuration Irregularities: Calibrating Current Standards and Practices, n.d.

Attary, N., Unnikrishnan, V.U., van de Lindt, J.W., Cox, D.T., Barbosa, A.R., 2017a. Performance-Based Tsunami Engineering methodology for risk assessment of structures. Engineering Structures 141, 676–686. https://doi.org/10.1016/j.engstruct.2017.03.071

Attary, N., Van De Lindt, J.W., Barbosa, A.R., Cox, D.T., Unnikrishnan, V.U., 2021. Performance-Based Tsunami Engineering for Risk Assessment of Structures Subjected to Multi-Hazards: Tsunami following Earthquake. Journal of Earthquake Engineering 25, 2065–2084. https://doi.org/10.1080/13632469.2019.1616335

Attary, N., van de Lindt, J.W., Unnikrishnan, V.U., Barbosa, A.R., Cox, D.T., 2017b. Methodology for Development of Physics-Based Tsunami Fragilities. J. Struct. Eng. 143, 04016223. https://doi.org/10.1061/(ASCE)ST.1943-541X.0001715

Bahmani, P., 2015. PERFORMANCE-BASED SEISMIC RETROFIT (PBSR) METHODOLOGY FOR MULTI- STORY BUILDINGS WITH FULL-SCALE EXPERIMENTAL VALIDATION.

Bahmani, P., van de Lindt, J.W., Gershfeld, M., Mochizuki, G.L., Pryor, S.E., Rammer, D., 2016. Experimental Seismic Behavior of a Full-Scale Four-Story Soft-Story Wood-Frame Building with Retrofits. I: Building Design, Retrofit Methodology, and Numerical Validation. J. Struct. Eng. 142, E4014003. https://doi.org/10.1061/(ASCE)ST.1943-541X.0001207

Baker, J.W., 2015. Efficient Analytical Fragility Function Fitting Using Dynamic Structural Analysis. Earthquake Spectra 31, 579–599. https://doi.org/10.1193/021113EQS025M

Bandyopadhyay, K.K., Hofmayer, C.H., Kassir, M.K., Pepper, S.E., 1990. Seismic fragility of nuclear power plant components (Phase II) (No. NUREG/CR-4659-Vol.3, BNL-NUREG--52007-Vol.3, 7252519). https://doi.org/10.2172/7252519

Barbato, M., Petrini, F., Unnikrishnan, V.U., Ciampoli, M., 2013. Performance-Based Hurricane Engineering (PBHE) framework. Structural Safety 45, 24–35. https://doi.org/10.1016/j.strusafe.2013.07.002

Barbosa, A.R., Ribeiro, F.L.A., Neves, L.A.C., 2017. Influence of earthquake ground-motion duration on damage estimation: application to steel moment resisting frames. Earthquake Engineering & Structural Dynamics 46, 27–49. https://doi.org/10.1002/eqe.2769

Belejo, A., Barbosa, A.R., Bento, R., 2017. Influence of ground motion duration on damage index-based fragility assessment of a plan-asymmetric non-ductile reinforced concrete building. Engineering Structures 151, 682–703. https://doi.org/10.1016/j.engstruct.2017.08.042

Belliazzi, S., Lignola, G.P., Di Ludovico, M., Prota, A., 2021. Preliminary tsunami analytical fragility functions proposal for Italian coastal residential masonry buildings. Structures 31, 68–79. https://doi.org/10.1016/j.istruc.2021.01.059

Biskinis, D.E., Roupakias, G.K., Fardis, M.N., 2004. Degradation of Shear Strength of Reinforced Concrete Members with Inelastic Cyclic Displacements. SJ 101, 773–783. https://doi.org/10.14359/13452

Bommer, J.J., Magenes, G., Hancock, J., Penazzo, P., 2004. The Influence of Strong-Motion Duration on the Seismic Response of Masonry Structures. Bulletin of Earthquake Engineering 2, 1–26. https://doi.org/10.1023/B:BEEE.0000038948.95616.bf

Bommer, J.J., Martínez-Pereira, A., 1999. THE EFFECTIVE DURATION OF EARTHQUAKE STRONG MOTION. Journal of Earthquake Engineering 3, 127–172. https://doi.org/10.1080/13632469909350343

Boore, D.M., Stewart, J.P., Seyhan, E., Atkinson, G.M., 2014. NGA-West2 Equations for Predicting PGA, PGV, and 5% Damped PSA for Shallow Crustal Earthquakes. Earthquake Spectra 30, 1057–1085. https://doi.org/10.1193/070113EQS184M

Borrero, J.C., Lynett, P.J., Kalligeris, N., 2015. Tsunami currents in ports. Phil. Trans. R. Soc. A. 373, 20140372. https://doi.org/10.1098/rsta.2014.0372

Breiman, L., 2001. Random Forests. Machine Learning 45, 5–32. https://doi.org/10.1023/A:1010933404324

Bruneau, M., Chang, S.E., Eguchi, R.T., Lee, G.C., O'Rourke, T.D., Reinhorn, A.M., Shinozuka, M., Tierney, K., Wallace, W.A., Von Winterfeldt, D., 2003. A Framework to Quantitatively Assess and Enhance the Seismic Resilience of Communities. Earthquake Spectra 19, 733–752. https://doi.org/10.1193/1.1623497

Burns, P.O., Barbosa, A.R., Olsen, M.J., Wang, H., 2021. Multihazard Damage and Loss Assessment of Bridges in a Highway Network Subjected to Earthquake and Tsunami Hazards. Nat. Hazards Rev. 22, 05021002. https://doi.org/10.1061/(ASCE)NH.1527-6996.0000429

Capozzo, M., Rizzi, A., Cimellaro, G.P., Domaneschi, M., Barbosa, A., Cox, D., 2019. Multi-Hazard Resilience Assessment of a Coastal Community Due to Offshore Earthquakes. J. Earthquake and Tsunami 13, 1950008. https://doi.org/10.1142/S1793431119500088

Carey, T.J., Mason, H.B., Barbosa, A.R., Scott, M.H., 2019. Multihazard Earthquake and Tsunami Effects on Soil–Foundation–Bridge Systems. J. Bridge Eng. 24, 04019004. https://doi.org/10.1061/(ASCE)BE.1943-5592.0001353

Carvajal, M., Cisternas, M., Gubler, A., Catalán, P.A., Winckler, P., Wesson, R.L., 2017. Reexamination of the magnitudes for the 1906 and 1922 Chilean earthquakes using Japanese tsunami amplitudes: Implications for source depth constraints. J. Geophys. Res. Solid Earth 122, 4–17. https://doi.org/10.1002/2016JB013269

Celik, O.C., Ellingwood, B.R., 2010. Seismic fragilities for non-ductile reinforced concrete frames – Role of aleatoric and epistemic uncertainties. Structural Safety 32, 1–12. https://doi.org/10.1016/j.strusafe.2009.04.003

Celik, O.C., Ellingwood, B.R., 2008. Modeling Beam-Column Joints in Fragility Assessment of Gravity Load Designed Reinforced Concrete Frames. Journal of Earthquake Engineering 12, 357–381. https://doi.org/10.1080/13632460701457215

Chandramohan, R., Baker, J.W., Deierlein, G.G., 2016. Quantifying the Influence of Ground Motion Duration on Structural Collapse Capacity Using Spectrally Equivalent Records. Earthquake Spectra 32, 927–950. https://doi.org/10.1193/122813eqs298mr2

Charvet, I., Suppasri, A., Kimura, H., Sugawara, D., Imamura, F., 2015. A multivariate generalized linear tsunami fragility model for Kesennuma City based on maximum flow depths, velocities and debris impact, with evaluation of predictive accuracy. Nat Hazards 79, 2073–2099. https://doi.org/10.1007/s11069-015-1947-8

Chen, L., Huang, C., Chen, H., Zheng, Z., 2022. Seismic fragility models of a bridge system based on copula method. Earthquake Spectra 38, 1417–1437. https://doi.org/10.1177/87552930211052573

Chen, T., Guestrin, C., 2016. XGBoost: A Scalable Tree Boosting System, in: Proceedings of the 22nd ACM SIGKDD International Conference on Knowledge Discovery and Data Mining. pp. 785–794. https://doi.org/10.1145/2939672.2939785

Chou, T.-C., Talalay, P., 2005. Generalized Equations for the Analysis of Inhibitions of Michaelis-Menten and Higher-Order Kinetic Systems with Two or More Mutually Exclusive and Nonexclusive Inhibitors. European Journal of Biochemistry 115, 207–216. https://doi.org/10.1111/j.1432-1033.1981.tb06218.x

Chua, C.T., Switzer, A.D., Suppasri, A., Li, L., Pakoksung, K., Lallemant, D., Jenkins, S.F., Charvet, I., Chua, T., Cheong, A., Winspear, N., 2021. Tsunami damage to ports: cataloguing damage to create fragility functions from the 2011 Tohoku event. Nat. Hazards Earth Syst. Sci. 21, 1887–1908. https://doi.org/10.5194/nhess-21-1887-2021

Cox, D., Barbosa, A., Alam, M., Amini, M., Kameshwar, S., Park, H., Sanderson, D., 2022. Report, in Seaside Testbed Data Inventory for Infrastructure, Population, and Earthquake-Tsunami Hazard. https://doi.org/10.17603/DS2-SP99-XV89

Dal Zilio, L., Ampuero, J.-P., 2023. Earthquake doublet in Turkey and Syria. Commun Earth Environ 4, 71. https://doi.org/10.1038/s43247-023-00747-z

De Risi, R., Goda, K., Yasuda, T., Mori, N., 2017. Is flow velocity important in tsunami empirical fragility modeling? Earth-Science Reviews 166, 64–82. https://doi.org/10.1016/j.earscirev.2016.12.015

Del Zoppo, M., Di Ludovico, M., Prota, A., 2022. A mechanics-based method towards risk assessment of RC buildings under tsunami and flow-type hazards. Engineering Structures 264, 114452. https://doi.org/10.1016/j.engstruct.2022.114452

Del Zoppo, M., Wijesundara, K., Rossetto, T., Dias, P., Baiguera, M., Di Ludovico, M., Thamboo, J., Prota, A., 2021. Influence of exterior infill walls on the performance of RC frames under tsunami loads: Case study of school buildings in Sri Lanka. Engineering Structures 234, 111920. https://doi.org/10.1016/j.engstruct.2021.111920

Division of Financial Regulation : Earthquake insurance : Storm damage : State of Oregon [WWW Document], n.d. URL https://dfr.oregon.gov/insure/home/storm/pages/earthquake.aspx (accessed 8.22.24).

Ellingwood, B., 1980. Development of a probability based load criterion for American National Standard A58 236.

Fardis, M.N., Biskinis, D., 2003. Deformation capacity of RC members, as controlled by flexure or shear. Otani Symposium 511–530.

FEMA, 2022. Hazus Tsunami Model User Guidance [WWW Document]. URL https://www.emat-tx.org/News/12989969 (accessed 3.25.24).

Ferrotto, M.F., Cavaleri, L., 2021. Masonry structures: A proposal of analytical generation of fragility functions for tsunami impact – Application to the Mediterranean coasts. Engineering Structures 242, 112463. https://doi.org/10.1016/j.engstruct.2021.112463

Fiorillo, G., Ghosn, M., 2018. MPI Parallel Monte Carlo Framework for the Reliability Analysis of Highway Bridges. J. Comput. Civ. Eng. 32, 04017087. https://doi.org/10.1061/(ASCE)CP.1943-5487.0000735

Folz, B., Filiatrault, A., 2001. Cyclic Analysis of Wood Shear Walls. J. Struct. Eng. 127, 433–441. https://doi.org/10.1061/(ASCE)0733-9445(2001)127:4(433)

Frankel, A., Wirth, E., Marafi, N., 2018. The M9 Project Ground Motions. https://doi.org/10.17603/DS2WM3W

Fraser, S., Raby, A., Pomonis, A., Goda, K., Chian, S.C., Macabuag, J., Offord, M., Saito, K., Sammonds, P., 2013. Tsunami damage to coastal defences and buildings in the March 11th 2011 M w 9.0 Great East Japan earthquake and tsunami. Bull Earthquake Eng 11, 205–239. https://doi.org/10.1007/s10518-012-9348-9

Ginting, B.M., Mundani, R.-P., 2019. Parallel Flood Simulations for Wet–Dry Problems Using Dynamic Load Balancing Concept. J. Comput. Civ. Eng. 33, 04019013. https://doi.org/10.1061/(ASCE)CP.1943-5487.0000823

Goda, K., 2020. Multi-Hazard Portfolio Loss Estimation for Time-Dependent Shaking and Tsunami Hazards. Front. Earth Sci. 8, 592444. https://doi.org/10.3389/feart.2020.592444

Goda, K., 2012. Nonlinear Response Potential of Mainshock-Aftershock Sequences from Japanese Earthquakes. Bulletin of the Seismological Society of America 102, 2139–2156. https://doi.org/10.1785/0120110329

Goda, K., De Risi, R., De Luca, F., Muhammad, A., Yasuda, T., Mori, N., 2021. Multi-hazard earthquake-tsunami loss estimation of Kuroshio Town, Kochi Prefecture, Japan considering the Nankai-Tonankai megathrust rupture scenarios. International Journal of Disaster Risk Reduction 54, 102050. https://doi.org/10.1016/j.ijdrr.2021.102050

González-Dueñas, C., Padgett, J.E., 2021. Performance-Based Coastal Engineering Framework. Front. Built Environ. 7, 690715. https://doi.org/10.3389/fbuil.2021.690715

Greco, W.R., Bravo, G., Parsons, J.C., 1995. The search for synergy: a critical review from a response surface perspective. Pharmacol Rev 47, 331–385.

Günay, S., Mosalam, K.M., 2013. PEER Performance-Based Earthquake Engineering Methodology, Revisited. Journal of Earthquake Engineering 17, 829–858. https://doi.org/10.1080/13632469.2013.787377

Hamburger, R.O., Krawinkler, H., Malley, J.O., Adan, S.M., 2009. Seismic design of steel special moment frames: a guide for practicing engineers (No. NIST GCR 09-917-3). National Institute of Standards and Technology, Gaithersburg, MD. https://doi.org/10.6028/NIST.GCR.09-917-3

Han, R., Li, Y., van de Lindt, J., 2014. Seismic risk of base isolated non-ductile reinforced concrete buildings considering uncertainties and mainshock–aftershock sequences. Structural Safety 50, 39–56. https://doi.org/10.1016/j.strusafe.2014.03.010

Hancock, J., Bommer, J.J., 2007. Using spectral matched records to explore the influence of strong-motion duration on inelastic structural response. Soil Dynamics and Earthquake Engineering 27, 291–299. https://doi.org/10.1016/j.soildyn.2006.09.004

Harati, M., Mashayekhi, M., Ashoori Barmchi, M., Estekanchi, H., 2019. Influence of Ground Motion Duration on the Structural Response at Multiple Seismic Intensity Levels. NMCE 3, 10–23. https://doi.org/10.29252/nmce.3.4.10

Harati, M., Mashayekhi, M., Mohammadnezhad, H., Jaberi, H., Estekanchi, H.E., 2021. On the reduction of the number of required motions in the dynamic analysis using a refined

spectral matching. Earthquakes and Structures 21, 425–444. https://doi.org/10.12989/eas.2021.21.4.425
Harati, M., van de Lindt, J.W., 2024. Methodology to generate earthquake-tsunami fragility surfaces for community resilience modeling. Engineering Structures 305, 117700. https://doi.org/10.1016/j.engstruct.2024.117700
Harati, Mojtaba, 2024. Simulation of Successive Events for Multi-hazard Community Resilience Analysis (Doctoral Dissertation). Colorado State University.
Harati, Mojtaba, van de Lindt, John W., 2024a. Impact of Long-duration Earthquakes on Successive Earthquake-tsunami Fragilities for Reinforced Concrete Frame Archetypes. Journal of Structural Engineering 150, 1–19.
Harati, Mojtaba, van de Lindt, John W., 2024b. Fragility Function Development of RC Building Portfolio for Use in Earthquake-Tsunami Community Resilience Studies. Journal of Performance of Constructed Facilities.
Harati, Mojtaba, van de Lindt, John W., 2024c. Community-Level Resilience Analysis using Earthquake-Tsunami Fragility Surfaces. Resilient Cities and Structures.
Hardyniec, A., Charney, F., 2015. A new efficient method for determining the collapse margin ratio using parallel computing. Computers & Structures 148, 14–25. https://doi.org/10.1016/j.compstruc.2014.11.003
Haselton, C.B., 2006. Assessing seismic collapse safety of modern reinforced concrete moment frame buildings (Thesis). Stanford University.
Haselton, C.B., Goulet, C.A., Mitrani-Reiser, J., Beck, J.L., Deierlein, G.G., Porter, K.A., Stewart, J.P., Taciroglu, E., 2008. An Assessment to Benchmark the Seismic Performance of a Code-Conforming Reinforced Concrete Moment-Frame Building 382.
Haselton, C.B., Liel, A.B., Deierlein, G.G., Dean, B.S., Chou, J.H., 2011. Seismic Collapse Safety of Reinforced Concrete Buildings. I: Assessment of Ductile Moment Frames. J. Struct. Eng. 137, 481–491. https://doi.org/10.1061/(ASCE)ST.1943-541X.0000318
Hashimoto, T., Honda, T., Oda, Y., 2023. Study on the Effect of Density Change Due to Suspended Fine Sediment on Tsunami Force. Presented at the The 33rd International Ocean and Polar Engineering Conference, OnePetro.
Hatzigeorgiou, G.D., Beskos, D.E., 2009. Inelastic displacement ratios for SDOF structures subjected to repeated earthquakes. Engineering Structures 31, 2744–2755. https://doi.org/10.1016/j.engstruct.2009.07.002
Hazus Earthquake Model Technical Manual, 2020. 436.
Hazus Earthquake Model Technical Manual, n.d.
Hu, J., Wen, W., Zhai, C., Pei, S., Ji, D., 2023. Seismic resilience assessment of buildings considering the effects of mainshock and multiple aftershocks. Journal of Building Engineering 68, 106110. https://doi.org/10.1016/j.jobe.2023.106110
Hu, S., Wang, W., Shahria Alam, M., 2021. Comparative Study on Seismic Fragility Assessment of Self-Centering Energy-Absorbing Dual Rocking Core versus Buckling Restrained Braced Systems under Mainshock–Aftershock Sequences. J. Struct. Eng. 147, 04021124. https://doi.org/10.1061/(ASCE)ST.1943-541X.0003082
Ibarra, L.F., Krawinkler, H., 2005. Global Collapse of Frame Structures under Seismic Excitations, John A. Blume Earthquake Engineering Center Technical Report Series.
Ibarra, L.F., Medina, R.A., Krawinkler, H., 2005. Hysteretic models that incorporate strength and stiffness deterioration. Earthquake Engng Struct. Dyn. 34, 1489–1511. https://doi.org/10.1002/eqe.495

IN-CORE [WWW Document], n.d. URL https://incore.ncsa.illinois.edu/ (accessed 9.14.24).
Ishibashi, H., Akiyama, M., Frangopol, D.M., Koshimura, S., Kojima, T., Nanami, K., 2021. Framework for estimating the risk and resilience of road networks with bridges and embankments under both seismic and tsunami hazards. Structure and Infrastructure Engineering 17, 494–514. https://doi.org/10.1080/15732479.2020.1843503
Iwai, S., Goto, K., 2021. Threshold flow depths to move large boulders by the 2011 Tohoku-oki tsunami. Sci Rep 11, 13434. https://doi.org/10.1038/s41598-021-92917-2
Jafari, S., Mahini, S.S., 2023. Enhancement of the Fragility Capacity of RC Frames Using FRPs with Different Configurations at Joints. Polymers 15, 618. https://doi.org/10.3390/polym15030618
Jalayer, F., Cornell, C.A., 2009. Alternative non-linear demand estimation methods for probability-based seismic assessments. Earthquake Engineering & Structural Dynamics 38, 951–972. https://doi.org/10.1002/eqe.876
Jiang, W., Wang, F., Zheng, Xiaocui, Zheng, Xinxin, Qiao, X., Li, X., Meng, Q., 2022. Toward Interoperable Multi-hazard Modeling: A Disaster Management System for Disaster Model Service Chain. Int J Disaster Risk Sci 13, 862–877. https://doi.org/10.1007/s13753-022-00450-1
Jojok Widodo, S., Entin, H., Faizatus, S., 2021. A literature review: model of disaster risk reduction for decision support system. E3S Web Conf. 331, 04011. https://doi.org/10.1051/e3sconf/202133104011
Kajitani, Y., Chang, S.E., Tatano, H., 2013. Economic Impacts of the 2011 Tohoku-Oki Earthquake and Tsunami. Earthquake Spectra 29, 457–478. https://doi.org/10.1193/1.4000108
Karafagka, S., Fotopoulou, S., Pitilakis, K., 2018. Analytical tsunami fragility curves for seaport RC buildings and steel light frame warehouses. Soil Dynamics and Earthquake Engineering 112, 118–137. https://doi.org/10.1016/j.soildyn.2018.04.037
Kazama, M., Noda, T., 2012. Damage statistics (Summary of the 2011 off the Pacific Coast of Tohoku Earthquake damage). Soils and Foundations 52, 780–792. https://doi.org/10.1016/j.sandf.2012.11.003
Kazantzi, A.K., Righiniotis, T.D., Chryssanthopoulos, M.K., 2008. Fragility and Hazard Analysis of a Welded Steel Moment Resisting Frame. Journal of Earthquake Engineering 12, 596–615. https://doi.org/10.1080/13632460701512993
Kempton, J.J., Stewart, J.P., 2006. Prediction Equations for Significant Duration of Earthquake Ground Motions considering Site and Near-Source Effects. Earthquake Spectra 22, 985–1013. https://doi.org/10.1193/1.2358175
Kern, S.E., Xie, G., White, J.L., Egan, T.D., 2004. A Response Surface Analysis of Propofol–Remifentanil Pharmacodynamic Interaction in Volunteers. Anesthesiology 100, 1373–1381. https://doi.org/10.1097/00000542-200406000-00007
Koliou, M., Van De Lindt, J.W., 2020. Development of Building Restoration Functions for Use in Community Recovery Planning to Tornadoes. Nat. Hazards Rev. 21, 04020004. https://doi.org/10.1061/(ASCE)NH.1527-6996.0000361
Koliou, M., van de Lindt, J.W., McAllister, T.P., Ellingwood, B.R., Dillard, M., Cutler, H., 2020. State of the research in community resilience: progress and challenges. Sustainable and Resilient Infrastructure 5, 131–151. https://doi.org/10.1080/23789689.2017.1418547

Kourehpaz, P., Molina Hutt, C., Lallemant, D., 2023. Toward multivariate fragility functions for seismic damage and loss estimation of high-rise buildings. Earthq Engng Struct Dyn 52, 4164–4182. https://doi.org/10.1002/eqe.3993

Li, T., Yang, Y., Dai, K., Ge, Q., Wang, J., 2022. Influence of ground motion duration on seismic performance of RC frame isolated by high damping rubber bearings. Engineering Structures 262, 114398. https://doi.org/10.1016/j.engstruct.2022.114398

Li, Y., Song, R., Van De Lindt, J.W., 2014. Collapse Fragility of Steel Structures Subjected to Earthquake Mainshock-Aftershock Sequences. J. Struct. Eng. 140, 04014095. https://doi.org/10.1061/(ASCE)ST.1943-541X.0001019

Liel, A., Deierlein, G., 2008. ASSESSING THE COLLAPSE RISK OF CALIFORNIA'S EXISTING REINFORCED CONCRETE FRAME STRUCTURES: METRICS FOR SEISMIC SAFETY DECISIONS.

Liel, A.B., Haselton, C.B., Deierlein, G.G., 2011. Seismic Collapse Safety of Reinforced Concrete Buildings. II: Comparative Assessment of Nonductile and Ductile Moment Frames. J. Struct. Eng. 137, 492–502. https://doi.org/10.1061/(ASCE)ST.1943-541X.0000275

Lignos, D.G., Krawinkler, H., 2011. Deterioration Modeling of Steel Components in Support of Collapse Prediction of Steel Moment Frames under Earthquake Loading. J. Struct. Eng. 137, 1291–1302. https://doi.org/10.1061/(ASCE)ST.1943-541X.0000376

Lindt, J.W. van de, Ellingwood, B., McAllister, T.P., Gardoni, P., Cox, D., Peacock, W.G., Cutler, H., Dillard, M., Lee, J., Peek, L., Mitrani-Reiser, J., 2018. Modeling Community Resilience: Update on the Center for Risk-Based Community Resilience Planning and the Computational Environment IN-CORE. NIST.

Lynett, P.J., Wu, T.-R., Liu, P.L.-F., 2002. Modeling wave runup with depth-integrated equations. Coastal Engineering 46, 89–107. https://doi.org/10.1016/S0378-3839(02)00043-1

Ma, X., Zhang, W., Li, X., Ding, Z., 2021. Evaluating tsunami damage of wood residential buildings in a coastal community considering waterborne debris from buildings. Engineering Structures 244, 112761. https://doi.org/10.1016/j.engstruct.2021.112761

Mashayekhi, M., Harati, M., Ashoori Barmchi, M., Estekanchi, H.E., 2019. Introducing a response-based duration metric and its correlation with structural damages. Bull Earthquake Eng 17, 5987–6008. https://doi.org/10.1007/s10518-019-00716-y

Mashayekhi, M., Harati, M., Darzi, A., Estekanchi, H.E., 2020a. Incorporation of strong motion duration in incremental-based seismic assessments. Engineering Structures 223, 111144. https://doi.org/10.1016/j.engstruct.2020.111144

Mashayekhi, M., Harati, M., Darzi, A., Estekanchi, H.E., 2020b. Incorporation of strong motion duration in incremental-based seismic assessments. Engineering Structures 223, 111144. https://doi.org/10.1016/j.engstruct.2020.111144

Matsutomi, H., Okamoto, K., 2010. Inundation flow velocity of tsunami on land. Island Arc 19, 443–457. https://doi.org/10.1111/j.1440-1738.2010.00725.x

McFall, B.C., Fritz, H.M., 2016. Physical modelling of tsunamis generated by three-dimensional deformable granular landslides on planar and conical island slopes. Proc. R. Soc. A. 472, 20160052. https://doi.org/10.1098/rspa.2016.0052

McLaren, T.M., Myers, J.D., Lee, J.S., Tolbert, N.L., Hampton, S.D., Navarro, C.M., 2008. MAEviz: an earthquake risk assessment system, in: Proceedings of the 16th ACM SIGSPATIAL International Conference on Advances in Geographic Information Systems. Presented at the GIS '08: 16th International Symposium on Advances in Geographic

Information Systems, ACM, Irvine California, pp. 1–2. https://doi.org/10.1145/1463434.1463534

Medina, S., Lizarazo-Marriaga, J., Estrada, M., Koshimura, S., Mas, E., Adriano, B., 2019. Tsunami analytical fragility curves for the Colombian Pacific coast: A reinforced concrete building example. Engineering Structures 196, 109309. https://doi.org/10.1016/j.engstruct.2019.109309

Mojtaba Harati, John van de Lindt, 2024. Methodology to Generate Earthquake-tsunami Fragility Surfaces for Community Resilience Modeling. Engineering Structures.

Moon, W.C., Lau, T.L., n.d. Experimental Modelling of Tsunami-Like Waves Approaching the Gentle Coast of Malaysia.

N, P, R, 2019. Why Only 13% Of California Homeowners Have Earthquake Insurance. NPR.

Nofal, O.M., van de Lindt, J.W., 2020. Minimal Building Flood Fragility and Loss Function Portfolio for Resilience Analysis at the Community Level. Water 12, 2277. https://doi.org/10.3390/w12082277

Paez-Ramirez, J., Lizarazo-Marriaga, J., Medina, S., Estrada, M., Mas, E., Koshimura, S., 2020. A comparative study of empirical and analytical fragility functions for the assessment of tsunami building damage in Tumaco, Colombia. Coastal Engineering Journal 62, 362–372. https://doi.org/10.1080/21664250.2020.1726558

Panagiotakos, T.B., Fardis, M.N., 2001. Deformations of Reinforced Concrete Members at Yielding and Ultimate. SJ 98, 135–148. https://doi.org/10.14359/10181

Pang, Y., Wang, X., 2021. Cloud-IDA-MSA Conversion of Fragility Curves for Efficient and High-Fidelity Resilience Assessment. J. Struct. Eng. 147, 04021049. https://doi.org/10.1061/(ASCE)ST.1943-541X.0002998

París, J., Colominas, I., Navarrina, F., Casteleiro, M., 2013. Parallel computing in topology optimization of structures with stress constraints. Computers & Structures 125, 62–73. https://doi.org/10.1016/j.compstruc.2013.04.016

Park, H., Cox, D.T., Alam, M.S., Barbosa, A.R., 2017a. Probabilistic Seismic and Tsunami Hazard Analysis Conditioned on a Megathrust Rupture of the Cascadia Subduction Zone. Front. Built Environ. 3, 32. https://doi.org/10.3389/fbuil.2017.00032

Park, H., Cox, D.T., Barbosa, A.R., 2017b. Comparison of inundation depth and momentum flux based fragilities for probabilistic tsunami damage assessment and uncertainty analysis. Coastal Engineering 122, 10–26. https://doi.org/10.1016/j.coastaleng.2017.01.008

Park, S., van de Lindt, J.W., Cox, D., Gupta, R., Aguiniga, F., 2012. Successive Earthquake-Tsunami Analysis to Develop Collapse Fragilities. Journal of Earthquake Engineering 16, 851–863. https://doi.org/10.1080/13632469.2012.685209

Park, Y., Ang, A.H. -S., 1985. Mechanistic Seismic Damage Model for Reinforced Concrete. J. Struct. Eng. 111, 722–739. https://doi.org/10.1061/(ASCE)0733-9445(1985)111:4(722)

Peacock, W.G., Gladwin, H., Morrow, B.H. (Eds.), 1997. Hurricane Andrew: Ethnicity, Gender and the Sociology of Disasters. Routledge, London. https://doi.org/10.4324/9780203351628

Petrone, C., Rossetto, T., Baiguera, M., la Barra Bustamante, C.D., Ioannou, I., 2020. Fragility functions for a reinforced concrete structure subjected to earthquake and tsunami in sequence. Engineering Structures 205, 110120. https://doi.org/10.1016/j.engstruct.2019.110120

Petrone, C., Rossetto, T., Goda, K., 2017. Fragility assessment of a RC structure under tsunami actions via nonlinear static and dynamic analyses. Engineering Structures 136, 36–53. https://doi.org/10.1016/j.engstruct.2017.01.013

Porter, K.A., Beck, J.L., Shaikhutdinov, R.V., 2002. Sensitivity of Building Loss Estimates to Major Uncertain Variables. Earthquake Spectra 18, 719–743. https://doi.org/10.1193/1.1516201

Presidential Policy Directive -- Critical Infrastructure Security and Resilience, 2014.

Publications :: FEMA P-695, Quantification of Building Seismic Performance Factors - Applied Technology Council Online Store [WWW Document], 2009. URL https://store.atcouncil.org/index.php?dispatch=products.view&product_id=210 (accessed 11.30.09).

Raghunandan, M., Liel, A.B., Luco, N., 2015. Aftershock collapse vulnerability assessment of reinforced concrete frame structures: AFTERSHOCK COLLAPSE ASSESSMENT OF REINFORCED CONCRETE STRUCTURES. Earthquake Engng Struct. Dyn. 44, 419–439. https://doi.org/10.1002/eqe.2478

Roohi, M., Hernandez, E.M., Rosowsky, D., 2019. Nonlinear seismic response reconstruction and performance assessment of instrumented wood-frame buildings—Validation using NEESWood Capstone full-scale tests. Struct Control Health Monit 26. https://doi.org/10.1002/stc.2373

Rosenheim, N., 2021. Detailed Household and Housing Unit Characteristics: Data and Replication Code. https://doi.org/10.17603/DS2-JWF6-S535

Rosenheim, N., Guidotti, R., Gardoni, P., Peacock, W., 2019. Integration of detailed household and housing unit characteristic data with critical infrastructure for post-hazard resilience modeling. Sustainable and Resilient Infrastructure 6, 1–17. https://doi.org/10.1080/23789689.2019.1681821

Rosenheim, N., Guidotti, R., Gardoni, P., Peacock, W.G., 2021. Integration of detailed household and housing unit characteristic data with critical infrastructure for post-hazard resilience modeling. Sustainable and Resilient Infrastructure 6, 385–401. https://doi.org/10.1080/23789689.2019.1681821

Rossetto, T., De la Barra, C., Petrone, C., De la Llera, J.C., Vásquez, J., Baiguera, M., 2019. Comparative assessment of nonlinear static and dynamic methods for analysing building response under sequential earthquake and tsunami. Earthquake Engng Struct Dyn 48, 867–887. https://doi.org/10.1002/eqe.3167

Ruiz-García, J., Negrete-Manriquez, J.C., 2011. Evaluation of drift demands in existing steel frames under as-recorded far-field and near-fault mainshock–aftershock seismic sequences. Engineering Structures 33, 621–634. https://doi.org/10.1016/j.engstruct.2010.11.021

Salmon, M.W., Short, S.A., Kennedy, R.P., 1992. Strong motion duration and earthquake magnitude relationships (No. UCRL-CR--117769, 67453). https://doi.org/10.2172/67453

Sanderson, D., Kameshwar, S., Rosenheim, N., Cox, D., 2021. Deaggregation of multi-hazard damages, losses, risks, and connectivity: an application to the joint seismic-tsunami hazard at Seaside, Oregon. Nat Hazards 109, 1821–1847. https://doi.org/10.1007/s11069-021-04900-9

Shi, F., Saygili, G., Ozbulut, O.E., Zhou, Y., 2020. Risk-based mainshock-aftershock performance assessment of SMA braced steel frames. Engineering Structures 212, 110506. https://doi.org/10.1016/j.engstruct.2020.110506

Spence, S.M.J., Arunachalam, S., 2022. Performance-Based Wind Engineering: Background and State of the Art. Front. Built Environ. 8, 830207. https://doi.org/10.3389/fbuil.2022.830207

Su, J., Wu, D., Wang, X., 2023. Influence of ground motion duration on seismic behavior of RC bridge piers: The role of low-cycle fatigue damage of reinforcing bars. Engineering Structures 279, 115587. https://doi.org/10.1016/j.engstruct.2023.115587

Suppasri, A., Koshimura, S., Imamura, F., 2011. Developing tsunami fragility curves based on the satellite remote sensing and the numerical modeling of the 2004 Indian Ocean tsunami in Thailand. Nat. Hazards Earth Syst. Sci. 11, 173–189. https://doi.org/10.5194/nhess-11-173-2011

Tagle, S.J., Jünemann, R., Vásquez, J., de la Llera, J.C., Baiguera, M., 2021. Performance of a reinforced concrete wall building subjected to sequential earthquake and tsunami loading. Engineering Structures 238, 111995. https://doi.org/10.1016/j.engstruct.2021.111995

The Highest and Lowest Income Areas in Seaside, CA, 2023.

Titov, V.V., Moore, C.W., Greenslade, D.J.M., Pattiaratchi, C., Badal, R., Synolakis, C.E., Kânoğlu, U., 2011. A New Tool for Inundation Modeling: Community Modeling Interface for Tsunamis (ComMIT). Pure Appl. Geophys. 168, 2121–2131. https://doi.org/10.1007/s00024-011-0292-4

Todorov, B., Billah, A.H.M.M., 2021. Seismic fragility and damage assessment of reinforced concrete bridge pier under long-duration, near-fault, and far-field ground motions. Structures 31, 671–685. https://doi.org/10.1016/j.istruc.2021.02.019

Toma, M., Oshima, M., Takagi, S., 2016. Decomposition and parallelization of strongly coupled fluid–structure interaction linear subsystems based on the Q1/P0 discretization. Computers & Structures 173, 84–94. https://doi.org/10.1016/j.compstruc.2016.06.001

Umesha, P.K., Venuraju, M.T., Hartmann, D., Leimbach, K.R., 2007. Parallel Computing Techniques for Sensitivity Analysis in Optimum Structural Design. J. Comput. Civ. Eng. 21, 463–477. https://doi.org/10.1061/(ASCE)0887-3801(2007)21:6(463)

Van De Lindt, J.W., Kruse, J., Cox, D.T., Gardoni, P., Lee, J.S., Padgett, J., McAllister, T.P., Barbosa, A., Cutler, H., Van Zandt, S., Rosenheim, N., Navarro, C.M., Sutley, E., Hamideh, S., 2023. The interdependent networked community resilience modeling environment (IN-CORE). Resilient Cities and Structures 2, 57–66. https://doi.org/10.1016/j.rcns.2023.07.004

van de Lindt, J.W., Kruse, J., Cox, D.T., Gardoni, P., Lee, J.S., Padgett, J., McAllister, T.P., Barbosa, A., Cutler, H., Van Zandt, S., Rosenheim, N., Navarro, C.M., Sutley, E., Hamideh, S., 2023. The interdependent networked community resilience modeling environment (IN-CORE). Resilient Cities and Structures, Integrated Modeling of Cities to Improve Natural Hazards Resilience 2, 57–66. https://doi.org/10.1016/j.rcns.2023.07.004

Vicente da Silva, M., Castro, L.M.S., Pereira, E.M.B.R., 2015. On the parallel implementation of a hybrid-mixed stress formulation. Computers & Structures 158, 71–81. https://doi.org/10.1016/j.compstruc.2015.05.022

Wang, J., Li, B., 2022. Seismic fragility analysis of CFT frames with buckling-restrained braces and steel braces under long- and short-duration ground motions. Structures 39, 848–865. https://doi.org/10.1016/j.istruc.2022.03.078

Wang, P.-T., Naaman, A.E., Shah, S.P., 1978. High-Strength Concrete in Ultimate Strength Design. Journal of the Structural Division 104, 1761–1773. https://doi.org/10.1061/JSDEAG.0005033

Wang, T., Han, Q., Wen, J., Wang, L., 2022. Analysis of the Effect of Mainshock-Aftershock Sequences on the Fragility of RC Bridge Columns. Buildings 12, 1681. https://doi.org/10.3390/buildings12101681

Wang, W. (Lisa), van de Lindt, J.W., 2022. Quantifying the effect of improved school and residential building codes for tornadoes in community resilience. Resilient Cities and Structures 1, 65–79. https://doi.org/10.1016/j.rcns.2022.04.001

Wang, W. (Lisa), van de Lindt, J.W., 2021. Quantitative modeling of residential building disaster recovery and effects of pre- and post-event policies. International Journal of Disaster Risk Reduction 59, 102259. https://doi.org/10.1016/j.ijdrr.2021.102259

Wang, W. (Lisa), van de Lindt, J.W., Rosenheim, N., Cutler, H., Hartman, B., Sung Lee, J., Calderon, D., 2021. Effect of Residential Building Wind Retrofits on Social and Economic Community-Level Resilience Metrics. J. Infrastruct. Syst. 27, 04021034. https://doi.org/10.1061/(ASCE)IS.1943-555X.0000642

Wang, W. "Lisa," Watson, M., Van De Lindt, J.W., Xiao, Y., 2023. Commercial Building Recovery Methodology for Use in Community Resilience Modeling. Nat. Hazards Rev. 24, 04023031. https://doi.org/10.1061/NHREFO.NHENG-1728

Watson, M., Xiao, Y., Helgeson, J., Dillard, M., 2020. Importance of Households in Business Disaster Recovery. Nat. Hazards Rev. 21, 05020008. https://doi.org/10.1061/(ASCE)NH.1527-6996.0000393

Wen, W., Zhai, C., Ji, D., Li, S., Xie, L., 2017. Framework for the vulnerability assessment of structure under mainshock-aftershock sequences. Soil Dynamics and Earthquake Engineering 101, 41–52. https://doi.org/10.1016/j.soildyn.2017.07.002

Wijerathne, M.L.L., Hori, M., Kabeyazawa, T., Ichimura, T., 2013. Strengthening of Parallel Computation Performance of Integrated Earthquake Simulation. J. Comput. Civ. Eng. 27, 570–573. https://doi.org/10.1061/(ASCE)CP.1943-5487.0000235

Xu, B., Wang, X., Pang, R., Zhou, Y., 2018. Influence of strong motion duration on the seismic performance of high CFRDs based on elastoplastic analysis. Soil Dynamics and Earthquake Engineering 114, 438–447. https://doi.org/10.1016/j.soildyn.2018.08.004

Xu, C., Deng, J., Peng, S., Li, C., 2018. Seismic fragility analysis of steel reinforced concrete frame structures based on different engineering demand parameters. Journal of Building Engineering 20, 736–749. https://doi.org/10.1016/j.jobe.2018.09.019

Xu, J.-G., Wu, G., Feng, D.-C., Fan, J.-J., 2021. Probabilistic multi-hazard fragility analysis of RC bridges under earthquake-tsunami sequential events. Engineering Structures 238, 112250. https://doi.org/10.1016/j.engstruct.2021.112250

Yu, F., Zeng, Y., Guan, Z.Q., Lo, S.H., 2020. A robust Delaunay-AFT based parallel method for the generation of large-scale fully constrained meshes. Computers & Structures 228, 106170. https://doi.org/10.1016/j.compstruc.2019.106170

Zhang, S., Wang, G., Pang, B., Du, C., 2013. The effects of strong motion duration on the dynamic response and accumulated damage of concrete gravity dams. Soil Dynamics and Earthquake Engineering 45, 112–124. https://doi.org/10.1016/j.soildyn.2012.11.011

Zhang, Y., Peacock, W.G., 2009. Planning for Housing Recovery? Lessons Learned From Hurricane Andrew. Journal of the American Planning Association 76, 5–24. https://doi.org/10.1080/01944360903294556

Zhu, M., 2021. OpenSeesPy Documentation (Technical No. Release 3.2.2.9).